Proceedings of the

XXI INTERNATIONAL SCIENTIFIC CONFERENCE ELECTRONICS AND APPLIED PHYSICS

APHYS 2025

October, 21-24, 2025, Kyiv, Ukraine

Taras Shevchenko National University of Kyiv

Faculty of RadioPhysics, Electronics and Computer Systems

Organizing Committee

A. Netreba, Dean – Chairman, Faculty of RadioPhysics, Electronics and Computer Systems, Taras Shevchenko National University of Kyiv.
O. Nedybaliuk, Deputy Dean – Vice-Chairman, Faculty of RadioPhysics, Electronics and Computer Systems, Taras Shevchenko National University of Kyiv.
V. Moiseienko, Laboratory Head – Secretary, Faculty of RadioPhysics, Electronics and Computer Systems, Taras Shevchenko National University of Kyiv.
I. Anisimov, Head of Department, Faculty of RadioPhysics, Electronics and Computer Systems, Taras Shevchenko National University of Kyiv.
Y. Boyko, Head of Department, Faculty of RadioPhysics, Electronics and Computer Systems, Taras Shevchenko National University of Kyiv.
A. Veklich, Head of Department, Faculty of RadioPhysics, Electronics and Computer Systems, Taras Shevchenko National University of Kyiv.
V. Vysotskiy, Head of Department, Faculty of RadioPhysics, Electronics and Computer Systems, Taras Shevchenko National University of Kyiv.
A. Karlash, Head of Department, Faculty of RadioPhysics, Electronics and Computer Systems, Taras Shevchenko National University of Kyiv.
S. Radchenko, Head of Department, Faculty of RadioPhysics, Electronics and Computer Systems, Taras Shevchenko National University of Kyiv.
S. Savenkov, Head of Department, Faculty of RadioPhysics, Electronics and Computer Systems, Taras Shevchenko National University of Kyiv.
V. Skryshevsky, Head of Department, Educational and Scientific Institute of High Technologies, Taras Shevchenko National University of Kyiv.
M. Bartlova, Associate Professor, Department of Physics, Faculty of Electrical Engineering and Communication, Brno University of Technology, Czech Republic.
O. Bondarchuk, Professor, International Iberian Nanotechnology Laboratory, Braga, Portugal.
S. Nadtochiy, Associate Professor, University of Rochester School of Medicine & Dentistry, Rochester, NY, USA.
I. Fedirchuk, Research Fellow, Antwerpen University, Belgium.
M. Strikha, Professor, Faculty of RadioPhysics, Electronics and Computer Systems, Taras Shevchenko National University of Kyiv.
A. Goriachko, Associate Professor, Faculty of RadioPhysics, Electronics and Computer Systems, Taras Shevchenko National University of Kyiv.
O. Ivanenko, Assistant, Faculty of RadioPhysics, Electronics and Computer Systems, Taras Shevchenko National University of Kyiv.
M. Kononov, Associate Professor, Faculty of RadioPhysics, Electronics and Computer Systems, Taras Shevchenko National University of Kyiv.
R. Bohdanov, Assistant, Faculty of RadioPhysics, Electronics and Computer Systems, Taras Shevchenko National University of Kyiv.
A. Komarov, Assistant, Faculty of RadioPhysics, Electronics and Computer Systems, Taras Shevchenko National University of Kyiv.
A. Konovalov, Assistant, Faculty of RadioPhysics, Electronics and Computer Systems, Taras Shevchenko National University of Kyiv.
O. Murmantsev, Assistant, Faculty of RadioPhysics, Electronics and Computer Systems, Taras Shevchenko National University of Kyiv.
O. Mokhonko, PhD Student, Faculty of RadioPhysics, Electronics and Computer Systems, Taras Shevchenko National University of Kyiv.

General information

Date	October, 21-24, 2025
Location for mails	Taras Shevchenko National University of Kyiv Volodymyrska Str. 64/13, 01601 Kyiv – Ukraine
Physical location	Faculty of RadioPhysics, Electronics and Computer Systems, Taras Shevchenko National University of Kyiv, Prospect Glushkova, 4g, Kyiv 03022, Ukraine
Organization	Taras Shevchenko National University of Kyiv, Faculty of RadioPhysics, Electronics and Computer Systems

Scientific program

The Conference contributions are accepted from the following areas:
Laser Physics and Optoelectronics
Physics of Magnetism
Surface Physics, Nano- and Microelectronics
Physics of Semiconductors and Dielectrics, Semiconductor Devices
Medical Physics
Plasma Physics
Computer Technologies
Radio Engineering and Communications
Polarimetry: Theory and Applications
Mathematical Problems of Applied Physics

Conference site

All events associated with the XXI INTERNATIONAL SCIENTIFIC CONFERENCE ELECTRONICS AND APPLIED PHYSICS will take place in on-line regime in 2025.

Time

Local time is one hour ahead of Middle European time – EEST (UTC+3).

Conference language

The language of the Conference Proceedings is English.

Presentation

The Conference program includes invited lectures and contributed papers. All reports will be lectured in oral presentation.
Invited talks: 40 minutes (including discussion)
Other talks: 20 minutes (including discussion)

Edited by O. Nedybaliuk and A. Netreba

E-mail: aphys@univ.kiev.ua
APHYS web-site: http://www.aphys.knu.ua/

PREFACE

The XXI INTERNATIONAL SCIENTIFIC CONFERENCE ELECTRONICS AND APPLIED PHYSICS (APHYS 2025) will be held October, 21-24, 2025, in the capital of Ukraine Kyiv. The famous scientific and cultural center of Europe welcomes over 100 delegates from different Universities and Scientific Centers of European, American and Asian countries. This conference is dedicated to the 100^{th} anniversary of professor Mykola Hryhorovych Nakhodkin (1925-2018) birthday – an outstanding Ukrainian physicist, academician of the NASU, organizer of national science and higher education.

The goal of APHYS 2025 is to create a forum for discussing recent and relevant achievements in applied physics (radiophysics and electronics), bringing together scientists from various fields of physics, fostering collaboration, and encouraging international research in applied physics. Physics, development, manufacturing, and application of new physical ideas in relevant devices are particularly important for Ukraine as a member of the European community.

The APHYS 2025 is organized by Faculty of Radiophysics, Electronics and Computer Systems of Taras Shevchenko National University of Kyiv.

The Conference technical program is divided into ten sessions; one invited lecture and 66 oral contributions will be presented, discussed and argued.

We believe that APHYS 2025 will provide an opportunity for researchers, postgraduates and students to discuss their problems and provide and inspire the development of future research and success.

We hope the delegates will enjoy the meeting.

The next XXII INTERNATIONAL SCIENTIFIC CONFERENCE ELECTRONICS AND APPLIED PHYSICS (APHYS 2026) will be held in Kyiv, in October, 2026.

We will be glad to see you next year.

Sincerely yours,

Chairman of organizing committee of APHYS 2025 Dr. A. Netreba

INVITED LECTURES

TO THE 100th ANNIVERSARY OF M.G. NAKHODKIN'S BIRTH

I.O. Anisimov
Taras Shevchenko National University of Kyiv,
Faculty of Radio Physics, Electronics and Computer Systems
e-mail: anisimov1958igor@gmail.com

The report is dedicated to the life path and scientific achievements of Mykola Grygorovych Nakhodkin, an outstanding Ukrainian physicist, academician of the National Academy of Sciences of Ukraine, Honored Worker of Science and Technology, and laureate of the State Prizes of Ukraine in Science and Technology

January 25, 2025 marked the 100th anniversary of the birth of Mykola Grygorovych Nakhodkin, an outstanding Ukrainian physicist, academician of the National Academy of Sciences of Ukraine, Honored Worker of Science and Technology, and laureate of the State Prizes of Ukraine in Science and Technology. His entire professional career was connected with Taras Shevchenko National University of Kyiv.

M.G. Nakhodkin was born on January 25, 1925, in the village of Prokhorivka near Kaniv. His father, Gryhorii Pavlovych Nakhodkin (1896-1972), was a surgeon. His mother, Tetyana Yurievna Nakhodkina (Mikhnovska, 1993-1975), worked as a laboratory assistant in medical institutions.

Nikolai Grigoryevich's maternal grandfather was Yuri (Georgy) Mikhnovsky (1866-1937), Archbishop of the Ukrainian Autocephalous Orthodox Church, who was shot by the NKVD on suspicion of anti-Soviet activities.

Mykola Grygorovych's wife, Valentina Zakharovna Nakhodkina (Shegera, 1925-2008), was a candidate of chemical sciences and worked in the sugar industry.

Shortly after the birth of their son, the Nakhodkin family moved to Kyiv. Before the war, they lived in Mykilskaya Slobodka, where Mykola attended school. When the war began, he witnessed with his own eyes the blowing up of the bridges across the Dnieper, which were used by the retreating Red Army units. He witnessed the Old Arsenal building being blown up. During the occupation, Mykola worked as a blacksmith and studied at a river technical school (the only educational institution available to young Kyiv residents at the time).

After the war, M.G. Nakhodkin became a student at Kyiv University. He initially enrolled in the Faculty of Mechanics and Mathematics, but after his first year he transferred to the Faculty of Physics. After graduating from the physics faculty in 1950, he entered graduate school and in 1954 defended his thesis “Investigation of Secondary Emission of Certain Metals and Semiconductors”. The scientific supervisor of this work was N.D. Morgulis, a corresponding member of the Academy of Sciences of the Ukrainian SSR and founder of the Kyiv School of Physical Electronics. In 1966, Mykola Grygorovych defended his doctoral dissertation, “Interaction of Electrons and Soft X-rays with Matter in a Thin Layer”. In 1973, he was elected a corresponding member of the Academy of Sciences of the Ukrainian SSR, and in 1990, a full member of the Academy of Sciences of Ukraine (in the field of “radio physics”).

Since 1952, M.G. Nakhodkin has been working as a lecturer at the Cathedra of Electronics, headed by N.D. Morgulis. The Faculty of Radio Physics was established on the basis of this department.

In 1972, M.G. Nakhodkin organized the Cathedra of Cryogenics and Microelectronics (now the Department of Nanophysics and Nanoelectronics) at the Faculty of Radio Physics, which he headed for 26 years. On his initiative, two scientific laboratories (electronic spectroscopy and optical information processing and theory of media) were opened at the department. In 1981, a branch of the cathedra was opened at the S.P. Korolev Kyiv Production Association, and in 1989, a branch of the cathedra of high-temperature superconductivity was opened at the Institute of Metal Physics of the Academy of Sciences of the Ukrainian SSR.

In 1972, M.G. Nakhodkin was elected dean of the Faculty of Radio Physics (since 2014 – the Faculty of Radio Physics, Electronics and Computer Systems) of the Taras Shevchenko State University of Kyiv (now Taras Shevchenko National University of Kyiv). He held this position for 19 years. As a leader, he created a highly effective team of like-minded people, which included, in particular, his deputies P.S. Kuts and P.V. Melnik, department heads D.O. Gorodetsky, V.V. Danilov, S.M. Levitsky, V.I. Stryha, and Y.I. Chutov. On his initiative, the Department of Medical Radio Physics was organized at the Faculty of Radio Physics (headed by Mykola Hryhorovych's student M.K. Novoselets) and a special faculty for retraining personnel in the field of functional electronics and high-temperature superconductivity. Leading specialists of the Academy of Sciences of the Ukrainian SSR were invited to teach at the faculty, in particular, academicians V.G. Baryakhtar, M.S. Brodin, A.G. Naumovets, corresponding members M.O. Kryvoglaz, V.G. Litovchenko, E.G. Petrov, S.M. Ryabchenko, M.S. Soskin, P.I. Fomin, M.K. Sheinkman. The working style and traditions of the faculty, formed at that time, have largely been preserved to this day.

M.G. Nakhodkin devoted a lot of effort to organizing the scientific and industrial association “Electronics”, whose goal was to coordinate the work of relevant higher education institutions, scientific institutes, and industrial establishments in the field of training highly qualified specialists in electronics, conducting relevant research, and implementing its results in industry.

Science has always been at the center of Mykola Grygorovych's professional interests. A brilliant experimenter, he achieved a number of fundamental results in the fields of physical electronics, surface physics, and nanophysics. The result of Mykola Grygorovych's many years of scientific work was the formation of a scientific school of emission electronics and electronic spectroscopy, which he headed and which continues the tradition of the school of physical electronics of his teacher N.D. Morgulis. Among his students are 5 doctors and 29 candidates of science, winners of the State Prizes of Ukraine in the field of science and technology.

Nakhodkin M.G.'s scientific achievements include more than 350 scientific works and 41 author's certificates. With the participation of Mykola Grygorovych and under his editorship, 3 monographs have been published.

In 1970, M.G. Nakhodkin became a laureate of the UkrSSR State Prize in Science and Technology for a series of works related to thermoplastic information recording. In 1997, he was awarded the State Prize of Ukraine in Science and Technology for a series of works on the study of a number of new effects on the surface of a solid body, in particular, the effect of interference of channels of elastic and inelastic scattering of medium-energy electrons, the use of which made it possible to develop new methods for diagnosing surfaces.

M.G. Nakhodkin led creative teams of Ukrainian physicists working on solving the problem of “Physical, chemical, structural, and emission properties of thin films and solid surfaces”. For a long time, together with Nobel laureate Zh.I. Alferov, he headed the Ukrainian-Russian program on nanoelectronics.

M.G. Nakhodkin devoted a lot of energy and effort to scientific and organizational activities. At the same time, he was able to think on a scale that encompassed not just a single scientific or educational institution, but the entire country. Back in the late 1950s, while working on the research project “Cathode,” led by N.D. Morgulis, he visited all the factories in the USSR that produced electronic tubes. The project resulted in specific recommendations that were implemented at all Soviet enterprises in the relevant field.

In the early 1960s, M.G. Nakhodkin was actively involved in a working group, which resulted in the creation of the Ministry of Electronic Industry of the USSR. The members of the working group were received by M.S. Khrushchev to discuss this issue.

M.G. Nakhodkin was deputy chairman of the Scientific and Technical Council of the Ministry of Higher and Secondary Specialized Education of the Ukrainian SSR for six years, a member of the section of the Committee

on State Prizes of the Ukrainian SSR, chairman of the section and member of the presidium of this committee, one of the founders and first president of the Ukrainian Committee of the Radio Union (URSI branch).

In the 1990s, Mykola Grygorovych was one of the initiators and chairman of the National Council for Science and Technology, a member of the Main Council of the Higher Attestation Commission of the Cabinet of Ministers, and chairman and member of the Expert Council of the Higher Attestation Commission of Ukraine.

M.G. Nakhodkin was a member of the editorial board of the Ukrainian Physical Journal, a member of the editorial board of the Journal of Scientific and Applied Photography and Cinematography (published by the USSR Academy of Sciences), the collections Quantum Electronics, "Physics of Semiconductors and Dielectrics", "Physical Electronics", and was a member of the editorial board of the "Bulletin of Kyiv University". He was the founder and, for 20 years, editor-in-chief of the interdepartmental collection "Fundamental Principles of Optical Memory and Media".

Mykola Grygorovych was a member of the Scientific Councils on Physical Electronics and Holography of the USSR Academy of Sciences, several sections of the Ukrainian Academy of Sciences, scientific director of several interdepartmental scientific programs and programs of the Ministry of Education of Ukraine, and a member of the presidium of the Department of Physics and Astronomy of the National Academy of Sciences of Ukraine.

Until the last days of his life, Mykola Grygorovych continued to work as a teacher. He knew how to convey the most complex material to students and built the educational process based on scientific work. M.G. Nakhodkin's rich teaching experience is embodied in three textbooks and two teaching aids, which are very popular with both students and colleagues.

Mykola Grygorovych's achievements were recognized with the Order of Honor, medals, certificates of honor from the Presidium of the Supreme Soviet of the Ukrainian SSR and the Supreme Council of Ukraine (2002), a certificate of honor from the Cabinet of Ministers of Ukraine (2004), and an award from the National Academy of Sciences of Ukraine. and he was a full Knight of the Order of Merit. In 1995, Mykola Grygorovych was awarded the title of "Honored Worker of Science and Technology." In 1999, he became an Honored Professor of Taras Shevchenko National University of Kyiv. A minor planet, 8065 Nakhodkin=1979 FD3 (1989), was named in his honor.

Mykola Grygorovych was an extremely demanding and wise man, an excellent leader and organizer, and a person of high moral character. His participation in any meeting guaranteed that the discussion would be both critical and constructive.

M.G. Nakhodkin was a highly cultured man who loved art, literature, and poetry in particular. When the mass demolition of pre-revolutionary buildings began in Kyiv, he took a unique series of photographs of old houses that no longer exist today.

The grateful memory of Mykola Grygorovych Nakhodkin – an outstanding scientist, teacher, talented organizer of science and higher education, a wonderful person, and a patriot of his homeland – is preserved in the hearts of his family and friends, numerous colleagues and students, and all who knew him.

LASER PHYSICS AND OPTOELECTRONICS

PULSED INFRARED IRRADIATION EFFECTS ON THE MICROWAVE RESPONSE OF A MOLYBDENUM–RHENIUM ALLOY MICROSTRIP SUPERCONDUCTING RESONATOR

O.A. Kalenyuk*,, S.I. Futimsky*,**, I. O. Martynenko*,**, A.P. Shapovalov*,****
** G. V. Kurdyumov Institute for Metal Physics, N.A.S. of Ukraine, Kyiv, 03142, Ukraine*
*** Kyiv Academic University, Kyiv, 03142, Ukraine*

The time-dependent microwave response of a fractal microstrip superconducting resonator made of Moret alloy under pulsed infrared irradiation was investigated. An instantaneous reaction to the pulse onset was observed, followed by a slow relaxation of the activated losses at the resonance frequency. The detection sensitivity of the system was also calculated.

Introduction

Superconducting thin films are highly sensitive detectors of a wide range of electromagnetic radiation. Two main detection principles are commonly employed: bolometric and kinetic. The bolometric method relies on the sharp change in resistance—from nearly zero in the superconducting state to a large value in the normal state—upon photon absorption. This approach is typically implemented using superconducting nanowires biased with currents close to their critical values. When a photon is absorbed, a transverse hotspot is formed, which rapidly self-heats and expands along the nanowire. In this way, even single photons can be detected. However, the system operates in a two-state regime and is thus more suitable as a photon counter. It requires a complex measurement setup with multiple wiring connections and a recovery circuit to return the nanowire to the superconducting state after each detection event. During the recovery period—from photon absorption to the restoration of superconductivity—the detector remains inactive, introducing a so-called *dead time*. As a result, continuous detection becomes impossible.

In contrast, the kinetic detection method exploits the breaking of Cooper pairs upon photon absorption, which alters their concentration. Since the binding energy of Cooper pairs is very low, on the order of ~1 meV, photons with frequencies above ~100 GHz can be detected. A change in the concentration of superconducting pairs modifies the kinetic inductance of the film, thereby shifting the resonance frequency of a resonator fabricated from such a film. For this purpose, large arrays of resonators with different resonance frequencies are often employed, all coupled to a single microwave transmission line. The use of resonators narrows the signal bandwidth, leading to a significant improvement in noise performance. The main drawback of this method is the extremely low operating temperatures—on the order of hundreds of millikelvin—which severely limits practical applications. Consequently, such detectors are mainly used in astronomy.

In many practical scenarios, however—such as in medical applications or security sensing—the ultimate sensitivity to single photons is not required. Therefore, we propose a hybrid detection approach, combining both bolometric and kinetic mechanisms, by developing an infrared detector based on the response of a superconducting MoRe fractal microstrip resonator operated at temperatures close to its critical temperature.

Experimental Procedure

The microwave response of a fractal superconducting microstrip MoRe resonator [1] was measured using a two-port method. The resonator was exposed to pulsed infrared radiation. As a source of infrared radiation, a tungsten filament of a miniature incandescent lamp was employed. The glass bulb of the lamp exhibits strong absorption in the infrared region for wavelengths longer than 4 μm [2]. To suppress radiation with wavelengths shorter than 1 μm, a silicon wafer of 0.5 mm thickness was used as an optical filter. Thus, the resonator was irradiated by the emission from the tungsten filament in the wavelength range of 1–4 μm. The resonator was mounted on a copper sample holder. The lamp, silicon filter, and resonator were all placed in a helium vapor environment at a temperature of 4.65 K to ensure efficient cooling during the measurements. The measured values of the unloaded quality factor and the resonant frequency of the resonator were approximately $Q_0 \approx 1800$ and

f_0=1.71 GHz respectively. The excitation frequency was tuned to the resonant frequency f_0. The time-dependent characteristics of the insertion loss (*IL*) were recorded (fig. 1). This parameter represents the ratio of the transmitted power P_{out} to the input probing power P_{in} through the resonator and is expressed in decibels (dB). As can be seen, when the IR pulse arrives, the insertion loss (*IL*) rapidly decreases with a delay of about 10 ms. At this moment, the filament power is approximately 1 mW (fig.1 b)) at a filament temperature of 780 K [1]. The power directly incident on the resonator at the onset of detection was estimated. The resonator, measuring 3.7 × 3.7 mm², is positioned 7.5 mm from the filament, which is approximated as a point source. Under this assumption, the incident power on the resonator is approximately 20 μW. Accounting for transmission losses through the lamp's glass envelope (~10%) and the silicon wafer (~50%), as well as the relatively low emissivity of the tungsten filament at 780 K (~10% of a blackbody), the effective power reaching the resonator is reduced to roughly 0.9 μW. This corresponds to a detectable flux of approximately 0.066 W/m², consistent with the sensitivity threshold of the detection system. As shown in Fig. 1(b), the response rate of the system is equal to or exceeds the rate of increase of the filament's radiated power. After the pulse ends, a slow recovery of the resonator response occurs with a relaxation time of $\tau \approx 0.3$ s, corresponding to a thermal relaxation process.

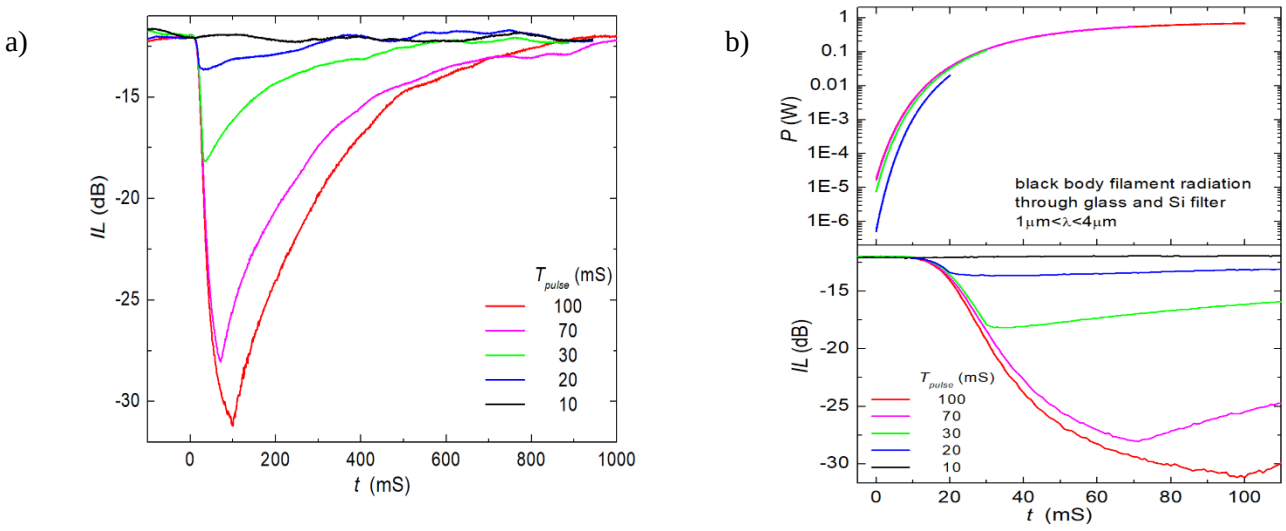

Fig. 1. Effect of an infrared (IR) pulse on the MoRe superconducting resonator, shown as the time dependence of the insertion loss a). Time dependence of the infrared (IR) pulse power emitted by the blackbody filament in the wavelength range of 1–4 μm b)

Acknowledgments

This research was carried out within the framework of the project 2023.04/0157 funded by the National Research Foundation of Ukraine «High-speed matrix kinetic detector of long-wave infrared radiation».

References

[1] O.A. Kalenyuk, S.I. Futimsky , I.A. Martynenko, A.P. Shapovalov, V.I. Shnyrkov , and A.A. Kordyuk. Development of microwave kinetic inductance detectors suitable for fast infrared thermography. Fizyka Nyzkykh Temperatur/Low Temperature Physics, 2025, Vol. 51, No. 11

[2] M. Dauphin, S. Albin, M. El-Hafi, Y.Le Maoult, F.M. Schmidt, Towards thermal model of automotive lamps, *Proc. 11 international conference on Quantitative Infrared Thermography*, Naples, Italy (2012), p. 10. http://dx.doi.org/10.21611/qirt.2012.262

REFRACTORY METAL VAPOR LASERS: EXPERIMENT VS. THEORY

Oleksii Komarov*, Andrii M. Dobrovolskiy**
** Institute of Physics of the National Academy of Sciences of Ukraine, Kyiv, Ukraine, e-mail: alexis.komarov@iop.kiev.ua*
*** Institute of Physics of the National Academy of Sciences of Ukraine, Kyiv, Ukraine, e-mail: dobr@iop.kiev.ua*

Experimentally demonstrated Ta and V metal vapor lasing supports theoretical models for refractory metal lasers, suggesting Mo and W systems are feasible at vapor densities ≥10^{15} cm^{-3} under high-density ablation or HiPIMS vapor generation.

Introduction

Metal vapor lasers (MVLs) were developed in the 1950s–1960s alongside dye and semiconductor lasers. Despite the commercial dominance of CO_2, fiber, and diode-pumped solid-state lasers, MVLs remain scientifically important due to their access to hundreds of discrete UV–visible wavelengths (224–6457 nm), nanosecond pulse durations, narrow spectral lines, and high repetition rates. Emission has been reported for >30 metals and select metalloids. This work connects experimentally demonstrated Ta and V MVLs to semi-classical modeling for refractory and actinide metals and evaluates lasing feasibility for Mo, W, Hf, Re, Th, and U using theoretical criteria.

Experimental background

Tantalum (Ta) and vanadium (V) lasing have been demonstrated using pulsed Nd:YAG ablation to generate vapor plumes and excimer pumping (KrF 248 nm for Ta; XeCl 308 nm for V). Reported small-signal gains lie in the ~0.09–0.46 cm^{-1} range and peak outputs in published conditions reach up to tens of watts for Ta and single-digit watts per pulse for V. Reported optical-to-optical efficiencies are very low ($\lesssim 10^{-4}$ in published plume experiments). These empirical benchmarks provide targets for model validation and for setting experimental thresholds.

Methodology of Refractory Metal Lasing Feasibility Analysis

The assessment of lasing feasibility in refractory metals (Mo, W, Hf, Re, Th, U), copper (Cu), tantalum (Ta), and vanadium (V) employs a blend of semi-classical and classical methodologies.

Semi-classical rate equations and gain estimation for a 3-level system:

$$\frac{dN_2}{dt} = W_p N_1 - \frac{N_2}{\tau_{21}} - \sigma_{\text{stim}} I (N_2 - N_1)$$

Where W_p is the pump rate, τ_{21} – upper-state lifetime, σ_{stim} – stimulated emission cross-section, $\Delta N = N_2 - N_1$ is the population inversion.

Population inversion linking gain to inversion density:

$$\gamma = \sigma_{\text{stim}} \Delta N$$

Laser gain threshold equation used to calculate minimum gain required for lasing:

$$\gamma_{\text{th}} = \frac{-\ln(R_1 R_2)}{2L} + \alpha_{\text{scattering}}$$

Stimulated emission cross-section used to relate Einstein coefficients (A_{21}) to gain:

$$\sigma_{\text{stim}} = \frac{\lambda^2 A_{21}}{8\pi\Delta\nu}$$

The framework uses two- or three-level rate equations to model population dynamics, leveraging Einstein coefficients (A_{21}) and phenomenological inversion fractions ΔN (10–25%) to estimate gain. In addition, adjustments for Doppler and Stark broadening are made to the semi-classical rate equations.

Conclusions

In summary, the measured lasing gains and outputs for Ta and V fall in line with semi-classical model predictions. Theoretical estimates for group-6 metals indicate comparable or higher gains under analogous conditions, marking Mo and W as strong candidates for future in-depth modeling and experiments. In all cases, the very low optical efficiencies mean that only high-peak-power pumping (e.g. KrF/XeCl lasers or pulsed ablation) can reach threshold. These results underline that Ta and V lasing are well-explained by the model, and motivate exploration of Mo, W, (with Re, Hf, Th, U as lower priory) vapors using high-density techniques (e.g. femtosecond ablation or HiPIMS) as feasible new laser media.

As expected, the lasing potential of neutral copper vapor at these densities and temperatures is high, the calculated small-signal gain coefficients exceed the threshold by $10^{1.7} – 10^3$ orders of magnitude. It should be noted that conventional copper vapor lasers operate at around 1,550 K for pure Cu vapor or at 700–750 K in copper-bromide systems, aligning with the calculated optimal operating temperature near 700 K.

For refractory metals, molybdenum (Mo) exhibits robust lasing potential in both neutral (Mo I, 550 nm) and singly ionized (Mo II, 340 nm) states at 700 K, requiring vapor densities exceeding 10^{15} cm^{-3}. Similarly, tungsten (W) demonstrates strong lasing activity in neutral (W I, 600 nm) and ionized (W II, 400 nm) configurations at 750 K, with comparable density thresholds. Hafnium (Hf) shows moderate feasibility in its singly ionized state (Hf II, 290 nm) at 600 K, though requiring higher vapor densities ($>3\times10^{15}$ cm^{-3}). Rhenium (Re) displays weaker but discernible potential in neutral (Re I, 620 nm) and ionized (Re II, 360 nm) transitions at 800 K, contingent on achieving 10^{15} cm^{-3} vapor densities.

References

[1] Fowles, G. R., & Silfvast, W. T. (1965). High-gain laser transition in lead vapor. *Applied Physics Letters*, *6*(12), 236-237.
[2] Little, C.E., Metal vapour lasers: Physics, engineering and applications (1999).
[3] Yoshida, H., Takashima, N., & Ninomiya, H., Appl. Phys. Lett. 59, 1290 (1991).
[4] Yoshida, H., Ninomiya, H., & Takashima, N., J. Appl. Phys. 70, 7253 (1991).
[5] Yoshida, H., Takashima, N., & Ninomiya, H., J. Appl. Phys. 71, 1044 (1992).
[6] Jones, D.R., Maitland, A., & Little, C.E., IEEE J. Quantum Electron. 30, 2385 (1994).

PHOTOINDUCED EXCITATION OF AUTOWAVE AND CHAOTIC SCATTERING IN PHOTOREFRACTIVE MEDIA

V. Lemeshko

Faculty of RadioPhysics, Electronics and Computer Systems Taras Shevchenko National University of Kyiv, Kyiv 01601, Ukraine, e-mail: vvlem@knu.ua

Autowaves of scattering can appear under excitation of nonlinear crystal by focused laser radiation as moving light ring structures. Periodic behavior of the ring generation could be related to competition of two types of refractive index gratings (reflecting and transmission gratings). Chaotic regime arises if control parameters (pump intensity, impurity concentration) are under threshold. The correlation characteristics of self-wave scattering of light in lithium niobate crystals have been studied. It is shown that the temporal oscillations of the self-wave scattering process have periodic and stochastic components. At the same time, in the suprathreshold generation regime, the spatial distribution of self-waves has a correlation radius comparable to the radius of the optical self-wave ring.

Photorefractive lithium niobate crystals are a promising medium for optical recording of information. However, their practical application is constrained, in particular, by the effect of photorefractive light scattering, which plays the role of a powerful optical noise in holographic recording. The development of PRLS in LiNbO3 crystals is least effective when propagating exciting light beams at small angles to the optical axis of the crystal. When studying the effects of photoinduced light scattering that arise during holographic recording in z-sections of LiNbO3:Fe crystals, a new phenomenon called autowave light scattering (AWS) was discovered [1] which appeared in the form of the backward scattering (quasi)periodically oscillating in time.

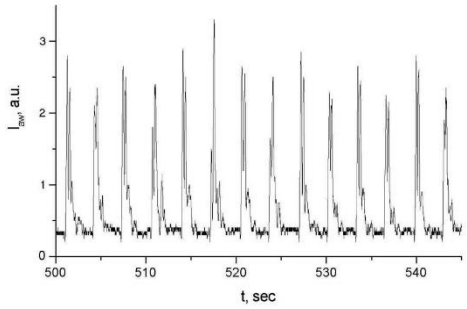

Fig. 1. AWS temporal dependence

The conception of running waves of impurity centers overcharge [2] could be used to explain the AWLS effect. Instabilities could appear in nonlinear system “photorefractive crystal + laser radiation” which can lead to formation of different transversal structures [3-5]. Spatial-temporal instabilities in this kind of system were considered in [6, 7]. The theory below is based on their results.

Let us consider a photorefractive nonlinear crystal without inversion centre. The crystal is illuminated by stationary laser beam of TEM00 mode. The following calculation geometry is used: the central wave vector of the pump beam is directed along Z axis (the latter can be parallel or antiparallel to optical axis C of the crystal). The pump polarization is in XY plane, the origin of coordinates is placed in the pump beam centre on the front crystal side (see fig. 1). Symmetry group of the crystal is 3m, its thickness is *l*. The crystal is considered infinite in transversal direction (in XY plane).

Laser field in the crystal could be presented as follows:

$$\mathbf{E}^{\omega} = \mathbf{A}_1(\mathbf{r},t)\exp\left[i\left(k_0 z - \omega t\right)\right] + \mathbf{A}_{-1}(\mathbf{r},t)\exp\left[-i\left(k_0 z + \omega t\right)\right] + c.c.$$

and shortened equations for amplitudes of direct A_1 and backward A_{-1} waves take such a form:

$$\begin{cases} \dfrac{\partial \mathbf{A}_1}{\partial z} - \left(\dfrac{i}{2k_0}\right)\Delta_\perp \mathbf{A}_1 = i\dfrac{k_0}{2\varepsilon_0}\left[\Delta\hat{\varepsilon}_0\,\mathbf{A}_1 + \left(\Delta\hat{\varepsilon}_2 + \delta\,\hat{\varepsilon}_2(\vec{\mathbf{r}})\right)\mathbf{A}_{-1}\right] \\ \dfrac{\partial \mathbf{A}_{-1}}{\partial z} + \left(\dfrac{i}{2k_0}\right)\Delta_\perp \mathbf{A}_{-1} = -i\dfrac{k_0}{2\varepsilon_0}\left[\hat{\Delta}\varepsilon_0\,\mathbf{A}_{-1} + \left(\Delta\,\hat{\varepsilon}_2^* + \delta\,\hat{\varepsilon}_2^*(\mathbf{r})\right)\mathbf{A}_1\right] \end{cases}$$

The general equation system describing interaction of light waves with photorefractive medium, subject to longitudinal and transversal components of internal electric field, can be written down in the following form:

$$\frac{\partial}{\partial z}A_1 - ip_0\Delta_\perp A_1 = i\left(W_\parallel + W_\perp + \delta W\right)A_{-1}$$

$$\frac{\partial}{\partial z}A_{-1}^* - ip_0\Delta_\perp A_{-1}^* = i\left(W_\parallel + W_\perp + \delta W\right)A_1^*$$

$$\tau_\perp\frac{\partial}{\partial t}W_\perp + W_\perp = -Q_\perp A_1 A_{-1}^* + iM_\perp W_\parallel - R_\perp^n(\mathbf{r})$$

$$\tau_\parallel\frac{\partial}{\partial t}W_\parallel + W_\parallel\left(1 - iM_\parallel\right) = -\left(Q_\parallel + iD\right)A_1 A_{-1}^* - R_\parallel^n(\mathbf{r})$$

Solution of the inhomogeneous linear differential equation system has got the following form:

$$\tilde{W}_\parallel(\mathbf{q},s,t) = I_0\left[R_1 + \frac{R_1\alpha_2 - R_2}{\alpha_1 - \alpha_2}\exp\left[\lambda_1 t\right] + \frac{R_2 - \alpha_1 R_1}{\alpha_1 - \alpha_2}\exp\left[\lambda_2 t\right]\right],$$

$$\tilde{W}_\perp(\mathbf{q},s,t) = I_0\left[R_2 + \alpha_1\frac{R_1\alpha_2 - R_2}{\alpha_1 - \alpha_2}\exp\left[\lambda_1 t\right] + \alpha_2\frac{R_2 - \alpha_1 R_1}{\alpha_1 - \alpha_2}\exp\left[\lambda_2 t\right]\right],$$

Theoretically calculated spatial and temporal characteristics of optical autowaves are well compliant with the experimental data for $LiNbO_3 : Fe$ crystals.

The following conclusions can be drawn based on the theory developed above:

Both longitudinal and transversal photovoltaic/diffusive currents should be taken into account to describe optical autowave generation effect. Under discussed conditions, the transversal currents destroy stationary charge redistribution created by longitudinal currents which results in appearance of cyclic (in time) charge transfer.

Autowave light scattering is a threshold effect: periodic in time conic radiation appears in a photorefractive crystal when control parameters (pump intensity, photoactive impurity concentration) exceed the appropriate critical values.

References

1. V.V.Lemeshko and V.V.Obukhovsky, "Autowaves of photoinduced light scattering," Sov. Tech. Phys. Lett. 11, 573-574 (1985).
2. A.S. Furman, "Spontaneous growth of trap charge exchange waves in crystals without inversion center under homogeneous illumination," Sov. Phys. Solid State 29 (1987) (Fizika Tverd. Tela 29, 1076-1085 (1987)).
3. M. Safiman, A. Zozulya, D.Z. Anderson, "Transverse instability of energy-exchanging counterpropagating waves in photorefractive media," J. Opt.Soc.Am. B 11, 1409-1417 (1994).
4. J. Leonardy, F. Kaiser, M. Belic, O. Hess, "Running transverse waves in optical phase conjugation", Phys. Rev. A 53, 4519-4527 (1996).
5. O. Sandfuchs, J. Leonardy, F. Kaiser and M. Belic, "Transverse instabilities in photorefractive counterpropagating two-wave mixing," Opt.Lett. 22, 498-500 (1997)
6. A.N. Morozovskaya and V.V. Obukhovskii, "Autowave Instability in Refractive Crystals," Optics and Spectroscoopy 88, 225-231 (2000).
7. A.N. Morozovskaya and V.V. Obukhovskii," Optical Autowaves in Photorefractive Ferroelectric Crystals," Optics and Spectroscoopy 98, 247-257 (2005).

SURFACE PHYSICS, NANO- AND MICROELECTRONICS

OPTIMIZATION OF CHROMATIC SPR SENSOR FOR GASEOUS MEDIUM BASED ON REFLECTED BEAM COLOR REGISTRATION: MODELING AND EXPERIMENT

A.I. Biletskiy, O.L. Kukla, O.N. Fedchenko

V.E. Lashkaryov Institute of Semiconductor Physics, National Academy of Sciences of Ukraine, 03028, Kyiv, Nauky Ave., 41, Ukraine, e-mail: belanton11@gmail.com

In this work, the modeling of the optical characteristics of a SPR chromatic sensor for detecting gaseous media is presented, which works on the principle of registering color spectrum responses of the reflected beam during SPR excitation in thin films of highly conductive metals in the Kretschmann configuration. Modeling takes into account the spectral characteristics of all components of the optical system: the radiation source, the multilayer plasmon-generating structure, and the photodetector (webcam). A comparative analysis of the sensitivity of multilayer structures with films of various highly conductive metals: silver (Ag), gold (Au), copper (Cu), and aluminum (Al) was carried out. The developed approach, which includes the calculation of the reflection coefficient using the Jones matrix method and spectral integration of R, G, B components, allows predicting the colorimetric response of the sensor and evaluating its instrumental sensitivity.

Abstract

In this work, the modeling of the optical characteristics of a SPR chromatic sensor for detecting gaseous media is presented, which works on the principle of registering color spectrum responses of the reflected beam during SPR excitation in thin films of highly conductive metals in the Kretschmann configuration. Modeling takes into account the spectral characteristics of all components of the optical system: the radiation source, the multilayer plasmon-generating structure, and the photodetector (webcam). A comparative analysis of the sensitivity of multilayer structures with films of various highly conductive metals (silver, gold, copper, and aluminum) was carried out. The developed approach, which includes the calculation of the reflection coefficient using the Jones matrix method [1] and spectral integration of R, G, B components, allows predicting the colorimetric response of the sensor and evaluating its instrumental sensitivity.

Introduction

The effect of surface plasmon-polariton resonance (SPR) is a reliable method for developing sensors that respond to changes in the refractive index of adjacent media. Although traditional SPR sensors use expensive spectrophotometers or goniometric tables, interest in chromatic SPR sensors has recently been growing. They use simple colorimetric registration of reflected light using readily available web cameras (CMOS-matrices), which significantly simplifies the final device [2]. However, the transition to the colorimetric method requires a review of modeling approaches. The physical response of the sensor, registered by a web camera, is not simply a reflection spectrum, but an integral photo-signal, which depends on the spectrum of the radiation source, the spectral transfer function of the multilayer structure, and the spectral sensitivity of the camera's RGB filters [3]. Neglecting these factors leads to an incorrect assessment of instrumental sensitivity. The goal of this work is to develop a detailed model for calculating the color response of a chromatic SPR sensor with multilayer structures based on various plasmon-generating metals (Ag, Au, Cu, Al) and experimental verification of the model for optimizing a gaseous medium sensor [4].

Modeling of Response

To obtain the integral color response corresponding to the web camera signal, an integral approach was applied. The signal registered by the k-th photodetector is the integrated product of three key spectral functions in the range of λ=400...700 nm:

$$I_k(\theta) = \int S(\lambda)\, R(\lambda,\theta)\, F_k(\lambda)\, d\lambda, \quad k \in \{R, G, B\}$$

- $S(\lambda)$ – Measured spectrum of the light source (LED).
- $R(\lambda,\theta)$ – Calculated reflection coefficient of the multilayer structure (by the Jones matrix method).
- $Fk(\lambda)$ – Spectral transfer function (sensitivity) of the photodetector ($k \in$ R, G, B component) of the web camera.

Calculating the integral R, G, B functions with changing angle θ allows simultaneously obtaining three independent signals, which are the color transfer function of the entire sensor. The construction of these functions enables the transition from the obtained angular dependencies of the R, G, B color components to a computer color scale for the purpose of constructing the resulting model reflection spectrum.

Results and Discussion

Extended modeling of the SPR response for different metals confirmed their different functionalities in the visible spectrum: **Silver:** Provides a full-fledged SPR across the entire visible range (400-700 nm). The high quality of the resonance makes it ideal for a chromatic sensor using three color channels. **Gold and Copper:** Due to high losses (large imaginary part ϵ''), effective SPR is realized only in the long-wavelength region (from 550 nm and 600 nm, respectively). This limits their effectiveness for R,G,B-detection, but allows them to be used for sensors with red and partially green response. **Aluminum:** Best suited for the short-wavelength (blue) region of the spectrum, where other metals have significant limitations.

Conclusions

A comparison of the calculated color reflection spectra with experimentally obtained images from the web camera showed a fairly good similarity and confirmed the correctness of the proposed integral model. This proves that accurate consideration of the spectral characteristics of the light source and photodetector is necessary for detailed prediction of the instrumental sensitivity of chromatic SPR sensors. A method for detailed modeling of the optical characteristics of a chromatic SPR sensor for detecting gaseous media has been developed and implemented, which takes into account the spectral characteristics of all components (source, multilayer film structure, R, G, B photodetector) of the optical system. Modeling the reflection coefficient in the visible range of 400-700 nm and integral calculations of the color spectra allow accurately predicting the response of the sensor system. It is shown that the detection of the color of the reflected SPR beam provides the possibility of obtaining multi-responses due to the use of different wavelengths in certain ranges of the light incidence angles.

References

[1] R.M.A. Azzam, N.M. Bashara. *Ellipsometry and Polarized Light*. North-Holland Publishing Company, 1977. 529 p.

[2] O.V. Riabchenko, O.L. Kukla, O.N. Fedchenko, Yu.M. Shirshov, Z.I. Kazantseva. SPR chromatic sensor with colorimetric registration for detection of gas molecules. *Semiconductor Physics, Quantum Electronics & Optoelectronics*. 2023. V.26. No.3. P. 343-351.

[3] T.-Z. Lin, C.-H. Chen, Y.-P. Lei and C.-S. Huang. Gradient guided-mode resonance biosensor with smartphone readout. *Biosensors*, 2023, 13, 1006.

[4] O.L. Kukla, Yu.M. Shirshov, A.I. Biletskiy, O.N. Fedchenko. Spectral SPR effect in thin films of high-conductive metals and features of implementation of SPR-biosensors in chromatic mode. *Semiconductor Physics, Quantum Electronics & Optoelectronics*. 2024. V.27. No.4. P. 478-488.

DISORDER-ENHANCED SUPERCONDUCTIVITY IN AMORPHOUS MOLYBDENUM SILICIDES

D. Mindich*, I. Martynenko*, O. Zraichenko, O. Leha**, V. Lyakhno**, A. Shapovalov****
**Kyiv Academic University, Academician Vernadsky Blvd. 36, 03142 Kyiv, Ukraine*
*** B.Verkin Institute for Low Temperature Physics and Engineering of NAS of Ukraine,*
47 Nauky Ave., Kharkiv, 61103, Ukraine
e-mail: d.mindich@kau.edu.ua, dennis.mindich.official@gmail.com

The relationship between superconductivity and disorder remains a key challenge in condensed matter physics. According to BCS theory, superconductivity originates from the formation of Cooper pairs that create a macroscopic quantum coherent state. The Anderson theorem states that weak disorder preserving time-reversal symmetry does not affect superconductivity, but this applies only to ideal isotropic and homogeneous materials. Later studies showed that in non-uniform systems, disorder can degrade or even enhance superconducting properties. Consequently, our research focuses on exploring and explaining disorder-enhanced superconductivity in amorphous molybdenum silicates.

Introduction

Amorphous solids, which are disordered assemblies of atoms or larger particles, possess mechanical rigidity without the thermodynamically stable, stress-free microstructure characteristic of crystalline solids. Since the earliest experiments with films deposited on cryogenically cooled substrates, amorphous superconducting materials have been the subject of extensive experimental and theoretical exploration [1]. Early studies indicated that atomic-scale disorder can enhance electron-phonon coupling when transitioning from crystalline to amorphous states. MoSi-based structures are highly promising for single-photon detection in the microwave and millimeter-wave frequency ranges, where conventional detectors lose efficiency [2]. Their integration into superconducting circuits enables the development of tunable photon detectors and low-noise amplifiers. Traditional SNSPD materials like NbN are limited to a narrow infrared range due to their large superconducting gap and sensitivity to crystalline defects. Extending detection to longer wavelengths remains challenging, especially since common fabrication techniques restrict compositional control. Amorphous superconductors such as MoGe, MoC, WSi, and particularly MoSi offer improved performance and flexibility. MoSi, with a Tc of about 7.5 K and strong superconducting stability even in ultrathin films, allows efficient operation using simpler and more affordable cryogenic systems [3].

Experimental and Discussion

Our technological capabilities enable precise tuning of the normal resistance value of the MoSi superconducting film by controlling its thickness and composition. Films were produced by DC magnetron sputtering from two separate sources within argon gas so we can modify the film composition. The surface morphology of the obtained MoSi films was studied using AFM. Figure 1a shows the characteristic appearance of the MoSi film surface, which is distinguished by the absence of defects — a major advantage for the fabrication of modern micro- and nanoelectronic devices. Since XRD analysis shows that there are no additional peaks on the diffraction pattern (Fig. 1b), it can be concluded that the films are amorphous. The superconducting properties of the samples were measured using the four-point probe technique. The samples were mounted on a rod and placed in a liquid helium dewar, where they were gradually cooled during immersion. The observed hysteresis is attributed to the specifics of the measurement procedure — data were collected both during cooling of the samples to liquid helium temperature and during their subsequent warming to room temperature (Fig. 1c, 1d). The significant differences observed in the graphs may be due to a deviation from the optimal compositional ratio of the film components. The search for optimal parameters that provide the best superconducting properties, as well as the enhancement of these properties through structural amorphization of the films, is the subject of our further research.

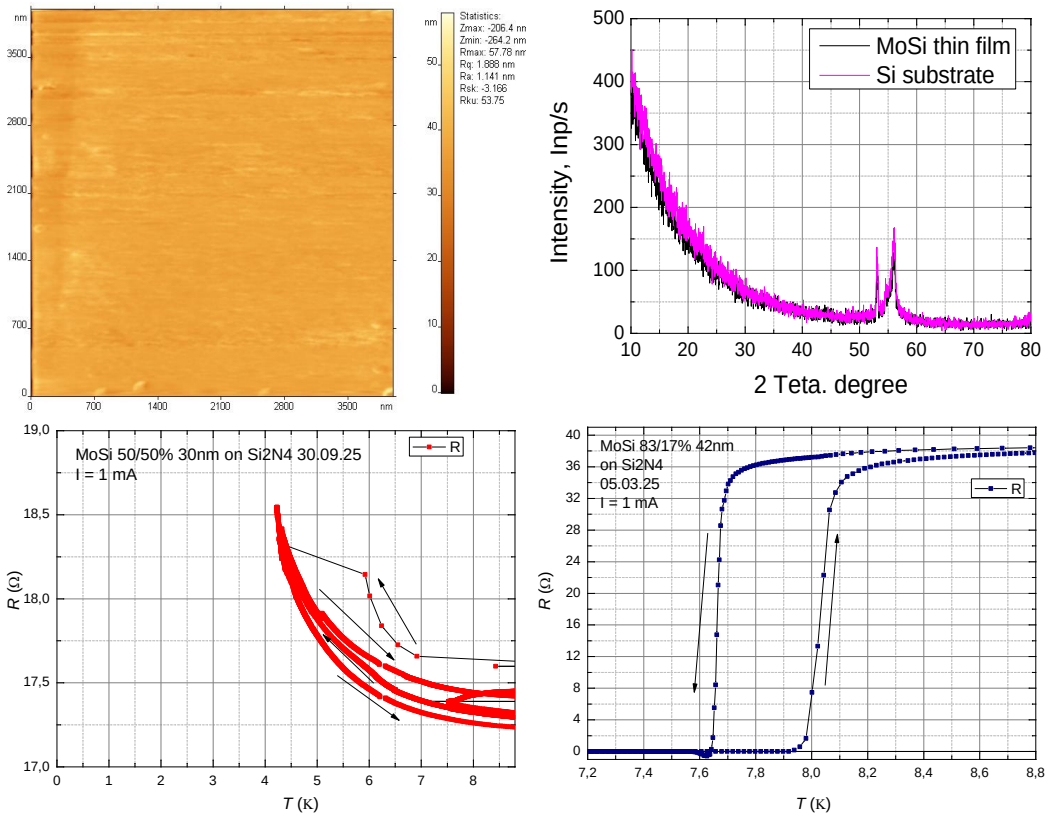

Fig. 1. a) AFM picture of morphology of MoSi film, b) diffraction pattern of studied samples of MoSi films done by XRD analysis, c,d) temperature dependencies of electrical resistance of MoSi films of different chemical composition done by 4-point probe technique (c – $Mo_{50}Si_{50}$, d – $Mo_{83}Si_{17}$)

Conclusions

The interplay between disorder and superconductivity is a fascinating fundamental phenomenon in quantum physics. The famous Anderson's theorem states that conventional superconductors are insensitive to dilute nonmagnetic impurities. Even more, in the strong disorder regime far beyond the scope of the Anderson's theorem application, destruction of superconductivity and even superconductor- insulator transitions may take place. Our goal was the preparation of thin amorphous films with high Tc and high sheet resistance. The results are promising and elaborate technology should enable us to produce superconducting structures which could interfere with quantum coherent objects.

Acknowledgments.

This work was partially supported by the National Academy of Sciences of Ukraine through the research program No. 0125U000295

References

[1] G. Bergmann, Phys. Rep., 27: 159 (1976).

[2] A. Semenov, B. Günther, U. Böttger, et al. Phys. Rev. B 80, 054510 (2009).

[3] Y. Pan, H. Zhou, X. Zhang, et al., Opt. Express 30, 40044-40052 (2022).

NEAR-SURFACE SUPERCONDUCTIVITY IN ELECTROCHEMICALLY REDUCED INDIUM–TIN OXIDE FILMS

D. Menesenko*,, O. Feia*,**,***, A. Shapovalov*,****

**Kyiv Academic University, 36 Academician Vernadsky Blvd., UA-03142 Kyiv, Ukraine*
*** G. V. Kurdyumov Institute for Metal Physics, N.A.S. of Ukraine*
**** Leibniz Institute for Solid State and Materials Research*
e-mail: d.menesenko@kau.edu.ua

Electrochromic oxide-based superconductors are a promising platform for integrated quantum photonics, but the microscopic origin of superconductivity in reduced indium tin oxide (ITO) remains controversial. As we show in previous works ITO superconducting transition temperature Tc – can be tuned by changing oxygen vacancies. Here we investigate the influence of oxygen vacancies on the SC properties of ITO by density functional theory simulation.

Introduction

Indium tin oxide (ITO), widely used for its ≈80% visible transmittance and low resistivity, becomes superconducting after electrochemical reduction with onset of T_c = 5 K [1] accompanied by a change in optical characteristics. Electrochemical treatment at negative potentials can partially dissolve the film and generate metallic species; XPS indicates formation of metallic In via breaking metal–oxygen bonds. ToF-SIMS detects electrolyte ions in the top layers; and a 4 s etch in a 1:100 TE-100 solution suppresses superconductivity entirely [2].

Experiment

To rationalize previous observations, we modeled oxygen-deficient bixbyite In_2O_3 and Sn-doped In_2O_3 using density functional theory (DFT). Calculations employed GGA-PBE with PBEsol ultrasoft pseudopotentials in Quantum ESPRESSO. Converged parameters included planewave/charge cutoffs up to 120/1200 Ry, Monkhorst–Pack meshes from 2x2x2 (relaxation) to 4x4x4 (SCF) and 12x12x12 (non-SCF) for band structures and densities of states. This protocol balances accuracy and cost and was validated for both pristine and oxygen-deficient supercells.

Our goal was to investigate the influence of oxygen vacancies on the SC properties of ITO. In our previous work we revealed that the most likely mechanism for surface superconductivity is the formation of oxygen vacancies due to the reduction of Indium. In addition, the role of injected alkali metal ions trapped in the surface layer of treated films has not been sufficiently studied. The removal of oxygen ions is facilitated by applied extermal electrical potential or electochemical potential at the ITO-electrolyte (ITO-electronegative metalic layer). To assess the effect of structural changes on the band diagram for different number of oxygen vacancies, we calculated band structures and density of states (DOS) for pristine ITO(Fig. 2 a), ITO with 1 oxygen vacancy, and 2 vacancies (Fig. 2 b). The band structure of pristine ITO aligns very well with literature data. The introduction of additional vacancies causes the shift of the Fermi level higher into the conduction zone. This is accompanied by an increase in the number of states at the Fermi level, leading to enhanced conductivity. This trend is in accordance with changes in the band structure of In_2O_3 when creating oxygen vaccancies. Another observed feature is the flattening of bands near the Γ-point, suggesting a continuation of this trend with an increasing number of vacancies. This can be an indirect sign of enhanced superconducting properties.

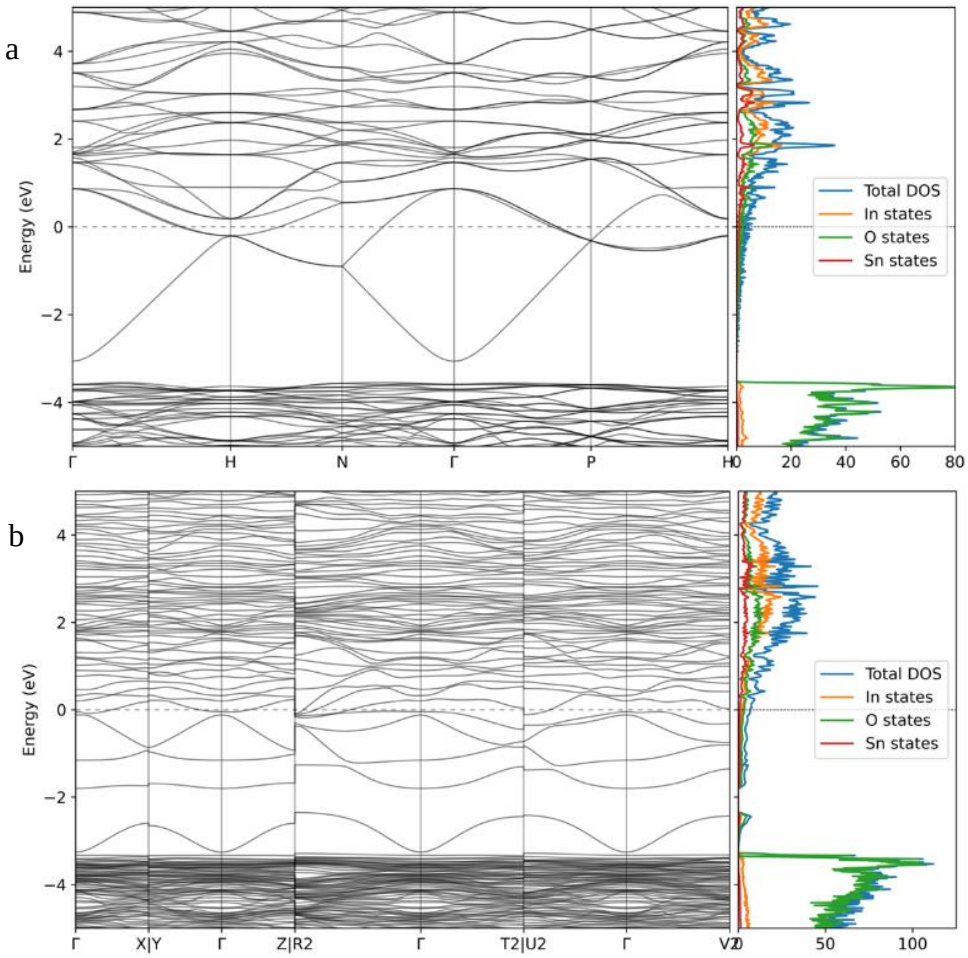

Fig. 1. Electronic band diagram (left panel) and density of states (right panel): (a) for pristine ITO, (b) for ITO with two distant vacancies

In summary, the combined evidence points to a two-dimensional superconducting state stabilized by electrochemically driven oxygen migration and cation intercalation that reshape the near-surface electronic structure. Our DFT provides a mechanistic link between electrolyte chemistry, defect charge states, and the emergence—and fragility—of superconductivity, and explains systematic differences between electrochemical and vacuum-grown oxygen-deficient ITO. This framework guides controlled tuning of superconducting sheet thickness and disorder via treatment time, potential, and post-growth oxygen activity, enabling transparent superconducting layers for integrated quantum photonics. This research is supported by the NATO Science for Peace and Security Programme, project SPS G6082. This work was also partially supported by the Ministry of Education and Science of Ukraine under contract No.M/32-2025

References

[1] A.P. Shapovalov et al. Metallofiz. Noveish. Tekhnol. 46, 517 (2024).
[2] A. Parra et al. *IEEE Trans. Appl. Supercond.* 35, 7000105 (2025).

DENSITY FUNCTIONAL THEORY IN THE NANOSCALE ERA: CAPABILITIES, CHALLENGES, AND ADVANCES IN ELECTRONIC STRUCTURE MODELING

Oleh Holubovskyi, Anatoliy Ivanisik, Andrii Goriachko

Faculty of RadioPhysics, Electronics and Computer, Systems Taras Shevchenko National University of Kyiv, Kyiv 01601, Ukraine, e-mail: oleh.holubovskyi@knu.com

Faculty of RadioPhysics, Electronics and Computer, Systems Taras Shevchenko National University of Kyiv, Kyiv 01601, Ukraine, e-mail: anatoliyivanisik@gmail.com

Faculty of RadioPhysics, Electronics and Computer Systems, Taras Shevchenko National University of Kyiv, Kyiv 01601, Ukraine, e-mail: goriachko@knu.ua

Capabilities and Achievements

Density Functional Theory (DFT) is the most widely used electronic structure method in chemistry, physics, and materials science. It provides high accuracy and is routinely applied to the computational modeling of molecules and materials. The foundation of DFT is the Hohenberg–Kohn theorems, which establish the ground-state electron density as the key variational quantity. DFT serves as an indispensable tool for theoretically predicting and understanding material properties. This is particularly true for nanostructured materials, such as two-dimensional (2D) systems (e.g., TMDs, graphene), which are crucial for advancements in electronic devices, energy storage, and catalysis. DFT has significantly contributed to the understanding of these 2D materials. DFT provides a robust framework for the predictive modeling of a wide array of properties, including optical, optoelectronic, catalytic, and magnetic characteristics of nanomaterials. DFT is essential for modeling specialized experimental techniques such as Scanning Tunneling Microscopy (STM). The theoretical description of STM images relies on the local density of states (LDOS) and the Tersoff–Hamann model.

Scaling and Computational Efficiency

To overcome the inherent computational challenge associated with conventional Kohn–Sham DFT (KSDFT), which typically exhibits $O(N^3)$ scaling due to the use of orbitals, Orbital-Free Density Functional Theory (OFDFT) is employed. OFDFT entirely circumvents the explicit use of orbitals, leading to dramatic simplification and achieving near-linear scaling with system size ($O(N)$) regardless of the system state. This capability makes simulations involving millions of atoms feasible. OFDFT applications span across solids, nanostructures, quantum dots, liquid metals, and materials under extreme conditions like Warm Dense Matter (WDM). The development of Kinetic Energy Density Functionals (KEDFs), such as LKT, VT84F, HC, and LMGP, is central to the success of OFDFT.

Functional Development and Corrections

1. Hybrid and Meta-GGA Functionals: Advanced functionals have been developed to enhance accuracy. Range-separated hybrid (RSH) functionals with full long-range exact exchange are recognized as among the most accurate DFAs currently used. Optimally tuned RSH functionals can satisfy Koopmans' theorem, thereby improving predictions of excitation energies. Modern semilocal functionals, like the meta-GGAs SCAN and r2SCAN, are valued for their broad applicability to both molecular and extended systems.

2. Machine Learning: Machine-Learnt KEDFs (ML-KEDFs) represent a new class of functional approximations. The DeepMind 2021 (DM21) functional, for instance, utilizes a deep neural network and specific physical constraints (including fractional charge/spin constraints) to correct delocalization and multireference errors.

3. Dispersion Corrections: Accurate modeling of 2D materials requires the incorporation of dispersion forces. Methods such as Tkatchenko–Scheffler (TS) and its variants (e.g., FI-TS) provide improved efficiency and accuracy by making dispersion coefficients dependent on electron density partitioning, which is vital for simulating interlayer physics and adsorption.

Problems and Challenges

Despite the advancements, the application of DFT is hindered by several limitations inherent to approximate functionals:

1. Delocalization Error (DE): This is widely regarded as the greatest outstanding challenge in DFT. DE often leads to qualitative or substantial quantitative errors.

2. Band Gap Underestimation: The delocalization error is directly responsible for the systematic tendency of many DFAs (especially LSDA and GGAs) to underestimate the band gaps of semiconductors and insulators.

3. Transferability Issues: The parameters used in advanced functionals, such as the optimal range-separation parameter ω in RSH functionals, are highly system dependent. This prevents a single parameterization from achieving high transferability across a diverse mix of small and large molecules or materials.

4. Strong Correlation and Excitations: Standard DFT is optimized for the ground state and struggles with systems exhibiting strong electronic correlation or accurate descriptions of electronic excitations. For these cases, methods beyond standard DFT, such as DFT+U, GW, or the Bethe–Salpeter Equation (BSE), are typically necessary.

5. OFDFT Implementation Hurdles: For OFDFT to reach its full potential, the development of transferable Local Pseudopotentials (LPPs) must improve. The construction of high-quality LPPs for certain elements, particularly second-row and transition metals, remains highly challenging and is considered a possible "Achilles' heel" for the broader applicability of OFDFT.

Conclusion

DFT continues its evolution through concurrent progress in theoretical foundation, algorithmic efficiency, and hardware capabilities. The ongoing effort to mitigate the pervasive problem of delocalization error via sophisticated functionals and the drive towards increased scalability via OFDFT represent critical future directions. By addressing these core challenges, DFT will enhance its already pivotal role in accelerating the rational design and discovery of novel materials, especially complex nanostructures.

References

[1] Bryenton K.R., Adeleke A.A., Dale S.G., Johnson E.R. Delocalization error: The greatest outstanding challenge in density-functional theory. WIREs Comput Mol Sci. 2023;13:e1631.

[2] Makkar P., Ghosh N.N. A review on the use of DFT for the prediction of the properties of nanomaterials. RSC Adv., 2021, 11, 27897.

[3] Mi W., Luo K., Trickey S.B., Pavanello M. Orbital-Free Density Functional Theory: An Attractive Electronic Structure Method for Large-Scale First-Principles Simulations. Chem. Rev. 2023, 123, 12039–12104.

[4] Hasan M.A., Abdulhussein H.A. Review: beyond the surface—exploring the complexities of 2D materials with density functional theory. J Mater Sci (2025) 60:13191–13235.

[5] Marzari N., Ferretti A., Wolverton C. Electronic-structure methods for materials design. Nat. Mater. 2021, 20, 298–314.

PHYSICS OF SEMICONDUCTORS AND DIELECTRICS, SEMICONDUCTOR DEVICES

ION-STIMULATED MODIFICATION OF THE PHASE AND DEFECT STRUCTURE OF VOx FILMS

K.V. Kovalov*, O.M. Ivanyuta*, T.M. Sabov**

**Taras Shevchenko National University of Kyiv, Faculty of Radiophysics, Electronics and Computer Systems, 60 Volodymyrska Street, Kyiv, Ukraine*

***V.E. Lashkaryova Institue of Semiconductor Physics of the NAS of Ukraine, 41 Nauka Ave., Kyiv, Ukraine*

Introduction

Vanadium oxides, particularly VO_2, belong to materials exhibiting a metal–semiconductor phase transition, making them promising for the development of microbolometers, optoelectronic sensors, and energy-saving coatings [1, 2]. Optimization of their phase and defect structure ensures improvement of the functional properties of the films. The main goal was to study the effect of magnetron deposition parameters, thermal annealing, and ion implantation on the formation of the phase structure of VOx films and the metal–semiconductor phase transition.

Materials and methods

VOx films were deposited using the magnetron method onto silicon substrates [3]. For modification, thermal annealing and ion implantation [4] with Ar^+ were applied. Structural characteristics were studied using X-ray diffraction (XRD), X-ray photoelectron spectroscopy (XPS) [5,6], and temperature resistance dependencies (TCR) [7].

Results

It was established that films deposited at an emission current of 150 A and voltage of 340 V, followed by annealing, demonstrated a distinct VO_2 phase transition at temperatures of 58.8–63.2 °C. XRD analysis showed the formation of 66% VO_2 phase and 33% V_4O_9 at optimal deposition parameters. XPS confirmed the dominance of VO_2 in samples after annealing and a decrease in the amount of V_2O_5. After Ar^+ ion implantation (5 keV, 1–2 min), the VO_2 amount increased by 128%, indicating improved crystalline ordering and phase stability of the films.

Conclusions

Argon ion implantation is an effective method for modifying the structure of VOx films, promoting an increase in the VO_2 fraction and stabilization of the metal–semiconductor phase transition. The obtained results can be used in the development of sensor and thermal imaging technologies, namely in 2D matrices and arrays of transducers (microbolometers) that form thermal images, where VO_2 films can serve as the main functional element.

References

[1] Charles Petitweg. Uncooled detectors for thermal imaging cameras. FLIR Technical Note, 2015.
[2] Yu. Goltvyanskyi et al. Structural transformation and functional properties of vanadium oxide films after low-temperature annealing. Thin Solid Films, 564 (2014): 179–185.
[3] Ye.P. Kalinushkin et al. Thin-film materials and methods of their fabrication. Dnipro: NMetAU, 2009.
[4] T.M. Sabov et al. Oxygen ion-beam modification of vanadium oxide films for reaching a high value of the resistance temperature coefficient. Semiconductor Physics, Quantum Electronics & Optoelectronics, 20 (2), 2017.
[5] Paul Van Der Heide. X-Ray Photoelectron Spectroscopy: An Introduction to Principles and Practices. Wiley, 2012.
[6] CasaXPS: Peak Fitting in XPS. http://www.casaxps.com (accessed 9.08.2025).
[7] V.P. Kladko et al. Phase transition in vanadium oxide films formed by multistep deposition. Semiconductor Physics, Quantum Electronics & Optoelectronics, 24 (4), 2021.

MICROWAVE PROPERTIES OF ACTIVATED CARBON FIBER–POLYURETHANE COMPOSITE PLANAR STRUCTURES

V.D. Malovychko*, V.E. Diyuk*,, V.H. Demchenko**, M.O. Popov*, H.L. Chumak*, V.A. Moiseienko***, L.M. Grishchenko**,*******

**Taras Shevchenko National University of Kyiv, Kyiv 01601, Ukraine, e-mail: viktoriia.malovychko@gmail.com*
*** Institute of Engineering Thermophysics, NAS of Ukraine, Kyiv 03057, Ukraine, e-mail: vdiyuk@gmail.com*
**** Independent Research & Development Laboratory "200k Electronics" Kyiv 01030, Ukraine, e-mail: vamrpd@gmail.com*
***** O.O. Chuiko Institute of Surface Chemistry, NAS of Ukraine, Kyiv 03164, Ukraine e-mail: liudmyla.grishchenko@gmail.com*

Activated carbon fiber (ACF) derived from viscose and a polyurethane (PU) solution in ethyl acetate were employed to fabricate film composite materials. Both the pristine ACF and ACF–PU composites were characterized using scanning electron microscopy with energy-dispersive X-ray spectroscopy, thermogravimetric analysis, and ACF was studied by temperature-programmed desorption mass spectrometry, and nitrogen adsorption–desorption techniques. The microwave properties of the ACF–PU composites were investigated in the 8–12 GHz frequency range using a scalar network analyzer.

Introduction

The rapid development of modern electronic devices and communication technologies has given rise to a new environmental problem: electromagnetic pollution. In this regard, materials for electromagnetic shielding and microwave absorption have attracted considerable attention from scientists worldwide. Due to their excellent properties, such as high electrical conductivity, light weight, flexibility, good mechanical properties, low cost, biocompatibility, and environmental friendliness, carbon materials play a key role in shielding film compositions. The purpose of this work is to produce thin composite films based on polyurethane and activated carbon fiber in in different ratios of fiber and polymer and investigate the microwave properties of the obtained composites in the centimeter wave range, namely, in the X-band (8-12 GHz).

Experimental

Activated carbon fiber (ACF) derived from viscose and a polyurethane (PU) solution in ethyl acetate were employed to fabricate film composite materials. Composites were obtained in different ratios of fiber and polymer. They were obtained as follows. A 12 wt% solution of polyurethane in ethyl acetate was added to the carbon material. This mixture was stirred thoroughly for several minutes to ensure the fillers were distributed uniformly. The resulting suspension was poured onto a polymer substrate and spread according to the template. Then, it was left to dry at room temperature for 24 hours. Both the pristine ACF and ACF–PU composites were characterized using scanning electron microscopy with energy-dispersive X-ray spectroscopy, thermogravimetric analysis, and ACF was studied by temperature-programmed desorption mass spectrometry, and nitrogen adsorption–desorption techniques. The microwave properties of the ACF–PU composites were investigated in the 8–12 GHz frequency range using a scalar network analyzer.

Results and discussion

From the data presented on the Figure 1 it is seen that the microwave properties of the ACF-PU composites demonstrate a clear monotonous tendency toward increased reflection and decreased transmission in the X-band as the amount of ACF filler increases. This can be attributed to the material's increased electrical conductivity, since larger conductivity corresponds to larger real part of dielectric constant. Larger dielectric constant results in more pronounced impedance mismatch, which increases the power reflection coefficient Γ, and leads to bigger S_{11} values (Fig. 1 a). Specifically, reflection increases from approximately –20 dB (or ≈1%) for the pristine composition to –(4÷5) dB or (33÷42)% (depending on the frequency) for the ACF2:2 composite. Simultaneously, larger conductivity results in larger microwave losses, thus more microwave power is absorbed inside the sample

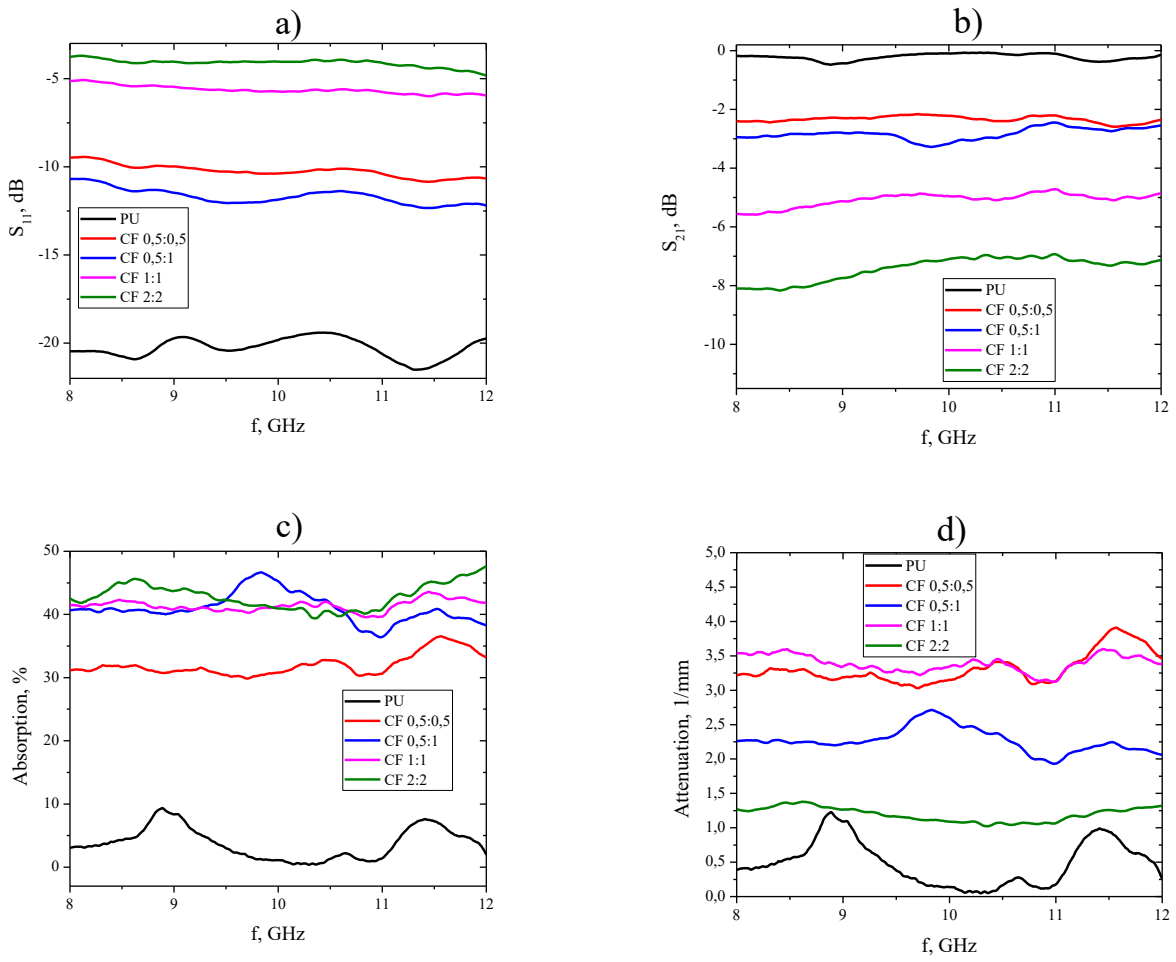

Fig. 1. Frequency dependencies of (a) S_{11}, (b) S_{21}, (c) absorption A and (d) attenuation α of the ACF-PU composites in the X-band

and transmission coefficient decreases (Fig. 1 b). For the pristine PU film the transmission is –(0-0.5) dB which is 90–98% and for the ACF2:2 it drops down to –(7-8) dB is which is only 15-20%. The absorption coefficient (Fig.2 c) rises from <10% for the initial composition to 30-35 % for ACF0.5:0.5 and to 38–45% for the compositions with larger amount of ACF filler. However, the frequency spectra of attenuation constant show somewhat different picture. According to the Fig.1 d, among the carbon composites the largest attenuation is attained for the ACF0.5:0.5 and ACF1:1 films, trailed shortly by ACF0.5:1. The ACF 2:2 demonstrate a noticeably lower attenuation, hence its large absorption (Fig.2 c) is explained, primarily, by much greater thickness of the sample. Likewise, somewhat smaller attenuation of the ACF0.5:0.5 specimen (in spite of its rather large α value) is in accordance with the fact that it has the smallest thickness among all composite samples.

Acknowledgment

V.E.D., V.H.D, L.M.G. are in debt to the Presidium of the National Academy of Science of Ukraine for the partial support of the work.

PREPARATION OF POLYVINYL CHLORIDE/CARBON NANOTUBES THIN-FILM COMPOSITES AND THEIR MICROWAVE ABSORPTION PRORERTIES

D.O. Zhytnyk*, I.P. Matushko*, Yu.V. Noskov **, V.A. Moiseienko*, and L.M. Grishchenko****,*******

**Taras Shevchenko National University of Kyiv, Kyiv 01601, Ukraine, e-mail: radiodima2000@gmail.com*
***Kukhar Institute of Bioorganic Chemistry and Petrochemistry, NAS of Ukraine, Kyiv 02160, Ukraine, e-mail: yuriy.noskov@gmail.com*
****Independent Research & Development Laboratory "200k Electronics" Kyiv 01030, Ukraine, e-mail: vamrpd@gmail.com*
*****O.O. Chuiko Institute of Surface Chemistry, NAS of Ukraine, Kyiv 03164, Ukraine*
******Institute of Engineering Thermophysics, NAS of Ukraine, Kyiv 03057, Ukraine, e-mail: liudmyla.grishchenko@gmail.com*

This study presents the preparation of thin composite films using polyvinylchloride as the base material and carbon nanotubes samples as a filler, their study by the methods of SEM, TPD MS, TGA, FTIR. The microwave absorbing properties of the resulting films in the X-band were investigated.

Introduction

With the rapid development of electronic devices and communication technologies, as well as their wide application in various areas of our lives, the problem of electromagnetic pollution is becoming increasingly acute [1]. Electromagnetic radiation can not only affect the normal operation of electronic devices, but also harm human health [2]. To eliminate the negative impact of electromagnetic radiation or reduce it, materials for its shielding are actively being developed. These materials reflect or absorb incident electromagnetic waves mainly through electrical and magnetic loss mechanisms. The purpose of this work was to obtain a composite material based on polyvinyl chloride (PVC) as a polymer matrix and carbon nanotubes (CNT) samples as a filler and to study the microwave properties of the obtained composites.

Experimental

A series of $(PVC)_{100-x}/(CNT)_x$ films were obtained by the method of hot pressing of powders of PVC and CNT taken in different weight ratio x =0,2 -10 wt% of CNT. In the typical preparation, the CNT powder was first ground in an agate mortar. Then 0.2 g of PVC powder was mixed with the required amount of CNT. This mixture was reground in the same mortar to a relatively homogeneous state. It was then poured into a mold on a polyamide substrate and 70 mg of di-butyl phthalate (DBP) plasticizer for PVC was added. The $(PVC)_{100-x}/(CNT)_x$ films were prepared by pressing at 175 °C and 10 MPa pressure for 1 minute. The resulting $(PVC)_{100-x}/(CNT)_x$ composites and pure hot-pressed PVC samples prepared without CNT were approximately 0.25 mm thick and 23 × 12 mm in size. These films samples were used for further testing.

Results and discussion

TGA studies have shown that CNTs are practically anhydrous, since they practically do not lose mass when heated to 100-150 °C. Moreover, they almost do not lose mass up to a temperature of 500 °C, and then burn out sharply. CNTs burn when in contact with oxygen in the air with the release of CO_2. After their combustion, approximately 10% of the solid phase remains in the crucible, which does not burn out and consists of iron oxides. The nanotubes used contain a small amount of iron oxides, which are used as a seed when growing CNTs.

The obtained film composite samples were investigated for the transmission and reflection of microwave waves in the X frequency range (8.15 GHz - 12.05 GHz). When comparing the reflection values for samples with different CNT concentrations, it was found that low filler concentrations (0.2 - 1%) have a weak effect on the reflection values in the X range. Compared with the original PVC without filler (-22.8 dB), the addition of 0.2% CNT increases the reflection by 0.4 dB, the addition of 0.5% CNT increases the reflection by 1.4 dB, and the

addition of 1% CNT - by 2.0 dB. When the filler concentration increases to 5%, the reflection increases significantly to -17 dB, and when the CNT concentration increases to 10%, a sudden increase in reflection to -6.4 dB is observed, which is a significant increase for relatively low concentrations.

Table 1: Minimum, average and maximum values of reflection loss and transmission loss in the X-band for composite films depending on the filler concentration

Sample	S_{11}, dB			S_{21}, dB		
	Min.	Mean.	Max.	Min.	Mean.	Max.
PVC	-23.7	-22.8	-21.6	-0.1	-0.1	-0.1
0.2%	-23.3	-22.4	-21.4	-0.2	-0.2	-0.1
0.5%	-22.2	-21.4	-20.4	-0.3	-0.1	-0.1
1%	-21.6	-20.8	-19.7	-0.3	-0.1	-0.1
5%	-17.7	-17.0	-16.2	-0.4	-0.3	-0.3
10%	-7.7	-6.4	-5.8	-4.4	-4.2	-3.8

The value of the transmission of microwave waves of the X range does not undergo significant changes for CNT concentrations from 0.2% to 5% and lies in the range of 0.1 dB - 0.3 dB, which does not allow us to even talk about a tendency to reduce the value of the transmission for these concentrations. A sample with the maximum concentration (10%) of CNT is distinguished, which demonstrates a significantly lower value of the transmission: -4.2 dB. Such a jump-like nature of the increase in reflection and a decrease in transmission may be due to the physical interaction of the filler inside the composite.

The conducted microwave studies, in the X frequency range, of PVC composite films with carbon nanotubes as a filler demonstrate an insignificant dependence of the microwave characteristics of the studied material at filler concentrations up to 1%. Increasing the concentration to 5% leads to an increase in the reflection value and a decrease in the transmission value, which is characteristic of composite materials with conductive fillers. Further increase in the concentration of CNTs in the polymer matrix leads to a sudden increase in reflection and a decrease in the transmission of microwave waves, which may be associated with the physical interaction of the filler in the volume of the polymer matrix and requires additional studies. (determination of specific conductivity, microscopic analysis, study of intermediate concentration values, etc.).

Acknowledgment

M.I.P. expresses gratitude to the Ministry of Education and Science of Ukraine for partial funding of the work: The Grant of the Ministry of Education and Science of Ukraine for the perspective development of a scientific direction “Mathematical sciences and natural sciences” at the Taras Shevchenko National University of Kyiv. G.L.M. is in debt to the Presidium of the National Academy of Science of Ukraine for the partial support of the work.

References

[1] C.L. Russell, “5G wireless telecommunications expansion: Public health and environmental implications”, *Environ. Res*., vol. 165, pp. 484-495, Aug. 2018, doi: 10.1016/j.envres.2018.01.016.

[2] K.V. Singh et al., “Acute radiofrequency electromagnetic radiation exposure impairs neurogenesis and causes neuronal DNA damage in the young rat brain”, *NeuroToxicology*, vol. 94, pp. 46-58, Jan. 2023, doi: 10.1016/j.neuro.2022.11.001.

POROUS SILICON BRAGG MIRRORS AS OPTICAL SENSORS

Ostapenko O.Yu.*, Ivanov I.I.**

** Taras Shevchenko National University of Kyiv 03022, Kyiv, Hlushkova Avenue, 4g, e-mail: oleksandrostapenko615@gmail.com*

*** Taras Shevchenko National University of Kyiv 03022, Kyiv, Hlushkova Avenue, 4g, e-mail: ivanko@gmail.com*

The optical spectral characteristics of a porous silicon-based Bragg mirror with integrated microcavity were investigated. The shifts of the transmission peaks for the analytes in the range of 1.2..1.4 were determined when the pores were filled with the analyte. The developed structure demonstrated spectral sensitivity (S≈175 nm/RIU). Coolorimetric conversion was implemented via the application of an Thorlab optical bandpass filter (FBH520-40), yielding a colorimetric sensitivity of Sc≈90 nm/RIU coupled with high excitation purity EP>0.9.

Introduction

Porous silicon (PS), obtained by anodic etching, is an attractive material for sensor technology [1]. PS shows a wide variety of interesting properties leading to applications in several fields ranging from micro- and optoelectronics to biomedical applications [2]. In this work we perform a quantitative analysis of PS sensitivity and demonstrate the possibility of converting a highly sensitive spectral response into a controlled and standardised colorimetric signal.

Methodology and structure modelling

The structure under investigation is an optical reflector consisting of a set of alternating layers with low (n_L) and high (n_H) refractive indices. It is classified as a Bragg mirror, which is a type of one-dimensional photonic crystal [2]. The structure consists of 10 periods divided into two blocks of 5 refractive indexes periods (nL/nH) with a subsequent change in sequence to (H/L), which creates a phase shift (Figure 1). The geometric thicknesses of the layers are fixed: d_L=75 nm and d_H=50 nm. The porosity of the layers P_L and P_H was determined as a material constant based on n_{eff} for dry PS. This periodic modulation of the refractive index ensures the formation of a clear reflection/transmission band in the visible spectrum.

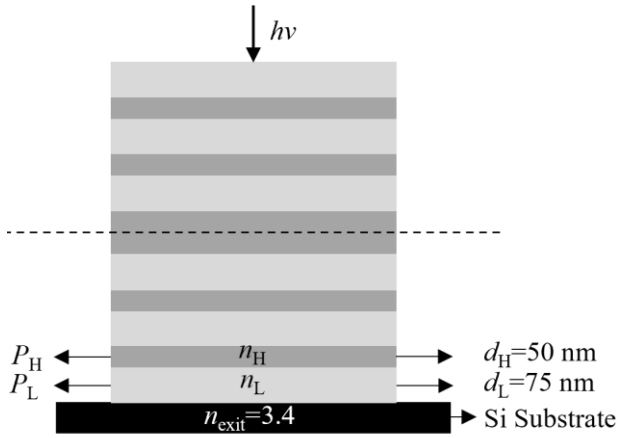

Fig. 1. Schematic profile of a Bragg mirror on PS. The structure consists of N=5 periods (d_L/d_H) followed by a change in sequence to N=5 periods (d_H/d_L). The dotted line reflects the change in the structure sequence

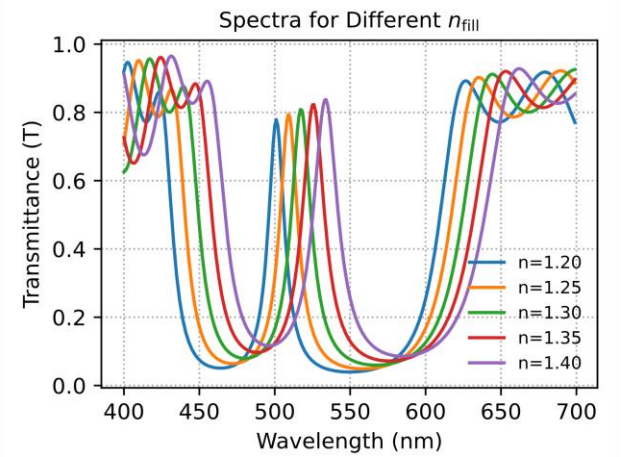

Fig. 2. Transmission spectra of a Bragg mirror on PS in the working range of analytes (n_{fill})

Spectral response and quantitative analysis

To describe the optical properties of the structure, the Bruggeman Effective Medium Approximation (BEMA) was used. The BEMA model allows us to calculate effective refractive index n_{eff} of a layer as a composite index that depends on the porosity (P) and the refractive index of the filler medium (n_{fill}) [1]. The transmission spectra (Figure 2) show a transmission peak shift of $\Delta\lambda \approx 35$ nm when n_{fill} is varied in the range 1.2–1.4 RIU. This provides an extremely high spectral sensitivity of the structure $S \approx 175$ nm/RIU. The use of the FBH520-40 bandpass optical filter (Thorlabs) allowed selective isolation of the most sensitive part of the Bragg mirror spectrum (Figure 3). Analysis in the CIE 1931 colour space showed that limiting the range with filter results in a clear shift in the dominant wavelength (λ_d) from 511 nm to 529 nm (Figure 4). Controlled colorimetric conversion ($S_C \approx 90$ nm/RIU) ensured high excitation purity (EP>0.9), confirming the potential for portable biosensors.

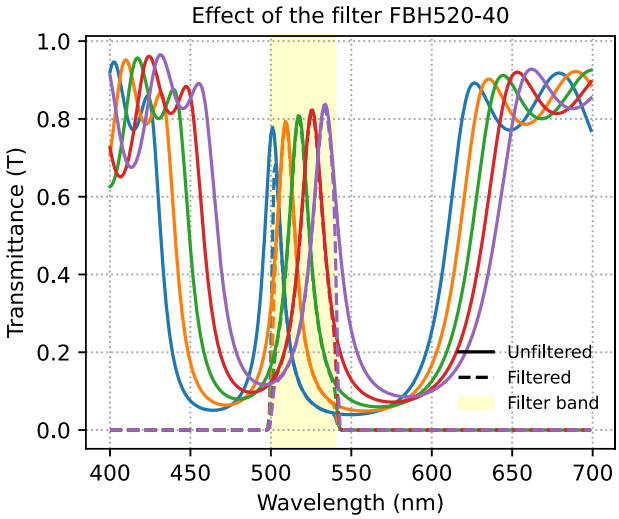

Fig. 3. Effect of the FBH520-40 filter on the transmission spectra of a Bragg mirror. Solid lines represent unfiltered spectra, while dashed lines represent filtered signals for refractive indices (n_{fill}) in the range of 1.2–1.4

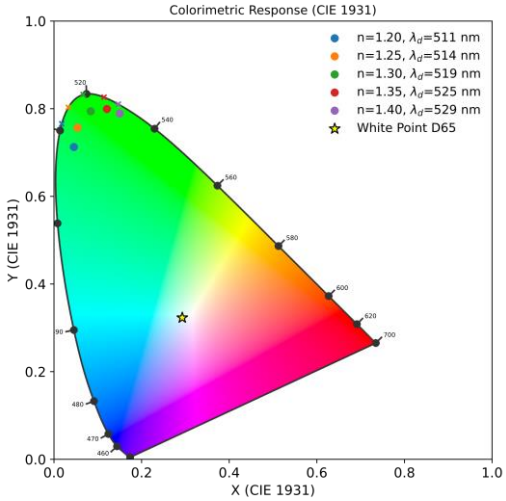

Fig. 4. Visualisation of sensory response in the CIE 1931 colour space. Colour points in the working range of analytes (n_{fill}) demonstrate a linear shift of λ_d in the green filter band

Conclusions

The Bragg mirror sensor structure with microcavity demonstrates has transmission peaks that provide spectral sensitivity $S \approx 175$ nm/RIU, confirming the potential of PS for high-precision laboratory sensing. The use of the FBH520-40 filter ensured signal standardisation and colorimetric sensitivity $S_C \approx 90$ nm/RIU. This shift is accompanied by high colour purity (>0.9), which minimises background noise. Due to its functional similarity to an optical filter, the structure is ideal for the development of reliable, portable colour-based sensors that do not require the use of complex spectrometers.

References

[1] M.J. Sailor, Porous Silicon in Practice: Preparation, Characterization and Applications. Weinheim, Germany: Wiley-VCH, 2011.

[2] V. Torres-Costa and R.J. Martín-Palma, "Application of nanostructured porous silicon in the field of optics. A review," *J. Mater. Sci.*, vol. 45, no. 11, pp. 2823–2838, June 2010, doi: 10.1007/s10853-010-4251-8.

[3] Ivanov I.I., Klyui N.I., "Colorimetric analysis of optical reflection from thin porous silicon for detection of organic liquids", *Sens. and Act., B: Chemical*, vol. 280, pp. 102 – 108, 10.1016/j.snb.2018.10.021

MICROWAVE PROPERTIES OF $ZnFe_2O_4$/POLYVINYL CHLORIDE COMPOSITES

I.V. Fesych*, O.O. Kharchenko*, I.P. Matushko*, Yu.V. Noskov, V.A. Moiseienko***, L.M. Grishchenko****,*******

**Taras Shevchenko National University of Kyiv, Kyiv 01601, Ukraine, e-mail: ihor.fesych@knu.ua*
***Kukhar Institute of Bioorganic Chemistry and Petrochemistry, NAS of Ukraine, Kyiv 02160, Ukraine, e-mail: yuriy.noskov@gmail.com*
****Independent Research & Development Laboratory "200k Electronics" Kyiv 01030, Ukraine, e-mail: vamrpd@gmail.com*
*****Institute of Engineering Thermophysics, NAS of Ukraine, Kyiv 03057, Ukraine, e-mail: liudmyla.grishchenko@gmail.com*
******O.O. Chuiko Institute of Surface Chemistry, NAS of Ukraine, Kyiv 03164, Ukraine*

This study presents the preparation of thin composite films using polyvinylchloride as the base material and $ZnFe_2O_4$ samples as a filler, their study by the methods of SEM, PXRD, TGA, FTIR. The microwave properties of the $ZnFe_2O_4$–PVC composites were investigated in the 8–12 GHz frequency band using a scalar network analyzer.

Introduction

The rapid development of science and technology creates comfort for human life. At the same time, the level of electromagnetic pollution is rapidly increasing, which, in turn, negatively affects human health [1]. A significant number of publications demonstrate the harmful effects of electromagnetic radiation on living organisms, it leads to the development of onco- and neurodegenerative diseases, disrupts the work of the endocrine, cardiovascular, nervous systems, and the hematopoietic process [2].

The purpose of this work was to obtain a composite material based on polyvinyl chloride (PVC) as a polymer matrix and $ZnFe_2O_4$ samples as a filler and to study it by SEM, TGA, PXRD, FTIR methods and to investigate the microwave properties of the obtained composites.

Experimental

Synthesis of ferrite nanopowder was carried out in this way. The sol-gel method was chosen for the synthesis of samples. Citric acid was used as a gelling agent and complexing agent. The number of moles of acid was equal to the total number of moles of zinc and iron nitrates. During the gradual evaporation of water from the reaction vessel, the formation of a brown nitrate-citrate gel was observed. After thermal initiation and as a result of the redox reaction between the nitrate groups and organic acid, the dried gel was self-ignited. The resulting brown-black powder was placed in porcelain crucibles and thermally treated. Ferrite nanopowders were obtained at different temperatures: 200, 400, 600, 800 and 1000°C.

Then a series of $(PVC)_{100-x}/(ZnFe_2O_4)_x$ films were obtained by the method of hot pressing of powders of PVC and $ZnFe_2O_4$ taken in equal weight ratio x = 30 wt% of $ZnFe_2O_4$. In the typical preparation, the $ZnFe_2O_4$ powder was first ground in an agate mortar. Then 0.2 g of PVC powder was mixed with the required amount of $ZnFe_2O_4$. This mixture was reground in the same mortar to a relatively homogeneous state. It was then poured into a mold on a polyamide substrate and 70 mg of dibutyl phthalate (DBP) plasticizer for PVC was added. The $(PVC)_{100-x}/(ZnFe_2O_4)_x$ films were prepared by pressing at 175 °C and 10 MPa pressure for 1 minute. The resulting $(PVC)_{100-x}/(ZnFe_2O_4)_x$ composites and pure hot-pressed PVC samples prepared without $ZnFe_2O_4$ were approximately 0.25 mm thick and 23 × 12 mm in size. These films samples were used for further testing. The microwave properties of the composites were investigated in the 8–12 GHz frequency band using a scalar network analyzer.

Results and discussion

Phase analysis of zinc ferrite samples synthesized at different temperatures was performed using X-ray diffraction. It was shown that the target spinel phase forms after calcination at 200°C. In addition, the diffractograms of samples obtained at 200°C, 400°C, and 600°C showed low intensity reflections corresponding

to impurity ferric oxide. At the same time, zinc ferrite calcined at 800°C and 1000°C was single phase. Such changes in the phase composition of ferrites suggest that at relatively low temperatures (200-600°C), nanopowders with an unstable mixed spinel structure are formed, in which Zn^{2+} and Fe^{3+} cations randomly occupy both octahedral and tetrahedral positions. At high temperatures, the degree of crystallinity of zinc ferrites and the size of crystallites increases, thereby stabilizing the structure of normal ferrospinel.

The films of this composite material turned out to be practically radio-transparent in the studied frequency range (Fig. 1 a). They have a very low reflection, which is within the X-band (at 10 GHz) -22.85 – - 21.37 dB compared to the original PVC, for which this reflection value is -23.45 dB. At the same time, for all samples of ferrites on the basis of which the films were made, there is a dependence of the reflection of electromagnetic waves on the temperature of ferrite synthesis (except for the temperature of 400 °C) – the reflection increases with increasing temperature of obtaining ferrite and is maximum for the film containing ferrite obtained at the maximum temperature (1000 °C). The temperature of 0 °C in the graphs corresponds to a sample of pure PVC (without ferrite).

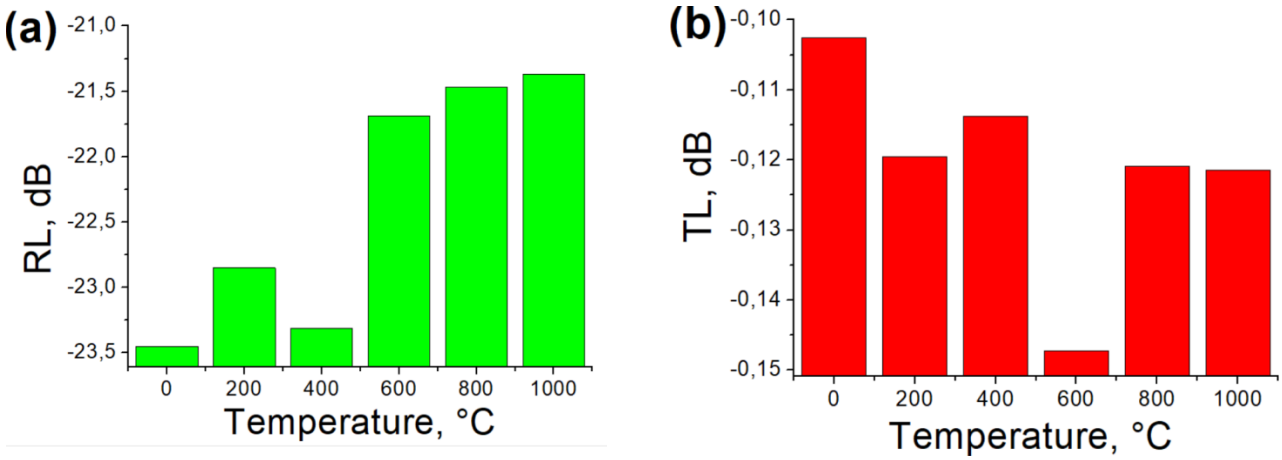

Fig. 1. Frequency dependencies of (a) reflection, (b) transmission of $(PVC)_{100-x}/(ZnFe_2O_4)_x$ composites films in the X-band (at 10 GHz) on the ferrite synthesis temperature

When analyzing the transmission of electromagnetic waves through the studied $(PVC)_{100-x}/(ZnFe_2O_4)_x$ films, it can be concluded that the transmission value changes very slightly, its change is from -0.12 to -0.15 dB (is within the X-band – at 10 GHz), which indicates that the electromagnetic wave almost completely passes through the samples. For the original PVC, this value is -0.10 dB. Unlike reflection for transmission, there is no clear dependence on the temperature of obtaining ferrites, changes in the transmission value are within the measurement error of the devices. The calculated value of the absorption of electromagnetic waves in this range at a frequency of 10 GHz is up to 2.2%.

Acknowledgment

The authors are thankful to the department of Inorganic Chemistry for providing necessary laboratory facilities and personally to PhD Ivanov O.V. for performing PXRD measurements.

References

[1] D.O. Carpenter, "Human disease resulting from exposure to electromagnetic fields", *Reviews on Environmental Health*, vol. 28, no. 4, pp. 159–172. November 2013, doi: 10.1515/reveh-2013-0016.

[2] P. Bandara, D.O. Carpenter, "Planetary electromagnetic pollution: It is time to assess its impact", Lancet Planet, vol. 2, issue 12, pp. E512–E514, December 2018, doi: 10.1016/S2542-5196(18)30221-3.

MICROWAVE PROPERTIES OF COMPOSITES FILMS BASED ON THERMOPLASTIC POLYURETHANE AND BIRCH ACTIVATED CARBON

V.D. Malovychko*, O.M. Gonchar, M.O. Popov*, H.L. Chumak*, V.A. Moiseienko***, I.P. Matushko*, L.M. Grishchenko****,*****

** Taras Shevchenko National University of Kyiv, Kyiv 01601, Ukraine, e-mail: viktoriia.malovychko@gmail.com*

*** Institute of macromolecular Chemistry, the NAS of Ukraine, Ukraine; e-mail: lexgon@ukr.net*

**** Independent Research & Development Laboratory "200k Electronics" Kyiv 01030, Ukraine, e-mail: vamrpd@gmail.com*

***** O.O. Chuiko Institute of Surface Chemistry, NAS of Ukraine, Kyiv 03164, Ukraine*

****** Institute of Engineering Thermophysics, NAS of Ukraine, Kyiv 03057, Ukraine, e-mail: liudmyla.grishchenko@gmail.com*

Films of composite materials based on thermoplastic polyurethane (TPU) with birch activated carbon (TPU/BAC) were obtained with a filler concentration from 10 to 40 % by mass. The films' average thickness varied from 0.22 to 0.33 mm. The reflection and transmission coefficients of electromagnetic waves interacting with the materials under study were measured depending on the concentration of the BAC.

Introduction

In recent years, the extensive development of electronic devices has led to the emergence of parasitic electromagnetic radiation and electromagnetic interference, which seriously threaten human health, information security and the normal operation of electronic devices [1]. In this regard, multifunctional microwave absorbing materials with low density and thickness have been widely used in various fields of science and technology, such as microelectronics, aerospace and automotive industries [2]. Various 3D porous materials have been successfully synthesized, demonstrating promising microwave absorption characteristics. Electromagnetic wave absorbers can be used to protect electronic devices and create effective protective clothing against microwaves, while providing shock resistance, thermal insulation properties and protecting electronic equipment and the health of living organisms.

The purpose of this work is to produce thin composite films based on TPU and BAC in the wide range of filler concentrations (10-40%) and investigate the microwave properties of the obtained composites in the centimeter wave range, namely, in the X-band (8-12 GHz).

The starting material used was carbon made from wood (birch). The original carbon was in the form of fairly large granules, which were ground to a powdery state before being introduced into the polymer. The samples were prepared by adding BAC to a solution of TPU in dimethylformamide (DMF) with subsequent mixing and ultrasonic treatment at a frequency of 20 kHz. The resulting mixture was cast into silicone molds and dried for two days.

Experimental

The thermal decomposition profiles of filler samples were investigated via thermoprogrammed desorption mass spectrometry (TPD MS) utilizing a monopolar quadrupole mass spectrometer MX 7304 A. Thermogravimetric analysis (TGA) was performed to characterize thermal stability using a custom thermal analyzer. Scanning electron microscopy (SEM) using a Tescan Mira 3 LMU microscope was employed for surface morphology imaging. An P2-60 X-band scalar network analyzer was used to analyze microwaves interaction with carbon fiber material. Reflection S_{11} and transmission S_{21} coefficients were measured directly, whereas the power absorption coefficient A was calculated according to:

$$A = 1 - 10^{S_{21}/10} - 10^{S_{11}/10}$$

Results and discussion

It was shown that BAC consists mainly of carbon and oxygen, the concentration of which is about 95% and 5%, respectively. No other heteroatoms were recorded bur some granules contain small amounts of calcium. According to TGA performed in air, the carbon sample exhibits thermal stability up to ~350°C. Upon further heating, oxidative decomposition occurs, leading to the release of carbon oxides, with complete combustion observed at ~635 °C. FTIR spectroscopy analysis of the composite films showed that the absorption bands of the IR spectra of the TPU polymer matrix and composites based on it with AC are practically identical. There is only a slight decrease in the absorption intensity of the Amide I, ν(C=O) – urethane free and Amide I, ν(C=O) – urethane bend bands in the composites, which may be associated with the influence of the filler as a loosener of the polyurethane microstructure.

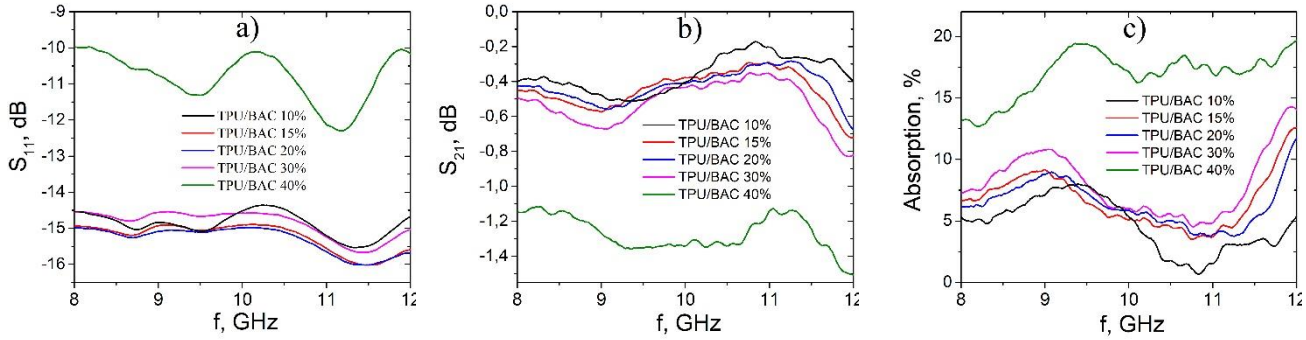

Fig. 1. Frequency dependencies of the microwave properties of TPU/BAC composites with activated carbon filler percentage equal to 10-40%. Section a) shows measured reflection coefficient in dB, section b) - transmission coefficient in dB and section c) - calculated absorption in percents

The reflection and transmission coefficients of electromagnetic waves interacting with the materials under study were measured depending on the concentration of the BAC. The microwave studies indicate that the investigated TPU/BAC composites are generally transparent in the X-band. They have small transmission losses (about 0.2- 0.8 dB for 10-30 wt.% concentration and 1.1-1.5 dB for 40 wt.%) and reflection coefficient remained below –10 dB for all investigated samples in the whole frequency range. However, for 40 wt.% BAC concentration both transmission and reflection losses abruptly increased, with absorption reaching almost 20% at some frequencies. Radio transparency is retained only below 40 wt.% carbon filler. Higher concentrations presumably result in formation of a conductive network that strongly reflect incident electromagnetic wave.

Acknowledgment

M.I.P. expresses gratitude to the Ministry of Education and Science of Ukraine for partial funding of the work: The Grant of the Ministry of Education and Science of Ukraine for the perspective development of a scientific direction “Mathematical sciences and natural sciences” at the Taras Shevchenko National University of Kyiv. L.M.G. is in debt to the Presidium of the National Academy of Science of Ukraine for the partial support of the work.

References

[1] W.C. Ren et al., “Superhigh electromagnetic interference shielding of ultrathin aligned pristine graphene nanosheets,” *Adv. Mater.*, vol. 32, no. 14, Feb. 2020, Art. no. 1907411. doi: 10.1002/adma.201907411.

[2] J. Yuan et al., “Electromagnetic response and energy conversion for functions and devices in low-dimensional materials,” *Adv. Funct. Mater.*, vol. 29, no. 25, Apr. 2019, Art. no. 1807398. doi: 10.1002/adfm.201807398.

APODIZED POROUS-SILICON RUGATE FILTER FOR COLORIMETRIC/REFRACTOMETRIC SENSING

Nytsenko A.S.*, Ivanov I.I.**

** Taras Shevchenko National University of Kyiv 03022, Kyiv, Hlushkova Avenue, 4g, e-mail: nitsenkoas@gmail.com*

*** Taras Shevchenko National University of Kyiv 03022, Kyiv, Hlushkova Avenue, 4g, e-mail: ivanko@gmail.com*

An apodized porous-silicon (p-Si) rugate filter was modeled to evaluate refractometric and colorimetric readout. Transfer-matrix simulations with Bruggeman effective-medium layers predict a narrow resonance whose bandwidth (FWHM) decreases upon ethanol infiltration, while the peak shifts by ~61 nm near λ_0 = 700 nm. To enable compact instrumentation, a fixed ±30-nm spectral window together with source and instrument weighting was used to compute an effective wavelength λ_eff that varies almost linearly with the design wavelength across 450–650 nm. The results support the use of apodized rugate filters as high-resolution sensing elements implementable with simple colorimetric readout.

Introduction

Porous silicon obtained by electrochemical (anodic) etching combines a high internal surface area with a tunable refractive index, which is advantageous for chemical and biosensing [1]. A rugate filter is a one-dimensional photonic crystal in which the refractive index varies continuously—typically sinusoidally—along the depth; apodization suppresses sidelobes and yields a single, narrow spectral feature [2]. To bridge spectral features with portable devices, an effective wavelength λ_eff is adopted as a robust colorimetric metric computed within a fixed window.

Methodology and structure modelling

Porous-Si layers were described by the Bruggeman effective-medium approximation [3]. Optical constants for crystalline Si, air and ethanol were taken from curated datasets accessible via a consolidated database of refractive indices [4]. Normal-incidence reflectance R(λ) was computed using the transfer-matrix method. The rugate employed an apodized sinusoidal index profile with average index n_avg = 2.2, modulation Δn = 0.5 and 100 periods (10 slices per period); the resulting depth profile n(z) is illustrated in (Figure 1). Representative reflectance spectra for air versus ethanol used for analysis are shown in (Figure 2).

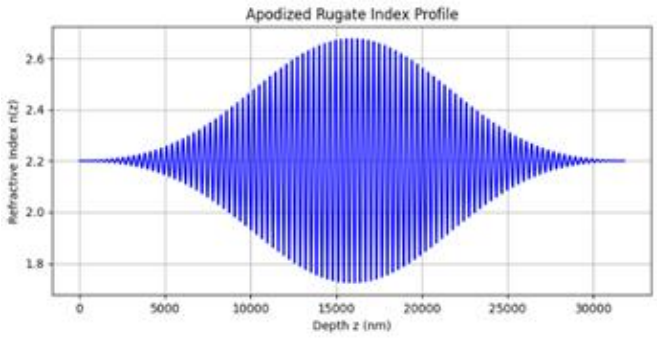

Fig. 1. Apodized rugate index profile n(z)

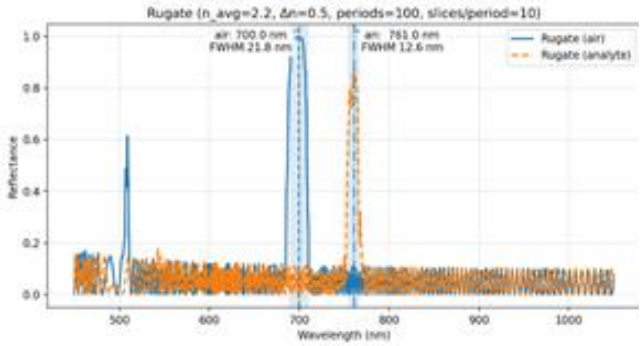

Fig. 2. Rugate reflectance spectra for air and ethanol; peak shift and FWHM annotated

Design wavelengths λ_0 spanned 450–650 nm. To quantify bandwidth evolution, the full-width at half-maximum (FWHM) versus λ_0 is summarized in (Figure 3). For compact readout, spectra were weighted by the illumination source and convolved with a 5-nm Gaussian instrument function; the colorimetric effective

wavelength λ_eff was evaluated within a fixed ±30-nm window around the resonance, and its dependence on λ_0 is presented in (Figure 4).

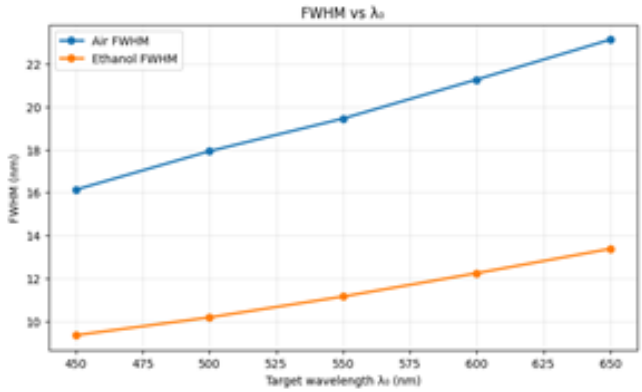

Fig. 3. Rugate bandwidth (FWHM) vs target wavelength λ_0 for air and ethanol

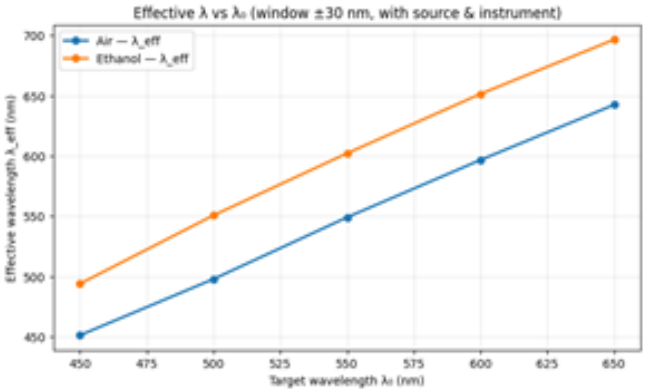

Fig. 4. Effective wavelength λ_eff vs λ_0 using a fixed ±30-nm window with source & instrument weighting

Simulation results

Across 450–650 nm, the rugate exhibits narrowband resonances whose FWHM increases moderately with the design wavelength. Ethanol infiltration narrows the band and red-shifts the resonance relative to air, with a representative shift of ~61 nm near λ_0 = 700 nm. Within the ±30-nm integration window, λ_eff is nearly linear in λ_0 and remains consistently larger for ethanol than for air. These properties support calibration by a single slope plus offset and enable readout without a full spectrometer. Across the design band, the air–ethanol separation in the resonance position remains larger than the 5-nm instrument function width, enabling reliable discrimination under moderate noise. For both media, the effective-wavelength traces are well described by a single linear fit over 450–650 nm, which simplifies one-time calibration and subsequent drift checks.

Conclusion

The modeling demonstrates concrete performance gains under analyte infiltration. Relative to air, ethanol shifts the rugate resonance by ≈61 nm near λ_0 = 700 nm, which corresponds to an ~8.7% change in the optical period. The simulated mean bandwidth remains ≈17 nm, while ethanol narrows the band by roughly 3–4 nm (~20% reduction), easing peak localization under noisy conditions. Using the fixed ±30-nm window, the effective-wavelength readout preserves the same direction and magnitude of change as the spectral peak, enabling calibration with a single linear coefficient across 450–650 nm. In sum, within the tested conditions the apodized p-Si rugate provides larger signal excursions (tens of nanometers) and narrower features (≈20% smaller FWHM in ethanol) than the air baseline—a combination that improves detectability and supports compact colorimetric sensing.

References

[1] M.J. Sailor, Porous Silicon in Practice: Preparation, Characterization and Applications. Wiley-WCH, 2011.

[2] H.A. Macleod, Thin-Film Optical Filters, 4th ed., CRC Press, 2010.

[3] D.A.G. Bruggeman, “Berechnung verschiedener physikalischer Konstanten von heterogenen Substanzen,” Ann. Phys., 416(7), 636–664 (1935).

[4] RefractiveIndex.INFO database (optical constants for Si, air, ethanol; accessed 2025).

MEDICAL PHYSICS

ABSORPTION AND SCATTERING OF COPPER VAPOR LASER RADIATION IN BIOLOGICAL TISSUES

Oleksandra Shokun*, Anatolii Ivanisik**

**Depertament of Biomedicine and Neurosciences, Kyiv Academical University, Kyiv 03142, Ukraine, e-mail: o.shokun@kau.edu.ua*

***Faculty of Radiophysics, Electronics and Computer Systems, Taras Shevchenko National University of Kyiv, Kyiv 01601, Ukraine, e-mail: anatoliyivanisik@gmail.com*

Laser radiation is widely used in medicine due to its high spatial precision and the ability to selectively affect biological tissues. The aim of this work was to experimentally investigate the absorption, scattering, and cutting of biological tissues (pork muscle and calf liver) under copper vapor laser radiation at wavelengths of 510.6 nm (green) and 578.2 nm (yellow). The results are important for optimizing laser parameters in biomedical applications such as surgery and optical diagnostics. The research was carried out during the author's bachelor studies at Taras Shevchenko National University of Kyiv.

Introduction

Laser–tissue interaction depends on the wavelength, intensity, and exposure duration of the radiation, as well as on the optical and thermal properties of the tissue. Copper vapor lasers (CVL) are of particular interest because they provide short, high-power pulses at visible wavelengths, making them suitable for medical research and precise tissue manipulation.

The visible range (green and yellow) corresponds to strong absorption by hemoglobin and melanin, which allows localized heating and controlled tissue modification. Understanding absorption and scattering processes in biological media is essential for determining safe and efficient laser operation modes in medicine.

Experimental Setup and Methods

The experiments were carried out using an ILGI-101 copper vapor laser operating with an average power of 0.75–0.8 W. Biological samples included pork muscle (1–3 mm thick) and calf liver (1 mm thick).

A calibrated silicon photodiode (ФД-24) was used to measure the intensity of scattered light at angles from 0° to 180°. The temperature distribution on the tissue surface and its rear side was measured using a non-contact infrared thermometer.

Additionally, temperature dynamics were analyzed for different tissue types to estimate heat diffusion and identify the threshold conditions for visible ablation.

Results and Discussion

Angular dependence of scattered radiation showed a characteristic Mie-type distribution, with intensity minima around 90° and maxima near 150–180°. For thicker samples, scattering increased due to multiple internal reflections and absorption.

Absorption experiments revealed that transmitted laser power decreases nonlinearly with tissue thickness: for 1.4 mm samples, about 33 % of the energy was absorbed, while for 2.7 mm, absorption reached nearly 60 %.

Temperature measurements demonstrated that energy absorption is mainly localized near the surface (front temperature up to 32 °C, back side ~25 °C). The highest surface heating was observed in liver samples, consistent with their homogeneous structure and higher water content. In contrast, muscle tissue exhibited lower heat propagation due to fibrous anisotropy.

When focused using a 5 cm lens, the beam achieved a power density sufficient for tissue incision (~1 kW/mm²). After ~10 minutes of exposure, visible charring and perforation were observed in muscle and liver samples, confirming ablation thresholds consistent with theoretical predictions.

Conclusions

The optical and thermal responses of biological tissues to copper vapor laser radiation strongly depend on their structure and thickness.

Liver tissue absorbs and distributes heat more uniformly.

Muscle tissue demonstrates stronger surface absorption and scattering.

The results can be applied to optimize laser parameters for biomedical technologies — particularly in minimally invasive surgery and optical diagnostics.

References

[1] Tuchin V.V., Tissue Optics: Light Scattering Methods and Instruments for Medical Diagnosis, SPIE Press, 2015.

[2] Rastegar S., Laser–Tissue Interactions, Springer, 2018.

[3] Michael J. Withford, Daniel J.W. Brown, Richard P. Mildren, Robert J. Carman, Graham D. Marshall, James A. Piper, Progress in Quantum Electronics: Advances in copper laser technology: kinetic enhancement 2004 – 165-196 c.

AN APPROACH TO INCORPORATING PHYSICAL DISTORTIONS INTO NEURAL NETWORKS FOR MEDICAL IMAGE RECONSTRUCTION

D.G. Sliusarenko[1,2], A.V. Netreba[1]

[1]Faculty of RadioPhysics, Electronics and Computer Systems Taras Shevchenko National University of Kyiv, Kyiv 01601, Ukraine, e-mail: avn@univ.kiev.ua

[2]National Cancer Institute of Ukraine, Yulii Zdanovskoi Street, 33/43, Kyiv, Ukraine, 03022, e-mail: d.fulhem@gmail.com

The work explores the possibility of improving the quality of MRI image reconstruction by integrating knowledge about artifacts obtained from phantom experiments. Statistical analysis of "clean" and distorted phantoms was performed, and a basis for training a neural network was formed. The further goal is to use these data to create more robust models that can effectively work with clinical images.

Introduction

In modern medical imaging tasks, improving the quality of reconstructed images is of particular importance, since the presence of noise and artifacts reduces the informativeness of diagnostics. Most of the known methods are based on statistical approaches or the use of deep neural networks, but they often do not take into account the physical nature of distortions that arise in real conditions. To study this problem, we used phantom images, which allows us to model both "clean" data and data with distortions.

Matherial and methods

For the study, phantoms were used, which allow modeling both "clean" images and images with distortions(Fig. 1.). This creates an opportunity for direct comparison of control and deformed data. A statistical analysis of phantom images was performed: intensity distributions, average values, standard deviations were studied, and quality metrics (PSNR, SSIM) were calculated. Based on this, a comparative database was formed, which serves as the basis for future training of the neural network.

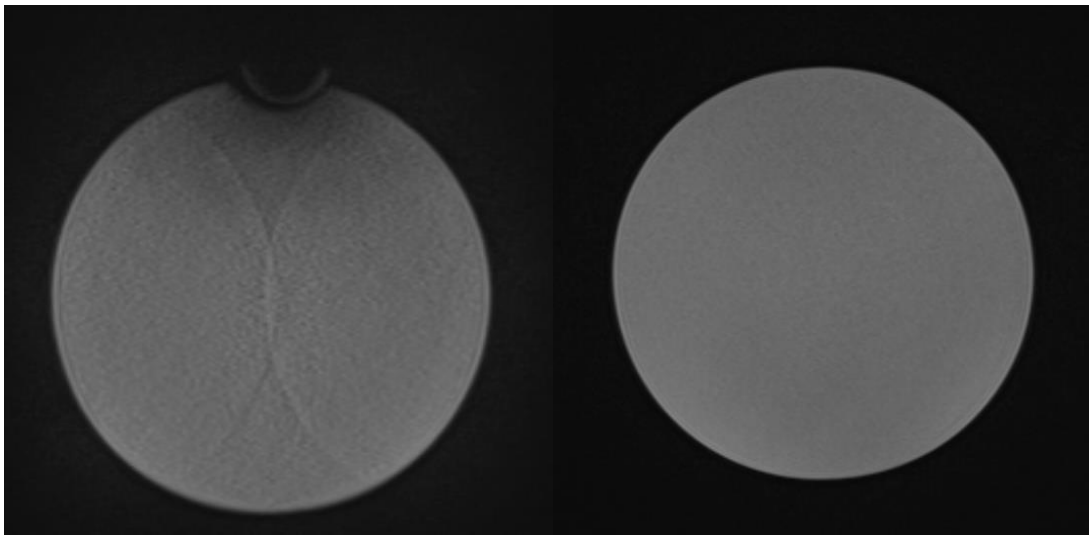

Fig. 1. Examples of images of a phantom with damage (left) and a clean phantom (right) made using a 1.5T

Clear differences between the characteristics of clean and distorted phantoms were found, which confirms the feasibility of including statistical parameters in the model. The results obtained demonstrate that combining traditional quality metrics with statistical characteristics of phantom images can provide a more complete picture of the nature of distortions. The next stage of the research involves integrating knowledge about distortions directly

into the structure of the neural network, in particular through additional inputs or special statistical modeling modules (Fig. 2.). It is expected that such an approach will increase the resistance of algorithms to artifacts and allow for more efficient recovery of clinical data.

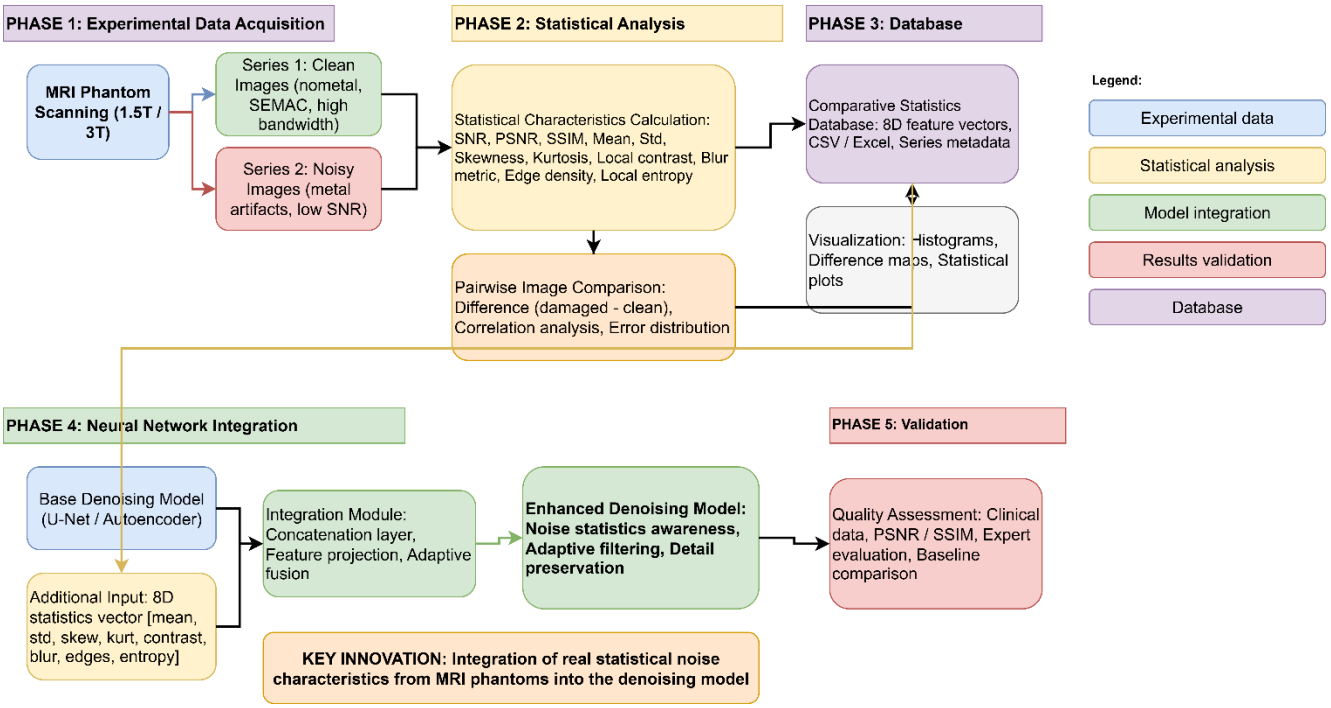

Fig. 2. Schematic representation of the jeneral idea

Conclusions

Statistical analysis of the obtained phantom images was performed, in particular, intensity distributions, average values, deviations and quality metrics (PSNR, SSIM) were studied. On this basis, a basis was formed for further training of neural networks, where controlled conditions (pure phantom) were compared with conditions with added artifacts.

References

[1] M. Li, S. Shan, S. S. Chandra, F. Liu, and S. Crozier, 'Fast geometric distortion correction using a deep neural network: Implementation for the 1 Tesla MRI-Linac system', *Med. Phys.*, vol. 47, no. 9, pp. 4303–4315, 2020, doi: 10.1002/mp.14382.

[2] F. Tan, J. G. Delfino, and R. Zeng, 'Evaluating Machine Learning-Based MRI Reconstruction Using Digital Image Quality Phantoms', *Bioengineering*, vol. 11, no. 6, p. 614, Jun. 2024, doi: 10.3390/bioengineering11060614.

OPTIMIZATION OF CONVOLUTIONAL NEURAL NETWORKS FOR MEDICAL IMAGE ANALYSIS

Vadym Kyrychenko
Faculty of RadioPhysics, Electronics and Computer Systems, Taras Shevchenko National University of Kyiv, Kyiv 01601, Ukraine, e-mail: vk.kyrychenko@gmail.com

The paper investigates an approach to optimizing Convolutional Neural Networks (CNNs) for medical image analysis. An experimental study was conducted to examine the influence of architecture, hyperparameters, and regularization methods on classification accuracy. The ResNet152V2 model, optimized using the transfer learning technique, demonstrated the best results. The findings confirm the effectiveness of comprehensive CNN optimization in improving the quality of automated medical diagnostics.

Keywords: convolutional neural network, optimization, transfer learning, augmentation, regularization, medical images.

Introduction

Convolutional Neural Networks (CNNs) represent one of the most effective tools for image analysis, particularly for medical images. However, their effectiveness significantly depends on the proper architecture, hyperparameter settings, and regularization techniques. The objective of this study is to develop an approach for optimizing CNN parameters to improve the accuracy of medical image classification while working under limited computational resources.

Methods

For training, we utilized pre-trained architectures (VGG19, DenseNet201, EfficientNetV2S, ConvNeXt, ResNet152V2) applying the transfer learning technique. Data preprocessing and augmentation (shifting, rotation, scaling, normalization) were performed. We investigated the influence of key hyperparameters: learning rate, mini-batch size, number of epochs, and the type of optimizer (Adam, SGD, RMSprop). Dropout and EarlyStopping were employed to prevent overfitting.

Results

The ResNet152V2 architecture demonstrated the best efficiency among the specified architectures with the following optimized hyperparameters:

- Optimizer: Adam;
- Learning Rate: 0.0001;
- Mini-batch Size: 8;
- Dropout: 0.5.
- Overfitting Prevention Methods: Dropout and EarlyStopping.

We achieved a classification accuracy of 92.3%, an F1-score of 0.91, and an AUC (Area Under the Receiver Operating Characteristic Curve) of 0.96 on the test set. The application of data augmentation reduced overfitting and improved training stability.

Conclusions

The optimization of CNN architecture and hyperparameters provides a significant increase in accuracy while preserving computational efficiency. The proposed approach can be generalized for a wide range of medical

diagnostic tasks, such as pathology classification, analysis of histological images, and tomographic data. This presented approach yields optimal results with limited computing hardware resources.

References

[1] Ruuskanen, O.; Lahti, E.; Jennings, L.C.; Murdoch, D.R. Viral pneumonia. Lancet 2011, 377, 1264–1275. https://doi.org/10.1016/S0140-6736(10)61459-6

[2] Yamashita, R., Nishio, M., Do, R.K.G. et al. Convolutional neural networks: an overview and application in radiology. Insights Imaging 9, 611–629 (2018). https://doi.org/10.1007/s13244-018-0639-9

[3] W.W. McCulloch and W. Pitts, A Logical Calculus of the Ideas Inminent in Nervous Activity, Bulletin of Mathematical Biophysics, 5:115–133, 1943.

[4] Hebb, D. O. The organization of behavior: a neuropsychological theory. New York, 1949.

[5] Siddiqi R, Javaid S. Deep Learning for Pneumonia Detection in Chest X-ray Images: A Comprehensive Survey. Journal of Imaging. 2024; 10(8):176. https://doi.org/10.3390/jimaging10080176

[6] Sousa, R.T.; Marques, O.; Soares, F.A.A.M.N.; Sene, I.I.G.; de Oliveira, L.L.G.; Spoto, E.S. Comparative Performance Analysis of Machine Learning Classifiers in Detection of Childhood Pneumonia Using Chest Radiographs. Procedia Comput. Sci. 2013, 18, 2579–2582.

MULTITAPER K-SPACE DENOISING OF MAGNETIC RESONANCE IMAGES

S.P. Mamotenko*, A.V. Netreba**
** Faculty of Radiophysics, Electronics and Computer Systems, Taras Shevchenko National University of Kyiv. Volodymyrska Street, 64/13, Kyiv-01601, Ukraine, e-mail: serzhulka@univ.net.ua*
*** Faculty of Radiophysics, Electronics and Computer Systems, Taras Shevchenko National University of Kyiv. Volodymyrska Street, 64/13, Kyiv-01601, Ukraine, e-mail: avn@univ.kiev.ua*

Medical images such as MRI are not represented directly as images; their data are stored in k-space, which corresponds to the spatial frequency spectrum. The high-frequency part of this signal can be influenced by noise. Noise reduction is typically performed using high-pass filters or by applying different types of windowing functions to the signal. We suggest exploring a recently developed approach called multitaper analysis, which uses multiple orthogonal windows (tapers) to process the signal. The result will be evaluated using SSIM and PSNR and compared to a traditional windowing function.

Methodology

MRI raw data are typically represented in k-space, which corresponds to the spatial frequency spectrum. The center of k-space contains low-frequency components that describe gradual intensity variations, while high-frequency components are located near the Nyquist boundary and are responsible for fine details and sharp transitions. Noise usually appears at high frequencies; however, high-frequency filtering inevitably leads to the loss of fine image details. Several methods have been developed to balance noise suppression and detail preservation.

A study covering the periodogram method of MR image processing [1] highlights the method's non-parametric nature and its ability to smooth the spectrum over neighboring frequencies. The periodogram, however, is known to be a poor spectral estimator because the use of a rectangular window introduces bias and high variance. Importantly, increasing the data length does not reduce this variance.

Different windowing functions, such as Hann and Hamming, have been investigated to reduce spectral leakage. More recent studies [2] show that instead of a single taper, using multitaper analysis, which averages spectra from multiple DPSS tapers (Discrete Prolate Spheroidal Sequences), provides better noise suppression and more stable estimates. Multitaper has several parameters; the most notable are Δf, N, TW, and L.

Spectral resolution, or Δf, is essentially the size of the main lobe. Its value controls the degree to which two neighboring oscillations can be separated. The value of Δf needs to be smaller than the minimum frequency distance between two neighboring oscillations. Spectral window size N determines the length of the input data segment in seconds over which the signal is assumed stationary. The time–half-bandwidth TW controls the trade-off between frequency resolution and variance reduction and is defined as:

$$TW = \frac{N\Delta f}{2}$$

Number of tapers L is a number of DPSS tapers.

To avoid manual tuning of multitaper parameters, Stein's Unbiased Risk Estimate (SURE) will be used. SURE provides an unbiased estimate of the mean squared error through a SURE map.

Results

An MRI brain scan was used for the study with the following characteristics: a 24-year-old male patient, sagittal orientation images, and dimensions of 255 × 255 pixels. A test run of the image reconstruction implemented using the Daniell periodogram method, which uses a single rectangular window, will be demonstrated first:

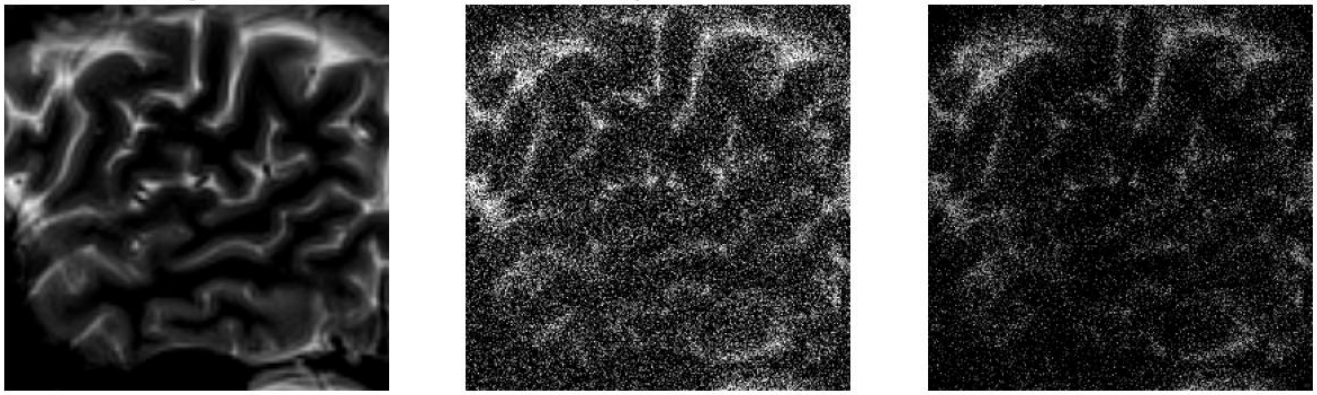

(a) (b) (c)

Fig. 1. Daniell Periodogram method. Original brain MR image (a), image with noise (b), reconstructed image (c)

When a rectangular window is applied, it results in a highly distorted reconstructed image, which lacks sufficient contrast to distinguish details in the cortical structure. This outcome of using a single taper is expected: the rectangular window introduces bias, high variance, and inconsistent estimators.

The next test run was conducted using the Multitaper method:

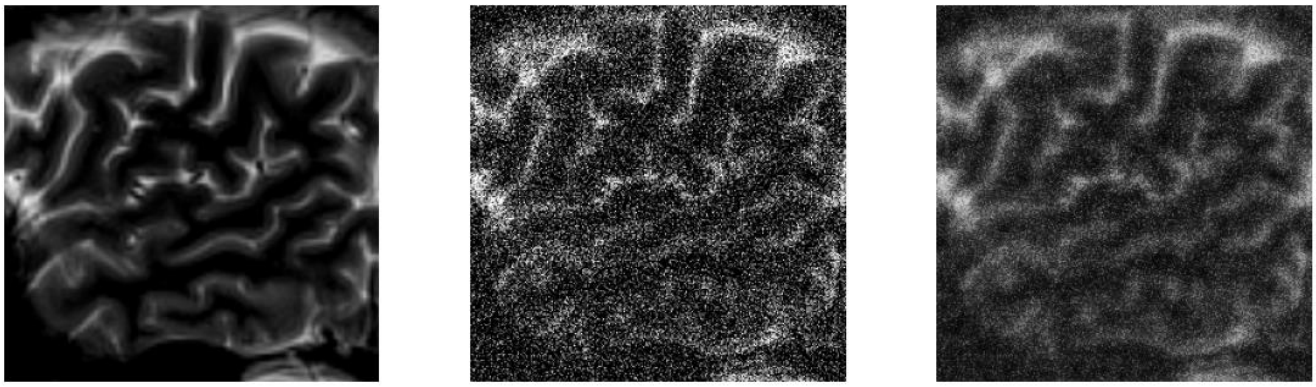

(a) (b) (c)

Fig. 2. Multitaper method. Original brain MR image (a), image with noise (b), reconstructed image (c).

The main difference of the Multitaper method is that the reconstructed image in Figure 2(c) has much more distinctive edges and does not lack signal and contrast, unlike the reconstructed image in Figure 1(c). Multitaper reduces estimate variance (noise) through averaging across multiple windows (tapers); therefore, it is beneficial to use as many tapers as possible within the limits of the data assumptions. The Multitaper method improved the SSIM by about 3 times and the PSNR by about 6 dB, while the periodogram method achieved only about a 1.4 SSIM increase and about a 2.8 dB PSNR gain.

References

[1] Mamotenko, S., Netreba, A., “Magnetic resonance image data processing by the periodogram method”, Radioelectronics and Communications Systems, 2025.

[2] Prerau M.J., Bianchi M.T., Brown R.E., Ellenbogen J.M., Patrick P.L., “Sleep Neurophysiological Dynamics Through the Lens of Multitaper Spectral Analysis”, Physiology (Bethesda), vol. 32, pp, 60-92, 2017.

MULTIMODAL HETEROGENEOUS DATA INTEGRATION FOR EXPLAINABLE MEDICAL SIGNAL RECOGNITION

V.I. Sapaiev *, A.V. Netreba **

**Faculty of RadioPhysics, Electronics and Computer Systems, Taras Shevchenko National University of Kyiv, Kyiv 01601, Ukraine, email: sapaiev.viktor@gmail.com*

***Faculty of RadioPhysics, Electronics and Computer Systems, Taras Shevchenko National University of Kyiv, Kyiv 01601, Ukraine, email: avn@univ.kiev.ua*

We present a modular, physics-informed hybrid pipeline that integrates deep representation learning with statistical dependence modeling and clinically grounded explainability. The system prioritizes transparency as a design constraint, not an afterthought, and is engineered to be robust to missing modalities, sparse labeling, and sensor noise—key realities in clinical deployment. Our approach consists of four stages: (1) domain-aware preprocessing, (2) hybrid feature extraction, (3) copula-based cross-modal dependency modeling, and (4) interpretable decision fusion.

Each modality is processed in a dedicated, anatomy-aware branch. ECG signals undergo band-pass filtering (0.5–40 Hz) to remove baseline wander and high-frequency noise, followed by segmentation into cardiac cycles and extraction of time-domain HRV metrics (SDNN, RMSSD), interval durations (QRS, QT), and morphological features (P-wave amplitude, T-wave symmetry). EEG is preprocessed with laplacian re-referencing, spectral power extraction (delta, theta, alpha, beta, gamma), and artifact flags from kurtosis and variance thresholds. Imaging inputs (X-rays) are normalized to Hounsfield units, resized to 512×512, and augmented with mild random contrast and rotation—symmetric with radiologist workflow as studied in [1]. Clinical notes are vectorized using domain-specific sentence embeddings (ClinicalBERT) rather than TF-IDF, to better capture symptom-context relationships such as “increased dyspnea with exertion” versus “effort intolerance,” improving semantic alignment with physiological signals.

Deep features are extracted via 1D CNNs for signals and lightweight Vision Transformers (ViT-Tiny) for images, producing latent embeddings of 128–256 dimensions—small enough to avoid dominance over engineered features, as recommended in [2]. These are concatenated with engineered descriptors (HRV, spectral bands, radiographic texture scores) to form a fused representation that preserves both data-driven abstraction and domain knowledge.

The core innovation lies in the copula-based dependency layer. Rather than fusing via concatenation or attention, we model the joint distribution of features across modalities using Gaussian and t-copulas, following the approach in [3], where tail dependencies between modalities—such as prolonged QT interval paired with low SpO_2 or subtle parenchymal infiltrates co-occurring with elevated troponin—capture clinically significant risk signatures missed by linear correlation. By separating marginal distributions from the dependence structure, copulas allow us to quantify extreme co-occurrence events with parameters like the tail dependence coefficient (λ) and degrees of freedom (ν), which are fed directly into the decision stage as interpretable risk indicators. For copula selection, we apply AIC-based model comparison to avoid overfitting, consistent with recommendations in [4].

Fusion occurs at the feature level, where deep embeddings, engineered features, and copula parameters are combined into a single vector. The final classifier is a calibrated Random Forest, selected for its robustness to mixed data types, insensitivity to scale, and native compatibility with SHAP-based attribution. We avoid end-to-end neural fusion (e.g., transformers) because recent benchmarks show they underperform on small, noisy datasets unless heavily regularized, and often lose interpretability even when paired with post-hoc methods [5]. Instead, our architecture supports plug-and-play substitution: future work may replace the RF with a calibrated logistic regression or a constrained neural net, without altering upstream branches.

Explainability is embedded at two levels. For global interpretability, SHAP values rank feature contributions across the cohort, identifying dominant predictors (e.g., “longest QT duration” or “right lower-lobe opacification + heart rate variability decrease”)—a practice endorsed by clinical AI consensus guidelines [6]. For local, visual reasoning in imaging, we compute Grad-CAM heatmaps over the ViT attention maps, overlayed on the original X-ray, providing clinicians with anatomical rationales. Crucially, all explanations are generated after training, avoiding the illusion of interpretable learning—an architecture already aligned with best practices in medical AI transparency [7].

We envision the pipeline’s potential through initial simulations and theoretical analysis on public benchmarks. Conceptual validation suggests that integrating copula-based dependence modeling with domain-aware features could enhance sensitivity to subtle, multimodal anomalies — such as concurrent QT prolongation and marginal SpO_2 drops — that are often missed by single-modality or linear fusion approaches. Empirical evaluation on standard datasets (MIT-BIH, TUH EEG, MIMIC-CXR) is planned as the next step, with the goal of demonstrating improved robustness and interpretability without sacrificing computational efficiency.

In summary, our framework demonstrates that combining physics-informed preprocessing, hybrid feature extraction, and statistical dependence modeling yields clinically meaningful gains in accuracy without sacrificing interpretability. It does not seek to replace clinicians with algorithms, but to equip them with a decision-support system whose reasoning mirrors their own: integrating cues across modalities, recognizing patterns of co-occurrence, and justifying conclusions in ways that are auditable, understandable, and actionable. For cardiology, neurology, and intensive care, this approach offers a pragmatic pathway toward trustworthy, deployable multimodal AI.

References

[1] J. Sapru, R. K. Giri, and M. D. R. P. Reddy, “Domain-aware preprocessing for medical imaging and time-series signals: best practices for clinical ML,” arXiv:2307.05329, 2023. https://arxiv.org/abs/2307.05329

[2] Z. Zhang, C. Liu, and T.J. Wang, “Why simple feature concatenation often fails in multimodal medical AI (and how to fix it),” arXiv:2308.07122, 2023. https://arxiv.org/abs/2308.07122

[3] A. Tosun, K. Patel, S. Chen, et al., “Copulas for capturing extreme joint events in multi-sensor health data,” arXiv:2211.14231, 2022. https://arxiv.org/abs/2211.14231

[4] Y. Chen, L. Wang, and H. M. Li, “Copula selection in high-dimensional health data,” arXiv:2103.04011, 2021. https://arxiv.org/abs/2103.04011

[5] S. Gupta and A. Rajpurkar, “Benchmarking fusion strategies on MIMIC-CXR + EHR: when engineered features outperform end-to-end models,” arXiv:2403.09155, 2024. https://arxiv.org/abs/2403.09155

[6] AMIA & RSNA Task Force on Clinical AI Interpretability, “Ethical standards for explainable AI,” arXiv:2401.10283, 2024. https://arxiv.org/abs/2401.10283

[7] E. Lehrer, M. M. Silva, and D. J. A. Chang, “Interpretable fusion architectures in medical AI: from post-hoc explanations to design-time transparency,” arXiv:2305.12089, 2023. https://arxiv.org/abs/2305.12089

COMPARISON ATP THEORETICAL AND EXPERIMENTAL IR SPECTRA

Yu.G. Terentieva*, K.O. Maiko, I.S. Voiteshenko*****
** Taras Shevchenko National University of Kyiv, Faculty of Radiophysics, Electronics and Computer Systems, Kyiv 01601, Ukraine, e-mail: kovskajulia@gmail.com*
*** Taras Shevchenko National University of Kyiv, Faculty of Radiophysics, Electronics and Computer Systems, Kyiv 01601, Ukraine, e-mail: maiko_kate@ukr.net*
**** Taras Shevchenko National University of Kyiv, Educational Scientific Institute of High Technologie, Kyiv 01601, Ukraine, e-mail: isvoiteshenko@knu.ua*

The spectral investigations of ATP aqueous solution have been made to prove their conformer existence. The theoretical calculation for molecule made by Gaussian 16 package [1]. We predict the existence at least of two stable conformer forms with relatively close concentrations. The calculated IR spectra have a good agreement with experimental FTIR spectra.

Experimental and theoretical investigation

Hydrotrope properties of ATP and its ability to prevent intracellular protein aggregation can explain wide-spreaded age-related vision-threatening ocular diseases such as age-related cataract, presbyopia, age-related macular degeneration, which appear with decreasing of ATP concentration [2]. It is well known that left and right enantiomers are frequently observed in nature, however, left form is useful for biological processes while influence of right form can be harmful for living organism. So investigation of conformer forms of potential drug molecules can be crucial. The spectral investigations of ATP aqueous solution have been made ($C=2\cdot10^{-4}$M, under ambient temperature) to prove their conformer existence. The theoretical calculation for molecule made by Gaussian 16 package (in ground and excited states with non-empirical DFT, TD-DFT/6-311G+(d,p)/B3LYP level of theory).

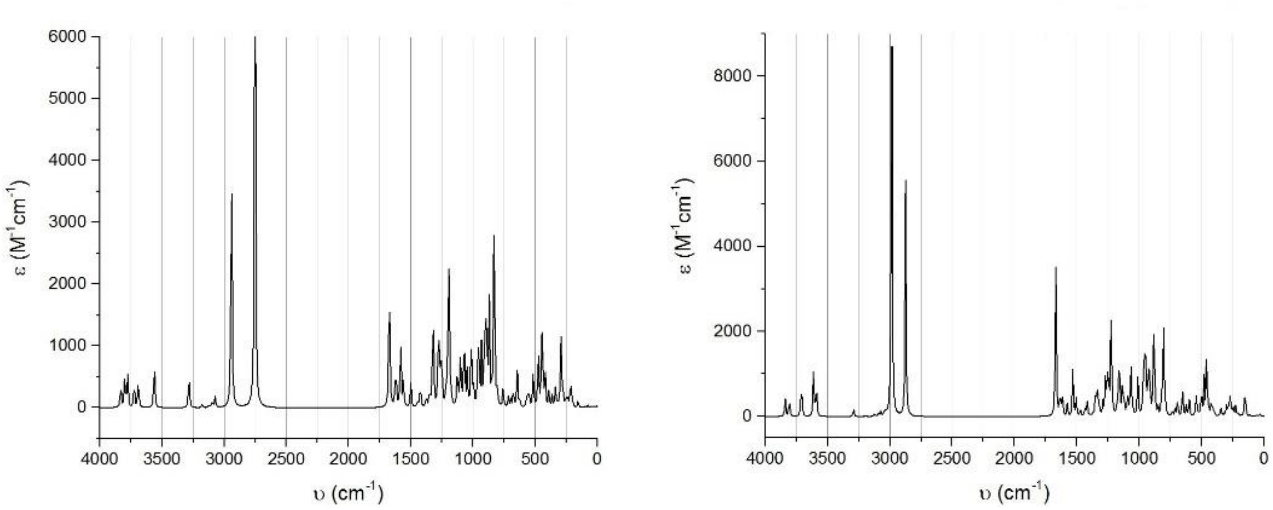

Fig. 1. Calculated IR spectra for two conformer forms of ATP molecule

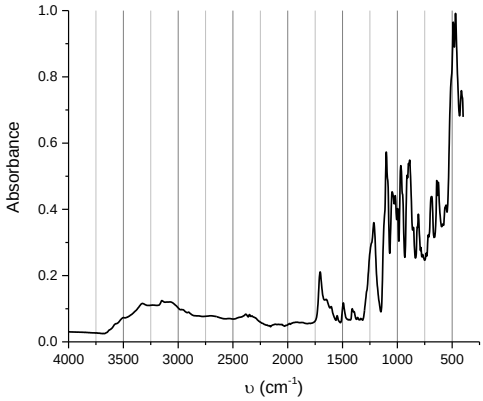

Fig. 2. FTIR spectrum of ATP molecule

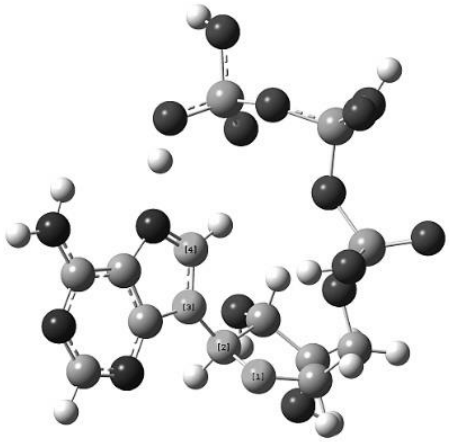

Fig. 3. Model ATP molecule

Conformational energy of ATP molecule has two minima separated by maximum ~ 5kT. This allows to predict the existence at least of two stable conformer forms with relatively close concentrations in water solution. The IR spectra were calculated for stable conformer forms of ATP molecule. The calculated IR spectra have a good agreement with experimental FTIR spectra. Theoretical part also includes quantum-chemical calculations of molecular geometry of ATP in ground and excited states with different values of fixed torsion angle (with step of 5°) between adenine and ribose (fig.3.), while the phosphate groups of molecule are free to fit to new spatial orientation. Water was chosen as a solvent for calculations. These calculations allowed to create conformer profiles for ATP molecule, and define two conformers with the lowest energies.

References

[1] Gaussian 16, Revision C.01, M. J. Frisch, G. W. Trucks, H. B. Schlegel, et al., Gaussian, Inc., Wallingford CT, 2016.

[2] Greiner JV, Glonek T. Adenosine Triphosphate (ATP) and Protein Aggregation in Age-Related Vision-Threatening Ocular Diseases // Metabolites.-2023-13(10):1100.

GENERATION OF STIMULATED RAMAN SCATTERING IN SEQUENTIALLY ARRANGED SELF-FOCUSING MEDIA

Oleksandr Mokhonko*, Anatoliy Ivanisik**
**Faculty of RadioPhysics, Electronics and Computer Systems, Taras Shevchenko National University of Kyiv, Kyiv 01601, Ukraine, e-mail: oleksandr.mokhonko@knu.ua*
***Faculty of RadioPhysics, Electronics and Computer Systems, Taras Shevchenko National University of Kyiv, Kyiv 01601, Ukraine, e-mail: anatoliyivanisik@gmail.com*

This study presents a numerical simulation of stimulated Raman scattering (SRS) in two sequentially arranged self-focusing organic media — toluene and benzene. The model visualizes the evolution of the laser beam, which forms two focal regions within each medium, and demonstrates the generation of Stokes and anti-Stokes components. In the example considered, the first medium partially limits the efficiency of component generation in the second; however, with appropriate optimization of system parameters, this interaction can become constructive, enhancing the overall Raman conversion efficiency.

Introduction

Stimulated Raman scattering (SRS) is one of the fundamental processes of nonlinear optics that enables the generation of new frequencies in a medium under the influence of laser radiation. Typically, the SRS process is studied within a single homogeneous medium. In this work, a new approach is proposed — the use of sequentially arranged self-focusing media, specifically toluene and benzene, which makes it possible to study the interaction of several nonlinear optical processes in a cascaded system.

The obtained results are important for a deeper understanding of the spatial–spectral evolution of a laser beam under self-focusing conditions, as well as for the development of controllable multicomponent sources of coherent radiation. In particular, the cascaded excitation of Stokes and anti-Stokes waves in media with different nonlinear coefficients opens up opportunities for controlling the spectral range of generation, reducing the SRS threshold, and creating efficient tunable Raman lasers. Moreover, the proposed model can be used to optimize laser parameters in systems where the effects of SRS and self-focusing occur simultaneously, which is relevant for spectroscopy, laser photonics, and optical diagnostics of materials [1].

Modeling results

The modeling of the double-cell system is performed in the Wolfram Mathematica environment. The first cell contains the organic substance toluene, and the second one — benzene, each having its own characteristic optical parameters. These substances were selected because they belong to the class of transparent self-focusing organic liquids with similar refractive indices but different nonlinear refractive coefficients (n_2) [2]. Such a combination provides a convenient model for studying cascaded energy transfer between nonlinear media and allows tracing the influence of varying nonlinearity on the conditions of self-focusing and the generation of Stokes. To describe the behavior of the laser beam in the medium, the following formula was used [3]:

$$a(z) = a_0 \sqrt{|1 - \frac{z^2}{z_f}|^{\mu/2} + \frac{{a_f}^2}{{a_0}^2}}$$

The simulation results for both media are presented in Figure 1.

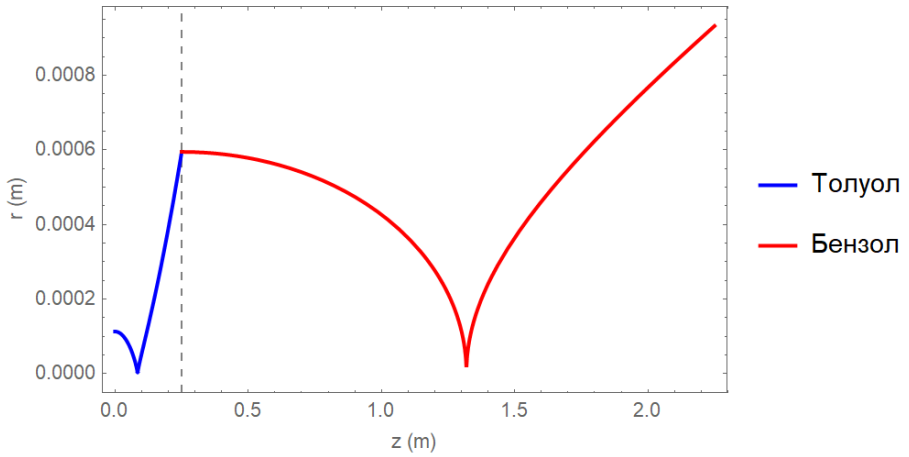

Fig. 1. Laser beam radius behavior

Two distinct focal regions can be observed within the cells. The first cell, filled with toluene and having a length of 0.25 m, exhibits a focus at approximately 0.08 m. The second cell, filled with benzene and having a length of 2 m, shows a focus at around 1.31 m.

Power of the Stokes components are presented in Figure 2.

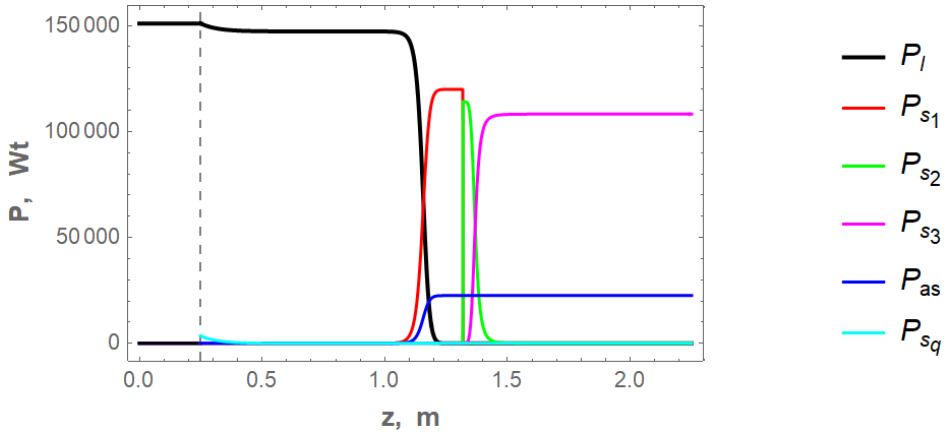

Fig. 2. Power of the Stokes components

The generation of the first three Stokes components in the second medium is presented, along with the anti-Stokes and backward Stokes components.

References

[1] Boyd, R.W. (2020). Nonlinear optics (4th ed.). Academic Press.
[2] Ivanisik, A.I. (2015). Dynamics of nonlinear optical processes in controllable liquids https://uacademic.info/ua/document/0516U000510
[3] Song, Y., Zhang, S., Lau, A. P. T., & Wang, D. (2024). SRS-Net: A universal framework for solving stimulated Raman scattering in nonlinear systems, 3, 109. https://doi.org/10.1038/s44172-024-00253-w

PLASMA PHYSICS

FORMATION OF HIGH-ENERGY SELF-INJECTED BUNCHES IN A LONGITUDINALLY INHOMOGENEOUS PLASMA CHANNEL AT LASER-PLASMA ACCELERATION

D.S. Bondar*, W. Leemans, V.I. Maslov***, I.N. Onishchenko******

**National Science Center "Kharkiv Institute of Physics and Technology", Akademichna street, b. 1, Kharkiv, Kharkiv region, Ukraine, e-mail: bondar.ds@yahoo.com*

*** Deutsches Elektronen-Synchrotron DESY, Notkestraße 85, Hamburg, Germany*

**** National Science Center "Kharkiv Institute of Physics and Technology", Akademichna street, b. 1, Kharkiv, Kharkiv region, Ukraine*

Deutsches Elektronen-Synchrotron DESY, Notkestraße 85, Hamburg, Germany, e-mail: vimaslov1955@gmail.com

***** National Science Center "Kharkiv Institute of Physics and Technology", Akademichna street, b. 1, Kharkiv, Kharkiv region, Ukraine, e-mail: ipenma@ukr.net*

For laser-plasma acceleration it was shown that the use longitudinally increasing plasma density gradient and conical channel leads to increasing of the accelerating gradient and the energy of a self-injected bunch.

The longitudinally increasing plasma density gradient helps to maintain the self-injected bunch in the acceleration phase and increases the accelerating gradient. The conical geometry of the channel allows to maintain and reduce the radius the laser pulse and increase the energy density on the axis. This leads to the formation of high-energy self-injected bunches in a inhomogeneous conical channel.

In laser wakefield acceleration (LWFA) high-energy electron bunches are obtained in compact setups, using intense laser pulse propagating through plasma to excite wakefield with > 100 GV/m longitudinal electric field [1, 2]. Self-injection occurs when plasma electrons are trapped to form bunch. The bunch parameters are sensitive to laser intensity, duration, and plasma density, so only indirect control is allowed. For example, inhomogeneous plasma schemes increase energy of the bunches [3, 5]. Inhomogeneous plasma density gradient using can help to produce electron bunch with low momentum spread and high quality [4]. Inhomogeneous profiles allow phase synchronization of self-injected bunches with accelerating wakefield [5]. Plasma channels enhance bunches longitudinal momentum, enhances electron bunches stability and propagation distance [6]. Numerical simulations completed using the 2D3V code WarpX [7].

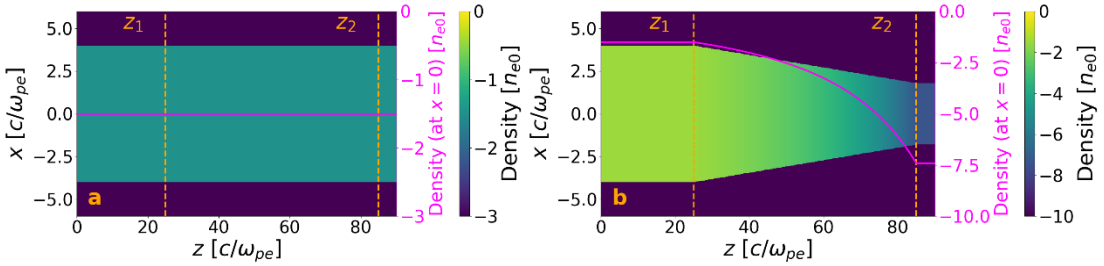

Fig. 1. Plasma electron density profiles $n_e(z, x)$ and $n_e(z, x=0)$.
(a) Cylindrical channel, (b) Inhomogeneous conical channel.

Compared with a homogeneous cylindrical plasma channel, the inhomogeneous conical plasma channel preserves particle number, strengthens laser focusing and boosts wake parameters. At t = 193.4 fs the acceleration field in the case of cylindrical channel reaches 216 GV/m, in the inhomogeneous conical channel is 1250 GV/m. In the case of cylinder channel the self-injected bunch is split into two parts: first bunch charge is 63.9 pC with average longitudinal momentum p_z = 36 $m_e c$ (5.64 pC and 46.47 $m_e c$ for the second). In the conical channel the bunch remains unchanged, charge rises to 75 pC and p_z increases to 76.9 $m_e c$.

On-axis EM energy density grows by 41 % in the conical channel case. The longitudinal momentum p_z in the case of a homogeneous cylinder reaches 44.2 $m_e c$ (22.78 % larger than in the case of homogeneous conical channel).

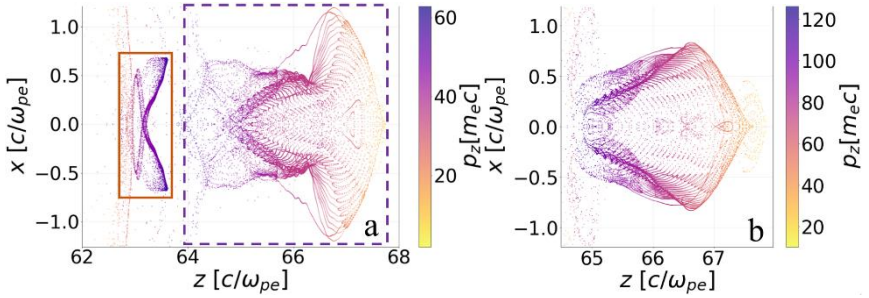

Fig. 2. (a) Cylindrical channel (ref. Fig 1(a)). Longitudinal momentum p_z of self-injected bunch electrons. The first bunch is highlighted with dots, the second bunch with a solid line. (b) Inhomogeneous conical channel (ref. Fig 1(b)). Longitudinal momentum p_z of self-injected bunch electrons, t=193.4 fs.

A clear advantage of using an inhomogeneous conical channel with plasma density increasing in the longitudinal direction was shown. This leads to an increase in the acceleration field by at least 5.79 times, and the longitudinal momentum of the self-injected bunch by 2.14 times. In addition, focusing of the laser pulse in the conical channel with an increase in energy on the axis was confirmed compared to the cylindrical case. Thus, the use of an inhomogeneous conical channel leads to stable acceleration of high charge and high-energy selfinjected bunches.

Acknowledgements

The study is supported by the National Research Foundation of Ukraine under the program "Excellent Science in Ukraine" (project # 2023.03/0182).

References

[1] T. Tajima and J. M. Dawson, "Laser Electron Accelerator," *Phys. Rev. Lett.*, vol. 43, no. 4, pp. 267–270, 1979, doi: 10.1103/PhysRevLett.43.267

[2] I.N. Onishchenko, "Wakefield acceleration based on high power pulsed lasers and electron beams (overview)," *Problems of Atomic Science and Technology*, no. 2(46), pp. 17–24, 2006

[3] V.I. Maslov, D. S. Bondar, and I. N. Onishchenko, "Investigation of the way of phase synchronization of a self-injected bunch and an accelerating wakefield in solid-state plasma," Photonics, vol. 9, p. 174, 2022, doi: 10.3390/photonics9030174

[4] C.G.R. Geddes *et al.*, "Plasma-Density-Gradient Injection of Low Absolute-Momentum-Spread Electron Bunches," *Phys. Rev. Lett.*, vol. 100, p. 215004, 2008, doi: 10.1103/PhysRevLett.100.215004.

[5] D.S. Bondar, V. I. Maslov, and I. N. Onishchenko, "On wakefield acceleration in inhomogeneous plasma," *Problems of Atomic Science and Technology*, no. 3(151), pp. 55–59, 2024, doi: 10.46813/2024-151-055

[6] C.G. R. Geddes, C. Tóth, J. van Tilborg, E. Esarey, C. B. Schroeder, D. Bruhwiler, C. Nieter, J. Cary, W.P. Leemans. "Production of high-quality electron bunches by dephasing and beam loading in channeled and unchanneled laser plasma accelerators" // Phys. Plasmas, 2005, v. 12, No. 5, p. 056709, doi: 10.1063/1.1882352

[7] L. Fedeli *et al.*, "Pushing the Frontier in the Design of Laser-Based Electron Accelerators with Groundbreaking Mesh-Refined Particle-In-Cell Simulations on Exascale-Class Supercomputers," *SC22: Int. Conf. for High Performance Computing, Networking, Storage and Analysis*, Dallas, TX, USA, 2022, pp. 25–36, doi: 10.1109/SC41404.2022.00008

SPACE-TIME DEPENDENCES OF FLOATING IN A A PLASMA OF HOLLOW CATHODE DISCHARGE INITIATED BY THE INJECTION OF A PLASMA BUNCH

V.Yu. Bazhenov*, V.V. Tsiolko*, V.M. Piun*
**Department of Gas Electronics, Institute of Physics NAS of Ukraine, Kyiv, Ukraine,*
e-mail: bazhenov@iop.kiev.ua, tsiolko@iop.kiev.ua, piun@iop.kiev.ua

*Spatial-temporal dependences of the floating potential of the plasma of a low-pressure pulsed discharge with a hollow cathode, which was ignited due to the injection of a plasma bunch, were experimentally determined. In particular, it was established that at certain moments of discharge glow, the electric field can reach values of ≈ 40 – 50 V/cm, which corresponds to a reduced electric field of ≈ 5*10^5 Td.*

Introduction

Reducing the content of microdroplets in the flows of "metal" plasma from vacuum-arc discharges used to create various coatings allows significant quality improvement of these coatings. Although the removal of microdroplets larger than ≈ 1…2 μm from plasma flows is achieved by fairly simple methods, the removal of microdroplets of smaller sizes is a rather complicated task. One of the approaches to reducing the number of microdroplets with sizes ≈ (0.1…1.0) μm is their evaporation when passing through an additionally created gas discharge plasma. It was shown in [1] that the use of pulsed hollow cathode (HC) discharge plasma in argon allows to reduce the number of Ti microdroplets with sizes ≈ (0.1…0.6) μm by several times. The studies conducted in [2] allowed us to establish the dependence of plasma parameters (density, electron temperature) on a type of power source used (voltage source or current source) and argon pressure. In particular, it was found that the electron temperature under certain discharge parameters (Ar pressure, discharge time etc) could reach ≈ (40…50) eV. In work [3] it was also shown that the reduced electric field in the plasma of such a discharge can reach 10^5 Td. The purpose of the presented research is a further study of spatial-temporal dependences of electric field strength in the discharge plasma by probe methods.

Experimental results and discussion

A cylindrical HC with an inner diameter of D = 120 mm and a length of L = 220 mm was enclosed with diaphragms under a floating potential - on the side of the vacuum-arc discharge, an input one with a 30 mm hole, and on the side of the collector with substrates - an output one with a hole with a diameter of 50 mm. Pulsed voltage with an amplitude of up to 10 kV and a duration of up to 10 ms was applied to the HC. The pulsed current of the arc discharge up to 120 A had a maximum duration of 1 ms. Voltage pulses on the arc and the HC were synchronized in such a way that the arc discharge ignited the HC discharge with its trailing edge. Argon pressure in the cathode cavity varied within the range of (2 – 10)*10^{-4} Torr. Floating potential in the discharge plasma was measured using six single Langmuir probes located at radii of 10 and 40 mm and at distances of 40, 110, and 180 mm from inlet diaphragm (these probes were azimuthally shifted from each other at an angle of 120^0).

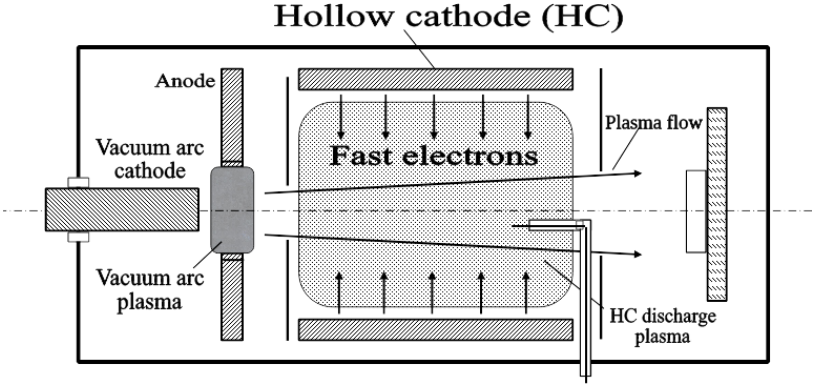

Fig. 1. Scheme of the experimental device

As can be seen from Fig. 2 and 3, the spatial-temporal dependences of the floating potential are quite complex - jumps in its magnitude in the first ≈ 0.5 ms of the discharge glow, a more or less smooth course of the dependence

in the next period ≈ (0.5 – 2.0) ms and again jumps that are poorly repeated from pulse to pulse. Fig. 2 and Fig. 3 also show an estimate of the electric field magnitude at the time of the discharge glow ≈ (1.25 – 1.50) ms (this time was chosen because, as shown in [3], the electron temperature reaches its maximum values at approximately the same time points). The radial field E_R reaches maximum values ≈ 40 V/cm (which corresponds to the reduced electric field E_R /N ≈ 5*10^5 Td) at small values of the distance L and decreases as it increases. The longitudinal electric field E_{II} is maximum at a radius of R = 40 mm (≈ 25 V/cm) and decreases towards the cathode axis.

An increase in argon pressure leads to both a certain change in the nature of the time dependence of U_f and a decrease in the electric field by almost an order of magnitude.

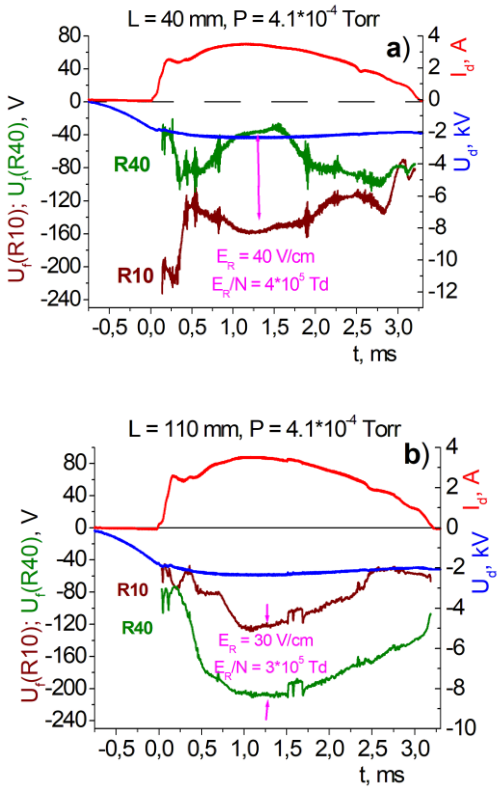

Fig. 2. Time dependences of the floating potential U_f of the probes at radii R of 10 and 40 mm and two distances L.

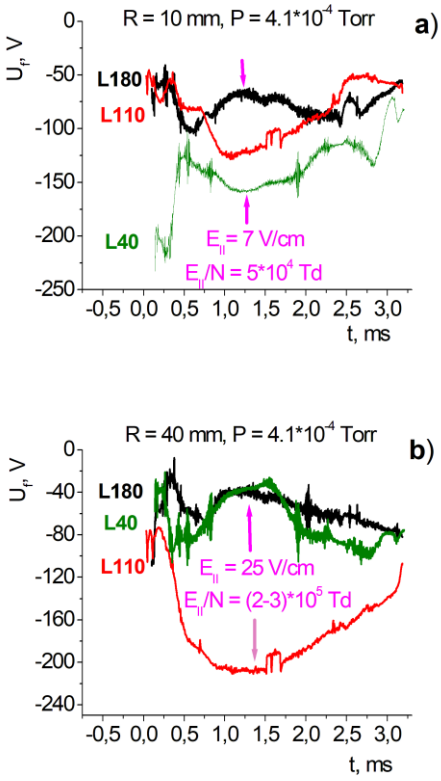

Fig. 3. Time dependences of the floating potential U_f of the probes at radii R of 10 and 40 mm and different L.

References

[1] A. Ryabtsev, V. Bazhenov, A. Goncharov, V. Maslov, V. Tsiolko. About possibility application a hollow cathode discharge for evaporation and filtration micro-droplets from erosion plasma source // *Proceedings of 10th International Conference on "Nanomaterials: Applications & Properties" (NAP-2021)* Odesa, Ukraine, 5-11 Sept. 2021, p. MTFC-A-03.

[2] V.Yu. Bazhenov, V.V. Tsiolko, V.M. Piun. Influence of power source type on time dependence of the plasma parameters of a pulse discharge with a hollow cathode // *Problems of Atomic Science and Technology. Series "Plasma Physics".* 2022, № 6, p. 95-98. DOI: 10.46813/2022-142-095.

[3] V.Yu. Bazhenov, V.V. Tsiolko, V.M. Piun. Some characteristics of pulsed discharge with hollow cathode in low pressure argon initiated by injection of plasma bunch. *Problems of Atomic Science and Technology.* 2025. №4(158), p. 83-86. https://doi.org/10.46813/2025-158-083.

PLASMA LENS FOR THE FOCUSING OF POSITRON BUNCHES

D.S. Bondar*, V.I. Maslov, I.N. Onishchenko*****
**National Science Center "Kharkiv Institute of Physics and Technology", Akademichna street, b. 1, Kharkiv, Kharkiv region, Ukraine, e-mail: bondar.ds@yahoo.com*
*** National Science Center "Kharkiv Institute of Physics and Technology", Akademichna street, b. 1, Kharkiv, Kharkiv region, Ukraine*
Deutsches Elektronen-Synchrotron DESY, Notkestraße 85, Hamburg, Germany, e-mail: vimaslov1955@gmail.com
**** National Science Center "Kharkiv Institute of Physics and Technology", Akademichna street, b. 1, Kharkiv, Kharkiv region, Ukraine, e-mail: ipenma@ukr.net*

This work presents a method for focusing positron bunches in plasma accelerators using a plasma lens operating in the linear regime, addressing the challenge of unstable focusing in nonlinear regimes. Numerical simulations of both Gaussian and flat-top bunch profiles demonstrate strong, high-quality transverse focusing. Furthermore, the system is shown to be effective for focusing a sequence of bunches and offers the potential to reduce the energy spread of bunches that follow a precursor.

Formation and parameters of self-injected bunches

Plasma lenses enable stable acceleration and simultaneous focusing of positron bunches, mitigating emittance growth and energy spread: simulations predict $> 5\,\mathrm{GV\,m^{-1}}$ gradients with nearly linear focusing forces, experiments have verified plasma focusing of 28.5 GeV beams, and comparative studies show poorer positron beam quality without tailored control; proposed solutions include hollow-beam drivers, tapered active plasma lenses, plasma-filled dielectric structures [1-6].

In this work proposed positioning the positron bunch so its head is decelerated while the tail is accelerated, leaving the core in near-zero field, thereby compressing energy spread similar to electron bunch [7].

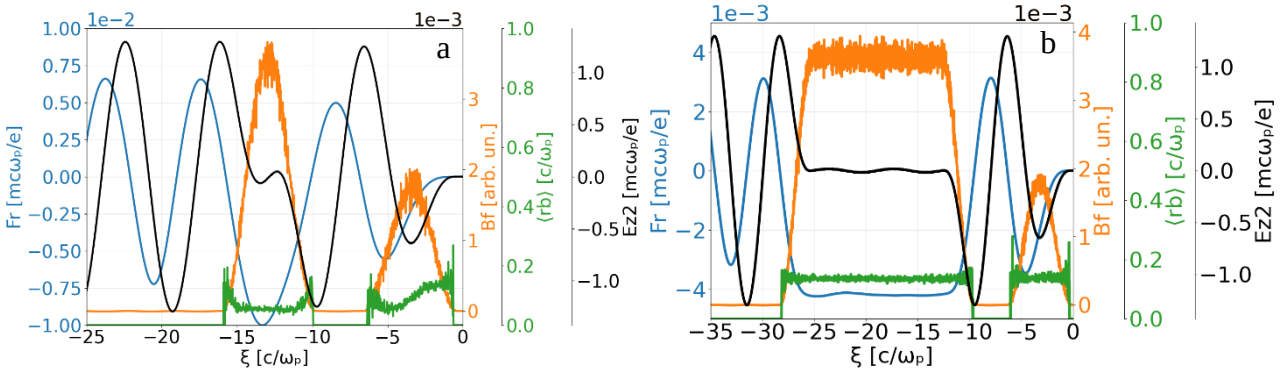

Fig. 1. Radial component of the Lorentz force Fr (blue) acting on bunch particles, azimuthal component of the magnetic field B_f, (orange) average bunch radius $<r_b>$ (green), on-axis longitudinal electric field E_{z2} (black). For all quantities r=0. ξ=z-ct. Simulation time is 45 ω_{pe}^{-1}. (a) Short Gaussian bunch. (b) Long bunch

In Fig. 1(a) it is illustrated that, in a 2D-cylindrical PIC simulation ($\gamma = 5$, $r_b = 0.1\ c/\omega_{pe}$), a short Gaussian positron bunch (λ_{pe}) positioned half a plasma wavelength behind a weaker precursor bunch situated in a wakefield phase where its head is decelerated and its tail accelerated; the resulting quasi-linear Lorentz force focuses ~70 % of the bunch core, reducing its radius by a factor ≈ 2.6 while equal and opposite head-tail energy exchange flattens the energy spread. Fig. 1(b) shows the same mechanism for a longer bunch with a flat-top center and Gaussian ends: uniform focusing persists only for $\lesssim 14\ \omega_{pe}^{-1}$, suggesting a pulsed-lens operation. Figure 2 confirms that adding a sequence of additional positron bunches at $0.5\,\lambda_{pe}$ intervals behind the first preserves identical focusing

conditions for each bunch, enabling a sequence of uniformly focused positron bunches with the exception of the first bunch that excited wakefield.

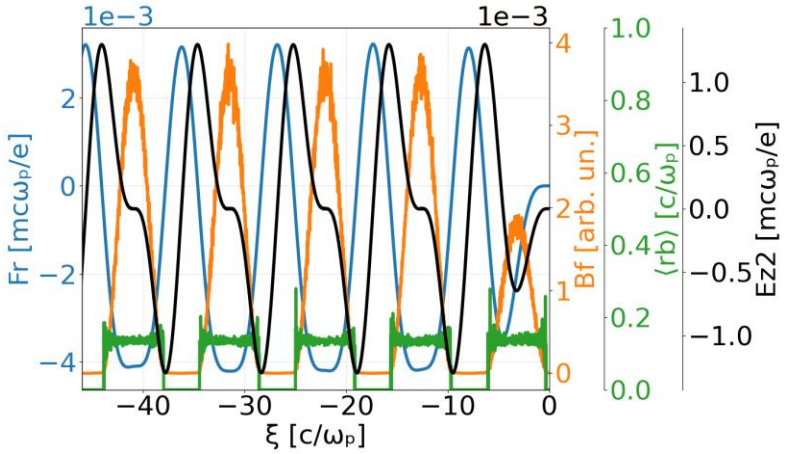

Fig. 2. Longitudinal component of the electric field on the axis E_z (blue), average longitudinal electric field at the bunch cross section $<E_z>$ (orange), average bunch radius $<r_b>$ (green). ξ=z-ct. Sequence of short positron bunches after first bunch-precursor

This paper presents a method for the focusing and of positron bunches by using a plasma lens in linear regime.

Numerical simulations show that by positioning the bunch in the correct phase of the wakefield where its head is decelerated while its tail is accelerated strong, high-quality transverse focusing is achieved, reducing the bunch radius by a factor of 2.6. The possibility of focusing of positron bunches sequences with identical and uniform focusing is demonstrated.

References

[1] S. Diederichs *et al.*, "Positron transport and acceleration in beam-driven plasma wakefield accelerators using plasma columns," *Phys. Rev. Accel. Beams*, vol. 22, no. 8, p. 081301, Aug. 2019, doi: 10.1103/PhysRevAccelBeams.22.081301.

[2] N. Jain, T.M. Antonsen, and J.P. Palastro, "Positron acceleration by plasma wakefields driven by a hollow electron beam," *Phys. Rev. Lett.*, vol. 115, no. 19, p. 195001, Nov. 2015, doi: 10.1103/PhysRevLett.115.195001.

[3] J.S.T. Ng *et al.*, "Observation of plasma focusing of a 28.5 GeV positron beam," *Phys. Rev. Lett.*, vol. 87, no. 24, p. 244801, Dec. 2001, doi: 10.1103/PhysRevLett.87.244801.

[4] D.S. Bondar, V.I. Maslov, I.N. Onishchenko, and R.T. Ovsiannikov, "Plasma lens for electron and positron beams," *Problems of Atomic Science and Technology*, no. 4(134), pp. 70–73, 2021, doi: 10.46813/2021-134-070.

[5] G.V. Sotnikov, R.R. Knyazev, P.I. Markov, and I.N. Onishchenko, "Focusing of positron bunch when moving in electron bunch wakefield in the dielectric waveguide filled with plasma," *Problems of Atomic Science and Technology*, no. 4(134), pp. 49–54, 2021, doi: 10.46813/2021-134-049.

[6] C. Yu *et al.*, "Sub-per-mille bunch energy spread in a quasi-linear laser-wakefield accelerator via periodical de-chirpings," *Commun. Phys.*, vol. 8, art. 137, Jul. 2025, doi: 10.1038/s42005-025-02057-6.

[7] I.V. Demydenko, V.I.Maslov. Passive plasma lens, reducing energy spread of Gaussian-kind bunches. *Problems of Atomic Science and Technology*, no. 3(151), pp. 67–72, 2024, doi: 10.46813/2024-151-067.

THE DAMAGING AND EROSION OF Li-CPS STRUCTURE UNDER TRANSIENT PLASMA LOADS

V.A. Makhlai*, I.E. Garkusha*, S.S. Herashchenko*, Y.E. Volkova*, Yu.V. Petrov*, D. V. Yelisyeyev*, P.B. Shevchuk*, Yu.V. Seromolot*,
T.W. Morgan**
** National Science Center, 'Kharkiv Institute of Physics and Technology', Institute of Plasma Physics, Akademichna, 1, Kharkiv, Ukraine makhlay@kipt.kharkov.ua*
*** DIFFER – Dutch Institute for Fundamental Energy Research, Eindhoven, the Netherlands*

The erosion of a selective laser melting (SLM) tungsten (W) Capillary Porous Structure (CPS) filled with Li was studied under both normal and oblique high-power plasma exposure in the QSPA Kh-50. The main experimental series consisted of about 50 QSPA plasma impacts with an energy density of ~ 3 MJ/m^2 and a pulse duration of 0.25 ms for each targets. The erosion of exposed CPS surface was discussed.

Introduction

The divertor in a tokamak reactor will be subjected to extreme heat and particle loads during transient events such as edge-localized modes (ELMs) and disruptions [1]. In addition to tungsten (W), which is currently selected as the baseline material for plasma-facing components (PFCs), alternative divertor designs incorporating liquid metals (LMs) are undergoing comprehensive assessment [1]. Liquid (Sn) and lithium (Li) are among the most promising candidates due to their low melting points, high thermal resilience, and ability to form a vapour shield, resulting in a significant decrease in surface heat load during transient plasma events [2-4]. LM divertors offer several advantages, including reduced mechanical stress in the liquid state and the ability to replenish eroded material through CPS. However, critical issues, such as droplet ejection, material transport, and plasma contamination, require dedicated simulations and experiments aimed at qualifying LM divertor concepts for a future DEMO-class reactor. This paper presents experimental studies of plasma-surface interactions during QSPA plasma exposures of Li-CPS prototypes at normal and inclined incidence, along with the analysis of the resulting damage to liquid-metal prototypes as a function of the applied energy loads.

Experimental conditions and results

Experimental simulations of fusion reactor transient conditions, including relevant surface heat load parameters such as energy density, pulse duration, and particle loads, were performed using the quasi-stationary plasma accelerator QSPA Kh-50 [5, 6]. The CPS targets filled with Li have been exposed to the plasma streams with an energy density varied in the range from 0.25 MJ/m^2 up to 3 MJ/m^2. The plasma loads above 1.1 MJ/m^2 typically cause strong melting and evaporation for pure tungsten samples in QSPA [5], while the smallest load applied is clearly below the W melting threshold. Other parameters of the QSPA hydrogen plasma streams were as follows: the ion impact energy of about 0.4 keV, the plasma stream diameter of 18 cm, and a maximum plasma pressure of 0.32 MPa. The plasma pulse shape was approximately triangular with a pulse duration of 0.25 ms. Targets used in the experiments were selective laser melting (SLM) tungsten (W) CPSs filled with Li and provided by DIFFER, with the detailed design described in [7]. The initial temperature of the sample (T_{base}) before plasma exposure remained at room temperature (T_{base}=RT). The surface of one target was oriented normal to the plasma stream (Fig. 1), while the other was oriented at an angle of 30° (Fig. 2). The main experimental series involved up to 50 plasma pulses. A high-speed digital camera PCO AG (10bit CMOS pco.1200 s) was employed for observing PSI and the ejections of erosion products. For clear monitoring of erosion product ejection from the affected surfaces, the exposure of 1.2 ms was selected.

High-speed camera observations of plasma-surface interactions (PSI) during CPS testing under high-intensity QSPA plasma demonstrated particle emission from the exposed targets (Fig. 1, 2). For the CPS target exposed normally to the plasma stream, it was found that the first plasma pulses with an energy density below 0.25 MJ/m^2 did not cause any particle ejection from the target surface. Intense particle ejection was recorded in the camera frames at energy densities between 1.2 and 3 MJ/m^2. The strongest bursts of droplets were observed at the

maximum energy density of the incident plasma flow (Q = 3 MJ/m^2). For both normal and inclined targets, the particle ejection was observed to occur in a nearly semi-spherical pattern, covering an area close to a 2π solid angle. The velocities of the ejected particles ranged from 1 to 33 m/s, with ejection occurring within the first few milliseconds of exposure. Notably, particles were still observed for more than 7 ms after the onset of PSI.

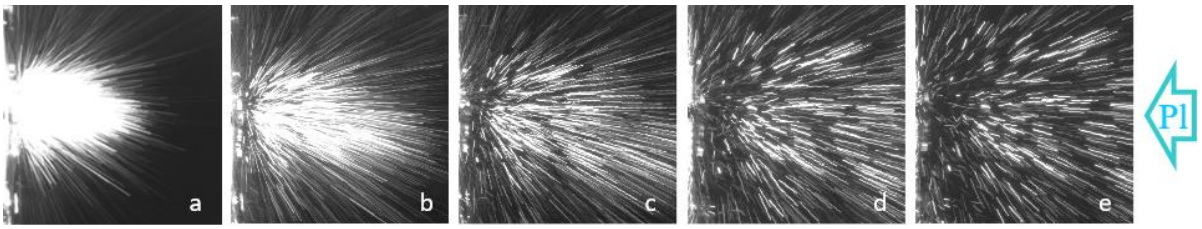

Fig. 1. Images of PSI after a plasma impact on a normally oriented CPS target (with an incoming plasma energy density of 3 MJ m^{-2}). The images correspond to 1.2-2.4 ms (a); 2.4-3.6 ms (b); 3.6-4.8 ms (c); 4.8-6 ms (d); 6-7.2 ms (e) after the start of the PSI ($t_{exposure}$=1.2 ms)

Fig. 2. Images of PSI after a plasma impact on an inclined CPS target (with an incoming plasma energy density of 3 MJ m^{-2}). The images correspond to 1.2-2.4 ms (a); 2.4-3.6 ms (b); 3.6-4.8 ms (c); 4.8-6 ms (d); 6-7.2 ms (e) after the start of the PSI ($t_{exposure}$=1.2 ms)

Summary

The irradiated CPS remained filled with Li during subsequent exposures. Surface analysis of normally irradiated CPS target did not reveal any visible changes in the W substrate. In contrast, for the CPS target exposed to inclined transient plasma, damage to the leading edge was observed. Similar behavior was also observed in the experiments with oblique irradiation of castellated W and Sn-CPS targets due to the formation of a non-uniform shielding layer on the target surface. The experiment showed that the plasma impacts with energy densities below 1.2 MJ/m^2 caused only a small number of particles to eject from the target surface. With higher plasma loads, the number of ejected particles increased significantly. The velocities of the ejected particles ranged from 1 to 33 m/s.

Acknowledgements

This work has been carried out within the framework of the EUROfusion Consortium, funded by the European Union via the Euratom Research and Training Programme (Grant Agreement № 101052200 – EUROfusion). This work has been supported in part by the Ministry of Education and Science of Ukraine within the project PH/ 56 - 2024. Four members of the team of authors are grateful to the Simons Foundation Program: Presidential Discretionary-Ukraine Support Grants, Award SFI-PD-Ukraine-00014575.

References

[1] J.H. You, et al. Fusion Eng. Des. vol. 175, 113010, (2022).
[2] J. Horacek et al. Nuclear Fusion vol. 65, 016014, (2025).
[3] J.G.Scholte et al., .Journal of Fusion Energy vol. 44, 22, (2025).
[4] T.W. Morgan et al Plasma Phys. Control. Fusion vol. 60, 014025, (2018).
[5] I.E. Garkusha, et al.. Nuclear Fusion. vol. 61, 116040, (2021).
[6] S.S. Herashchenko, S.S. et al. Fusion Engineering and Design. vol. 190, 113527, (2023).
[7] M. Morbey et. al. Nucl. Fusion vol. 65, 106017, (2025).

PLASMA SOURCE FOR ION-PLASMA MODIFICATION OF STRUCTURAL MATERIALS

V.O. Khomych*, S.M. Gubarev**

** Institute of Physics of NAS of Ukraine, 46, Nauky Av., Kyiv 03028, Ukraine, e-mail: khomich@iop.kiev.ua*

*** Institute of Physics of NAS of Ukraine, 46, Nauky Av., Kyiv 03028, Ukraine, e-mail: gubarev@iop.kiev.ua*

This paper presents the results of experimental studies of a plasma source based on a glow discharge with a hollow cathode for ion-plasma modification of the surface of structural materials. The volt-ampere characteristics of the discharge with a hollow cathode and the distribution of the saturation ion current density from the plasma to the Langmuir probe along the radius of the working chamber for different working gas pressures were obtained. The presented plasma source can be used in ion-plasma technological processes.

Experimental setup

Currently, methods based on the use of gas discharge plasma at low pressure have found wide application for modification of the surface layer of structural materials (heating, ion cleaning, nitriding, oxidation). The use of low-temperature gas discharge plasma for this purpose is promising both from the point of view of the environmental cleanliness of the process and in terms of energy efficiency. The development of reliable plasma equipment with a long service life is an urgent task.

Below we consider the design of a plasma source based on a glow discharge with a hollow cathode effect. The source using vacuum chamber as a cathode allows working with discharge currents of several amperes and a plasma environment of inert and reactive gases (N_2, O_2, H_2, etc.) with a fairly long operating life (hundreds of hours).

Fig. 1 shows the general scheme of the experimental setup.

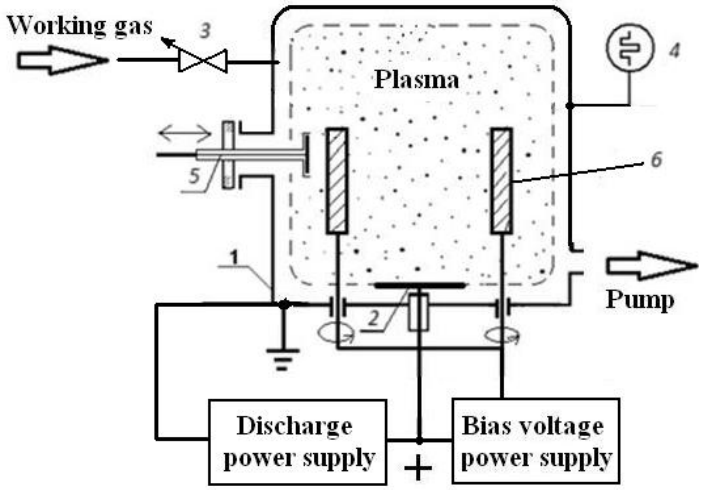

Fig. 1. Scheme of the experimental setup for ion-plasma surface modification: 1 – vacuum chamber (hollow cathode), 2 – anode, 3 – gas supply system, 4 – gauge, 5 – one-sided flat Langmuir probe, 6 – sample holder

The cathode is the inner surface of the vacuum chamber with a volume of 15 liters (0.25 m chamber diameter). The anode is installed in the lower part of the vacuum chamber. The working chamber is evacuated to a residual pressure of 10^{-1} Pa. The plasma-forming gas is supplied directly to the chamber and its pressure is varied in the range 0.1 ÷ 50 Pa. Argon is used as the working gas in the experiments. The plasma parameters are controlled by a movable one-sided flat Langmuir probe with a collecting-surface area of 1 cm^2, which measures the saturation

ion current. The discharge is powered by a high-voltage power supply with an open-circuit voltage of 1500 V with a steeply falling external characteristic.

By varying the discharge current, the power input into the plasma can be controlled, achieving an electron concentration in the plasma of 10^9 to $5*10^{10}$ cm^{-3} at an electron temperature of 2 to 4 eV [1].

Experimental data and discussion

The volt-ampere characteristics of the glow discharge with the hollow cathode effect for different argon pressures are shown in Fig. 2a. The distribution of the ion current density from the plasma to a flat one-sided Langmuir probe along the radius of the vacuum chamber (working gas argon, at fixed discharge power of 600 W) for different gas pressures in the chamber is shown in Fig. 2b. The probe potential is -100 V relative to anode potential.

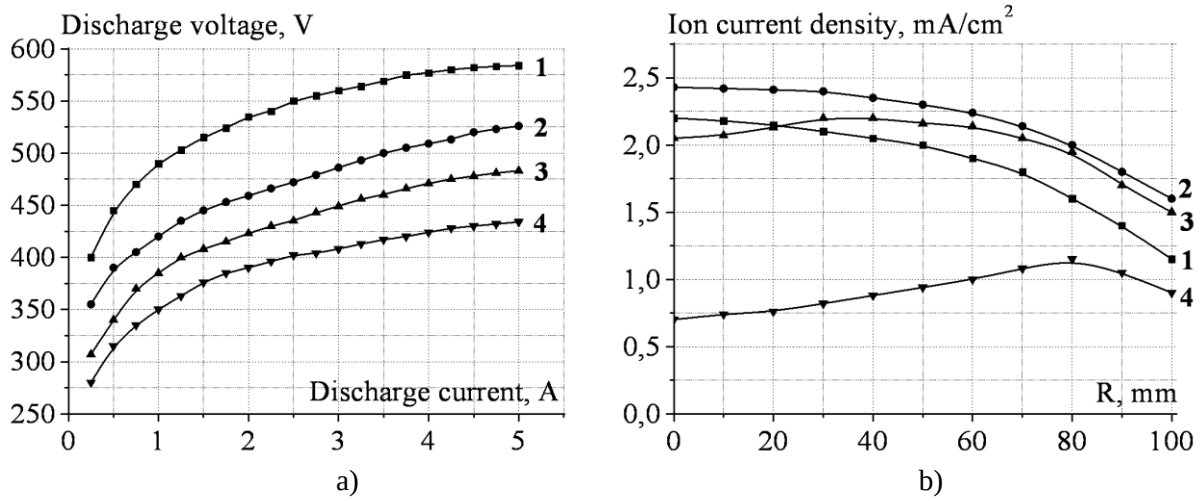

Fig. 2. a) Volt-ampere characteristics of a glow discharge with a hollow cathode for different gas (Ar) pressures. 1 – 1.8 Pa; 2 – 3 Pa; 3 – 7 Pa; 4 – 16 Pa; b) Distribution of ion saturation current density along the radius of the working chamber for different gas pressures. 1 – 1.8 Pa; 2 – 3 Pa; 3 - 7 Pa; 4 – 16 Pa

The saturation ion current reaches maximum values at an argon pressure in the working chamber of about 3 Pa. The non-uniformity of the plasma electron concentration in the working area (within a radius of 60 mm from the center of the working chamber) does not exceed 10% of its average value. To form a homogeneous modified layer, the sample holders are installed along the perimeter of the working chamber and can rotate around their axis. By applying a negative potential to the sample holders relative to the anode, optimal conditions are achieved for ion cleaning, heating and maintaining the temperature of the samples during the modification of the surface layer.

Conclusions

The design and main characteristics of a plasma source based on a glow discharge with a hollow cathode are presented. A bulk plasma with an electron concentration of 10^9 to $5*10^{10}$ cm^{-3} at an electron temperature of 2 to 4 eV was obtained. The ion saturation current density in the working area was achieved up to 2.3 mA/cm². Proposed plasma source can be used in the processes of ion-plasma technologies.

References

[1] V.Yu. Bazhenov, A.V. Ryabtsev, I.A., Soloshenko, A.G. Terent'eva, V.A. Khomich, V.V. Tsiolko, A.I. Shchedrin, "Investigation of the electron energy distribution function in hollow-cathode glow discharges in nitrogen and oxygen", Plasma physics reports, vol. 27, No. 9, p. 813, 2001.

ACCELERATED FORMATION OF A PLASMA DENSITY CAVITY DRIVEN BY SELF-FOCUSING OF AN INCIDENT ELECTROMAGNETIC BEAM

B.R. Mykhailenko, I.O. Anisimov
Taras Shevchenko National University of Kyiv, Faculty of RadioPhysics, Electronics and Computer Systems
e-mail: mihaylenko.bogdan12@gmail.com

Using computer simulation, the intermediate stage of channel formation in an overdense plasma barrier under the action of a low-power electromagnetic wave beam was investigated. At this stage, the density cavity formed at the point of beam incidence on the barrier surface deepens and narrows, gradually taking on a conical shape. This deepening is shown to accelerate over time due to a self-focusing effect of the incident wave beam, although the process exhibits non-monotonic behavior at certain intervals.

The propagation of waves through overdense plasma has been a subject of extensive research for decades [1], driven by its relevance to applications such as space communications, plasma diagnostics, laser thermonuclear fusion, and electron bunch acceleration. Our previous works [3-5] focused on the transillumination of plasma barriers, where a high-power electromagnetic beam creates a channel of reduced density. This paper investigates the dynamics of the initial density cavity formation, analyzing how its deepening accelerates due to self-focusing of the incident beam and how its shape evolves from a paraboloid to a cone. A similar effect, though in the context of ultra-high-power laser pulses and extremely dense plasma, was previously studied in relation to laser nuclear fusion [2].

The 3D simulations were conducted using PIConGPU package [6], a Particle-in-Cell code, which does not account for collisions between particles. Instantaneous values were visualized in three dimensions using ParaView [7], while a custom program was employed to process averaged values in OpenPMD format.

The following simulation parameters were used: fully ionized hydrogen plasma of a density $9 \cdot 10^{12} cm^{-3}$ (electron plasma frequency – 27 GHz); plasma temperature – 0.5 eV (isothermal plasma); the plasma layer thickness – 12.5 cm, radius – 21.5 cm; incident wave length – 3.33 cm (frequency – 9.9 GHz, i.e. plasma is opaque for this wave); pulse duration – 101 ns; pulse radius (at half maximum) – 4.9 cm; the maximum electric field amplitude is 0.964·MV/cm (4 times smaller than the amplitude of a moderate wave in [3-4]).

In the initial time points, the shape of the cavity on the plasma surface can be considered approximately a paraboloid. This surface reflects the incident wave beam similar to a parabolic mirror. At some distance from the plasma, the reflected wave is focused, and the amplitude of the standing wave reaches its maximum. As the cavity deepens, this maximum approaches the plasma surface, forming a maximal gradient of the electromagnetic field intensity and, consequently, a maximal ponderomotive force. As a result, the central part of the cavity deepens faster than its periphery, and the cavity gradually acquires a shape close to conical (Fig. 1a).

Fig. 1a-b shows the coordinate of the density cavity surface (Fig. 1a) and the corresponding velocity of its deepening (Fig. 1b). It is evident that with increasing depth, the rate of deepening grows, which is consistent with the hypothesis of enhanced focusing of the incident wave beam's field as the cavity deepens. At the same time, a non-monotonic behavior of the deepening velocity is observed in some time intervals. This is likely associated with the appearance of additional local deepenings on the surface, the formation velocity of which is added to the overall motion of the barrier surface. Fig. 2. shows electron density distributions.

Acknowledgment

This work has been carried out within the framework of the EUROfusion Consortium, funded by the European Union via the Euratom Research and Training Programme (Grant Agreement № 101052200 -EUROfusion). Views and opinions expressed are however those of the author(s) only and do not necessarily reflect those of the European

Union or the European Commission. Neither the European Union nor the European Commission can be held responsible for them.

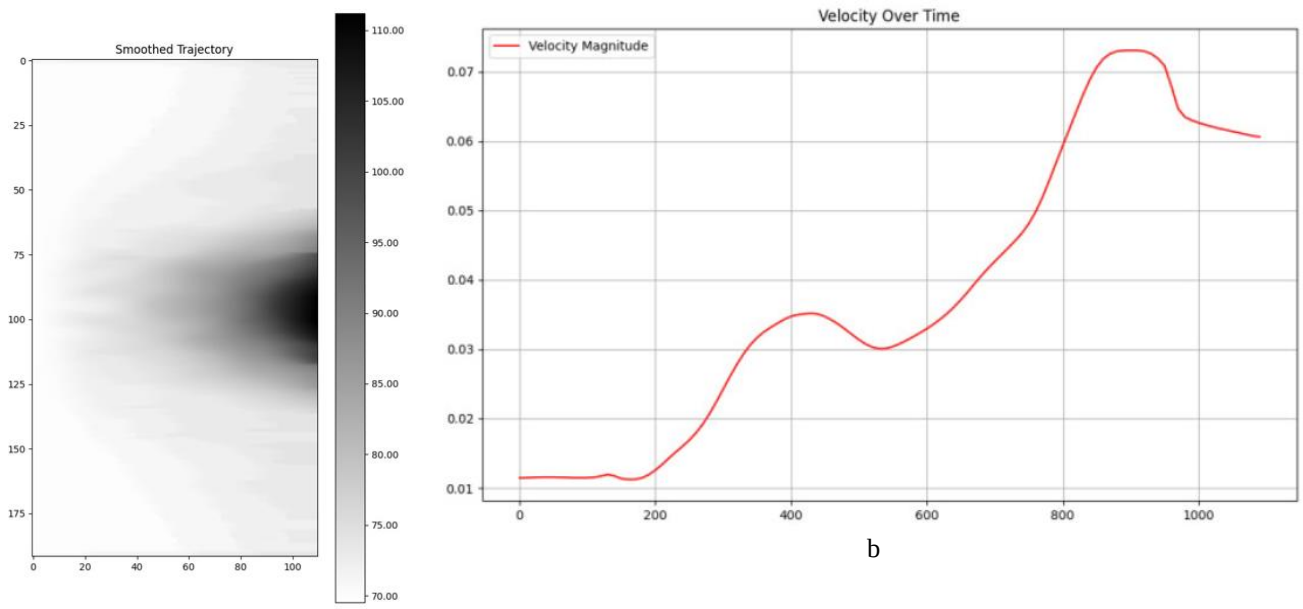

a b

Fig. 1. The coordinate (a) and instantaneous velocity (b) of the barrier boundary in the region of contact with the beam

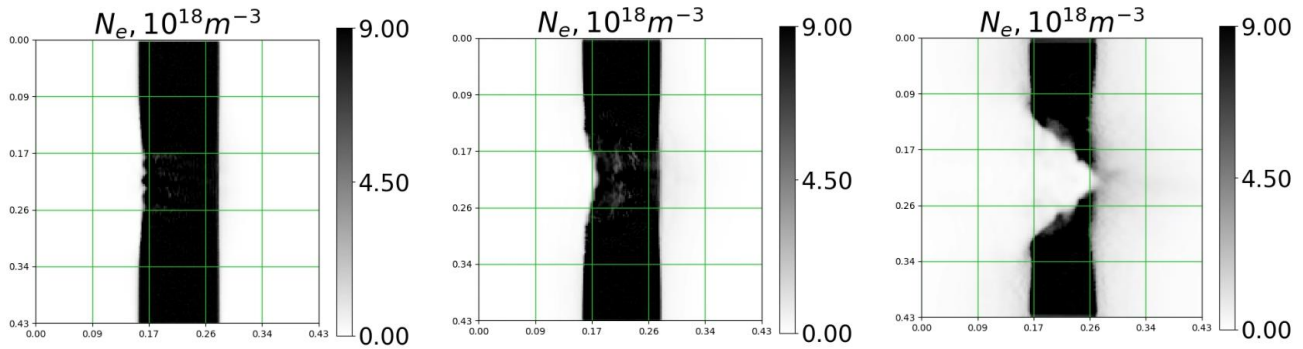

a b c

Fig. 2. Electron density distributions, when an electromagnetic beam is falling on plasma, at the time points 12 ns (a), 26 ns (b), and 62 ns (c)

References

[1] I.O. Anisimov, L.I. Romaniuk. // Ukr. Phys. Journ. Reviews. 6, 101 (2010). In Ukrainian.
[2] A.J. Kemp, Y. Sentoku, V. Sotnikov, S.C. Wilks. // Phys. Rev. Lett. 97 (23), 235001 (2006).
[3] B.R. Mykhailenko, I.O. Anisimov. // Probl. of Atomic Sci. and Techn. №6 (130), 64 (2020).
[4] B.R. Mykhailenko, I.O. Anisimov. // Probl. of Atomic Sci. and Techn. №4 (134), 3 (2021).
[5] B.R. Mykhailenko, I.O. Anisimov. // Probl. of Atomic Sci. and Techn. №6 (154), 31 (2024).
[6] M. Bussmann, H. Burau, T.E. Cowan, A. Debus, A. Huebl et al. // SC '13, 5:1–5:12 (2013).
[7] Ahrens, J., Geveci, B. & Law, C. (2005). ParaView: Data Visualization Tool. Visualization Handbook.

INVESTIGATION OF THE DEPENDENCE OF THE PLASMA DENSITY IN A LOW-PRESSURE HOLLOW-CATHODE ARC DISCHARGE ON GAS PRESSURE

A.V. Ryabtsev*, V.O. Khomych**
** Institute of Physics of NAS of Ukraine, Kyiv, Ukraine, e-mail: ryabtsev@iop.kiev.ua*
*** Institute of Physics of NAS of Ukraine, Kyiv, Ukraine, e-mail: khomich@iop.kiev.ua*

This work investigates the dependence of plasma density on gas pressure in a low-pressure hollow-cathode arc discharge. Experiments using a thermionic hollow cathode in argon showed a pronounced maximum in plasma density at ~0.6 Pa. A diffusion–transport model with Monte Carlo simulations of electron motion reproduced this behavior, indicating an optimal balance between ionization and collisional losses. The agreement between theory and experiment confirms the model's validity and offers guidance for optimizing plasma-based surface treatment processes.

Experimental Setup

Advanced plasma surface modification techniques, such as nitriding and oxidation, often employ autonomous plasma arc sources [1]. Compared with glow discharges, arc-based systems offer flexible control over technological parameters, reduced ion sputtering, and the ability to treat complex-shaped components, including those with internal cavities. An additional advantage is their high energy efficiency: they can generate a bulk plasma with an electron density of $n_e = 10^{10} – 5\times10^{11}$ cm^{-3}, sufficient for effective heating and cleaning during ion-plasma processing.

The experimental system consists of a vacuum chamber with a volume of about 0.1 m³. A thermionic hollow cathode is mounted at the top, and an anode is placed opposite to it. Argon, used as the plasma-forming gas, is fed through the hollow cathode, which also protects it from reactive gases. Gas pressures in the range of 10 – 0.1 Pa were maintained and adjusted using precision needle injectors. The discharge was powered by a low-voltage DC source (U = 35 – 80 V, I = 5 – 30 A). Varying the current allowed control of the discharge power and plasma parameters, yielding electron densities up to 10^{11} cm^{-3} at electron temperatures of 1.4–3 eV.

The plasma parameters were measured using a single Langmuir probe traversing the axis between the anode and cathode. To optimize energy efficiency in plasma-assisted processes, it is necessary to maximize plasma density at constant discharge power. Therefore, this study focuses on examining the dependence of plasma density on gas pressure while keeping voltage and current fixed at U = 40 V and I = 25 A. In more detail the installation is described in [2].

Theoretical Model

To analyze the effect of gas pressure on plasma density, a numerical model was developed for an axially symmetric discharge system. The model assumes that monoenergetic electrons emitted from the hollow cathode ionize the gas primarily near the discharge axis, and the generated plasma diffuses toward the chamber walls through ambipolar diffusion. The steady-state plasma density $n(r,z)$ is governed by the diffusion–transport equation:

$$D_a \nabla^2 n(r,z) + \mu\, e\, \mathrm{E}\, \nabla n(r,z) + S(r,z) = 0,$$

where D_a is the ambipolar diffusion coefficient, μ is the plasma mobility ($\mu = D_a/k_B T_e$), E is the electric field strength, and S(r,z) is the ionization rate density. Since only relative plasma densities are of interest, absolute values of D_a and S were scaled consistently. The diffusion coefficient was assumed inversely proportional to gas pressure: $D_a = 1/p$, where p is in pascals.

Previous studies show that ionization is localized near the discharge axis. Accordingly, the ionization function was defined as $S(r,z) = S_0(z)$ for $r < r_0$, and 0 for $r > r_0$, where $r_0 = 2$ cm. The function $S_0(z)$ was obtained from

Monte Carlo simulations of electron trajectories. Electrons were assumed to be emitted from the cathode with initial energy equal to the cathode potential ε_0 and to move in a uniform field $E = (U - \varepsilon_0)/L$, where L is the cathode–anode gap.

During motion, electrons undergo three types of collisions: (1) Ionization, with energy loss ε_i = 15.6 eV; (2) Excitation to the Ar(4s) level, ε_{ex} = 11.5 eV; (3) Elastic scattering, with up to 10% energy loss and 0.5 probability of direction reversal. Monte Carlo simulations yielded the axial distribution of ionization rates, which served as input for solving the diffusion–transport equation.

Results and Discussion

At low pressures, increasing p enhances the probability of ionizing collisions, thereby raising plasma density. However, as p increases further, elastic and excitation collisions dominate, causing more energy loss per electron and reducing ionization efficiency. Beyond $p \approx 0.6$ Pa, plasma density begins to decrease.

Both the experimentally measured ion current density (proportional to plasma density) and numerically calculated plasma density exhibit a pronounced maximum at $p \approx 0.6$–1.0 Pa. This maximum corresponds to the optimal balance between energy gained from the electric field and energy lost through collisions. The good agreement between experiment and simulation confirms the validity of the model.

Conclusions

A combined experimental and theoretical study was conducted to investigate the effect of gas pressure on plasma density in a low-pressure hollow-cathode arc discharge. Plasma density shows a distinct maximum at $p \approx 0.8$ Pa, in good agreement with the model predictions. The developed model provides a reliable description of plasma behavior and serves as a useful tool for optimizing plasma-assisted surface modification technologies.

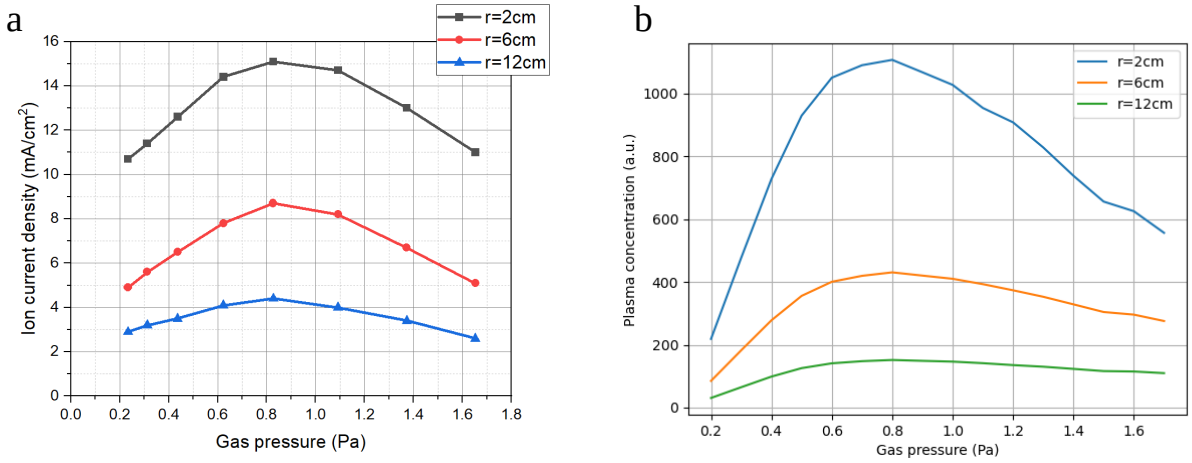

Fig. 1. (a) Experimentally obtained dependence of the ion current density (proportional to the plasma density); (b) calculated plasma density (in arbitrary units) as a function of gas pressure. The data are shown for three different radial positions at a distance of 9 cm from the cathode

References

[1] 1. A.A. Andreev, V.M. Shuvalov, L.P. Sablev. “Steel nitriding in a low-pressure gas arc discharge”, PSE, v. 4, N. 3 4, pp. 191-197, 2006.

[2] A.V. Khomich, A.V. Ryabtsev, V.G. Nazarenko “Low-Pressure Uniform Plasma Generator Based on Hollow Cathode for Ion Plasma Technologies” VANT, N 6, pp.89-94, 2022.

INFLUENCE OF GAS SUPPLY METHOD ON THE DISCHARGE GLOW IN A HALL TYPE DEVICE WITH AN ANODE LAYER

V.Yu. Bazhenov*, A.M. Dobrovolskii*, V.V. Tsiolko*, V.M. Piun*
**Gas Electronics Department, Institute of Physics NASU, Kyiv 28, pr. Nauku 46, Kyiv, Ukraine,*
e-mail: bazhenov@iop.kiev.ua, dobr@iop.kiev.ua, tsiolko@iop.kiev.ua, piun@iop.kiev.ua

The paper presents the results of studies of the influence of the method of argon supply (radial and along the axis) on the glow and ignition modes of the discharge in a Hall-type device with an anode layer. In particular, it was established that in the case of radial gas supply, the ignition process occurs with a time delay relative to the moment of voltage supply. It was also found that the magnitude of this delay depends on the argon pressure and decreases as it increases.

Introduction

Previously, we created the anode layer based source of a cylindrical plasma flow with enhanced efficiency of the discharge volume usage [1]. The source had the symmetric geometry of both stages. In this case, it is need to make the additional stage for resulted beam choice to make the thrust. In [2] we studied the modified version of the previous device in which one half of the cathode system was replaced by a ring-shaped cathode located in a region with weak magnetic field, so that instead of being symmetrical the system becomes an asymmetric one. The working gas Ar was injected along the axis of the system. Results of experimental studies of spatial-temporal dependencies of the discharge power and the electron energy distribution function inside the device were presented in [3, 4].

This paper presents the results of studies of the device operation with radial supply of argon through the anode cavity and a comparison with the case of gas supply along the system axis is done.

Experimental results and discussion

The block diagram of the experimental device is presented in Fig. 1. Anode 2 of the device with an internal diameter of 59 mm and a length of 63 mm was located inside a quartz cylinder with an internal diameter of 95 mm and a length of 150 mm. Argon was supplied into the anode cavity through tube 3. Then the gas entered the device through a 20 mm wide slit in the anode covered with a grid. The "internal" cathode 4 consisted of 6 rods with a diameter of 3 mm and a length of 20 mm located in a circle at a certain distance from the inner surface of the anode. The role of the "external" cathode 1 was performed by a metal ring with an inner diameter of 65 mm and a height of 20 mm. A magnetic field with a minimum on the axis and two cusps was created using a system of permanent magnets. A magnetic field with a minimum on the axis and two cusps was created using a system of permanent magnets.

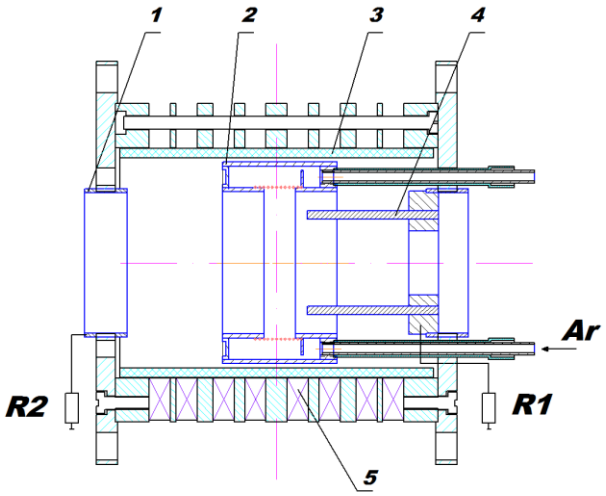

Fig. 1. Block diagram of the experimental device

When studying the electro-physical characteristics of the discharge, measurements were made of voltages and currents of inner and outer cathodes 4, 1 (UI, UO, JI, JO, respectively), anode voltage Ua, chamber current I at different values of argon pressure and values of resistances R1, R2. Pulsed voltage from the power source was applied to the discharge anode relative to the grounded chamber. Cathodes 1, 4 were connected to the grounded chamber through resistors R1, R2 of different

values. This made it possible to raise the potentials of the cathodes during the discharge glow to simulate the operation of the device in free space. In this particular case the experiments were performed with values of the resistors R1 = 10 k□ and R2 = 820 □.

Experiments have shown that when argon is supplied into the discharge gap through a circular slit in the anode, the discharge ignition occurs with a certain delay relative to the supply of the anode voltage pulse Ua. At the minimum possible operating pressure of argon $0.9*10^{-4}$ Torr, the delay reaches □ 2 ms. With increasing pressure, the delay decreases and is practically absent at a pressure of $2.9*10^{-4}$ Torr.

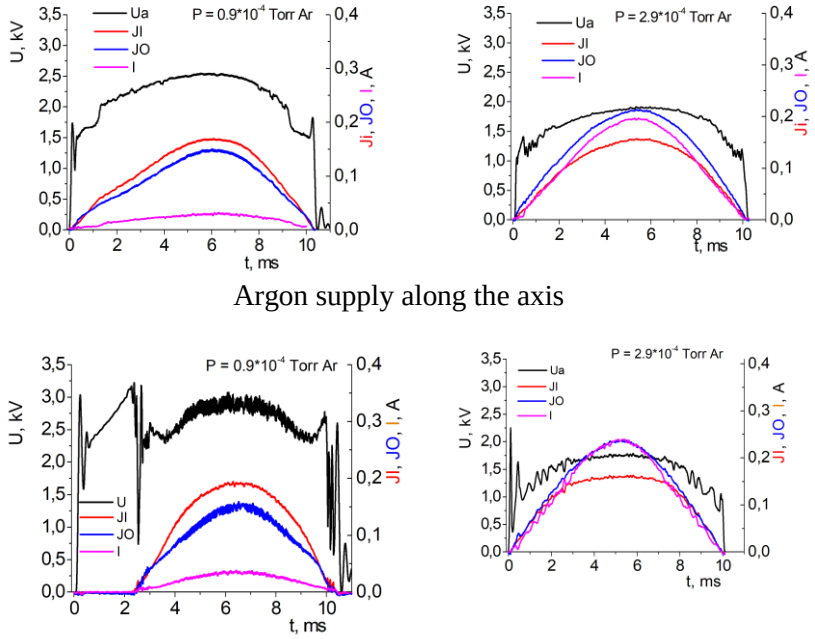

Fig. 2. Plots of discharge voltages Ua, and currents JI, JO, I at different argon pressures.

Fig. 2 presents examples of the behavior of the anode voltage Ua and currents JI, JO, I diagrams at the minimum and maximum values of the argon pressure in the chamber for both methods of argon supply to the discharge gap. As can be seen from the figure, such a delay in the ignition of the discharge is practically absent with the argon supply along the axis. At the moment, the reason for such a large delay in ignition with radial supply is not entirely clear. It is possible that the nature of the ignition in this case was influenced by the replacement of the laminar flow of argon at axial supply with a turbulent flow due to the collision of argon flows at radial supply.

References

[1] I. Litovko, A. Goncharov, A. Dobrovolskyi, and I. Naiko. Plasma Science and Technology The Emerging Field Trends Erosion-Free Electric Hall Thrusters Systems/ Edited by Aamir Shahzad, InTechOpen, London, Chapter 11, p. 195-214. 2022.

[2] V.Yu. Bazhenov, A.M. Dobrovolskiy, V.V. Tsiolko, V.M. Piun. Two stage plasma source for large scale beam generation//PAST. Series “Plasma electronics and new methods of acceleration”. № 4. p. 121-124. 2023.

[3] V.Yu. Bazhenov, A.M. Dobrovolskii, V.V. Tsiolko, V.M. Piun. Power distribution in the two stages Hall type plasma source. *Proceedings of the XX International Scientific Conference Electronics and Applied Physics* APHYS-2024, October 22-25, 2024, Kyiv, Ukraine, pp.153-154.

[4] V.Yu. Bazhenov, A.M. Dobrovolskii, V.V. Tsiolko, V.M. Piun. Evaluation of the electron energy distribution function in the two stages Hall type plasma source., *Proceedings of the XX International Scientific Conference Electronics and Applied Physics* APHYS-2024, October 22-25, 2024, Kyiv, Ukraine, pp. 176-177.

CHARGE NEUTRALIZATION AND CURRENT NEUTRALIZATION OF AN ELECTRON BUNCH IN A HOMOGENEOUS WARM PLASMA

A.V. Hortopan, I.O. Anisimov
Taras Shevchenko National University of Kyiv, Faculty of RadioPhysics, Electronics and Computer Systems,
e-mail: andrii.hotropan@univ.net.ua, anisimov1958igor@gmail.com

In this work, the processes of charge and current neutralization of an electron beam propagating in a homogeneous warm plasma are considered separately. The former process is driven by the electrostatic field, while the latter is driven by the vortical field. This separation simplifies the corresponding wave equations. It is shown that charge neutralization is associated with the excitation of Langmuir waves, whereas current neutralization is associated with the excitation of electromagnetic fields.

The problem of neutralizing charged particle beams has long attracted attention as an effective method for suppressing beam expansion—primarily that of electron beams, which have various applications in plasma electronics [1]. In recent years, considerable attention has also been devoted to the neutralization of ion beams, particularly in connection with issues related to ion surface processing [2] and beam-driven thermonuclear fusion [3].

In our previous report [4], we considered the simultaneous processes of charge and current neutralization of an electron beam propagating in a warm, homogeneous, isotropic plasma. As a result, a fourth-order wave equation was obtained.

However, the charge and current neutralization processes of the beam can be separated, since the former is driven by the electrostatic electric field, while the latter is driven by the vortical field [5–6]. One may expect that this approach will simplify the final equations.

An electron beam with density n_b propagates along the Z direction with velocity $\vec{v}_b$. The beam temperature is neglected. The beam motion is treated as prescribed. The beam moves in an unbounded homogeneous plasma with unperturbed electron and ion density n_0, and electron temperature – T_e, the ions are assumed immobile. To solve the problem, we use Maxwell's equations together with the electron equation of motion for a warm isotropic plasma.

We assume $n_e = n_0 + \tilde{n}(r,t), |\tilde{n}| \ll n_0$. To have the beam and background-plasma currents of the same small order, given $n_b \sim n_0$ we require $v_b \gg v_e$.

We now pass from the electromagnetic-field components $\vec{E}$ and $\vec{B}$ to the vector potential $\vec{A}$ and the scalar potential φ. Then the equations for the vector and scalar potentials take the form

$$\nabla\times\nabla\times\vec{A} = -\frac{4\pi}{c}en_0\vec{v}_e + \frac{4\pi}{c}\vec{j}_b - \frac{1}{c}\frac{\partial}{\partial t}\nabla\varphi - \frac{1}{c^2}\frac{\partial^2\vec{A}}{\partial t^2}; \tag{1}$$

$$m\frac{\partial\vec{v}_e}{\partial t} = e\left(\nabla\varphi + \frac{1}{c}\frac{\partial\vec{A}}{\partial t}\right) - \frac{k_BT}{n_0}\nabla\tilde{n}_e - m\vec{v}_e\nu. \tag{2}$$

$$\Delta\varphi = 4\pi e\left(\tilde{n}_e + n_b\right). \tag{3}$$

We represent the electron velocity as a sum $\vec{v}_e = \vec{v}_{ec} + \vec{v}_{en}$, where the terms are induced by the vortical ($\vec{v}_{ec}$) and potential ($\vec{v}_{en}$) components of the field, respectively. These components determine, respectively, the compensating and neutralizing currents excited by the electron bunch in the background plasma. As a result, Eqs. (1)–(2) can be split into two independent parts: for the vortical field

$$\nabla\times\nabla\times\vec{A} = -\frac{4\pi}{c}en_0\vec{v}_{ec} + \frac{4\pi}{c}\vec{j}_b - \frac{1}{c^2}\frac{\partial^2\vec{A}}{\partial t^2}; \tag{4}$$

$$\frac{\partial\vec{v}_{ec}}{\partial t} = \frac{e}{mc}\frac{\partial\vec{A}}{\partial t} - \nu\vec{v}_{ec} \tag{5}$$

and for the potential (electrostatic) field

$$\frac{4\pi}{c} e n_0 \vec{v}_{en} + \frac{1}{c}\frac{\partial}{\partial t}\nabla\varphi = 0 \quad ; \qquad (6)$$

$$\frac{\partial \vec{v}_{en}}{\partial t} = \frac{e}{m}\nabla\varphi - \frac{k_B T}{m n_0}\nabla\tilde{n}_e - \nu\vec{v}_{en} \quad . \qquad (7)$$

Impose the gauge condition $\nabla\cdot\vec{A} = 0$. Then Eqs. (4)–(5) take the form

$$\Delta\vec{A} - \frac{1}{c^2}\frac{\partial^2\vec{A}}{\partial t^2} = \frac{4\pi}{c} e n_0 \vec{v}_{ec} - \frac{4\pi}{c}\vec{j}_b \quad , \qquad (8)$$

$$\left(\frac{\partial}{\partial t} + \nu\right)\vec{v}_{ec} = \frac{e}{mc}\frac{\partial\vec{A}}{\partial t} \quad . \qquad (9)$$

Now act on Eq. (8) with the operator $\left(\partial/\partial t + \nu\right)$ and use (9) to eliminate the velocity $\vec{v}_{ec}$. As a result, we obtain the wave equation for the vector potential that determines the compensating current, in the form

$$\left[\left(\frac{\partial}{\partial t} + \nu\right)\left(\Delta - \frac{1}{c^2}\frac{\partial^2}{\partial t^2}\right) - \frac{\omega_p^2}{c^2}\frac{\partial}{\partial t}\right]\vec{A} = -\frac{4\pi}{c}\left(\frac{\partial}{\partial t} + \nu\right)\vec{j}_b \quad , \qquad (10)$$

where $\omega_p^2 = 4\pi e n_0 / m$ – the Langmuir frequency of the background plasma. This equation describes the excitation of a vortical (solenoidal) electromagnetic field in a collisional cold plasma by a prescribed spatial distribution of current density that varies in time. The left-hand side of (10) is the wave equation for electromagnetic waves.

Eliminate from Eq. (7) the quantities $\tilde{n}_e$ та $\vec{v}_{en}$, using Eqs. (3) and (6). We obtain:

$$\nabla\left(-\frac{\partial^2}{\partial t^2} + v_{Te}^2\Delta - \nu\frac{\partial}{\partial t} - \omega_p^2\right)\varphi = 4\pi e v_{Te}^2 \nabla n_b \qquad (11)$$

($k_B T/m = v_{Te}^2$ – is the electron thermal velocity in the plasma), in the final form,

$$\left[v_{Te}^2\Delta - \frac{\partial}{\partial t}\left(\frac{\partial}{\partial t} + \nu\right) - \omega_p^2\right]\varphi = 4\pi e v_{Te}^2 n_b \quad . \qquad (12)$$

This wave equation describes, in a warm plasma, the excitation of a potential (electrostatic) field—which determines the neutralization currents—by a prescribed spatial distribution of the beam charge density (which, in the present analysis, is time-dependent). The left-hand side of (12) is the wave equation for Langmuir waves.

Thus, charge neutralization of the beam is associated with the excitation of Langmuir waves in the plasma, whereas current neutralization is associated with the excitation of electromagnetic fields.

References

[1] O.F. Tseluyko and Ya.O. Hrechko, Physics of Intense Charged Particle Beams. Kharkiv: V.N. Karazin Kharkiv National University, 2022.

[2] J.P. Chang, J.C. Arnold, G.C.H. Zau, H.-S. Shin, and H.H. Sawin, J. Vac. Sci. Technol., A 15, 1853–1863 (1997).

[3] B.G. Logan, F.M. Bieniosek, C.M. Celata, J. Coleman, W. Greenway, E. Henestroza, J.W. Kwan, E.P. Lee, M. Leitner, P.K. Roy et al, Nucl. Instrum. Methods Phys. Res., Sect. A 577, 1–7 (2007).

[4] A.V. Hortopan, I.O. Anisimov. Charge and Current Neutralization of a Charged Particle Beam in an Unbounded Collisional Plasma, ICAP 2025

[5] R.B. Miller. An Introduction to the Physics of Intense Charged Particle Beams. Springer, 1982.

[6] I.O. Anisimov. Plasma electronics, 2024

NUMERICAL MODELING OF METAL PARTICLE AND ATMOSPHERIC PRESSURE CURRENT-CARRYING ARGON PLASMA INTERACTION

A.I. Momot[1,2], D.V. Antoniv[1,2] and I.V. Krivtsun[1]

[1]*Faculty of Physics, Taras Shevchenko National University of Kyiv, Academician Glushkov Avenue, 4, Kyiv, 03680, phys.univ.kiev.ua, momot.andriy@gmail.com*

[2]*E.O. Paton Electric Welding Institute NAS of Ukraine, 11, Kazymyr Malevich Street, Kyiv, 03650, paton.kiev.ua, adantoniv@gmail.com*

We consider a system of one spherical metallic particle of radii a and a jet of argon current-carrying plasma at atmospheric pressure surrounding it. spatial distributions of current density, potential, components of plasma, temperatures of electrons T_e and heavy particles T_h and heat fluxes are investigated. The range of particle radius $a = 10^{-5} \div 10^{-3}$ m and the range $(0.5 \div 2)\ 10^7\ A \cdot m^{-2}$ of current density j_0 in the unperturbed plasma were considered. Examining the interaction between fine metal particles and atmospheric pressure plasmas is crucial, as these interactions are prevalent in various technical plasma processes, including plasma spraying, plasma transferred arc (PTA) surfacing, metal powder spheroidization, and gas metal arc welding (GMAW). Understanding the thermal impact of plasma on particles and the effect of particles on plasma properties is essential for advancing research and development in these processes.

Model

The model of physical processes in the system under consideration was built using the approach proposed in [1], with the following assumptions: The particle is assumed to be stationary relative to the plasma with current density j_0. Thus, the system has cylindrical symmetry; particle surface temperature is assumed to be constant and the steady state is considered; the presence of doubly charged ions, as well as the particle material, is neglected. The plasma outside the space charge layer considered to be unperturbed. The mathematical model describing such a plasma includes the continuity equations, the equations of motion, and the energy equations for individual plasma components with the corresponding boundary conditions, which are set on the boundary between the space charge sheath and the quasineutral plasma ($l_{sh} \ll a$) of the particle and in the unperturbed plasma (far from the particle). Numerical calculations were performed using the finite element method in the FlexPDE program. The dependence of transport coefficients on T_e, T_h, and n_i was taken into account in the calculations, meaning that a fully nonlinear problem was solved.

Results

The heat flux from plasma to the particle surface depends nonlinearly on j_0. The main contribution to the heat flux comes from the kinetic energy of heavy particles. The energy released by ions during recombination on the particle surface becomes significant when $T_0 > 10$ kK.. Comparing present results with currentless case [5] we have one more heat source of convective nature q_{p6} and two other sources (the heat flux due to heavy particle thermal conductivity q_{p3} and the part that corresponds to inelastic collisions of ions with surface of the particle q_{p5}) are now exhibiting dependence on θ.

The modeling showed that flow of electrons of the plasma through conductive particle is almost non-existent. Current density on the particle surface j_s is not uniform. The maximum values of j_s are reached in the points on the axis along the $\boldsymbol{j_0}$. For the particle radii $a = 10^{-5} \div 10^{-4}$ m and $j_0 = (0.5 \div 2) \cdot 10^7$ A/m^2 the ratio $j_s/j_0 \in (0.03 \div 0.07)$. These results show that the simple model of highly conductive spherical particle in a uniform conducting medium, which predicts $j_s > j_0$ (up to $j_s/j_0 = 3$), can not describe the plasma conductivity with metal particles even qualitatively.

The sheath potential also depends on the angle θ, since the potential of the particle surface is set equal to zero in our modeling, the potential on the sheath outer boundary is positive and its average value is a few volts. The difference of φ_{sh} in points $\theta = 0°$ and $\theta = 180°$ grows with particle radius and current density in plasma.

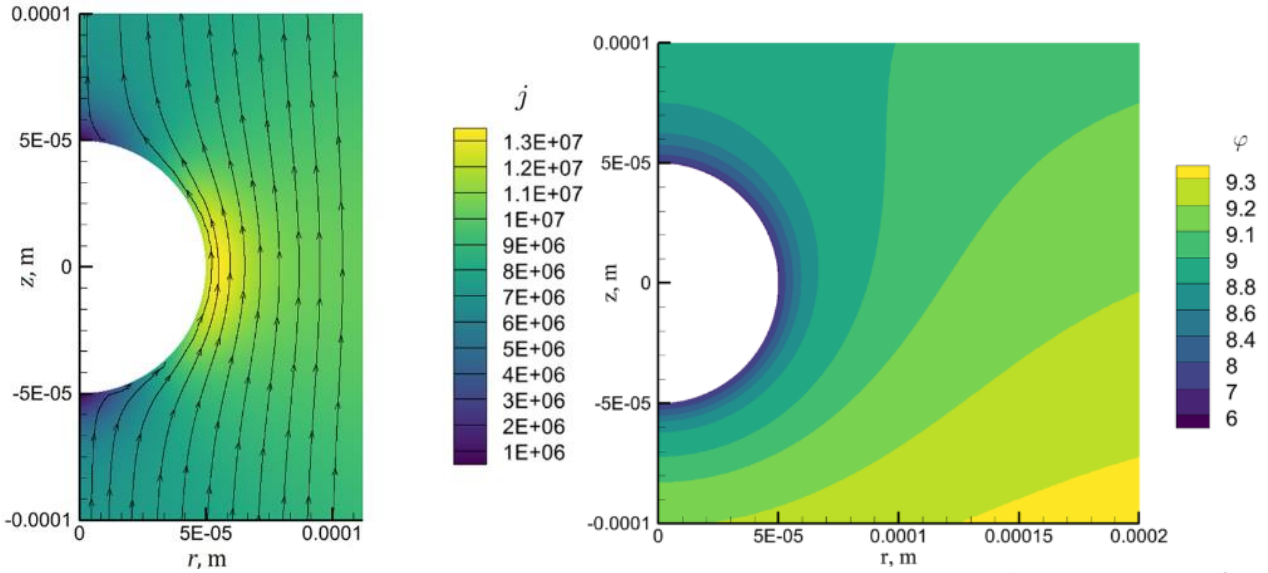

Fig. 1. Current density and potential near metallic particle with $a = 5 \cdot 10^{-5}$ m, $j_0 = 10^7$ *A/m*^{2}

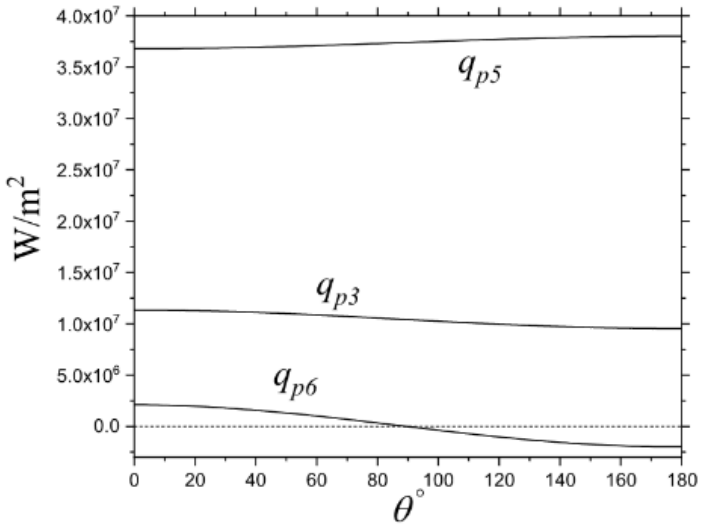

Fig. 2. Dependence of current-dependent heat fluxes on different points on the surface of metallic particle with $a = 5 \cdot 10^{-5}$ m, $j_0 = 10^7$ *A/m*^{2}

References

[1] N.A. Almeida, M.S. Benilov, and G.V. Naidis, *J. Phys. D: Appl. Phys.*, **2008** 41, 245201.

[2] I.V. Krivtsun, A.I. Momot, D.V. Antoniv and Binhao Qin, Welding and Related Technologies, **2025**. 129-135.

[3] S. Gao, A.I. Momot, I.V. Krivtsun, D.V. Antoniv and O.V. Momot, *East Eur. J. Phys.* **2025**, 1, 388-395.

[4] I.V. Krivtsun, A.I. Momot, D.V. Antoniv and Binhao Qin, Plasma Chemi. Plasma Proc., **2025**, 45, 971-991.

[5] I.V. Krivtsun, A.I. Momot, D.V. Antoniv, and Binhao Qin, *Phys. Plasmas*, **2023**, 30, 043513.

MODELING OF CHARGING OF DUST PARTICLES IN ARGON PLASMA IN PULSE REGIME

Vinnichenko V.V.*, Denysenko I.B.*
**V.N. Karazin Kharkiv National University, 61022 Kharkiv, Ukraine*
e-mails: vladvinni@ukr.net, igor.denysenko@karazin.ua

A theoretical model for charging of dust particles is presented. Using the model, plasma characteristics (electron and ion densities, electron temperature and densities of argon metastable atoms) as well as those of dust particles (mean dust charge, dust charge variance and dust charge distribution function) are analysed. The studies are carried out for two different energy distributions of electrons. Dust particles of different radii are considered.

Theoretical description of the model

A gas-discharge plasma of radius R = 15 cm and height L = 7 cm sustained in argon is considered. It is assumed that the plasma consists of electrons with density n_e and temperature T_e, positive ions Ar+ with temperature $T_i = T_g$, as well as argon atoms in different excited states Ar*(Ar_m, Ar_r and Ar_{4p}).The plasma is pulsed with frequency t_p = 4.75 ms. The plasma also contains dust particles with radius a_d and their charge is assumed to be negative. The model calculates the balance of argon atoms in different excited states, which can be presented in the following form:

$$\partial n^{(X)}/\partial t = \sum_i R_{G,i}^{(X)} - \sum_i R_{L,i}^{(X)}$$

where $R_{G,i}^{(X)}$ and $R_{L,i}^{(X)}$ are, respectively, the rates for reactions describing generation and loss processes of the species *X*.

Here, we consider the case when the dust density is small (the absolute value of dust charge density is smaller than the electron density), and the dust particles do not affect substantially on gas-discharge characteristics. It is also assumed that the energy distributions for ions are Maxwellian while for electrons we consider both Maxwellian and Druyvesteyn case, and that the positive ions and neutral atoms are at gas temperature T_g (294 K). We consider the power of the discharge to be different for different EEDFs in order to study charging of the dust particles for the same electron concentration but different EEDFs. The electron temperature T_e as a function of the discharge time t is found using the power balance equation (Eq. (6) in [1]).

The model assumes that dust particles of the same radius ad may have different charges Z_d = ke (where k is an integer and e is the elementary charge) due to stochastic charge fluctuations connected with charge discreteness. The dust charge distribution function (DCDF) F_k (normalized by $\sum_i F_k = 1$) is calculated from the master equation describing dust charging as a one-step process for both EEDFs at different stages of the discharge. We also calculate the mean dust charge Z_d and charge variance assuming that dust particles of the same radius have the same charge. More details on the model can be found in [2].

Results of numerical calculations

The model presented in the previous section has been used to study properties of plasma and dust charge as functions of time in pulsed Ar dusty plasma. The calculations have been carried out in the conditions of T_g= 294K, p = 0.075 torr. Different dust sizes a_d were considered and dust charge parameters calculated for both EEDFs.

We also analyzed the time dependences for other plasma parameters (electron density, electron temperature, densities of argon metastable atoms). The DCDF was compared with Gaussian distribution with calculated Z_d and variance for different dust particle sizes at different stages of the discharge (Fig.2) for both EEDFs. For small a_d some dust particles may attain positive charge.

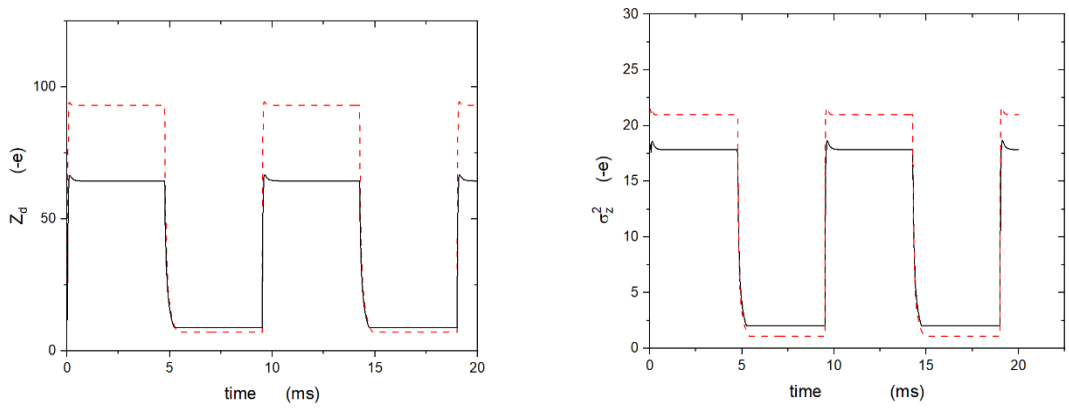

Fig. 1. Calculated mean dust charge and the variance of dust charge as functions of time in argon pulsed discharge. Solid lines — Maxwellian; dashed — Druyvesteyn distributions for a_d=25nm.

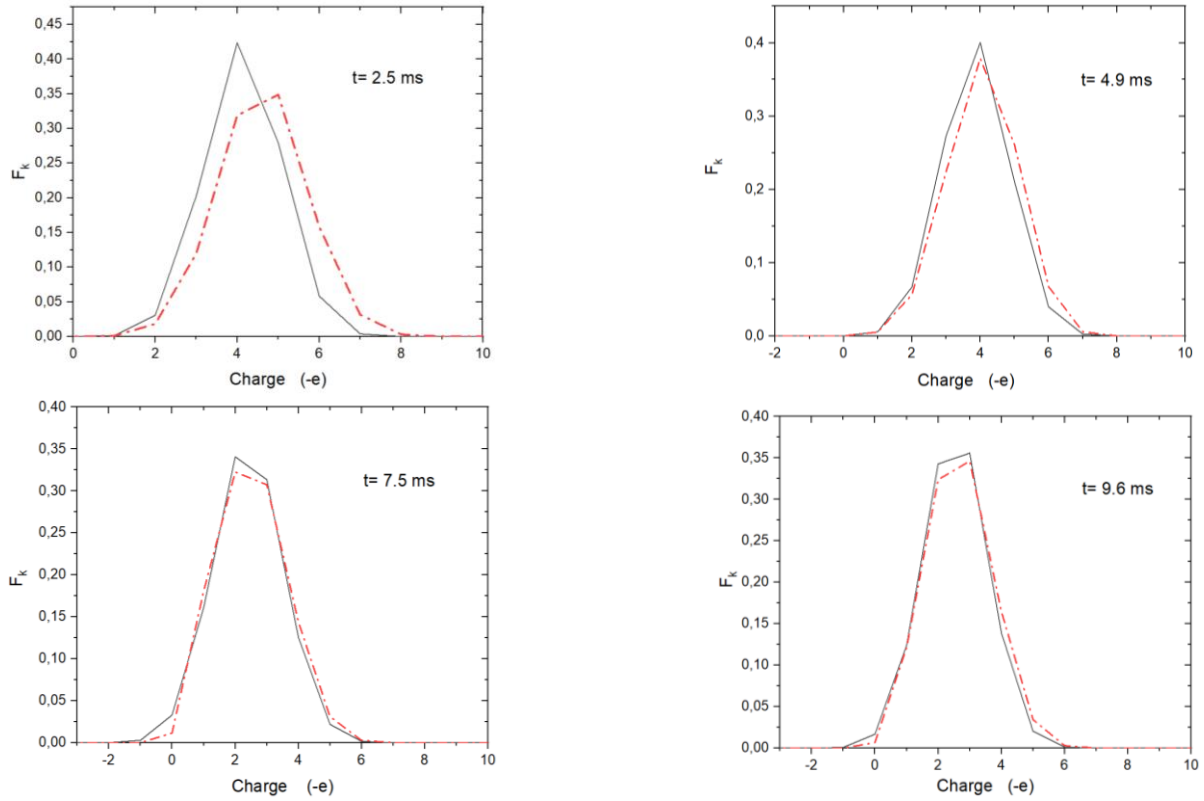

Fig. 2. Calculated Gaussian distribution (solid) and DCDF (dashed) for a_d = 1 nm at Druyvesteyn distribution.

References

[1] I.B. Denysenko, M. Mikikian, N.A. Azarenkov, "Plasma properties and discharging of dust particles in an Ar/C2H2 plasma afterglow," J. Phys. D: Appl. Phys., vol. 57, 145202, 12 pp., 2024.

[2] I.B. Denysenko, M. Mikikian, N.A. Azarenkov, Modeling results on the dust charge distribution in a plasma afterglow. *Phys. Plasmas* 1 September 2022; 29 (9): 093702.

THE PHASE CHARACTERISTICS OF IONS IN THE TWO STAGE PLASMA SOURCE WITH HALL CURRENT

A.M. Dobrovolsky*, O.A. Goncharov*, O.V. Fedorovskaya, V.I. Maslov**, I.N. Onishchenko****
**Institute of Physics NAS of Ukraine, Kyiv, Ukraine*
***NSC "Kharkiv Institute of Physics and Technology", Akademichna str, 1, Kharkiv, Ukraine*

With 2.5D PIC numerical simulation is shown that the argon ions in the two-stage plasma source, with the first stage based on the anode layer discharge and the second stage based on the dynamic ion space charge, can form a longitudinal ion beam under the influence of its own self-sustaining space charge.

Introduction

An early coaxial system with dynamic positive ion space charge was proposed [1]. Later, this system was transformed into a two-stage plasma source with an anode layer discharge as the first stage and a dynamic ion space charge as the second stage [2,3]. The possibility of plasma flow formation along the cylindrical symmetry axis of the device in a laboratory experiment was shown [4]. Now we study the phase characteristics of the positive ions in the system. The efficiency of longitudinal ion beam formation is the main goal of the investigation and the plasma beam source improvement.

Plasma source and model

The plasma source are shown on the Fig. 1. Inside the cylindrical magnetic system (1) are placed ring-shape anode (2) and two cathode blocks (3). The cathode blocks form partly virtual cathode of the anode layer discharge. The work gas argon is supply through the anode. The anode layer discharge exists in anode-cathode region and cover all anode surface. The argon ions move to the center of the ring and must turn out along the axis of symmetry of the device to go out.

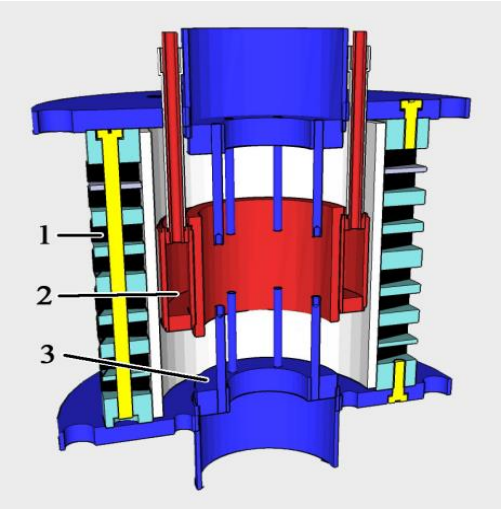

Fig. 1. The principal scheme of the two stage plasma source. 1 - permanent magnets system; 2 - anode; 3 - cathode

The theoretical model in numerical simulation was a cylinder with electrodes placed in it, between which the difference of potentials is applied (an accelerating field is formed). The magnetic field of cusp geometry is formed by coils. At the initial instant, the chamber contained a gas (argon) and seed electrons. Numerical simulations were performed in rz-geometry using the fully electromagnetic KARAT code. The collisional processes were modeled using the Mote-Carlo method.

Results

2.5D PIC numerical simulation shows that the argon ion flow arising in the process of gas ionization in crossed electric and magnetic fields with magnetized electrons is directed towards the axis of symmetry of the cylindrical system (see Fig. 2), where its density increases, therefore, a significant uncompensated space charge arises in this region. As a result of the action of the space charge of argon ions, a longitudinal component of the particle velocity arises (see Fig. 3), and an ion flow is formed along the system, where the particles scatter in opposite directions. In these studies, the flow density along the axis is less than the density accumulated in the center of the system region near the axis of symmetry. Further studies will make it possible to verify the possibility of creating an ion flow with a density that meets the requirements of the experiment along the chamber and to find out what parameters are required to obtain a beam with the required characteristics.

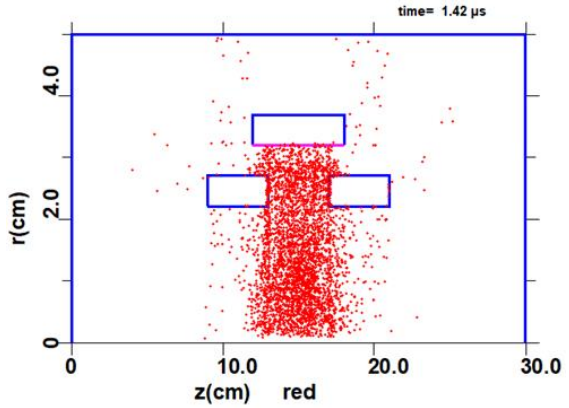

Fig. 2. rz-space for ions

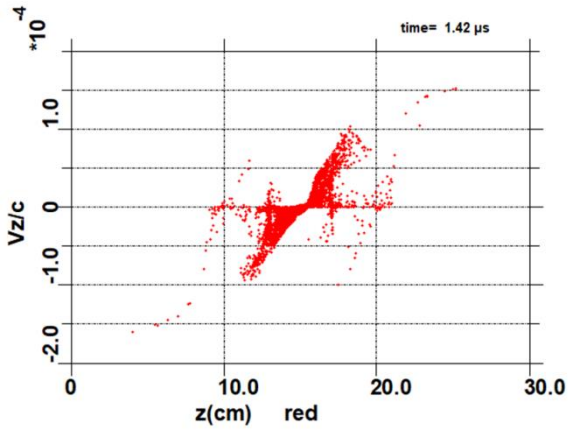

Fig. 3. Dependence of the longitudinal velocity of ions V_z on their longitudinal coordinate

References

[1] A.A. Goncharov, A.M. Dobrovol'skii, S.P. Dunets, A.N. Evsyukov, I.M. Protsenko. On a possibility of creation of positive space charge cloud in a system with magnetic insulation of electrons // Problems of Atomic Science and Technology. 2009. № 1. pp. 150-152.

[2] I. Litovko, A. Goncharov, A. Dobrovolskyi, and I. Naiko. Plasma Science and Technology The Emerging Field Trends Erosion-Free Electric Hall Thrusters Systems// Edited by Aamir Shahzad, InTechOpen, London, Chapter 11, pp. 195-214. 2022.

[3] V.Yu. Bazhenov, A.M. Dobrovolskiy, V.V. Tsiolko, V.M. Piun. Two stage plasma source for large scale beam generation//PAST. Series "Plasma electronics and new methods of acceleration". 2023. № 4. pp. 121-124.

[4] I.V. Litovko, V.Yu. Bazhenov, A.A. Goncharov, A.N. Dobrovolsky, I.V. Naiko Emerging trends in wall-free Hall thrusters development // Problems of Atomic Science and Technology. 2021. No 6(136) pp. 111-116.

DATA PROCESSING OF NON-UNIFORM PLASMA WITH METAL VAPOURS ADMIXTURES

V. Apanasenko*, A. Murmantsev, A. Veklich
Taras Shevchenko National University of Kyiv, 63/13, Volodymyrska str., Kyiv 01601, Ukraine
e-mail: vdapanasenko@gmail.com

This study is devoted to the application of data processing technique developed for optical diagnostics of plasma of electric arc discharge with cylindrical symmetry. This technique has been tested in the investigation of arc discharge plasma with metal vapours admixtures (e.g. copper, tungsten, molybdenum etc.) using RGB CMOS sensor as an emission registration device.

Introduction

Accurate plasma diagnostics are crucial for both fundamental plasma research and industrial applications. However, conventional industrial spectrometers often do not provide the required spatial resolution. This presents a significant limitation, as averaging the emission intensity over the entire plasma volume can lead to a loss of critical information regarding the non-uniformities of the plasma source. Spatial resolution is essential for the correct determination of the radial distributions of excitation temperature, electron density, and particle number densities within different plasma zones. Therefore, there is a clear necessity to develop diagnostic approaches that provide spatial resolution and to improve methods for the precise, online monitoring of plasma parameters, including the concentrations of admixtures, electrons, and temperature. This necessitates the creation of software solutions for operating the registration element (e.g., a CMOS array) and for automatic data processing to significantly accelerate and automate the diagnostic procedure. This study addresses these needs by presenting a new data processing technique for the optical diagnostics of electric discharge plasma, specifically tested on an arc discharge plasma with metal vapour admixtures (e.g., copper).

Results and discussion

The initial stage involves processing the raw RGB images of plasma emission to determine the spatial distribution of spectral radiance in the discharge gap [1]. This is achieved through a sequence of steps. First, Bayer scheme interpolation is performed, followed by conversion to grayscale. Next, known spectral lines identification is carried out. The spectral coordinate is interpolated by a second-degree polynomial to account for nonlinear dispersion. Finally, the spectral sensitivity is taking into account in absolute intensity values [1]. After initial image processing, the focus shifts to extracting and analyzing the spatial and spectral profiles of individual spectral lines. The frame containing the spatial distributions (horizontal axis) of individual spectral lines (vertical axis) is cut out (see Figure 1, a). Experimental data is then smoothed using the Savitzky-Golay filter to reduce random noise while preserving crucial characteristics. The spatial center of the emission is found by summing the spatial distributions of the various spectral components of a single spectral line (as the line spans multiple pixels), and then identifying the maximum of this summed distribution (see Figure 1, b).

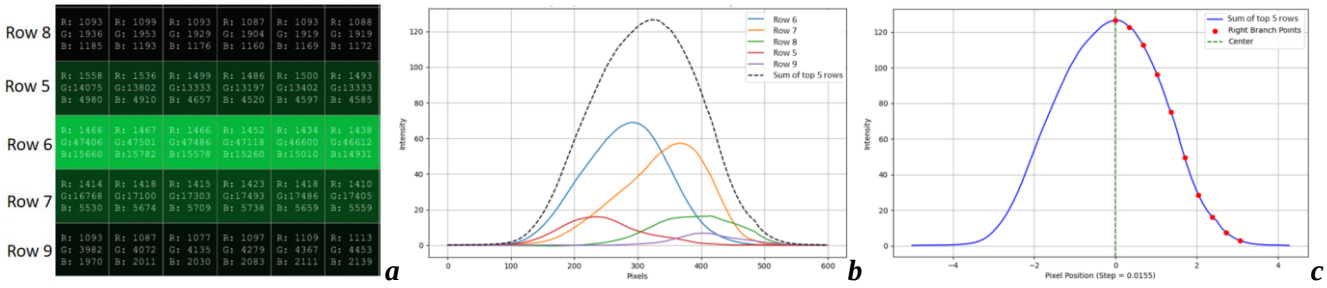

Fig. 1. (a) Part of a frame with spatial and spectral distribution of Cu I 515.3 nm spectral line by pixels, (b) distributions of various spectral components and (c) spatial distribution of total radiance of this spectral line

The process allows for the parallel analysis of the symmetry of spatial profiles and the uniformity of evaporation of different components of electrodes (e.g., composite or asymmetric electrodes). The pixel number is converted to a spatial coordinate. The spatial profile is subsequently divided into 9 equidistant spatial segments along the radius (Figure 1, c). At each of these spatial segments, the corresponding spectral profile is selected. Then the spectral line contours are approximated by a Gaussian at each of the 10 spatial points in the both edges of nine segments. This allows one to obtain the integral radiance of the spectral line at each spatial point and, in turn, spatial distribution of the radiance of spectral lines. This spatial profile is subjected to Abel inversion by the Bockasten method [2] in order to obtain the radial distribution of spectral line emission intensity. The radial distributions of absolute emission intensity are then used to construct Boltzmann plots and to obtain the radial distributions of plasma temperature and number density of emitting atoms.

To validate the performance of the proposed and realized software, a study of the plasma of electrical discharges between single-component copper electrodes with an arc current of 3.5 A was conducted. The radial distributions of the plasma temperature and the concentration of copper atoms, obtained using the software and manually (taken from work [1]), are shown in Figure 2, a and b, respectively.

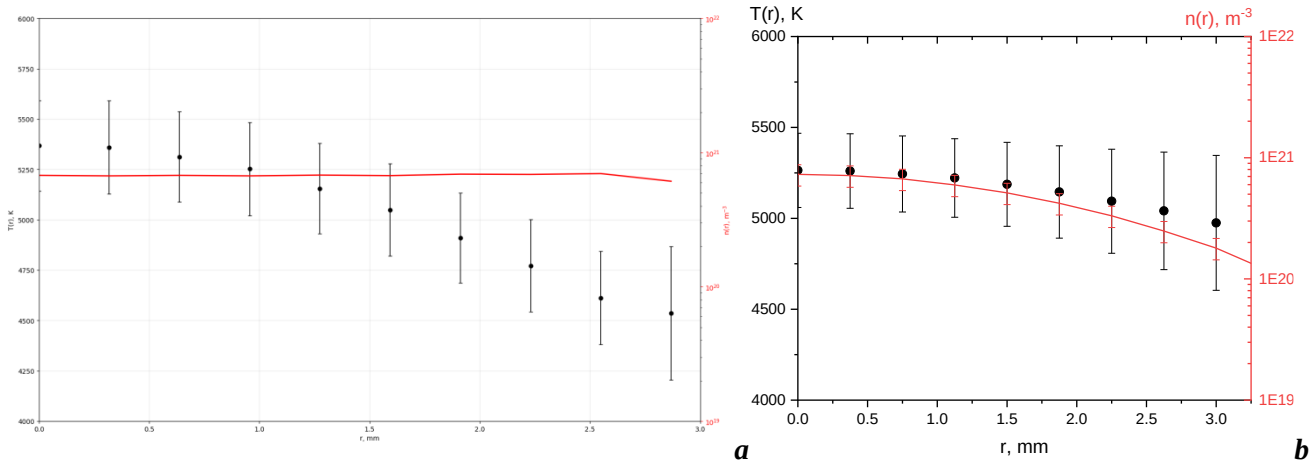

Fig. 2. Radial distributions of excitation temperature (black) and number density of copper atoms (red) obtained (a) during automatic processing and (b) during manual processing [1]

Conclusions

In this study, it was found that the radial distributions of plasma temperature and copper atom concentration obtained by manual and automatic processing using specially designed software agree within the experimental error. This suggests the viability of this development and its suitability for use for the investigation plasma discharges with cylindrical symmetry.

Acknowledgment

This work was supported by the National Research Foundation of Ukraine (Grant № 2023.03/0169).

References

[1] A. Murmantsev, “Investigation of Spatial Distribution of Metal Vapours Admixtures in the Plasma of an Electric Arc Discharge,” *Problems of Atomic Science and Technology*, vol. 146, no. 4, pp. 139–146, 2023.

[2] K. Bockasten. “Transformation of Observed Radiances into Radial Distribution of the Emission of a Plasma”. *Journal of the Optical Society of America*, 1960, № 9 (51), p. 943-947.

EFFECT OF GAS PRESSURE ON ANODE SHEATH STRUCTURE IN HALL THRUSTER

E.V. Romashchenko
Institute of Physics of the National Academy of Sciences of Ukraine, Nauky av., 46, Kyiv, 03028, Ukraine,
e-mail: ev.romashchenko@gmail.com

The near-anode region of a Hall thruster discharge is studied. The increased ionization is shown to result in the anode sheath structure. Two mechanisms of the formation of the sheath anode structure are found to be suitable to explain the presence of the "low-current" and "high-current" modes in the Hall thruster discharge.

Hall thrusters is the most advanced and efficient types of electrostatic propulsion devices [1]. The electric field in the Hall thruster is perpendicular to the magnetic field to confine the electrons. The passing the electron current across a magnetic field leads to an electron closed drift or Hall drift, that provides the necessary gas ionization and plasma formation at low gas pressure. Hall thruster with conductive walls belongs to the thruster with anode layer (TAL). An important feature of TAL is the formation of the sheath of the negative space charge near anode surface. The two-stage Hall thruster of TAL-type with a cusp-type magnetic field distribution was proposed in the previous work [2]. The configuration of magnetic and electric fields of such thruster was similar of that of cylindrical magnetron. The measured current-voltage characteristics in the pressure range (10^{-5} – 10^{-3}) Torr revealed the presence of "low" and "high" current discharge modes. At pressure $\boldsymbol{p > p_{cr}}$ the discharge current sharply increased from a few to hundreds milliamperes. To explain the observed phenomenon the theoretical model of the anode sheath is developed in this work.

The stationary one-dimensional fluid model describes the electron and ion transport in the near-anode region for two pressure regimes: low-pressure (p <10^{-4} Torr) and medium pressure (10^{-4} – 10^{-3}) Torr. Two types of anode sheaths corresponging of these regimes are shown in Fig. 1.

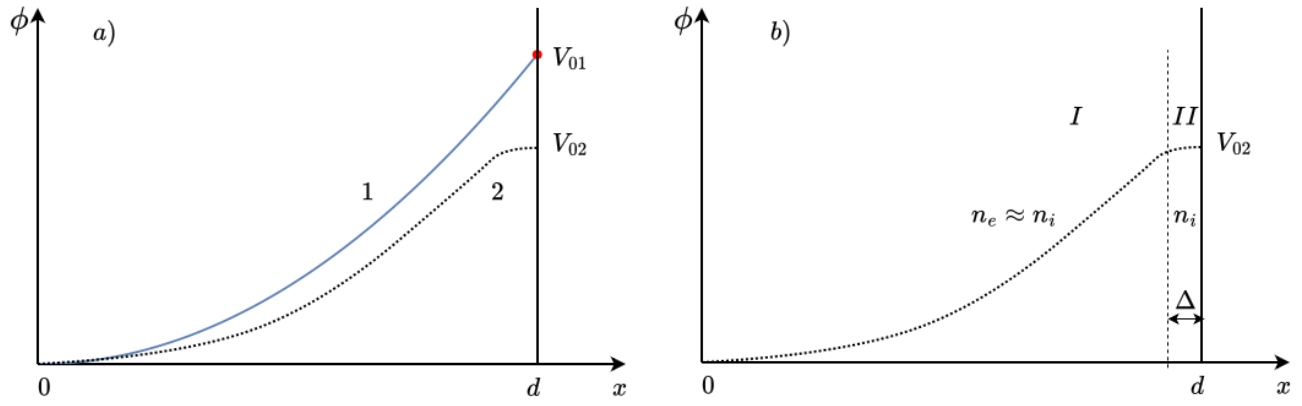

Fig. 1. (a) Sketch of the electrostatic potential profile of various types of the anode sheaths:1- anode layer (electron sheath), 2 - anode double layer; (b) - structure of an anode double layer, consisting of plasma sheath

At low pressures (p <10^{-4} Torr), the electron contribution to the space charge is negligible, and the near anode region is pure electron plasma. In this case, the sheath is called an anode layer or electron sheath. The collisions between the electrons and neutrals allow the electrons to cross the magnetic field, and to reach the anode. The ions are generated by electron impact ionization. The ions are accelerated by electric field of the sheath, and leave the sheath without collisions with neutral atoms. The electrons are magnetized, while the ions are unmagnetized. The electron transit time τ_e across the sheath is much longer than the ion transit time τ_i, $\tau_e \gg \tau_i$. The electron sheath

thickness of the anode layer d can be estimated from the equation of the balance between electron generation and their loss from the volume under assumption that the electrons are generated in the volume only as a result of ionization, and, finally, all of them reach the anode. In this case, the thickness of the anode layer is of the order of the electron Larmor radius.

At higher pressures $p > 10^{-4}$ Torr, both the electron and the ions contribute to the space charge, and the ion transit time τ_i is longer than the electron transit time τ_e, $\tau_i > \tau_e$. The ion density overtakes the electron density. As a result, an electron depletion occurs near-anode region. This case corresponds to an anode double layer. The thin layer of positive space charge with thickness Δ forms near the anode surface, and plasma sheath forms in the inner region. Transition from an anode layer to an anode double layer take places at pressure $p > p_{Cr}$. The formation of an anode double layer leads to peak in the electron concentration, and, in turn, to the significant increase in the current.

References

[1] D.M. Goebel and I. Katz, Fundamentals of Electric Propulsion: Ion and Hall Thrusters. New York: Wiley, 2008.

[2] V.Yu. Bazhenov, A.M. Dobrovolskiy, V.V. Tsiolko, "Two stage plasma source for large scale beam generation", V.M. Piun, *Problems of Atomic Science and Technology*. 2023. No 4 (146).

THE INFLUENCE OF COLLISIONS IN LOW-PRESSURE PLASMA ON THE ENERGY OF IONS IN THE NEAR-ELECTRODE LAYER

O.Yu. Kravchenko, A.A. Derkach
Taras Shevchenko National University of Kyiv, Kyiv 01601, Ukraine, e-mail: kay@univ.kiev.ua

Within the framework of the hydrodynamic model, a sheath is modeled that forms at the boundary between low-pressure plasma and the wall at a certain negative potential. It is shown that collisions of ions with neutral atoms and dust particles can significantly reduce the energy with which they bombard the wall. It is also shown that the calculation of ion energy according to the drift-diffusion approximation is acceptable at pressures $p > 1 Torr$.

Introduction

The problem of sheath formation in plasma boundaries is of great technological importance in many applications of plasma including plasma-assisted material processing, plasma nanofabrication, and plasma medicine [1]. In particular, it is well known that the ion energy arriving at the substrate is crucial in etching and deposition rates of the film, strongly affects the emission of electrons from the cathode and their sputtering in the magnetron discharge. The classical problem of the structure of the sheath was solved quite a long time ago for the case of plasma without collisions. In this case, the energy of the ions bombarding the wall is determined by the jump in the electric field potential near the wall. In the case of high-pressure plasma, when the free path length of ions is significantly less than the width of the sheath, the ion velocity can be determined using drift-diffusion approximation [2]. In the case of low pressure plasma (p=0.1 - 3 Torr), the free path length of ions is approximately equal to the width of the charged layer near the wall, and determining the velocity of ions based on their mobility becomes inaccurate.

The aim of our work is to study the energy of ions bombarding the wall when they collide with neutral atoms and nanoparticles in the sheath.

Model and simulation method

We consider the solid substrate, which interacts a neutral stationary plasma of density n_0 .and assume that it is under potential $\varphi_0 = -300\,V$. To describe the potential of a self-consistent electric field, we used the Poisson equation:

$$\frac{d^2\varphi}{dx^2} = -\frac{1}{\varepsilon_0} e\left(n_i - n_e\right) \tag{1}$$

where n_i, n_e are the densities of ions and electrons.

Ions are described by the equations of hydrodynamics

$$\frac{\partial u_i}{\partial t} + u_i \frac{\partial u_i}{\partial x} = -\frac{e}{m_i} \cdot \frac{\partial \varphi}{\partial x} - \nu_{in} u_i - \nu_{id} u_i , \tag{2}$$

$$\frac{\partial n_i}{\partial t} + \frac{\partial\left(u_i n_i\right)}{\partial x} = 0 , \tag{3}$$

where u_i, e, m_i are ion hydrodynamic velocity, charge and mass, ν_{in} is the frequency of ion-neutral atom collisions, ν_{id} is the frequency of ion-dust collisions.

Density of the electrons satisfies the Boltzmann distribution

$$n_e = n_0 \exp(e\varphi / kT_e) . \tag{4}$$

For the simulation of the nanoparticles, we use PIC method. According this method the dust component is modeled by a set of macroparticles each of which is a set of nanoparticles with roughly identical coordinates and velocities. The motion of macroparticles is described by equations

$$\frac{dx_{di}}{dt} = u_{di},$$

$$M_d \frac{du_{di}}{dt} = Q_{di} E(x_{di}) + F_{dn}.$$

Here x_{di}, u_{di}, M_d and Q_{di} are the spatial coordinate, velocity, mass and charge of the macroparticles, $E(x_{di})$ is an electric field at the point where the macroparticle is located. The friction force between the nanoparticle and the neutral is determined according to [3].

Results and discussion

Spatial distributions of plasma parameters in the cathode layer were obtained at different concentrations of neutral atoms at different times. It has been shown that over time, the distributions obtained become stationary. A charged layer forms near the cathode, in which the electric field accelerates ions toward the cathode. The energy of ions near the cathode depends on the friction force with neutral atoms and is shown in Figure 1 as a function of their concentration. The same figure shows the energy of ions calculated according to the drift-diffusion approximation, in which the velocity of the directed motion of ions is determined by the formula $u_i = \mu_i E$ (μ_i is ion mobility, E is electric field strength).

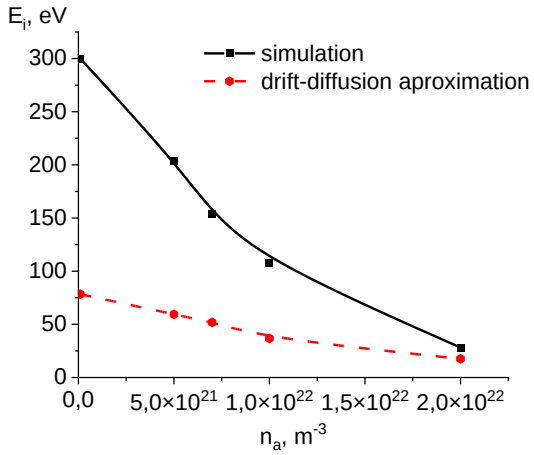

Fig. 1. Energy of ions near cathode as a function of neutral atom density. Solid curve: results our simulations, dash curve: results according drift-diffusion approximation.

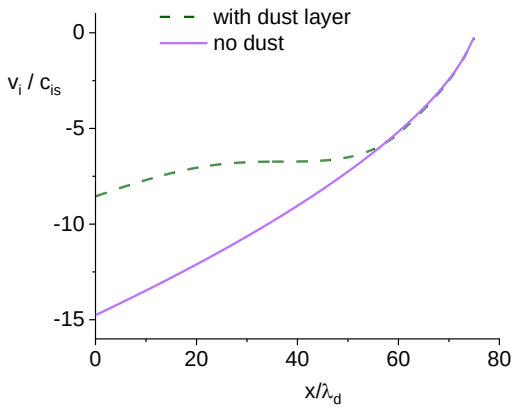

Fig. 2. Spatial distributions of ion velocity at $n_a = 10^{22}\ m^{-3}$ for case without dust particles (solid curve) and for case with dust particles layer (dash curve).

Fig. 2 shows the spatial distribution of ion velocity at a concentration of atoms $n_a = 10^{22}\ m^{-3}$ in the absence of dust particles in the cathode layer and in the presence of a dust layer. It can be seen that dust particles significantly reduce the drift velocity of ions near the cathode surface.

References

[1] D. Sharma, H. Ramachandran. Structure of a source-driven magnetized oblique presheath // Phys. Rev. E. – 2002. – V.66. – P. 026412-9.

[2] M.A. Lieberman, A.J. Lichtenberg, Principles of Plasma Discharges and Materials Processing, Wiley, New York, 1994.

[3] P.K. Shukla, A.A. Mamun. Introduction to Dusty Plasma. Physics, Bristol and Philadelphia: IoP Publishing Ltd., 2002.

PROPERTIES OF A SECONDARY DISCHARGE PLASMA SUPPORTED BY A ROTATING GLIDING DISCHARGE

V.Ya. Chernyak, V.V. Iukhymenko, K.V. Iukhymenko, D.D. Tretiakov, O.M. Tsymbaliuk, S.S. Nedovesov, Z.O. Prokofiieva

Taras Shevchenko National University of Kyiv, Kyiv, Ukraine, e-mail: chernyak_v@ukr.net; yvitaliy@ukr.net

In this work, the results of an experimental study of plasma parameters of a secondary discharge at atmospheric pressure, sustained by a low-power (~ 100 W) rotating gliding discharge in an air stream under conditions of a significant excess of the plasma channel length of the secondary discharge over the length of the self-sustained discharge channel in the range of 1...100, are presented. Plasma parameter determination was carried out using emission spectroscopy of the plasma with the SpecAir program.

The observed research trends in various fields of science indicate a great need for nanomaterials with multi-element composition. Typically, the generation of these nanomaterials during plasma activation of the process takes place in two stages: 1 - synthesis of molecules from elements introduced into the plasma of an inert gas, 2 - synthesis of nano-sized material from the obtained molecules during the quenching process. An alternative approach may be plasma activation of the process of transforming micro-sized material into nano-sized without changing the elemental composition using secondary discharges. Since the fundamental features of the plasma of secondary discharges supported by an independent discharge are both the generation of a non-equilibrium plasma of a much larger volume and the possibility of a significant impact on the electron energy distribution function (EEDF). A “two-temperature” EEDF can be created at average pressures of ≈ 0.1 mm Hg. [1], and EEDF “with a truncated tail” - at atmospheric pressure [2]. This work is devoted to a detailed comparison of the parameters of atmospheric pressure plasma of a self-discharge and a secondary discharge with a rotating gas flow.

The experimental set-up for transforming micro-sized substances into nano-sized ones is shown in Fig. 1, where 1 – high-voltage primary discharge electrode; 2 – grounding electrode; 3 – high-voltage secondary discharge electrode; 4 – gas inlet; 5 – quartz cylinder; 6 – dielectric; 7 – gas outlet; 8 – optical fiber; 9 – spectrometer; 10 – PC.

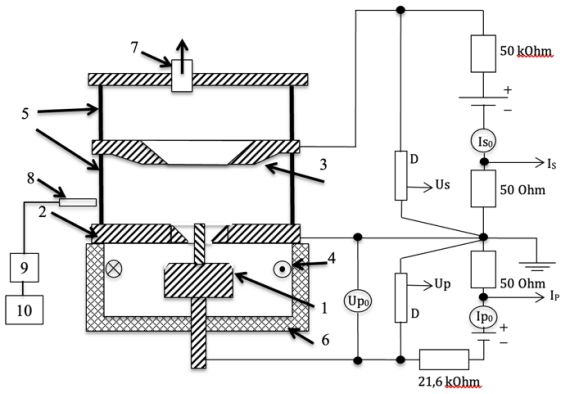

Fig. 1. Experimental set-up

The plasma parameters of the discharges were determined using UV and visible emission spectroscopy of the plasma (200...1000 nm). The emission spectra were recorded using a Solar TII spectrometer. The values of vibrational temperature Tv and rotational temperature Tr of the atomic and molecular levels were determined using calibrated curves for O atom, OH, and N2 molecules. The calibration curves were constructed based on the results of numerical simulation of the emission spectra of the O, N2 system (CB) bands, and OH system (A-X) bands using the SPECAIR code [4, 5] in the temperature range of 500…20000 K, taking into account the instrumental function of the Solar TII spectrometer (Gaussian with a width of 0.3 nm at half-height).

Typical emission spectra of air plasma RGD and SDSRGD at the same discharge current Ip = Is =80 mA are shown in Fig. 2. The plasma spectra of both discharges are characterized by bands of NO and OH molecules in equal proportions. At the same time, the behavior of the N_2 bands is significantly different, in the spectrum of the SDSRGD plasma these bands are completely absent. Taking into account the ratios of the excitation thresholds of the NO, OH, N_2 bands. This may be due to a significant difference in the high-energy part of the EEDF of electrons.

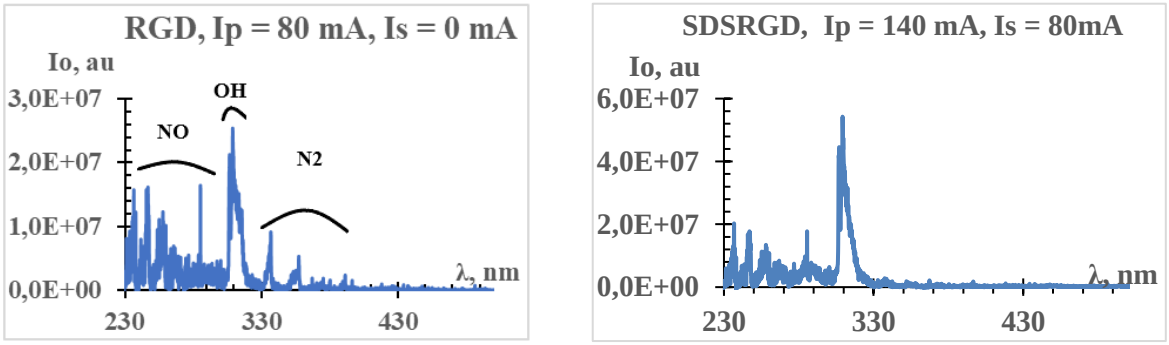

Fig. 2. Spectra of self-discharge (RGD) and secondary discharge (SDSRGD) plasma

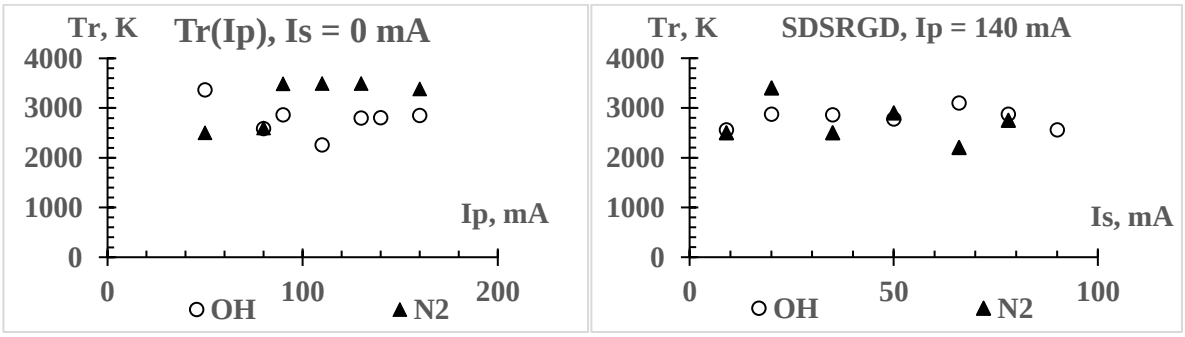

Fig. 3. Dependences of the population temperatures of the OH, N_2 rotational levels on the discharge currents

The dependences of the temperatures of population of rotational levels of OH and N_2 molecules on the discharge currents are shown in Fig. 3. From the given dependences it follows that Tr practically does not depend on the discharge currents and is equal to ~ 3000 K for the plasma of both discharges. This can be explained by the similarity of the low-energy parts of the EEDF for the plasma of both discharges.

Conclusions

The experimentally obtained regularities in the emission spectra of RGD and SDSRGD plasmas indicate significant differences in the EEDF in the high-energy region (≥ 9 eV).

The kinetic temperature of the heavy component of SDSRGD plasma reaches the melting temperatures of refractory substances.

References

[1] Chernyak V.Ya., Buchnev V.V. “Numerical modeling of the processes of formation of the electron energy distribution function in a non-independent discharge”, Bulletin of the University of Kyiv. Ser. FM, Vol. 4, pp. 278-284, 1998.

[2] V.Ya. Chernyak, V.V. Iukhymenko, K.V. Iukhymenko, D.D. at all, “Properties of a secondary discharge plasma supported by a rotating gliding discharge”, Problems of Atomic Science and Technology. Series: Nuclear and physical research. №6, pp. 145-149, 2023.

[3] A. Fridman. *Plasma chemistry*. Cambridge University. Press, 978 p., 2008.

EFFECTS OF NON-EQUILIBRIUM PLASMA PROCESSING ON SOLUTIONS OF L - NEUTRAL-POLAR AMINO ACIDES

Valeriy Chernyak*, Kostiantyn Iukhymenko*, Vitalii Iukhymenko*, Sergeiy Nedovesov*, Daniil Tretiakov*, Olexander Tsymbaliuk*, Sergeiy Shulga**

**Faculty of RadioPhysics, Electronics and Computer Systems, Taras Shevchenko National University of Kyiv, Ukraine, e-mail: chernyak_v@ukr.net*

***Institute of Hydromechanics NAS of Ukraine, Kyiv, Ukraine, e-mail: sergey.v.shulga@gmail.com*

This work is devoted to the study of the possibility of violating one of the basic provisions of chemical thermodynamics in a strongly non-equilibrium plasma-chemical system. Particular attention is paid to the fact that "living" biomaterials are characterized by both the arrangement of chiral components and the course of chemical transformations in organic chemistry under quasi-equilibrium conditions. In view of this, the features of the plasma effect on aqueous solutions of L - neutral-polar amino acides, *which is associated with the introduction of energy by the plasma flow sufficient for significant destruction of organic molecules. The non-equilibrium of the plasma-chemical system provides not only a significant energy-mass exchange with the environment, but also the absence of equivalence in the directions of motion of reagent particles, which is realized by the gas dynamics of the rotating gas flow in the system.*

Since plasma generation consumes the most expensive energy (electricity), the most interesting problems for non-equilibrium plasma chemistry are those related to the possibility of realizing chemical transformations forbidden by chemical thermodynamics in traditional chemistry, which usually works under quasi-equilibrium conditions. It is with the violation of the rule of organic chemistry "synthesis of chiral [1] compounds from achiral reagents always leads to racemic modification, and optically inactive reagents generate optically inactive products" [2], which is a prohibitive statement of chemical thermodynamics, that the experimental results of this work are related.

The relevance of these studies is due to the fact that today in a number of branches of the national economy (such as medicine, cosmetology and agro-industry) technologies based on the interaction of particle beams at high energies with biomaterials are used. The energy of the beam particles is equal to or exceeds the energy of chemical and physical bonds in atoms or molecules. Such particles are photons of the UV optical range (in cosmetology), charged and neutral particles with kinetic and internal energy in the range from units to tens of electron volts (plasma medicine and Agro plasma), from units to tens of kiloelectron volts (medicine...).

In physics, such a process of beam interaction with matter is characterized (described) as the introduction of energy into the system, which leads to the transfer of the system from an equilibrium to a non-equilibrium state, in which the rates of dissociative (destructive) processes exceed the rates of the reverse (the inverse of the associative ones). After the termination of the external influence, the excited system relaxes, passing from a non-equilibrium state to an equilibrium state, in which the rates of dissociative processes decrease, and the rates of associative processes increase.

Living matter, unlike non-living matter, has chiral purity: all proteins consist of left-handed amino acids, and DNA and RNA are built on right-handed ribose. In Miller's experiment on plasma activation of synthesis and other experiments on abiogenic synthesis, left-handed and right-handed isomers of sugars and amino acids are formed in equal proportions [3-4]. If you try to build proteins and nucleic acids from such a mixture, you usually get a random alternation of left-handed and right-handed links. Such DNA cannot fold into a double helix, and proteins - into a certain stable shape and therefore cannot work as enzymes [5].

In fact, this may mean that any of the above-mentioned physical therapy is likely to be accompanied by negative consequences during treatment!

Avoiding such negative consequences may be facilitated by conducting therapy in conditions of special imbalance of systems, which take into account the physical essence of the properties of an equilibrium macrosystem established by the molecular kinetic theory (MKT), which consists of a large number of particles. MKT establishes the laws of behavior of a macroscopic system through the averaged characteristics of the motion of individual molecules and their interaction with each other using statistical methods [6]. The main assumption here is that the molecules of a substance are always in a state of chaotic motion, and the main feature of the chaotic motion of molecules is the equiprobability of the directions of their motion.

When the system's non-equilibrium is ensured not only by energy and mass exchange with the environment, but also by a violation of the equiprobability in the directions of the rotational motion of molecules, the above-mentioned prohibition of thermodynamics may be violated, as was experimentally shown in [7-8] and indicated by the kinetic model of a three-particle associative process developed by the authors with the participation of three particles in a certain direction of the rotational motion of molecules [9].

This work is devoted to the continuation of experimental studies of the influence of plasma activation on the optical activity of aqueous solutions of three neutral polar amino acids (L-Cysteine, L-Threonine, L-Serine) in a plasma-liquid system by a gas discharge plasma in a rotating gas flow, which is described in [7-8]. It is shown that a significant influence of the direction of rotation of the gas flow on the optical activity after plasma activation exists only for L-Serine. Plasma activation of the L-Threonine solution for 20 min led to a slight increase in optical activity (~ 40 C), for the L-Cysteine solution to a decrease (200 C. At the same time, the dependence of the change in optical activity on the direction of rotation of the gas flow in the plasma-chemical system within the limits of measurement errors was not detected. The dependence of the optical activity of the L-Serine solution after plasma activation on the direction of rotation was detected.

References

[1] https://uk.wikipedia.org/wiki/Хіральність
[2] J. Sarfati, "*Origin of life: the polymerization problem",* CEN Technical Journal, vol.12 (3), pp. 263-266, 1998.
[3] S.L. MillerA, " A Production of Amino Acids Under Possible Primitive Earth Conditions", Science, vol. 117, pp. 528-529, May 1953.
[4] A.P. Johnson at all, "The Miller Volcanic Spark Discharge Experiment", Science, vol. 322, pp. 400-411, Oct. 2008. www.sciencemag.org
[5] M. Nikitin, *The Origin of Life. From Nebula to Cell*. Alpina Non-Fiction Publishing House, 2016.
[6] See details here: https://physics.zfftt.kpi.ua/mod/book/view.php?id=296&chapterid=21
[7] V.Ya. Chernyak, V.V. Iukhymenko, K.V. Iukhymenko at all, "*Plasmochemical synthesis of optically active substances",* IEEE Transactions on Plasma Science. No. 3 (49), pp. 1050-1054, 2021.
[8] V. Chernyak, S. Shulga, V. Iukhymenko at all, "*Effects of Non-Equilibrium Plasma Processing on Solutions of D-, L-Isomers*", Journal of Biomedical Sciences and Biotechnology Research, Vol. 3(1), pp. 1-8, 2025.
[9] V. Chernyak, D. Tretiakov, V. Iukhymenko at all, *Distinctive Properties of Non-Equilibrium Dynamic Plasma-Chemical Systems // Abs.7th International Conference on Chemistry" and 5thMass Spectrometry and Analytical Techniques* Nov. 11-12, 2024 | Barcelona, Spain. - P. 54.

COMPUTER TECHNOLOGIES

EXPERIMENTAL INVESTIGATION OF CODETRANS T5 AND T5 MODELS FOR COMMIT MESSAGE GENERATION IN VERSION CONTROL SYSTEMS

Bohdan Semonov*, Sergiy Pogorilyy**
*Faculty of RadioPhysics, Electronics and Computer Systems Taras Shevchenko National University of Kyiv, Kyiv 01601, Ukraine, e-mail: *bohdan.semonov@gmail.com, **sdp@knu.ua*

The paper presents the results of an experimental evaluation of modern transformer-based models for the task of commit message generation based on changes in program source code. The models were compared using BLEU, ROUGE-1, ROUGE-2, ROUGE-L, BERTScore, and BLEURT metrics, which made it possible to assess both the surface accuracy and the semantic quality of the generated messages. The obtained results can be applied to the development of practical solutions for automatic generation of technical messages in software version control systems.

Introduction

Despite the importance of commit messages, there are no established standards for their composition, leading to diverse practices and complicating the consistency, completeness, and clarity of information regarding code changes. In this context, the development of automated methods for generating standardized and meaningful commit messages is highly relevant, with transformer-based models offering effective solutions due to their successful application of NLP techniques to code-related tasks [1].

Guidelines for presenting information in commit messages [2]:

1. commit messages should specify the reasons for the changes, describe their expected impact, and, in the case of a bug fix, indicate the specific issue that was resolved;
2. commit messages must be understandable and convey the changes' effects, regardless of the reader's familiarity with the code or problem.

Examples of commit messages that comply with Rule 2: "Add JWT-based session handling to replace deprecated cookie auth"; "Fix division by zero in invoice calculation to prevent crash".

The main objective of this study is to develop and experimentally validate an approach for automated generation of code change messages using transformer-based models. To achieve this objective, the task involves identifying model parameters θ^{opt} that minimize the loss function $\mathcal{L}$ on the validation dataset:

$$\theta^{opt} = arg\min_{\theta} \sum_{(x_i,y_i)\in D} \mathcal{L}(f_\theta(x_i), y_i).$$

After training, for a new example $x^{test} \in X$, the model generates a message:

$$y^{test} = f_{\theta^{opt}}(x^{test}).$$

Data Collection and Preprocessing

To construct the training dataset, one of the largest web services for hosting IT projects and collaborative software development – GitHub – was utilized. This platform provides a dedicated application programming interface known as the GitHub REST API [3].

After data acquisition, the records were preliminarily filtered, as the change descriptions varied in style, length, and level of detail. All previously defined rules can be implemented programmatically, except for Rule 4, for which formal methods are insufficient. Due to the absence of clear structured criteria for evaluating the semantic content of changes, fulfilling this rule requires the use of machine learning methods capable of modeling the

contextual semantics of commit messages. To address this, a filtering method for change descriptions based on MLP and RNN models was developed [4].

Transformer-based Method

To address the task of commit message generation, transformer-based models (SEBIS CodeTrans T5 (base), Mamiksik T5 model) were employed, selected based on their architecture and adaptability to working with source code. All models were fine-tuned on a curated dataset of change-message pairs covering multiple programming languages (C/C++, Ruby, Python, Java, JavaScript (JS), and PHP). During fine-tuning, the models' respective tokenizers (AutoTokenizer from the HuggingFace Transformers library [5]) were used. The choice of the HuggingFace Transformers library was motivated by the availability of models pre-trained on source code and their compatibility with the Google Colab execution environment.

The models' performance was evaluated using BLEU, ROUGE-1, ROUGE-2, ROUGE-L, BERTScore, and BLEURT, which enabled the measurement of both lexical accuracy and semantic consistency in the generated messages. The results of the models are presented in Table 1.

Table 1: Evaluation of commit message generation models

Модель	**Мова**	**BLEU**	**ROUGE-1**	**ROUGE-2**	**ROUGE-L**	**BERTScore**	**BLEURT**
SEBIS CodeTrans T5 (base)	C/C++	2.67	15.62	8.05	14.95	0.83	0.27
	Ruby	4.33	15.68	6.7	14.67	0.84	0.27
	Python	5.18	19.35	11.37	18.49	0.86	0.28
	Java	5.87	22.93	16.11	22.16	0.86	0.3
	JS	**14.53**	**30.21**	**24.52**	**29.67**	**0.88**	**0.35**
	PHP	3.34	15.83	5.04	15.13	0.85	0.24
Mamiksik T5 model	C/C++	3.8	23.95	12.24	22.14	0.88	0.34
	Ruby	5.8	25.34	11.26	22.87	0.86	0.34
	Python	5.86	27.86	14.55	25.59	0.87	0.36
	Java	5.35	28	17.54	26.28	0.88	0.35
	JS	**13.7**	**36.05**	**25.28**	**34.3**	**0.9**	**0.42**
	PHP	4.16	24.56	8.87	22.67	0.88	0.32

Conclusions

From the results table, it can be observed that the highest performance among the base models is achieved by Mamiksik T5 model (fine-tuned on JavaScript), with BLEU at 13.7%, ROUGE-1 at 36.05%, ROUGE-2 at 25.28%, ROUGE-L at 34.3%, BERTScore at 0.9, and BLEURT at 0.42. The obtained results demonstrate the effectiveness of transformer-based models for commit message generation. This, in turn, highlights the importance of adapting the training approach and making a justified selection of both n-gram and semantic metrics to enable an objective evaluation of the models.

References

[1] B. O. Semonov and S. D. Pogorilyy, "Research of the application of GPGPU and TPU technologies for ensuring comment quality in version control systems," *PROBLEMS IN PROGRAMMING*, no. 1, pp. 24–37, 2025, doi: 10.15407/pp2025.01.024.

[2] See details here: https://cbea.ms/git-commit/#seven-rules

[3] See details here: https://docs.github.com/en/rest?apiVersion=2022-11-28

[4] S. Pogorilyy and B. Semonov, "The Implementation of a Commit Messages Filter for Software Version Control Systems," in *The 9th International Conference on Control and Optimization with Industrial Applications*, 2024, pp. 175–179.

[5] T. Wolf *et al.*, "HuggingFace's Transformers: State-of-the-art Natural Language Processing." 2020. [Online]. Available: https://arxiv.org/abs/1910.03771

BENCHMARKING YOLO NANO ON EMBEDDED PLATFORMS: RASPBERRY PI ZERO W2, PI 4, AND PI 5

Yevhenii Hloba
Taras Shevchenko National University of Kyiv, Kyiv 03022, Ukraine, e-mail: yevhenii.hloba@knu.ua
Faculty of RadioPhysics, Electronics and Computer Systems Taras Shevchenko National University of Kyiv, Kyiv 01601, Ukraine

This paper presents a benchmarking analysis of the YOLO Nano neural network deployed across Raspberry Pi Zero W2, Raspberry Pi 4, and Raspberry Pi 5 platforms. The goal of this study is to assess the feasibility of real-time object detection on constrained embedded systems commonly used in UAVs and IoT devices. The performance metrics include inference latency, frames per second (FPS), detection accuracy (mAP), power consumption, and CPU utilisation.

Introduction

Real-time perception on low-cost embedded hardware enables autonomous drones, smart cameras, and on-device analytics where bandwidth, privacy, and latency constraints preclude cloud offloading. Raspberry Pi boards are ubiquitous in such deployments due to their availability, cost, and extensive ecosystem. However, performance varies substantially across generations—Zero W2 (Cortex-A53), Pi 4 (Cortex-A72), and Pi 5 (Cortex-A76)—and across inference backends (ONNX Runtime, TFLite/XNNPACK, OpenCV DNN). Selecting the correct platform and runtime for a given workload remains non-trivial.

Why YOLO Nano? YOLO-family detectors provide single-stage, low-latency detection. YOLO Nano is a compact architecture emphasizing depthwise separable convolutions and lightweight feature aggregation, making it a representative model for constrained devices while retaining practical accuracy. By fixing the model and varying only platform and runtime, we isolate the hardware/software impact on end-to-end performance [1], [2].

Methodology and Results

Method. A reproducible benchmarking protocol spanning accuracy, latency, throughput, energy, and thermals; a side-by-side comparison of Zero W2, Pi 4, and Pi 5 under unified datasets and preprocessing; analysis of architectural bottlenecks and guidance for embedded practitioners.

Architecture. Compact backbone with depthwise separable convolutions, squeeze-and-expand style bottlenecks, and lightweight PAN-style neck; single-stage detection head (three scales).

Justification. The network is small enough for SBCs without NPUs yet representative of single-stage detection pipelines used in UAVs/IoT.

Dataset and evaluation inputs: Domain: everyday objects and common outdoor scenes representative of embedded/robotic perception.

Sources: COCO-lite subset (10 classes). Resolution: evaluation at 640×640 (letterboxed

Hardware platforms: Zero W2, Pi 4 (4 GB), Pi 5 (8 GB).

Device	Backend	Model	Input size, px	Fps	Latency, ms	Samples
Pi 4	onnx	YOLO8n	640	1.72	582.4	1500
Pi 5	onnx	YOLO8n	640	4.52	240.82	1500
Pi Zero W2	onnx	YOLO8n	640	0.7	1433.44	1500

Discussion and Limitations

Throughput scales with compute capability: MacBook Air M4, Raspberry Pi 5, Raspberry Pi 4, Raspberry Pi Zero W2. Pi 5 exhibits a significant uplift versus Pi 4, closing part of the gap to laptop-class performance while retaining embedded constraints. Pi Zero W2 remains suitable for low-FPS or event-driven workloads.

Bottlenecks on Pi-class devices include CPU saturation and memory bandwidth; latency remains high for 640×640. Thermal behaviour is device-specific: sustained loads on Pi boards may induce throttling without adequate cooling. Limitations of this study include its focus on a single input resolution and a single ONNX build, as well as the lack of consideration for INT8 quantisation or hardware accelerators (e.g., Coral TPU).

Optimisation recommendations: reduce input size (e.g., 416 or 320), apply post-training quantisation (INT8), and evaluate hardware offload (Coral TPU / Jetson). These steps typically improve FPS by 2–10× with a modest accuracy trade-off, depending on the dataset and model.

Future work. Extend to Coral USB / Hailo-8 accelerators on Pi 4/5; evaluate alternate nano-detectors (e.g., YOLOv8-n, YOLOv10-n); integrate hardware video capture latency; and explore vulkan/compute backends on Pi

References

[1] Z. Cao, L. Kooistra, W. Wang, L. Guo, and J. Valente, “Real-Time Object Detection Based on UAV Remote Sensing: A Systematic Literature Review,” Drones, vol. 7, no. 10, p. 620, Oct. 3, 2023.

[2] A. Ramachandran and A. K. Sangaiah, “A review on object detection in unmanned aerial vehicle surveillance,” International Journal of Cognitive Computing in Engineering, vol. 2, pp. 215–228, 2021.

CLASS-AWARE POLYP SEGMENTATION IN COLON IMAGES WITH SEGFORMER MODELS

Volodymyr Matus*, Andriy Konovalov**
Taras Shevchenko National University of Kyiv,
Faculty of RadioPhysics, Electronics and Computer Systems, Kyiv 01601, Ukraine
e-mail: * volodymyrmatus@knu.ua, ** konam@knu.ua

This work updates the prior study of polyp binary segmentation [1] by reporting multiclass segmentation results on the BKAI-IGH NeoPolyp dataset [2] with 3 class labels (background, non-neoplastic polyp, neoplastic polyp). The segmentation model based on the SegFormer-B2 architecture showed the highest Dice coefficient values compared to other models presented in state-of-the-art studies.

Introduction

Class-aware polyp in colon images delineation is increasingly required in clinical workflows to separate non-neoplastic and neoplastic tissue. Whereas a prior report [1] focused on binary segmentation (polyp vs. background), in this work a three-class segmentation (non-neoplastic polyp vs neoplastic polyp vs. background) is adopted on the same dataset [2] to assess whether modern transformer-based models improve class discrimination without degrading overall mask quality.

Dataset

The BKAI-IGH-Neopolyp dataset [2] is a publicly available medical image segmentation dataset designed for the detection and delineation of polyps in images. It contains high-resolution RGB images and their corresponding ground truth masks, annotated by medical experts. The dataset features considerable variability in lighting conditions, camera angles, polyp shapes, and tissue textures. The three-class semantic segmentation models were built on the basis of the public part of the dataset consisting of 1000 images. All images were resized to a fixed resolution of 1024×1024 pixels for uniformity and compatibility with neural network architectures. The dataset was randomly split into training (900 examples) and validation (100 examples) subsets which were used to train the model and fit hyperparameters.

Model training and evaluation

The SegFormer-B2 model [3], pretrained on images of 1024×1024 pixels from the Cityscapes dataset, was used to perform three-class segmentation with the TensorFlow library. Fine-tuning was carried out using the AdamW optimizer with an adaptive learning rate schedule starting at 0.0001 and the early stopping method. Various data augmentation techniques, including random flips, zooms, translations, and rotations, were applied to improve model generalization, and an auto-contrast adjustment was applied to all input images. Training and augmentation parameters were selected based on performance on the validation subset. Model training and inference were conducted on two NVIDIA T4 GPUs with 16 GB of memory each. The high input resolution limited the batch size to 2. Model evaluation was based on the Dice coefficient, which was automatically computed by the Kaggle platform on a closed test set of 200 images [4].

Results

Fig. 1 shows the segmentation results of three images from the validation subset of the trained model as an example. It can be seen that, in general, the model segments non-neoplastic and neoplastic polyps qualitatively. The Dice coefficient value on the test sample reached 84.93%. Fig. 2 shows a comparative bar chart of the Dice coefficient values for SegFormer-B2 model trained by us and other modern models by different authors that perform three-class segmentation of BKAI-IGH-Neopolyp dataset images [5-7]. It can be seen that the Dice coefficient of model presented in this work exceeds the highest Dice coefficient value of other models by at least 5%.

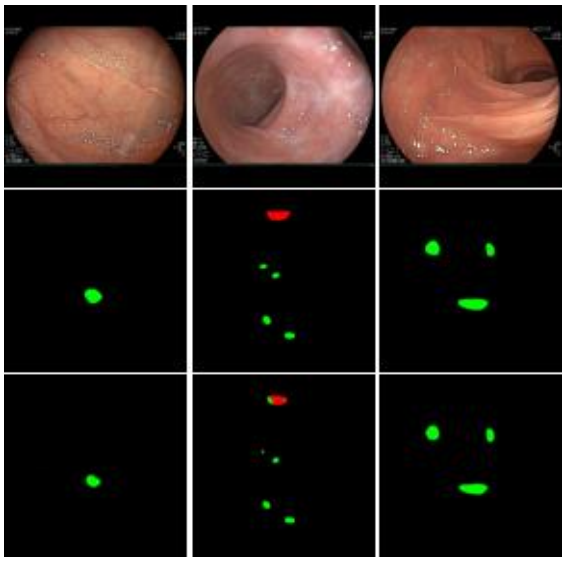

Fig. 1. Examples of input images, ground truth masks and predicted masks by the SegFormer-B2 model.

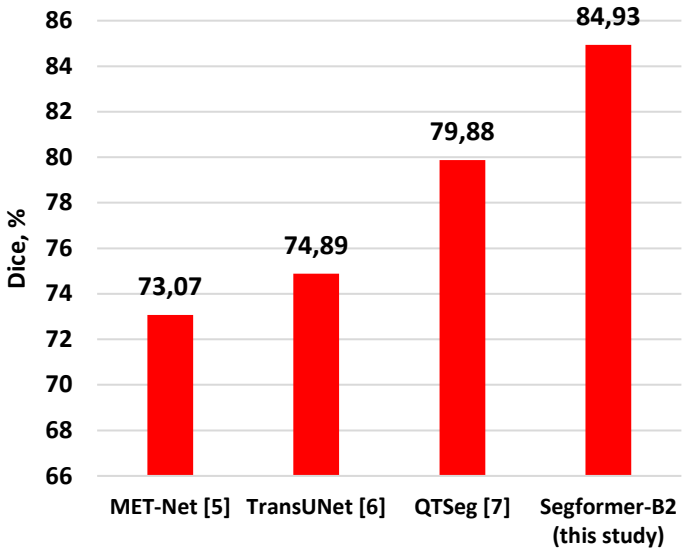

Fig. 2. Dice coefficient values of the SegFormer-B2 model trained in this study and the models [5-7] presented in 2024.

Conclusion

Multiclass polyp segmentation on the BKAI-IGH NeoPolyp dataset with the SegFormer-B2 model was demonstrated. The segmentation model showed the highest Dice coefficient values compared to other models presented in state of art studies and outperformed other three-class segmentation approaches by at least 5 percentage points.

References

[1] V. Matus and A. Konovalov, "DeepLabV3+ Architectures for Polyp Segmentation in Colon Medical Images," in Proc. *XXV Int. Young Scientists Conf. on Applied Physics*, Kyiv, Ukraine, May 20–23, 2025, pp. 155–156.

[2] P. Ngoc Lan et al., "NeoUNet: Towards Accurate Colon Polyp Segmentation and Neoplasm Detection," in Advances in Visual Computing, vol. 13018, G. Bebis, V. Athitsos, T. Yan, M. Lau, F. Li, C. Shi, X. Yuan, C. Mousas, and G. Bruder, Eds., Cham: Springer International Publishing, 2021, pp. 15–28. doi: 10.1007/978-3-030-90436-4_2.

[3] E. Xie, W. Wang, Z. Yu, A. Anandkumar, J. Alvarez, and P. Luo, "SegFormer: Simple and Efficient Design for Semantic Segmentation with Transformers," in Advances in Neural Information Processing Systems, vol. 34, 2021, pp. 12077–12090. doi: 10.48550/arXiv.2105.15203

[4] D. Sang, "BKAI-IGH NeoPolyp," *Kaggle*, 2021. [Online]. Available: https://www.kaggle.com/competitions/bkai-igh-neopolyp (accessed Oct. 13, 2025).

[5] D. Tan, R. Hao, X. Zhou, J. Xia, Y. Su, and C. Zheng, "A Novel Skip-Connection Strategy by Fusing Spatial and Channel Wise Features for Multi-Region Medical Image Segmentation," IEEE J. Biomed. Health Inform., vol. 28, no. 9, pp. 5396–5409, Sep. 2024, doi: 10.1109/JBHI.2024.3406786.

[6] A. Iqbal and M. Sharif, "Memory-efficient transformer network with feature fusion for breast tumor segmentation and classification task," Engineering Applications of Artificial Intelligence, vol. 127, p. 107292, Jan. 2024, doi: 10.1016/j.engappai.2023.107292.

[7] P.-N. Tran, N. T. Pham, D. N. M. Dang, E.-N. Huh, and C. S. Hong, "QTSeg: A Query Token Based Dual-Mix Attention Framework with Multi-Level Feature Distribution for Medical Image Segmentation," 2024, arXiv:2412.17241v1.

COMPARATIVE ANALYSIS OF EDGE-COMPUTE COMPANION COMPUTERS FOR ON-BOARD VISION IN AUTONOMOUS UAVS

Oleksandr Shevchenko
Faculty of RadioPhysics, Electronics and Computer Systems Taras Shevchenko National University of Kyiv, Kyiv 01601, Ukraine, e-mail: oleksandr.shevchenko.ua@gmail.com

This paper presents a focused comparison of compact companion computers for on-board visual perception and route planning in small autonomous aircraft under strict limits on latency, energy, and integration effort. Was defined selection criteria that prioritise throughput per unit of power, maturity of the camera pipeline, robustness of the software toolchain, and the risks associated with input–output, power delivery, and thermal design. Using documentation and deployment experience, was outlined a simple weighting method that ranks candidates before measurements are available and can later be replaced by latency, energy, and calibration results as prototypes mature. The review finds that readiness for time-critical perception and deterministic control depends more on drivers and tooling than on nominal arithmetic performance. As result, recommendation is selecting a primary platform with a proven imaging stack and configurable power modes, retaining a cost-effective alternative for constrained budgets, and validating the choice with end-to-end tests before field deployment.

Introduction

Scope was restricted to on-board perception and route planning with deterministic behaviour and approximately 20–30 frames per second. Companion computers are evaluated as the main compute element alongside flight controllers. On-device processing reduces radio delays and preserves data privacy. The camera link used across embedded stacks is the high-speed CSI-2 interface, widely adopted for sensors and supported on common platforms [8]. A qualitative platform comparison is summarised in Table 1 (see Table 1). Graphics-accelerated modules provide an official software stack (JetPack) that integrates drivers, toolchains and sample pipelines; the DeepStream plug-in “gst-nvinfer” performs pre-processing and dispatches inference to the TensorRT runtime [1]-[3]. Systems-on-chip with integrated neural processors rely on the RKNN-Toolkit2 for model conversion, inference and runtime APIs, operator support improves across releases and should be verified per model [4]. Single-board computers with external accelerators benefit from the Raspberry Pi camera stack (libcamera / rpicam-apps) [5]. Representative accelerators include a 4-TOPS USB device at about 2 W [6] and an M.2 module based on a 26-TOPS processor with typical power near 2.5 W [7]. A concise comparison follows in Table 1.

Evaluation criteria

Performance per watt for mobile-class vision models at 20–30 FPS; camera I/O maturity (CSI-2 lanes, driver stability, reference sensors) [5], [8]; SDK/toolchain robustness with maintained examples and export paths [1]-[4]; and integration risks (PCIe/USB topology, power delivery and thermal margins) informed by accelerator datasheets [6], [7].

Method

Was adopted a simple additive weighting scheme [9]. The main steps were to choose normalised weights over criteria with the sum equal to one, assign ordinal scores from public documentation and integration maturity, and compute a total to rank platforms prior to measurements (see Table 2). As shown in in Figure 1. The workflow begins from mission constraints, converts them into normalised weights, applies documentation-based scores, and computes the SAW total S to produce a shortlist for prototyping. This clarifies how Table 1 (qualitative facts) feed into Table 2 (weighted ranking).

Results

As shown on Table 1, graphics-accelerated modules offer the lowest integration risk due to mature SDKs and camera pipelines [1]-[3]; integrated-NPU SoCs are cost-effective but require careful validation of operator coverage and camera bring-up [4]; single-board computers with external accelerators are attractive for low bill-of-materials but demand additional work on buses, power and cooling [5]-[7]. The subsequent entries in Table 1 reflect these trade-offs (see Table 1).

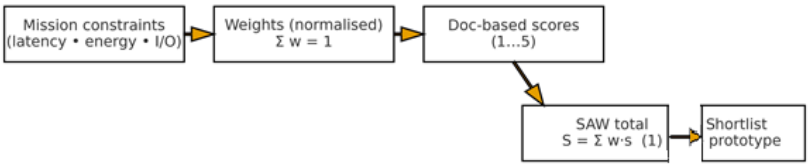

Fig. 1. Selection workflow from qualitative criteria to prototype shortlisting (SAW)

Table 1: Comparative analysis of candidate platforms (qualitative).

Platform	ML acceleration	Camera I/O	Energy profile	SDK/Ecosystem	Comment
Jetson family (Orin class)	GPU + runtime [3]	CSI-2; SDK camera pipelines [1], [2]	Configurable power modes [1]	JetPack, DeepStream, TensorRT [1]-[3]	Lowest integration risk
RK3588 boards (Orange Pi 5)	Integrated NPU (RKNN) [4]	CSI-2 (board-dependent)	Low–medium	RKNN Toolkit2 / Runtime [4]	Cost-effective; validate coverage
Raspberry Pi 5 + USB accelerator	Edge device 4 TOPS [6]	CSI-2; libcamera [5]	Low	libcamera stack [5]	Low BOM; extra USB/power
Raspberry Pi 5 + M.2 accelerator	Up to 26 TOPS [7]	CSI-2; libcamera [5]	Low–medium	Vendor SDK	High TOPS/W; ensure cooling
Allwinner A20/A30 class	—	Limited	Very low	Mixed	Companion controller role

Weights emphasise SDK/camera maturity to reduce time-to-demo, while energy and cost capture field constraints. Scores are illustrative and must be replaced by p50/p90 latency and FPS/W once prototypes are measured. The ranking produced by (1) is summarised in Table 2 (see Table 2).

References

[1] NVIDIA, “JetPack Software for Jetson,” https://developer.nvidia.com/embedded/jetpack, accessed Oct. 2025.
[2] NVIDIA, “Gst-nvinfer — DeepStream documentation,” https://docs.nvidia.com/metropolis/deepstream/dev-guide/text/DS_plugin_gst-nvinfer.html, accessed Oct. 2025.
[3] NVIDIA, “TensorRT Documentation (Overview/Quick Start),” https://docs.nvidia.com/deeplearning/tensorrt/latest, accessed Oct. 2025.
[4] Rockchip, “RKNN-Toolkit2,” https://github.com/rockchip-linux/rknn-toolkit2, accessed Oct. 2025.
[5] Raspberry Pi, “Camera software (libcamera / rpicam-apps),” https://www.raspberrypi.com/documentation/computers/camera_software.html, accessed Oct. 2025.
[6] Coral, “USB Accelerator” https://coral.ai/static/files/Coral-USB-Accelerator-datasheet.pdf, accessed Oct. 2025.
[7] Hailo, “Hailo-8” https://hailo.ai/products/ai-accelerators/hailo-8-ai-accelerator/, accessed Oct. 2025.
[8] MIPI Alliance, “Camera Serial Interface 2 (CSI-2),” https://www.mipi.org/specifications/csi-2, accessed Oct. 2025.
[9] I. Kaliszewski and P. Podkopaev, “Simple additive weighting—A metamodel for multiple criteria decision analysis methods,” Expert Systems with Applications, vol. 54, pp. 155–161, 2016.

QUANTUM-RESISTANT SD-WAN: IMPLEMENTING POST-QUANTUM CRYPTOGRAPHIC SOLUTIONS IN ENTERPRISE NETWORKS

V.A. Marianovskyi*, E.A. Korinnyi**
**Taras Shevchenko National University of Kyiv, Ukraine, Kyiv, e-mail: vitalik_m@univ.kiev.ua*
***Taras Shevchenko National University of Kyiv, Ukraine, Kyiv, e-mail: eduard.korennyi@knu.ua*

The emergence of quantum computing poses fundamental threats to current cryptographic systems protecting enterprise SD-WAN deployments. This article examines the integration of post-quantum cryptographic algorithms into SD-WAN architectures, focusing on key exchange protocol transitions and practical implementation challenges facing network engineers.

Keywords: Software-Defined Wide Area Network (SD-WAN), Post-Quantum Cryptography (PQC), Key Exchange, NIST algorithms, quantum resistance.

Introduction

Software-Defined Wide Area Networks (SD-WAN) rely on asymmetric cryptography for IPsec tunnel establishment and control plane authentication. Current RSA and Diffie-Hellman implementations face vulnerabilities from Shor's quantum algorithm, while Grover's algorithm reduces symmetric key security by half [1]. The "harvest now, decrypt later" (HNDL) attack vector creates immediate risks despite quantum computers not yet reaching cryptanalytically relevant capabilities [2].

National Institute of Standards and Technology (NIST) finalized post-quantum standards in 2024, specifying Module-Lattice Key Encapsulation Mechanism (ML-KEM) for key encapsulation, Module-Lattice Digital Signature Algorithm (ML-DSA) for digital signatures, and Stateless Hash-Based Digital Signature Algorithm (SLH-DSA) for hash-based signatures [3]. The U.S. National Security Agency (NSA) in its Commercial National Security Algorithm Suite 2.0 (CNSA 2.0) document establishes a mandatory requirement for the implementation of post-quantum algorithms for all national security systems by 2030. At the same time, for network infrastructure (including SD-WAN), it is recommended to begin implementation as early as 2025-2026 [4].

Key Exchange Protocol Modifications

Traditional SD-WAN deployments use IKEv2 with Diffie-Hellman groups for key establishment. Two primary quantum-resistant approaches exist:

RFC 8784 Implementation: Defines mixing post-quantum pre-shared keys (PPK) with classical Diffie-Hellman exchanges [5]. The security model combines three elements through key derivation: classical shared secret, post-quantum PPK, and authentication credentials. For SD-WAN environments spanning hundreds of sites, this creates key management complexity for full-mesh topologies or for hub-and-spoke architectures.

RFC 9370 Hybrid Approach: Implements ML-KEM alongside classical methods within IKEv2 itself [6]. This specification performs simultaneous classical elliptic curve and ML-KEM-768/1024 exchanges. The combined shared secret provides security if either algorithm remains unbroken, but requires protocol stack modifications in heterogeneous vendor environments.

Performance and Bandwidth Implications

Post-quantum algorithms introduce overhead disproportionately affecting SD-WAN deployments. ML-KEM-1024 generates 1,568-byte public keys and ciphertexts versus 256 bytes for classical Diffie-Hellman Group 14. This increase approaches path MTU limits on cellular and satellite links common in SD-WAN scenarios.

ML-DSA-87 signatures reach approximately 4,627 bytes compared to 256 bytes for ECDSA P-256. This impacts certificate-based authentication for both control and data plane connections, particularly affecting

certificate distribution and revocation operations. SD-WAN controllers managing thousands of concurrent tunnel establishments may experience aggregate computational impact during network convergence events.

Implementation Strategies

Hybrid Cryptographic Approach: Industry consensus supports combining classical and post-quantum algorithms. This provides security if either component remains unbroken while enabling gradual rollout through phased introduction. SD-WAN fabrics can initially deploy RFC 8784 PPK mixing at strategic sites while maintaining classical exchange elsewhere, progressively expanding coverage as operational experience accumulates.

Key Management Architecture: The Secure Key Integration Protocol (SKIP) enables SD-WAN devices to retrieve quantum-resistant keys from centralized or distributed infrastructure through standardized APIs [7]. SKIP facilitates automated Post-Quantum Pre-Shared Key (PPK) distribution and rotation for RFC 8784 implementations, supporting both pull and push models. Integration between SD-WAN orchestration and SKIP-compliant key management enables policy-driven allocation based on tunnel classification or compliance requirements.

Alternative architectures embed post-quantum key generation directly within network devices or controllers, eliminating external dependencies while trading increased device complexity for reduced operational overhead.

Conclusion

Post-quantum cryptography migration in SD-WAN solutions requires handling changes to key exchange protocols, performance and bandwidth effects, and key management architecture.

The model constructed here provides core considerations, but end-to-end deployment strategies for the production must be tested empirically through pilot trials over the long term and real-world performance benchmarking. Optimization of performance in various network conditions, hardware acceleration requirements, most crucial lifecycle management across hybrid environments, interoperability testing across heterogeneous vendor environments, and security analysis of hybrid mode vulnerabilities are future research directions.

References

[1] Mosca, M. (2018). Cybersecurity in an Era with Quantum Computers: Will We Be Ready? IEEE Security & Privacy. https://eprint.iacr.org/2015/1075.pdf

[2] National Institute of Standards and Technology (NIST). (2024). Post-Quantum Cryptography: FIPS 203, 204, and 205. https://csrc.nist.gov/projects/post-quantum-cryptography

[3] Alagic, G., et al. (2022). Status Report on the Third Round of the NIST Post-Quantum Cryptography Standardization Process. NIST Interagency Report 8413. https://doi.org/10.6028/NIST.IR.8413

[4] National Security Agency (NSA). (2022). Commercial National Security Algorithm Suite 2.0 (CNSA 2.0). https://media.defense.gov/2022/Sep/07/2003071836/-1/-1/1/CSI_CNSA_2.0_FAQ_.PDF

[5] Fluhrer, S., et al. (2021). Mixing Preshared Keys in the Internet Key Exchange Protocol Version 2 (IKEv2). RFC 8784. https://datatracker.ietf.org/doc/rfc8784/

[6] Kampanakis, P., et al. (2023). Post-quantum Hybrid Key Exchange in IKEv2. RFC 9370. https://data-tracker.ietf.org/doc/rfc9370/

[7] Hill, C., & Benhase, A. (2024). Introduction to Quantum Safe Cryptography… And Why You Need it. https://www.ciscolive.com/c/dam/r/ciscolive/global-event/docs/2025/pdf/BRKSEC-2175.pdf

CYBERSECURITY IN NETWORKS

Mankovskyi Dmytro
Faculty of RadioPhysics, Electronics and Computer Systems, Taras Shevchenko National University of Kyiv, Kyiv 01601, Ukraine, e-mail: dimamankovskyi@knu.ua

There are a huge number of cyberattacks in the world, and their strength is constantly increasing. The main reason is network settings that allow malicious software elements to enter the network and cause damage to the system. Therefore, network security is key in this situation.

Introduction

Network security is a comprehensive set of measures and technologies designed to protect network infrastructure, data, and devices from a wide range of threats. Most cyberattacks occur through the Internet, including scams, phishing, and unauthorized access, which makes network security a critical line of defense. Its main goal is to minimize these risks and ensure the integrity, confidentiality, and availability of information. It is important to understand that no network environment can ever be made completely secure, as attackers continuously adapt and develop techniques to bypass new security systems.

Types of threats

Unauthorized access is a threat, when an attacker gains access to a network, system, or data without permission. This can lead to theft, manipulation, or destruction of sensitive information.

Data compromise occurs when confidential or sensitive data is exposed, stolen, or accessed by unauthorized individuals. This can result in financial loss, reputational damage, or legal consequences.

Phishing links are types of malicious links sent via email, messaging apps, or social media that trick users into revealing personal information, login credentials, or installing malware.

Trojans are malicious programs disguised as legitimate software. Once executed, they can give attackers control over the infected system, steal data, or install additional malware.

DDoS attacks (Distributed Denial of Service attacks) are attempts to overwhelm a network, server, or website with excessive traffic, making it unavailable to legitimate users. These attacks disrupt business operations and can damage reputation. Fig. 1. shows main cyber threats in the networks.

Protecting tools

Firewalls are security systems that monitor and control incoming and outgoing network traffic based on predetermined rules. Firewalls act as a barrier between trusted internal networks and untrusted external networks, helping prevent unauthorized access.

Anti-malware software – Programs designed to detect, prevent, and remove malicious software such as viruses, worms, and trojans. They help protect systems from infection and minimize damage caused by malware.

Encryption is the process of converting data into a coded format to prevent unauthorized access. Encryption ensures that even if data is intercepted, it remains unreadable without the proper decryption key.

Intrusion Detection and Prevention Systems are tools that monitor network or system activities for malicious actions or policy violations. They can detect attacks in real time and, in some cases, automatically block or mitigate them.

Artificial Intelligencetechnologies – enhance cybersecurity by analyzing large volumes of data, detecting anomalies, predicting potential threats, and automating responses to attacks more efficiently than traditional systems.

Role of AI

However, with the integration of advanced technologies, particularly artificial intelligence and machine learning, network security has become significantly more effective. AI can help detect anomalies, predict potential threats, and respond to attacks in real time, enhancing overall protection. As networks continue to grow in

complexity and cyber threats evolve, adopting a proactive, multi-layered approach to security remains essential for individuals and organizations alike. Artificial intelligence can provide advice and recommendations on the next steps to improve security, help detect cyberattacks on the network in their infancy, as well as analyze the situation in cyberspace and adjust the system's security strategy. As well as minimize the consequences of cyberattacks that have already occurred.

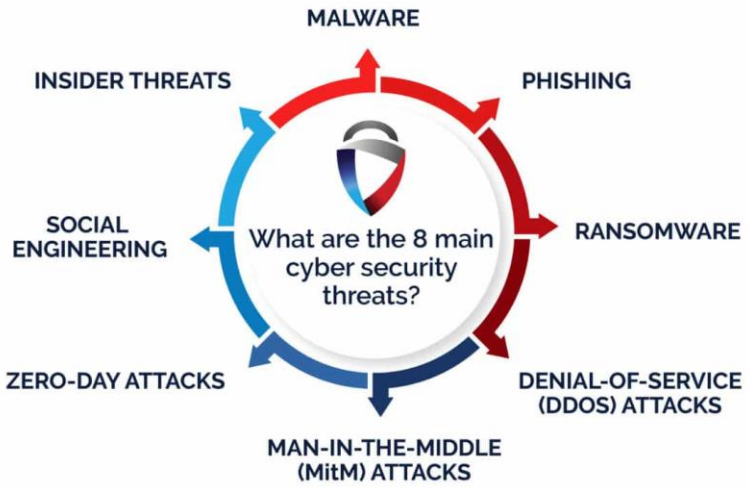

Fig. 1. Main cyber threats in the networks

Recommendations of improvement

Regularly updating software, operating systems, and applications to fix vulnerabilities and prevent attackers from exploiting known security flaws.

Continuously analyzing the cyber environment to detect potential threats, unusual activity, and emerging risks, allowing for timely response and mitigation.

Promoting caution and attentiveness among both everyday users and cybersecurity professionals to recognize suspicious activity, avoid risky behavior, and maintain a secure environment.

Using automated tools and AI-driven solutions to enhance the efficiency of security systems, reduce response times, and improve overall network protection.

Educating people who have little or no prior experience in cybersecurity on safe practices, password management, recognizing phishing attempts, and general online safety, helping to prevent human-related security breaches.

Conclusion

To sum up, network security is one of the most important, if not the most important niche of ensuring security in computer systems. Since most attacks come through the Internet, it is this area of protection that needs to be significantly strengthened. And here both basic security rules and cyber hygiene will come in handy, as well as more professional ones, such as the integration of artificial intelligence into such systems. And it is the tandem of simple and complex tools that can ensure the maximum possible security of networks.

References

[1] FortifyData, "What Are the 8 Main Cyber Security Threats?", FortifyData Blog. [Online]. Available: https://fortifydata.com/blog/what-are-the-8-main-cyber-security-threats/. [Accessed: Oct. 19, 2025].

RADIO ENGINEERING AND COMMUNICATIONS

IRRADIATION OF A TRANSIENT ELECTROMAGNETIC WAVE NEAR A DIELECTRIC MEDIUM

Havrylenko D.I.*, Dumin O.M., Berdnyk S.L.*****
Karazin Kharkiv National University of Ukraine, Kharkiv, Ukraine
School of Radiophysics, Biomedical Electronics and Computer Systems
**e-mail: dmytro.havrylenko@karazin.ua*
***e-mail: dumin@karazin.ua*
****e-mail: berdnik@karazin.ua*

The study of electromagnetic wave propagation in various media and their interaction with different materials has a long history and significant practical importance. For harmonic waves, such problems have been investigated in great detail. The situation becomes much more complicated in the case of pulsed waves, for which the traditional harmonic approach is no longer applicable. Meanwhile, pulsed fields are of great practical interest, with promising applications in radar systems, wireless sensor technologies, material testing, and medical diagnostics.

Statement of the problem

Let us consider a model radiator in the form of circular disk of a given radius and negligible thickness, positioned directly at the interface between two media. One medium is free half-space, while the other is an ideal dielectric with a prescribed positive permittivity. The disk generates a step-like current specified in cylindrical coordinates. Its center coincides with the origin of the coordinate system, and the longitudinal axis is directed downward into the dielectric. This current excites an H-wave that normally incident on the interface. The objective of the work is to analyze the behavior of the electromagnetic field after its interaction with the dielectric medium.

Solving of the problem

To analyze the transient process, we employ the method of evolutionary equations, adapted for open-structure problems such as antennas [1]. As a first step, the incident wave is considered. It is described by an inhomogeneous Klein-Gordon-type equation, whose solution provides the evolutionary determining the longitudinal magnetic component. This coefficient is obtained using the Riemann function method [1], [2], which serves as a fundamental solution for hyperbolic-type differential equations. In the present case, the corresponding Riemann function is represented by the zero-order Bessel function with an argument that involves the space-time distance. The evolutionary coefficients corresponding to the transverse electric and magnetic fields are derived by differentiating the obtained solution with respect to time and the longitudinal coordinate respectively. These expressions describe the wave dynamics in free half-space. The longitudinal electric field component is absent because by construction, since we deal with an H-wave.

Next, the reflected and transmitted (referred to as propagated in our notation) waves are analyzed. They are governed by homogeneous systems of evolutionary equations. The solutions are constructed via separation of variables with a hyperbolic substitution [3], leading to forms similar to the incident wave but, of course, modified by the physics of reflection and propagation. In general, the solutions appear as infinite series in Bessel and Neumann functions with weighting coefficients that account for temporal delays and advances, while the summation index ranges from minus to plus infinity. However, several constraints are imposed. First, the coefficients of the Neumann functions are set to zero due to the singular behavior of such cylindrical functions at the origin. Second, negative coefficients are discarded, since they would correspond to unphysical amplification of the wave. Their possible presence could hint at the emergence of surface modes, but because the radiator is located directly at the boundary, such modes do not have any time to form. Third, the zero-order coefficients are also set to zero in order to ensure natural faster attenuation of the longitudinal magnetic component.

The remaining unknown coefficients in these solutions are determined from the classical boundary conditions of electrodynamics, namely, the continuity of the tangential components of the electric and magnetic fields at the

interface. Substituting the modal expansions of the fields into these conditions, we project them onto the basis functions, followed by integration over the entire transverse cross-section of the infinite cylinder. This procedure yields continuity relations for the evolutionary coefficients that define the fields. Next, we substitute the evolutionary coefficients evaluated at the longitudinal coordinate corresponding to the boundary. At this stage, a difficulty arises: the coefficients should depend only on the spectral parameter and the physical constants, while the obtained equations still contain explicit time dependencies in the form of Bessel functions. To eliminate these dependencies, we proposed to apply the Hankel transform. This provides the orthogonality property of Bessel functions, which replaces temporal dependencies by delta-functions together with Kronecker symbols. The former is realized through integration over the spectral parameter, while the latter removes the infinite series present in the equations.

Thus, from the complicated equations of mathematical physics we reduce the problem to two systems of linear algebraic equations. The first system, corresponding to the even coefficients, yields trivial solutions [4]

$$B_{2k_r+2}^{m_r,ref}(\chi_r,\varepsilon)=0;\quad B_{2k_p+2}^{m_p,prop}(\chi_p,\varepsilon)=0;\quad k_r,k_p\geq 0,$$

which do not contribute to the wave process. The second system, associated with the odd coefficients, provides more interesting results. Together with the given coefficient describing the incident wave, they are given as follows [4]:

$$B^{m_i,inc}(\chi_i)=iA_0R\frac{\sqrt{\mu_0}}{2}\frac{J_1(\chi_iR)}{\chi_i\sqrt{\chi_i}}\left(\delta_{m_i,1}+\delta_{m_i,-1}\right);$$

$$\begin{cases} B_{2k_r+1}^{m_r,ref}(\chi_r,\varepsilon)=\dfrac{\sqrt{\varepsilon}-1}{\sqrt{\varepsilon}+1}iA_0R\dfrac{\sqrt{\mu_0}}{2}\dfrac{J_1(\chi_rR)}{\chi_r\sqrt{\chi_r}}\left(\delta_{m_r,1}+\delta_{m_r,-1}\right); \\ B_{2k_p+1}^{m_p,prop}(\chi_p,\varepsilon)=-\dfrac{2}{\sqrt{\varepsilon}+1}iA_0R\dfrac{\sqrt{\mu_0}}{2}\dfrac{J_1\left(\frac{v}{c}\chi_pR\right)}{\frac{v}{c}\chi_p\sqrt{\frac{v}{c}\chi_p}}\left(\delta_{m_p,1}+\delta_{m_p,-1}\right); \end{cases} \quad k_r,k_p\geq 0.$$

Inspection of the prefactors involving the dielectric permittivity reveals a clear analogy with the Fresnel formulas known from classical harmonic problems. However, in the present impulsive case, an important difference arises: while the reflection coefficient incorporates the material parameter only as an amplitude factor, the propagation coefficient contains it also in the spectral parameter (the denominator of last expression) and in the Bessel function argument. This indicates modifications in the profile of the impulsive wave after its passage into the dielectric.

Therefore, further investigations should include the dependence of the fields on spatial and temporal variables as well as on the dielectric permittivity, the associated energy characteristics, and possible extensions of the model to arbitrary incident pulses and to radiators placed at a finite distance from the boundary. For the present solution, the boundary conditions and the energy conservation law at the interface are satisfied, confirming the correctness of the obtained results.

References

[1] O.A. Tretyakov and A.N. Dumin, "Emission of Nonstationary Electromagnetic Fields by a Plane Radiator," *Telecommun. Radio Eng.*, vol. 54, no. 1, pp. 2–15, 2000. https://doi.org/10.1615/telecomradeng.v54.i1.10.

[2] R. Akhmedov, O. Dumin, and V. Katrich, "Impulse Radiation of Antenna with Circular Aperture," Telecommun. Radio Eng., vol. 77, no. 20, pp. 1767–1784, 2018. https://doi.org/10.1615/telecomradeng.v77.i20.10.

[3] W. Miller, *Symmetry and Separation of Variables*, Encyclopedia of Mathematics and its Applications, vol. 4. Reading, MA, USA: Addison-Wesley, 1977, 291 pp.

[4] D. Havrylenko, O. Dumin, S. Berdnyk, "*Exact Time-Domain Solution for Step-like H-Wave Radiation near a Dielectric Interface"*, in *Proc. IEEE 30th Int. Seminar/Workshop on Direct and Inverse Problems of Electromagnetic and Acoustic Wave Theory (DIPED)*, Sep. 2025, pp. 50–55 (in press).

STATE OF IONOSPHERIC RADIO PROPAGATION CHANNELS DURING GEOSPACE STORMS

L.F. Chernogor, V.O. Bessarabova
School of Radiophysics, Biomedical Electronics and Computer Systems,
V.N. Karazin Kharkiv National University, Kharkiv 61022, Ukraine, e-mail: Leonid.F.Chernogor@gmail.com

The state of space weather determines the conditions for radio wave propagation and the parameters of radio propagation channels. During geospace storms, changes in ionospheric parameters and changes in radio propagation channel properties are observed. For radio communication, radio astronomy, and oblique and vertical radio sounding of the ionosphere, the HF radio frequency range is used. The dependence between the minimum (maximum) usable frequency $f_{\mathrm{Min}UF}$ (f_{MUF}) and the ionosphere parameters should be taken into account. During the geomagnetic storms of May 10–11, 2024, and September 11–21, 2024, $f_{\mathrm{Min}UF}$ increased by 2–3 times, while f_{MUF}, on the contrary, decreased by 2–3 times. The blackout phenomenon was associated with the absorption of radio signals in the lower ionosphere. During X-class flares, $f_{\min}$ increased by ~4 times.

Introduction

The influence of high-energy processes on the ionosphere and ionospheric radio propagation channels has been studied for a long time. The Sun is a powerful source of energy. Solar storms are accompanied by coronal mass ejections (CME), bursts of electromagnetic and corpuscular radiations, and the generation of powerful streams of the solar wind [1, 2]. Upon reaching Earth, they cause geospace storms, which are an important factor in space weather. The state of space weather determines the conditions for radio wave propagation and the parameters of radio channels, and affects the functioning of telecommunication systems, radio navigation, and remote radio sounding of space from Earth and Earth from space. From time to time, solar processes cause severe and extreme geomagnetic storms. Among such storms are the geomagnetic storms of May 10–11, 2024 [3, 5] and September 11–21, 2024 [4]. Solar storms cause a change in the electron densities in the ionosphere. The electron densities, in turn, is closely related to the critical frequencies of the ionosphere. Solar flares ionize the atmosphere at the altitudes of the ionospheric D-region, which causes additional radio wave absorption and, as a result, blackouts. on the contrary, the electron densities in the ionospheric F-region can decrease or increase up to 10 times. A number of effects on radio propagation channel properties are associated with these effects.

Methods

Data of the F2 ionospheric layer critical frequency f_oF2, the F1 ionospheric layer critical frequency f_oF1, and the minimum observed frequency on ionograms $f_{\min}$ were obtained using the international global network of ionosondes GIRO (https://giro.uml.edu/index.html). Data from 17 stations across the Eastern and Western Hemispheres were analyzed. In the Eastern Hemisphere, data only from the Northern Hemisphere were analyzed, while in the Western Hemisphere, data from both hemispheres were analyzed. During geospace storms, significant variations are observed in the critical frequencies of the F2 layer f_oF2, the F1 layer f_oF1, the minimum observed frequency $f_{\min}$ and the phenomenon of blackout, which is the complete disappearance of reflections. The latter is associated with an increase in electron densities in the lower ionosphere by 1¬3 orders of magnitude, causing a significant increase in the radio signal absorption coefficient. Furthermore, the F1 layer critical frequency f_oF1 often becomes greater than the F2 layer critical frequency f_oF2. This effect is called the G condition. Another cause of blackout is a decrease in electron density by 10¬12 times, which leads to a decrease in f_oF2 by 3¬4 times. In this case, the situation $f_o\mathrm{F2} < f_{\min}$ may occur. Under such a condition, radio signals are completely absorbed in the lower ionosphere. For radio communication, radio astronomy, and oblique and vertical radio soundings of the ionosphere, the HF radio frequency range (3–30 MHz) is used. The properties of HF range radio signal propagation must be taken into account. Maximum Usable Frequency (MUF) f_{MUF} is closely related to the F2 layer critical frequency f_oF2 by the following relationship: $f_{MUF} = f_o\mathrm{F2}\sqrt{R_E/2z_r} \approx 3.2 f_o\mathrm{F2}$, where $R_E \approx 6400$ km is the Earth radius, and z_r is the height of radio wave reflection. In turn, the Minimum Usable Frequency $f_{\mathrm{Min}UF}$ is closely related to the $f_{\min}$ by the relationship: $f_{\mathrm{Min}UF} \approx 3 f_{\min}$.

Results

Extreme and very strong geomagnetic storms, according to the classification in [1, 2], were observed on May 10–11, 2024, and September 11–21, 2024. The storm of May 10–11, 2024, had a maximum K_p index of 9 [3], and the storm of September 11–21, 2024, had a K_p index that reached 7+ [4]. During the storm on May 11, 2024, primarily negative strong and very strong ionospheric storms were observed, and the I_{NIS} index reached ~8.43 dB. The value of the F2 layer critical frequency reached $f_oF2 \approx 2.5$ MHz, which is ~2.7 times less compared to the control day [3]. Thus, $f_{MUF} \approx 3.2 f_oF2 \approx 8$ MHz. During the May storm, the MUF decreased by 3 times. A blackout was observed on May 11 at the TR169 station (geomagnetic coordinates 19.20°,114.85°), which lasted ~50 hours. A possible reason for this effect is complete absorption in the lower ionosphere, as the condition $f_oF2 < f_{min}$ was met. On September 17, 2024, at some stations during the night, the I_{NIS} index reached ~8.97 dB, indicating the onset of a negative extremely strong ionospheric storm. The value of the F2 layer critical frequency reached $f_oF2 \approx 2.1$ MHz, which is ~3 times less compared to the control day [4]. Thus, $f_{MUF} \approx 3.2 f_oF2 \approx 6.7$ MHz. At the CAJ2M station (geomagnetic coordinates 45.00°,26.34°), located in the Western Hemisphere near the equatorial ionization anomaly, a strong ionospheric storm was observed on the same day with an I_{PIS} index of ~5.38 dB and $f_oF2 \approx 5.6$ MHz. In this case, the MUF increased by ~2 times and was equal to $f_{MUF} \approx 17.9$ MHz. During the storm on the night of September 16 to 17, 2024, a blackout occurred at the TR169 station, which lasted ~70 hours [4]. Since f_oF1 values were not recorded, a possible reason for this effect is the fulfillment of the condition $f_oF2 < f_{min}$. At the FF051 station (geomagnetic coordinates −2.50°,82.05°), the G condition phenomenon was observed, which lasted ~120 hours. Since the F1 layer critical frequency f_oF1 had a value of ~5 MHz, then according to the G condition, $f_oF2<5$ MHz. The minimum observed frequency f_{min} during the storm of September 11–21, 2024, increased by ~1.8 to 2 times. In this case, $f_{MinUF} \approx 16$ MHz. In addition, on September 13–16, 2024, X-class solar flares (X4.54 and X1.3) were observed, which caused the frequency f_{min} to increase by ~4 times [4]. This means that $f_{MinUF} \approx 24$ MHz.

Conclusions

Perturbations to the state of the ionospheric radio channel during extreme geomagnetic storms were studied using the examples of May 10–11, 2024, and September 11–21, 2024. The storms of May 10–11, 2024, were classified as extreme, and the storms of September 11–21, 2024, were classified as severe.

During the storms, a decrease in the MUF and an increase in the Minimum Usable Frequency by ~2 to 3 times were observed. The phenomenon of blackout occurred, which was caused by the complete absorption of radio signals in the lower ionosphere when $f_oF2<f_{min}$. Storms observed near the equatorial ionization anomaly led to an increase in the MUF by ~2 times. During X-class solar flares, f_{min} increased by ~4 times, which locally led to a blackout.

References

[1] Chernogor, L.F., Domnin, I.F., 2014. Physics of geospace storms. Kharkiv: V.N. Karazin Kharkiv National University Publ. https://doi.org/10.15407/knit2022.03.062.

[2] Chernogor, L.F., 2021. Physics of geospace storms. Space Science and Technology. 27, 3–77. https://doi.org/10.15407/knit2021.01.003.

[3] Chernogor, L.F., Bessarabova, V.O., 2025. Variations of ionospheric weather during geospace storm on May 10–11, 2024. Kinematics and Physics of Celestial Bodies. 41 (5), 209–220. https://doi.org/10.3103/S0884591325050022.

[4] Chernogor, L.F., Bessarabova, V.O., 2025. Global features of the multi-step ionospheric storm of September 11–21, 2024. Advances in Space Research. (In press).

[5] Pierrard V., Verhulst, T., Chevalier, J.-M., Bergeot, N., Winant, A., 2025. Effects of the geomagnetic superstorms of 10–11 May 2024 and 7–11 October 2024 on the ionosphere and plasmasphere. Atmosphere. 16 (3), 299. https://doi.org/10.3390/atmos16030299.

RADIOPHYSICAL EFFECTS OF MULTI-STEP IONOSPHERIC STORM

L.F. Chernogor, M.Yu. Tkachenko
V. N. Karazin Kharkiv National University, Ukraine, 61022, Kharkiv, Svobody Square, 4
e-mail: tkachenko.postgrad@gmail.com

The results of the analysis of spatiotemporal dependencies of the ionosphere and radio propagation channel caused by the multi-step magnetic storm on November 4-5, 2023, are presented. Significant disturbances in parameters describing radio propagation channel were determined and analyzed.

Introduction

Magnetic and ionospheric storms, regarded as components of the broader phenomenon of geospace storms, strongly affect the ionospheric radio propagation channel [1, 2]. Their influence is expressed through modifications of electron and ion densities, temperatures, and drift velocities in the ionosphere–thermosphere system, giving rise to irregularities, disturbances, and scintillations. Since amplitude and phase scintillations degrade the performance of communication, radar, satellite navigation, and radio astronomy, understanding their origin and developing mitigation strategies remains a major challenge.

While ionospheric scintillations have been studied for decades, the response of the coupled ionosphere–thermosphere system to multi-step geomagnetic storms (sequences of successive space weather disturbances) remains insufficiently explored. Such cascaded storms may trigger nonlinear effects, where weaker drivers cause more severe technological consequences than stronger ones. This study addresses this gap by examining the 4–5 November 2023 storm, which generated a multi-step ionospheric storm. Using solar wind and IMF parameters from OMNI, global and regional GNSS-based TEC and GEC data, ionospheric scintillation indices, and Swarm satellite observations, we conducted a multi-instrumental analysis. Although catalogued as two storms (G2 and G3), our results show that the disturbances formed consecutive phases of a single geospace storm.

The moderate disturbance on 4 November preconditioned the upper atmosphere by enhancing density (+45%) and turbulence, leading to strong scintillations ($S_4 > 0.6$) and GNSS signal loss in Northern Europe, despite weak geomagnetic activity (SYM-H ≈ −60 nT). By contrast, the stronger phase on 5 November (SYM-H ≈ −188 nT) caused a fourfold depletion of the thermospheric O/N_2 ratio in the Southern Hemisphere, producing a prolonged negative TEC phase but fewer scintillation impacts.

Comparison with storms in March 2015, March 2023, and May 2024 highlights the cascade nature of this event, in which electrodynamic drivers (PPEF, DDEF, **E×B** drifts were followed by composition-driven processes. A novel finding is that the 4 November disturbance acted as a “thermal preconditioning” stage, amplifying the subsequent response. The results further demonstrate that relatively weak forcing may generate severe GNSS disruptions, while stronger forcing can predominantly trigger composition-driven changes with less impact on radio propagation.

This paradox underscores the key role of thermospheric composition (O/N_2 ratio) and neutral winds in storm-time ionospheric dynamics. The study also confirms that geomagnetic indices alone are inadequate for predicting storm impacts, emphasizing the need for multiparametric monitoring frameworks integrating GNSS networks, LEO satellites, ionosondes, and optical instruments.

These findings improve understanding of ionosphere–thermosphere coupling during geomagnetic storms and contribute to the development of refined space weather forecasting approaches to enhance the resilience of navigation and communication systems.

Data and Methods

To investigate the multi-step geomagnetic storm of 4–5 November 2023, we analyzed a comprehensive dataset describing the coupled Sun–interplanetary medium–magnetosphere–ionosphere–atmosphere–Earth (SIMIAE) system. The study interval (2–8 November 2023) included two quiet days, two storm days, and two recovery days, with all data obtained from open sources.

Solar wind and IMF parameters (density, temperature, velocity, pressure, *By*, *Bz*) and geomagnetic indices (*Kp*, *Dst*) were taken from OmniWeb, with the Akasofu parameter calculated to estimate solar wind energy input

(1-h resolution) [3,4]. Global ionospheric and scintillation maps (S4, σ_φ; 5-min resolution) were retrieved from Madrigal [5]. Ground-based GNSS data from IGS stations provided 1-min TEC series, while Global Electron Content (GEC) from global TEC data characterized the overall ionosphere (15-min resolution).

ESA Swarm satellite measurements supplied additional parameters: TEC along orbits, electron density/temperature, thermospheric density, Rate of Density Change (ROD), Ionospheric Plasma Irregularities Index (IPIR), and equatorial electrojet characteristics—enabling spatiotemporal analysis of ionosphere–thermosphere coupling. Although scintillation indices were available only for 5–6 November, the combined use of interplanetary, GNSS, GEC, and satellite datasets allowed a multi-layered reconstruction of the storm's evolution and its comparison with similar events in recent years.

Results

The event's SYM-H and IMF Bz/Ey evolution confirms a cascade-like, multi-step main phase rather than two separate storms [6, 7]. We synthesize: (i) OMNI solar wind/IMF and *Kp/Dst*, (ii) global/ground GNSS TEC (including band-pass filtered 30–180 min components), GEC, and global scintillation maps (S_4, σ_φ), and (iii) Swarm electron density/temperature, along-track TEC, IPIR, ROD, and EEJ.

The main radiophysical effects of this multi-step ionospheric storm include: (a) Electrodynamic uplift and **E×B** transport (positive phase, 4 November). Prompt-penetration electric fields (PPEFs) and disturbance dynamo electric fields (DDEFs) enhanced the equatorial fountain, producing daytime TEC increases and poleward expansion of the EIA crests. (b) Strong scintillation and integrity outages under moderate geomagnetic forcing. Enhanced uplift steepened plasma gradients, favoring instabilities and generating multi-scale irregularities. (c) Large-scale traveling ionospheric disturbances with 30–180 min periods and ±5 TECU amplitude. (d) Thermospheric heating and turbulence with ~45% density increase. (e) Composition-driven negative phase (5 November) with fourfold O/N_2 decrease and deep TEC depression. (f) Equatorial electrodynamics showing intensified EEJ and CEJ perturbations.

Also we conclude that the 4 November stage preconditioned the system thermally and dynamically without strong O/N_2 depletion, favoring scintillation impacts. On 5 November, stronger forcing shifted control to composition, producing a negative storm with depressed TEC/GEC but fewer scintillations.

Compared with St. Patrick's Day 2015, March 2023, and the May 2024 superstorm, the November 2023 event is distinguished by cascade sequencing: electrodynamic uplift and scintillation first, then compositionally driven depletion. It was clearly shown that the operational risk assessments must augment *Dst*/SYM-H with multi-parameter nowcasts (LEO composition/density, IPIR/ROD, EIA morphology, GNSS scintillation maps). Sequencing and preconditioning history should be explicit in forecast models.

References

[1] L.F. Chernogor, A two-step geospace storm as a new tool of opportunity for experimentally estimating the threshold condition for the formation of a substorm current wedge, Ann. Geophys., vol. 43, pp. 15–35, 2025. https://doi.org/10.5194/angeo-43-15-2025.

[2] L.F. Chernogor, "Energetics of physical processes operated on May 8–12, 2024: from the solar storm to lithospheric disturbances. Adv. Space Res. https://doi.org/10.1016/j.asr.2024.12.069

[3] S.I. Akasofu, "Interplanetary energy flux associated with magnetospheric substorms," Planet. Space Sci., vol. 27, pp. 425–431, 1979. https://doi.org/10.1016/0032-0633(79)90119-3

[4] S.I. Akasofu, "Energy coupling between the solar wind and the magnetosphere," Space Sci. Rev., vol. 28, pp. 121–190, 1981. https://doi.org/10.1007/BF00218810

[5] M.A. Adil, T. Hadas, H. Yang, M. Hernandez-Pajares, "Quality assessment of the real-time global ionospheric maps following varying solar dynamics and a severe geomagnetic storm," GPS Solutions, vol. 29(1), pp. 1–16, 2025. https://doi.org/10.1007/s10291-024-01811-7

[6] I.G. Richardson, J. Zhang, "Multiple-step geomagnetic storms and their interplanetary drivers," J. Geophys. Res., vol. 113, A00A08, 2008. https://doi.org/10.1029/2007GL032025

[7] E. Agyei-Yeboah, P.R. Fagundes, A. Tardelli, V. Pillat, F.J.A. Vieira, M.J.A. Bolzan, "Global ionospheric response to a G2 and a G3 geomagnetic storms of November 4 and 5 2023," Adv. Space Res., vol. 75, pp. 5580–5602, 2025. https://doi.org/10.1016/j.asr.2025.01.046

TOOLKIT FOR MEDICAL TELECONSULTATION SYSTEM BASED ON WEB INTERFACE

M. Kononov *, V. Kononov **, G. Zhyrov***
Taras Shevchenko National University of Kyiv, Volodymyrska str.,64/13,
** e-mail:* m_v_k@univ.kiev.ua
*** e-mail:* viktor1998kononov@gmail.com
**** e-mail:* genna-g@ukr.net

Web architecture is convenient for implementing a resource for medical teleconsultations. However, to ensure high efficiency of consultations with maximum possible server-side data processing, certain implementation issues arise, especially considering the specific nature of medical data formats. It is also necessary to take into account the need to synchronize displayed data among session participants, to document all used data, and to provide means for their subsequent verification.

Features of a web-based telemedical system

Medical teleconsultation relies on general methods of information exchange between participants [1]. In general, any form of telecommunication can be used. Moreover, it is desirable when implementing such a system to provide users with the ability to choose methods and devices from some predefined set. Such choice flexibility of communication means can only be provided by its client-server architecture, where backend processing is applied to narrowly specialized data, unsuitable for handling by software components commonly used for frontend — for instance, specific medical data, which are usually served by special formats and protocols. When using such an architecture, data transmitted to the client side must be converted into universal formats suitable for browser visualization. Due to this, arbitrary network communicators can be used as a device for participating in a consultation session. As an example, we can cite the implementation of access to DICOM images via a browser [2].

The most effective architecture for such distributed data processing is a web. On one hand, it enables all necessary preprocessing on the server, and on the other, it provides versatility across user devices and platforms. Therefore, we consider the web architecture as the basis for implementation, but with the addition of a specific auxiliary level of data processing on the server side [3]. Another advantage of web-based solutions is the ability to filter data before sending them to the client, thus ensuring the required level of information security, for example, through anonymization [4].

Requirements for the teleconsultation system toolkit

It is desirable that a teleconsultation resource should support both interactive and delayed consultations on a single platform. Interactive teleconsultation can be based on live communication via audio channels. Thus, arbitrary messengers or teleconferencing tools can be used. The main disadvantage in this case is the ability to work with specific medical information only through screen broadcast, which is accompanied by a noticeable loss of informativeness and limits the functionality of the consultation process. Documentation of such a session is possible only as a video recording. Although the speech form of communication is easier to use, audio recording is less effective, for example, for tasks of later searching for the necessary fragment. Delayed consultation is a time-extended sequence of transactions. In this case a communication is based on typing similar to using e-mail and messengers. Despite being asynchronous, such a form of consultation, like interactive, is a session with a defined beginning and an end. This allows provide the unification of telecommunications and information support and the use of common tools with the previously described mode.

The purpose of a consultation is to form by consultant certain conclusions and recommendations based on a pre-prepared request and additional information provided during the session. Therefore, a web resource for teleconsultations should support tools for integrating data into the request before the session begins. For this purpose, it is advisable to use the form selection and completion for simplification of operations by non-

professional users. At the same time, the system should support file uploading in arbitrary formats, which will then be processed by specialized software of the teleconsultation resource itself. It should be taken into account that a certain part of medical documents is provided as images, including scans of text documents. Therefore, both when forming a request and during the consultation process, it is necessary to support adding overlay labels to the document based on text and graphic objects (arrows, rectangles and contours). Such tool will ensure the binding of the text components of the request to a section of the document or diagnostic image. A similar tool for the consultant will simplify the answer formation.

Consultations are based on the formation of new information, for which the legal responsibility rests with the person who generates it, in most cases the consultant. The most important part of such information is the final block, which is the outcome of the consultation. While intermediate data blocks may or may not be documented, depending on system design, the final block must be strictly documented and protected against further unauthorized modification. For this purpose the digital signature or blockchain can be used. Such features of data processing must be included in the information storage formats and processing protocols implemented on the server.

Another important toolkit component for a teleconsultation resource is a data binding system, namely, a link-based and this links to different data blocks may be not strictly sequential. This is critical important for the delayed mode of consultation and synchronization of data playback on the screens of participants during an interactive session. It is also desirable to provide a toolkit for adding linking to a recording of speech communication or video recording, including timestamps. Implementing this requires the use of additional user actions or subsequent authorized editing, which complicates the internal structure of the data documentation subsystem.

Documentation of teleconsultation data

Therefore, for the web implementation of a medical teleconsultation resource, the basic library [3] should be based on support at the semantic level of including data blocks with the further expansion possibility, which is implemented by including to the data format of the reference to the decoding and playback method. A significant number of actions (transactions, creation and editing overlay labels, etc.) can be implemented in the form of sequential lists. Nonlinear relationships can be included as list elements containing the parameters of a link to arbitrary component of a given data stream, or external resource. Such format extension is sufficient both for request formation and session documenting.

The subsystem of overlay labels and synchronization must rely on preliminary client-side event processing, but final encoding into the recording stream should be performed by the functionality of this additional library, also in the form of list whose nodes correspond to significant events, primarily those creating or modifying graphic elements.

References

[1] Stoltzfus M., Kaur A., Chawla A. et al. The role of telemedicine in healthcare: an overview and update. The Egyptian Journal of Internal Medicine. 2023. Vol. 35, Article no. 49. 5 p. doi: 10.1186/s43162-023-00234-z.

[2] Pereira H., Romero L., Miguel Faria P. et al. Web-Based DICOM Viewers: A Survey and a Performance Classification. Journal of Imaging Informatics in Medicine. 2024. ID 39349783. 19 p. doi: 10.1007/s10278-024-01216-5.

[3] Data structuring for medical teleconsultation system Kononov V. Proceedings of the 25 International Young Scientists Conference on Applied Physics May, 20-23, 2025, Kyiv, Ukraine. p.103-104

[4] Mackenzie A., Lewis E., Loveland J. et al. Successes and challenges in extracting information from DICOM image databases for audit and research. British Journal of Radiology. 2023. Vol. 96. Issue 1151. ID 20230104. 9 p. doi: 10.1259/bjr.20230104

THE MULTI-STEP GEOMAGNETIC STORM OF NOVEMBER 4–7, 2023, AS A TOPIC OF APPLIED PHYSICS

L.F. Chernogor, M.Yu. Holub, V.T. Rozumenko
School of Radiophysics, Biomedical Electronics and Computer Systems,
V.N. Karazin Kharkiv National University, Kharkiv 61022, Ukraine e-mail: Leonid.F.Chernogor@gmail.com

Analysis of the state of space weather during the November 2–8, 2023, period has revealed that the storm of November 4–7, 2023, was a five-step geospace storm. The data collected at sixteen INTERMAGNET network magnetometer stations, arranged in certain meridional chains in the eastern and western hemispheres, have been used to study the energetics of the geospace, magnetospheric, and geomagnetic storms, as well as to analyze the energetics of the five constituent storms in detail.

Introduction

Until the middle of November 4, 2023, the solar wind proton number density, n_{sw}, do not exceed 5×10^6 m^{-3}. In the second half of November 4, 2023, and on November 5, 2023, n_{sw} become larger than 52×10^6 m^{-2} and 42×10^6 m^{-3}, respectively, i.e., show an increase by more than an order of magnitude. The greatest n_{sw} burst occur on November 4, 2023, two other on November 5, 2023, while a significantly weaker one is observed on November 6, 2023. The radial plasma flow speed V_{sw} fluctuate around 400 km/s until 08:00 UT on November 5, 2023, after which it increase, fluctuating gradually, up to 700–735 km/s at the end of November 8, 2023. The speed shows a sharp increase on November 5, 2023, and two increases on November 6, 2023. The solar wind plasma temperature T_{sw} do not exceed ~10^5 K until November 5, 2023, whereas it increases, fluctuating wildly, to (3–5) × 10^5 K during November 5–8, 2023. The temperature T_{sw} shows a maximum of $T_{sw} \approx 5.1 \times 10^5$ K on the night of November 6, 2023, and several bursts during the November 5 and 6, 2023, period. The dynamic pressure, p_{sw}, of the solar wind calculated for quiet time conditions do not exceed ~1nPa, while it increases to 11 nPa and 16 nPa on November 4 and 5, 2023, respectively, almost in synchronism with the density variations; from November 6 to 8, 2023, it is smaller than 5 nPa; and it also shows 5 individual bursts during November 4, 5 and 6, 2023. The components of the interplanetary magnetic field (IMF) do not exceed a few nano teslas from November 2, 2023, to the first half of November 4, 2023. The IMF variations exhibit the strongest variations on November 5, 2023, when B_y changed from –31.8 nT to 10.2 nT, and B_z show variations from –23.4 nT to 22.5 nT. Five B_z southward turnings are noticeable during November 4, 5, and 6, 2023. Under quiet conditions, Akasofu's epsilon parameter, ε_A, fluctuated around ~1 GJ/s, whereas five bursts altogether appear during November 5 and 6, 2023; the strongest bursts attained 716 GJ/s and 515 GJ/s, respectively. Prior to the middle of November 4, 2023, the K_p index vary in the range 0–2.3. In the second half of November 4, 2023, it significantly increases, with a maximum of 7.3 on November 5, 2023, and five increases altogether during November 4, 5, 6, and 7, 2023. The variability in the D_{st} index about a smooth curve is ±(10–15) nT until the middle of November 4, 2023. After an insignificant increase of 14 nT over the interval 12:00–16:00 UT on November 4, 2023, the D_{st} index shows the first sufficiently sharp decrease down to –62 nT. Following considerable fluctuations during the period 23:30 UT on November 4, 2023, to 14:00 UT on November 5, 2023, the D_{st} index shows the second, more significant, decrease from –50 nT to –172 nT when the main phase of the storm occurs. The recovery phase of the storm begins after 22:00 UT on November 5, 2023, and persist until November 8, 2023. A significant, multi-fold decrease in B_z and D_{st} and considerable increase in Acasofu's parameter and K_p indicates the multi-step geomagnetic storm onset. A major feature of the November 4–7, 2023, geospace and geomagnetic storms is multi-fold increases in the solar wind and geomagnetic field parameters. In total, five increases and the same number of decreases in the D_{st} index, that are associated with five maxima in the K_p index are identified, from which it follows that the geomagnetic storm of November 4–7, 2023, is a multi-step storm consisting of five storms of different intensity.

The purpose of this work is to study longitudinal and latitudinal manifestations of the November 4–7, 2023, multi-step geomagnetic storm and to make intercomparisons between this and other major geomagnetic storms.

Calculations of Energetics

Generally, the energetics of geospace storm is determined by the dynamic pressure, magnetic pressure, and kinetic pressure of the solar wind, with the dynamic pressure giving the major contribution. The geospace storm power and energy of the five geomagnetic storms of November 4–7, 2023, have been estimated. The magnetospheric storm is caused by the solar wind magnetic pressure, which power is governed by Akasofu's parameter, and the magnetospheric storm energy is determined by Akasofu's parameter maximum value. The estimates of the geomagnetic storms are based on the D_{st} index that is obtained from magnetometer stations near the equator at latitudes where the northward component of the magnetic perturbations is mainly due to the intensity of the magnetospheric ring current. The geospace storm energy is greater than the magnetospheric storm energy by a factor of hundreds to thousands, while the power of the geomagnetic and magnetospheric storms are comparable.

Geomagnetic Storm Sources and Mechanisms

Over the period November 4–7, 2023, five geomagnetic storms, varying in intensity, occurred. The first four storms were preceded by increases in the solar wind plasma density, n_{sw}, radial plasma flow speed V_{sw}, Akasofu's parameter, ε_A, and by the interplanetary magnetic field B_z component showing greater negative values. A turbulent region between the shock and the interplanetary coronal mass ejection (ICME), called the sheath region, is a region where n_{sw}, $|B_z|$ *and* V_{sw}, show large, sharp variations; the sheaths and ICMEs are the only interplanetary structures that can cause extreme geomagnetic storms [1]. Similar structures led to the two-step geospace storm of April 23–24, 2023 [2], and they caused the first four constituent storms of the November 4–7, 2023, multi-step geomagnetic storm. During the November 4, 2023, storm, the density n_{sw} increased from 5×10^6 m^{-3} to 60×10^6 m^{-3}, speed V_{sw} from ~200 km/s to 250 km/s, and the strength of the B_z component decreased from about 0 nT to –10 nT. During the two storms of November 5, 2023, the proton density n_{sw} increased from 10×10^6 m^{-3} to 55×10^6 m^{-3} and from ~20×10^6 m^{-3} to 65×10^6 m^{-3}, respectively, speed V_{sw} increased from 200 km/s to 400 km/s and from 400 km/s to 500 km/s, strength of the B_z component decreased from ~0 nT to –20 nT and from ~0 nT to –25 nT. The storm of November, 6 2023, was preceded by an increase in the density n_{sw} from ~5×10^6 m^{-3} to 20×10^6 m^{-3} and speed V_{sw} from ~0 nT to –10 nT over the interval 08:00 UT–16:00 UT. The source of the fifth storm, which occurred during the end of November 6, 2023, to the end of November 7, 2023, period, was a sharp increase in the solar wind speed from 400 km/s to 700 km, while the proton density varied in the range (1–5) $\times 10^6$ m^{-3}, and the B_z component strength varied from approximately 0 nT to –8 nT. The mechanism behind this storm was a high-speed solar wind flow.

Main Results

The energy of the dynamic pressure of the constituent storms attains 1.1 EJ, 0.34 EJ, 2.2 EJ, 0.63 EJ, 0.56 EJ, and their powers are close to 49 TW, 38 TW, 103 TW, 44 TW, and 26 TW. The energy of the disturbed interplanetary magnetic field is 0.9 PJ, 1.8 PJ, 8.2 PJ, 3.7 PJ, and 0.44 PJ, and the powers do not exceed 126 GJ/s, 502 GJ/s, 716 GJ/s, 515 GJ/s, and 100 GJ/s. The energy of the constituent geomagnetic storms is in the range 3.7 PJ, 4.7 PJ, 8.6 PJ, 1.6 PJ, and 1.3 PJ. The geomagnetic storms of November 4, 2023; November 5, 2023 (first storm), November 5, 2023 (major, second storm); November 6, 2023; and November 6–7, 2023, pertain to the storm classes G1 (minor), G2 (moderate), G3 (strong), G2 (moderate), and G1 (minor), respectively. The major storm of November 5, 2023, is significantly smaller in comparison with the storms of November 5, 2023; April 23–24, 2024; May 10–11, 2024, and particularly the super storm, by all parameters.

References

[1] E. Kilpua, H. E. J. Koskinen, and T. I. Pulkkinen, "Coronal mass ejections and their sheath regions in interplanetary space," Living Rev. Sol. Phys., vol. 14, article No. 5, pp. 1–83, Nov. 24, 2017. http://doi.org/10.1007/s41116-017-0009-6.

[2] L. F. Chernogor, "A two-step geospace storm as a new tool for experimentally estimating the threshold condition for the formation of a substorm current wedge," Annales Geophysicae, vol. 43, pp. 15–35, Jan. 06, 2025. https://doi.org/10.5194/angeo-43-15-2025.

SYSTEMATIC SPECTRAL ANALYSIS OF SOLAR WIND PARAMETERS

L.F. Chernogor*, D.R. Novytska*

** School of radiophysics, biomedical electronics and computer systems V.N. Karazin Kharkiv National University, e-mail: Leonid.F.Chernogor@gmail.com, daria.novytska@student.karazin.ua*

The dynamics of the main parameters of the solar wind and the interplanetary magnetic field were studied based on satellite observations during the extreme geospace storm of May 10–11, 2024. It was found that during the storm, there was a significant increase in the concentration, velocity, temperature, and dynamic pressure of solar wind particles, as well as a sharp enhancement in the variations of the interplanetary magnetic field components, which contributed to the development of intense disturbances in the Earth's magnetosphere. Systematic spectral analysis showed that the spectra of solar wind and interplanetary magnetic field parameters were dominated by components with periods of 150–190 minutes.

Introduction

Space weather determines the state of the near-Earth environment and can have a significant impact on technological systems such as satellite communications, radio navigation, power grids, and spacecraft. Sudden changes in space weather pose threats to astronauts as well as to satellite and ground-based systems. Solar activity— including solar flares, solar cosmic rays, and coronal mass ejections (CMEs)— is the main source of disturbances in interplanetary space that can cause global storms in the magnetosphere, ionosphere, atmosphere, lithosphere, and geophysical fields (magnetic, electric, baric, and thermal). Studying the impact of solar activity on the Earth–atmosphere–ionosphere–magnetosphere (EAIM) subsystems is a pressing challenge in modern science, as adverse space weather conditions can have serious consequences for ground- and space-based technologies [1–3]. A significant number of studies have been devoted to processes occurring during geospace storms and to variations in space weather parameters. The physical foundations of geospace storm development and the mechanisms of energy transfer from the solar wind to the magnetosphere and ionosphere are described in monograph [1]. For obvious reasons, the greatest attention is usually paid to unique storms. A remarkable event in the current 25th solar activity cycle was the extreme storm of May 10–11, 2024 [4–8]. For this storm, the energy balance of all subsystems in the EAIM system was calculated in detail [5]. It has been shown that the storm was not only geospace but also pan-planetary. Details of the solar and geomagnetic storms are described in [7]. The ionospheric effects were analyzed by the authors in [4], while long-term ionospheric responses were studied in [8]. The latitudinal features of the geomagnetic storm were examined in [6]. However, variations in the parameters of the solar wind and the interplanetary magnetic field have not yet been sufficiently investigated.

The purpose of this work is to analyze space weather conditions and perform a systematic spectral analysis (SSA) of solar wind parameters and the interplanetary magnetic field (IMF) during the extreme storm of May 10–11, 2024.

Methods

Data on space weather conditions for the period May 9–15, 2024, were obtained from the OMNIWeb database [https://omniweb.gsfc.nasa.gov/form/omni_min.html]. The analysis of variations involved calculating the trend in the source data, determining deviations from the trend, and applying band-pass filtering (BPF) and SSA methods. The time resolution for measurements of concentration, temperature, velocity, and the B_y and B_z IMF components was 1 s. Band-pass filtering was performed in the period range of 1–3 hours.

SSA consisted of the combined application of mutually complementary short-time Fourier, adaptive Fourier, and wavelet transforms [9]. The short-time Fourier transform provides superior time resolution, while the adaptive Fourier transform offers higher period resolution. The wavelet transform (also known as a “mathematical microscope”) is used to investigate the fine temporal structure of a signal.

Summary

1. During the extreme geospace storm of May 10–11, 2024, significant variations in the main parameters of the solar wind and interplanetary magnetic field were recorded, in particular a rapid increase in solar wind velocity from 300 km/s to 1026 km/s.

2. The concentration of solar wind particles increased to 60 cm^{-3}, and their temperature reached approximately 2.1×10^6 K. The main phase of the storm was accompanied by a 15–20-fold increase in the B_y and B_z components of the IMF compared with background values, indicating strong coupling processes between the Sun and the Earth's magnetosphere.

3. It was established that the spectral composition of the signals was dominated by quasi-periodic oscillations with periods of 150–190 minutes, reflecting the complex nature of processes during the storm and the presence of global structures in the solar wind.

4. Recurrent impulses (on May 12 and 14, 2024) were detected, which caused additional disturbances and confirmed the prolonged influence of the storm on space weather conditions.

5. The results of this study are important for understanding the mechanisms of intense geospace storms and can be used to improve the accuracy of space weather forecasting and to mitigate adverse effects on technological systems.

References

[1] Chernogor L.F., Domnin I.F. (2014). Physics of Geospace Storms: monograph. Kharkiv: V. N. Karazin Kharkiv National University, 408 p.

[2] Chernogor L.F. (2021). Physics of Geospace Storms. *Space Sci. Tech*. 27(1), 03—77. https://doi.org/10.15407/knit2021.01.003

[3] Chernogor L. F. (2025). What are a geospace storm and a pan-planetary storm? *Adv. Space Res*. 76(9), 5640–5657. https://doi.org/10.1016/j.asr.2025.08.016

[4] Astafyeva E., Maletckii B., Förster M., Ouar I.D., Huba J.D., Hairston M.R., Coley W.R. (2025). Electrodynamic and Ionospheric Puzzles of the 10–11 May 2024 Geomagnetic Superstorm. *J. Geophys. Res.: Space Physics*. 2025. 130(5). e2024JA033284. https://doi.org/10.1029/2024JA033284

[5] Chernogor L.F. (2025). Energetics of Physical Processes Operated on May 8–12, 2024: From the Solar Storm to Lithospheric Disturbances. *Adv. Space Res*. 75(6), 4825–4849. https://doi.org/10.1016/j.asr.2024.12.069

[6] Chernogor L.F., Rozumenko V.T., Shevelev M.B., Wang J., Zheng Y. (2025). Global geomagnetic response to the extreme geospace storm of May 10–11, 2024. *Adv. Space Res*. 76(2), 939 – 967. https://doi.org/10.1016/j.asr.2025.05.004

[7] Hayakawa, H., Ebihara, Y., Mishev, A., et al. (2024). The Solar and geomagnetic storms in May 2024: A Flash Data Report. Astrophys. J., 979(1), 49. https://doi.org/10.3847/1538-4357/ad9335.

[8] Usman Ahmad, Waqar Younas, Majid Khan, Abbasi M. M. (2025). Longitudinal Variations in the Ionospheric Disturbances: Insights From the May 2024 Super Storm. *J. Geophys. Res.: Space Physics*. V. 130(7). https://doi.org/10.1029/2025JA033981

[9] Chernogor L.F. (2008). Advanced methods of spectral analysis of quasiperiodic wave-like processes in the ionosphere: Specific features and experimental results. *Geomag. Aeron.* 48(5), 652 – 673. https://doi.org/10.1134/S0016793208050101

MULTIFACTOR ANALYSIS OF GEOSPACE STORMS AFFECTING ATMOSPHERIC–IONOSPHERIC–MAGNETOSPHERIC RADIO PROPAGATION CHANNELS

L.F. Chernogor, D.R. Kulyk
V.N. Karazin Kharkiv National University, Department of Space Radiophysics, Kharkiv, Svobody sq. 4,
leonid.f.chernogor@gmail.com, dmytro.kulyk@karazin.ua

The atmosphere, ionosphere, and magnetosphere form natural radio channels enabling the operation of radio navigation, telecommunication, radar, and Earth remote sensing systems. Their state and performance conditions are significantly influenced by space weather, particularly by geoeffective solar storms that generate a complex of disturbances in the electromagnetic, thermal, and plasma environments. This study presents a multifactor analysis of the geospace storm occurred on September 11–21, 2024, one of the most intense events of Solar Cycle 25. The proposed cross-analysis format integrates solar wind parameters, geomagnetic indices, and ground-based observations, enabling a systematic assessment of disturbances affecting the atmosphere–ionosphere–magnetosphere radio channels. It is demonstrated that the combination of southward-oriented IMF Bz and dynamic pressure pulses determines the geoeffectiveness of storms and induces fluctuations in electron concentration and phase shifts in GNSS, HF, and over-the-horizon communication systems. The proposed approach establishes a systemic basis for further research on the impact of geospace storms on radio engineering systems and contributes to improving the forecasting of extreme space weather manifestations.

Introduction

The atmosphere, ionosphere, and magnetosphere are in a constant dynamic state determined by space weather. The most powerful and systematic natural driver of such variability is solar storms, accompanied by bursts of electromagnetic and corpuscular radiation and coronal mass ejections (CMEs). These events trigger a cascade of processes within the Sun–interplanetary medium–magnetosphere–ionosphere–atmosphere–Earth (SIMMIAE) system, shaping geospace storms that affect all subsystems and influence the performance of radio engineering systems [1–4]. During intense storms, large-scale disturbances occur across all geospheres, including the magnetosphere, ionosphere, and atmosphere, leading to variations in electron density and ionospheric plasma distribution. These disturbances strongly influence the performance of radio channels: GNSS signals suffer from phase fluctuations leading to positioning errors; HF communication is affected by absorption and reflection height variability; radar and satellite communication links disrupt from signal fading and scintillations. Geomagnetic storms have been studied mainly in the context of magnetospheric or ionospheric processes. However, modern approaches require a systemic perspective treating solar wind disturbances, magnetospheric response, ionospheric dynamics, and atmospheric effects as parts of a single interconnected chain [3,4], which is essential for reliable forecasting of space weather impacts on radio communications.

Data and Methods

The analysis of the storm sequence occurred on September 11–21, 2024, was conducted using data on solar wind parameters, satellite measurements of IMF components, geomagnetic indices (SYM-H, ASY-H, PCN/PCS, SMR, Dst etc.), energy coupling parameters (Akasofu parameter ε_A), and ground-based ionosonde and magnetometer observations. All datasets used in this study were obtained from open-access sources. A cross-analysis method was applied, integrating diverse parameters into a unified analytical framework. This approach made it possible to identify the key triggering mechanisms and establish their connection to storm energetics and magnetosphere–ionosphere electrodynamics.

Results

The storm sequence consisted of two major storms CME-driven storms. The first storm, on September 11–14, 2024, exhibited higher energetic characteristics, with a peak $\varepsilon_A \approx 0.62$ TW and a total energy input of ~10.3 PJ. During its main phase, dynamic pressure pulses and IMF fluctuations caused substorms, reintensifications, and asymmetric ring current enhancements. The second storm, on September 16–18, 2024, produced lower total energy input (~5.8 PJ) but confirmed the role of the combined effect of dynamic pressure and southward IMF orientation in enhancing instantaneous energy coupling. Key geoeffective processes included significant fluctuations in the disturbed solar wind dynamic pressure and in the IMF orientation, which triggered substorms, magnetic reconnection, and intensification of DP2 convection, confirmed by PC indices, alongside with variations in the

ionospheric electric field. This resulted in observation of prompt penetration electric fields (PPEF) during the early storm phases, disturbed dynamo electric fields (DDEF) during the later phases, substorm activity, and ring current intensifications that produced latitudinal and longitudinal asymmetries of storm parameters. These processes are directly related to the operation of atmosphere–ionosphere–magnetosphere radio channels and led to disturbances in the total electron content (TEC), resulting in the following effects: phase disruptions in GNSS signal transmission and positioning errors; blocking or shifts in the reflection height of HF links due to variations in the F region and absorption in the D region; signal fading, path distortions, and increased noise levels in over-the-horizon radar systems.

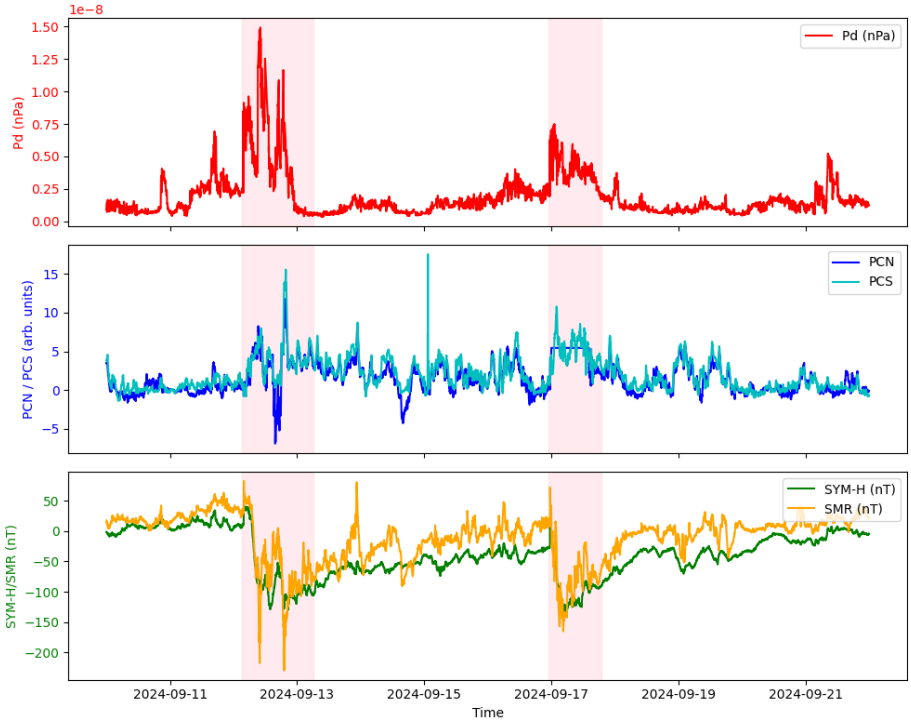

Fig. 1. Solar wind dynamic pressure (Pd), polar cap index (PCN/PCS), and SYM-H/SMR index variations during the September 11–21, 2024 storm sequence. The main phases of both storms are highlighted in pink

Discussion and Conclusions

The results confirm that the geoeffectiveness of storms is determined not only by the duration of southward IMF *Bz* but also by short-term dynamic pressure pulses acting as powerful triggers. Their combined impact produces complex magnetospheric–ionospheric responses leading to degradance in performance of radio channels across various frequency ranges. The proposed cross-analysis provides a systematic foundation for further studies, integrating fundamental geospace physics with applied tasks in radio engineering. It is demonstrated that the geospace storms of September 11–21, 2024, caused significant disturbances in atmosphere–ionosphere–magnetosphere radio propagation channels. The multifactor analysis of space weather disturbances, while systematically considering the processes within the SIMMIAE system and appliyng the concept of a pan-planetary storm, offers valuable applications for assessing and forecasting radio channel conditions during geospace storms.

References

[1] L.F. Chernogor and I.F. Domnin, *Physics of Geospace Storms* (V. N. Karazin Kharkiv Nat. Univ. Publ., Kharkiv, 2014).

[2] L.F. Chernogor, *Physics of Geospace Storms,* Space Sci. Tech. 27, 3–77 (2021).

[3] L.F. Chernogor, *Energetics of physical processes operated on May 8–12, 2024: From the solar storm to lithospheric disturbances*, Adv. Space Res. 75, 6, 4825–4849 (2025).

[4] L.F. Chernogor, *What are a geospace storm and a pan-planetary storm*?, Adv. Space Res. 76, 9, 5640-5657 (2025).

ANALYSIS OF DRIFT AND VARIABILITY OF THE OUTPUT SIGNAL OF CONTACT CONDUCTIVITY SENSORS DURING REPEATED MEASUREMENTS OF URBAN WATER SAMPLES

V. Kabernyk, S. Olszewski
Taras Shevchenko National University of Kyiv, 64/13, Volodymyrska Street, Kyiv, Ukraine,
e-mail: volodymyrkabernyk@gmail.com

The objective of this study is to identify and analyze the factors contributing to signal instability at the output of a two-electrode contact conductivity sensor with a cell constant of $K = 0.993\ cm^{-1}$ during repeated measurements of aqueous samples. The sensor was immersed in a sample of urban water and operated at an excitation frequency of approximately 1 kHz. The measured voltage values were converted into temperature-compensated conductivity readings, after which the drift dynamics were examined across fifty consecutive measurements to evaluate the reliability of the contact method and to determine the principal physical causes of signal fluctuations.

Introduction

The use of compact and cost-effective contact conductivity sensors represents an efficient approach for the rapid monitoring of water quality and the ionic composition of solutions. However, the accuracy of such systems is significantly influenced by the stability of the electrode characteristics and by external factors during repeated measurements [1]. To enhance the reliability of the readings, a preliminary analysis of the sensor's behavior is required—particularly the assessment of signal drift magnitude, signal fluctuations, temperature effects, and potential systematic shifts arising from electrode polarization or degradation during operation.

Experimental Methodology

The objective of the experiments was to investigate the stability of the output signal of a contact conductivity sensor during serial measurements of aqueous samples. The experimental setup was designed to replicate real operating conditions of the sensor, including variable temperature, gradual electrode changes, and repeated immersion into the sample. The hardware configuration consisted of a standard two-electrode conductivity sensor [2], a DFRobot EC V2.0 signal processing module, and an Arduino Uno microcontroller, which recorded the analog signal via a 10-bit ADC. Temperature was measured using a DS18B20 digital sensor, and real-time software compensation was applied. The experiments employed a water sample collected from an urban lake, with temperature fluctuations in the range of 22–26 °C. The excitation frequency of the sensor was approximately 1 kHz, while the sampling rate was 1 Hz, allowing the observation of slow signal drifts and fluctuations. The data were stored in digital form for subsequent statistical analysis.

Results and Discussion

A series of repeated experiments was conducted to evaluate the stability and reproducibility of the readings obtained from the contact conductivity sensor during consecutive measurements of the same water sample. The aim of the study was to determine the nature of changes in the output voltage and the calculated conductivity values under fixed conditions, including constant temperature, excitation frequency, and sensor geometry.

Each measurement session lasted approximately 1500 seconds and consisted of three stages: an initial sensor stabilization period (approximately 250 s), a main stage involving periodic excitation and repeated measurements (1000 s), and a final resting period used to observe signal recovery. The first 10 seconds of each series were utilized to calibrate the output voltage in the steady state, after which relative deviations from the initial level were computed.

The results demonstrated a gradual increase in the sensor's output voltage from 1.68 to 1.77 V, corresponding to a rise in temperature-compensated conductivity from 1.58 to 1.77 mS/cm. This drift was not associated with changes in the sample composition and is indicative of charge accumulation on the electrode surfaces and a slow variation in their polarization. After the active measurement stage, the signal level did not immediately return to its initial value, confirming the presence of capacitive effects and a delayed discharge of the near-electrode layer over time (Fig. 1). Linear approximation of the signal variation revealed that the measurement error in conductivity exhibited a quasi-linear behavior during the first 250 seconds, but gradually transitioned into a nonlinear form characterized by low-frequency components and a drift that could not be eliminated through simple averaging. This indicates the complex nature of the sensor's instability, where polarization processes interact with thermal and electronic factors, giving rise to a noise-like drift that accumulates over time.

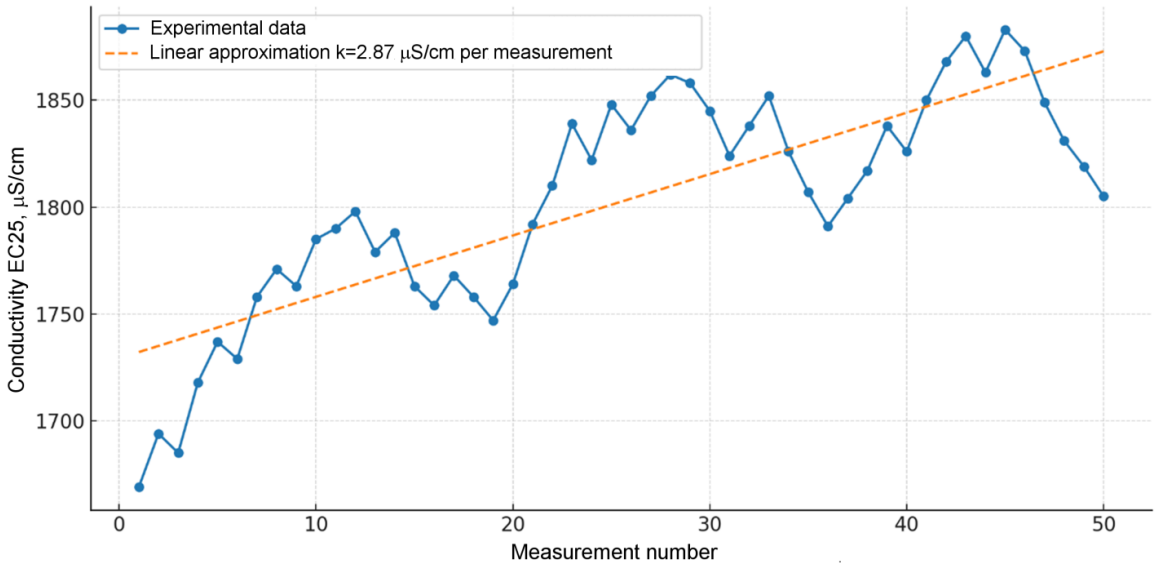

Fig. 1. Dynamics of the output signal of a contact conductivity sensor during a series of measurements on a single water sample, and linear approximation of its temporal drift

The obtained results confirm that even under constant temperature and unchanged sample conditions, the contact sensor exhibits a gradual shift in readings typical of systems with active electrodes. Further investigations should be carried out in both static and dynamic modes, incorporating extended frequency-domain analysis of the signal to more accurately separate the polarization and thermal components of the measurement error. According to the authors, a fundamental approach to overcoming this inherent limitation of contact conductometric sensors lies in the use of non-contact sensors and in registering their impedance spectrum as the working signal [5]. Since impedance measurements are optimally performed at frequencies significantly higher than the characteristic drift frequencies, the contribution of slow drift can be effectively eliminated by filtering out the low-frequency components of the signal.

Conclusions

Experimental investigations of zero drift and output signal variability in contact conductivity sensors demonstrated that the mean deviation of the zero level from its initial value exhibits a fundamentally nonlinear behavior as the number of measurements increases. This behavior is associated with the intrinsic processes governing the formation and dynamics of the near-electrode layer and cannot be mitigated by averaging a statistical series of identical measurements. As a potential approach to overcoming this inherent limitation of contact sensors, the use of non-contact sensors has been proposed, with the impedance spectrum serving as their operational signal.

References

[1] W.B. Owens and A. P. Wong, “An Improved Calibration Method for the Drift of the Conductivity Sensor on Autonomous CTD Profiling Floats,” Deep-Sea Research Part I: Oceanographic Research Papers, vol. 56, no. 3, pp. 450–457, 2009, doi: 10.1016/j.dsr.2008.09.008.

[2] V. Kabernyk, “Analysis of the output signal drift of a two-electrode contact conductivity sensor,” Proceedings of the Conference on Electronic Measurement and Instrumentation, Kyiv, Ukraine, 2025, pp. 45–49.

[3] A. Tůma, P. Kubáň, "Capacitively coupled contactless conductivity detection: Principles, limitations and recent trends," Analytical Methods, vol. 4, no. 1, pp. 25–33, 2012, doi: 10.1039/C1AY05424A.

[4] H. Benchakroun, C. R. Bell, and F. J. Meyer, “Probe Contact Force Monitoring during Conductivity Measurement,” Sensors, vol. 22, no. 20, p. 7895, 2022, doi: 10.3390/s22207895.

[5] Olszewski S.V., Bech I.I., Kabernyk V.O., Improvement of Aquatic Environmental Monitoring Systems through the Application of Non-Contact Electrochemical Impedance Sensors // Ecological sciences: scientific and practical journal, 2024, No. 2(53). 278 p. DOI https://doi.org/10.32846/2306-9716/2024.eco.2-53.6

GYRATOR ON OPERATIONAL AMPLIFIER IN BIPOLAR LC-OSCILLATOR

Bohdanov R.V.*, Bekh I.I.**

Faculty of RadioPhysics, Electronics and Computer Systems, Taras Shevchenko National University of Kyiv, 64/13, Volodymirska Str., City of Kyiv, Ukraine, 01601,

**e-mail: semsterfx2@gmail.com, roman.bohdanov@knu.ua*

***e-mail: igor_ivanovich_bekh@knu.ua*

With aim to get rid of the use of inductors in active RLC filters an "active inductor" – so called gyrator is often in use. It's a kind of RC-cell, which is included in a positive feedback circuit of an operational amplifier. In the study are formulated practical recommendations for choosing of the value of the feedback resistor resistance in gyrator circuits and it's influence on amplitude-frequency characteristic. Proposed an LC-oscillator scheme with the gyrator which may be useful in a laboratory workshop on radio electronics and other practical applications.

The "bipolar" LC-oscillator (Fig. 1) moslty based on transistors Q1 and Q2 can work with various parallel and series oscillating LC-circuits [1]. The calculation of the parameters of the gyrator elements *R*3, *R*4 (*C*1, *C*5), was carried out relative to the required equivalent inductance L_{EQ} and the input resistance of the operational amplifier R_{OAMP} according to [2]:

$$L_{EQ} = R3 \cdot R4 \cdot C_{(1|5)}\,,\; R4 < R3 \leq 200 \cdot R4 < 0{,}1 \cdot R_{OAMP}.$$

The results of simulation (in NI Multisim software) of the oscillator in the "300 Hz" and "3 kHz" modes are shown in Fig. 2(a).

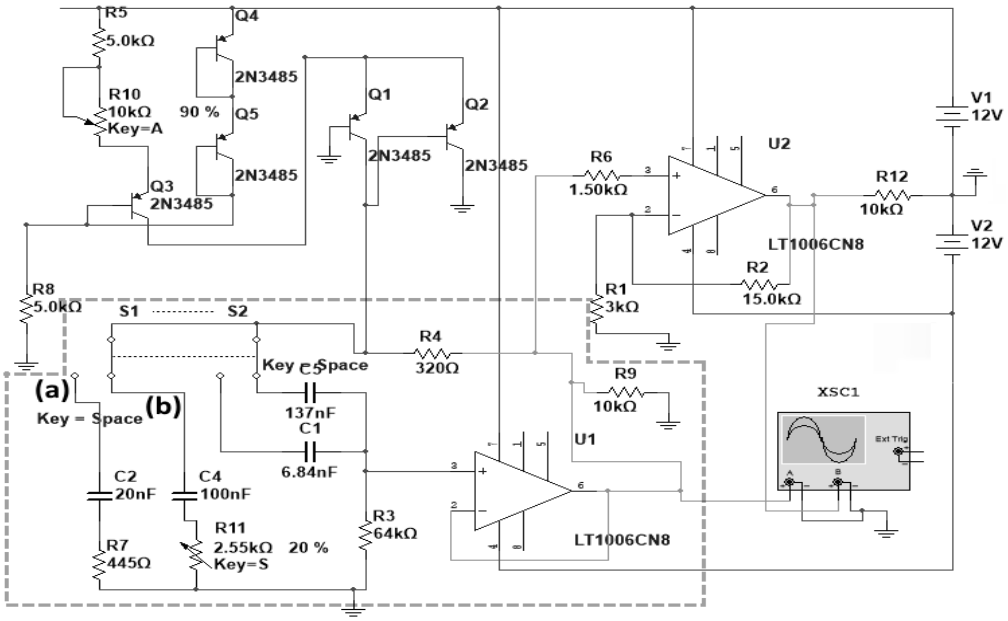

Fig. 1. Principal scheme of bipolar LC-oscillator with an RLC oscillating circuit (area limited by dash lines) based on "active inductor" – a gyrator R3R4(C1 or C5) on operational amplifier U1 (LT1006CN8). Switches S1 and S2 are in state (a) of "3 kHz" mode. State (b) of S1, S2 provides parameters for "300 Hz" mode

Simulated (in LTSpice software) dependences of the relative change in the resonant frequency of the parallel RLC-circuit (Fig. 2(b)) with the gyrator $f_{0-Gyrator-1}$ and $f_{0-Gyrator-2}$ were compared to the resonant frequency of the circuit with the inductor $f_{0-RLC-1}$ та $f_{0-RLC-2}$ depending on the resistance of the resistor *R*4 showed that

resonant frequencies of the circuit with the gyrator are closest to the "real inductor case" at the resistance of the resistor $R4 = \{200..400\}Ohm$. Similarly, the highest Q factor of the circuit with the gyrator is observed in the same range for $R4$ (Fig. 2(c)). Thus, it is possible to choose the optimal value of $R3$, $R4$ ($C1$, $C5$).

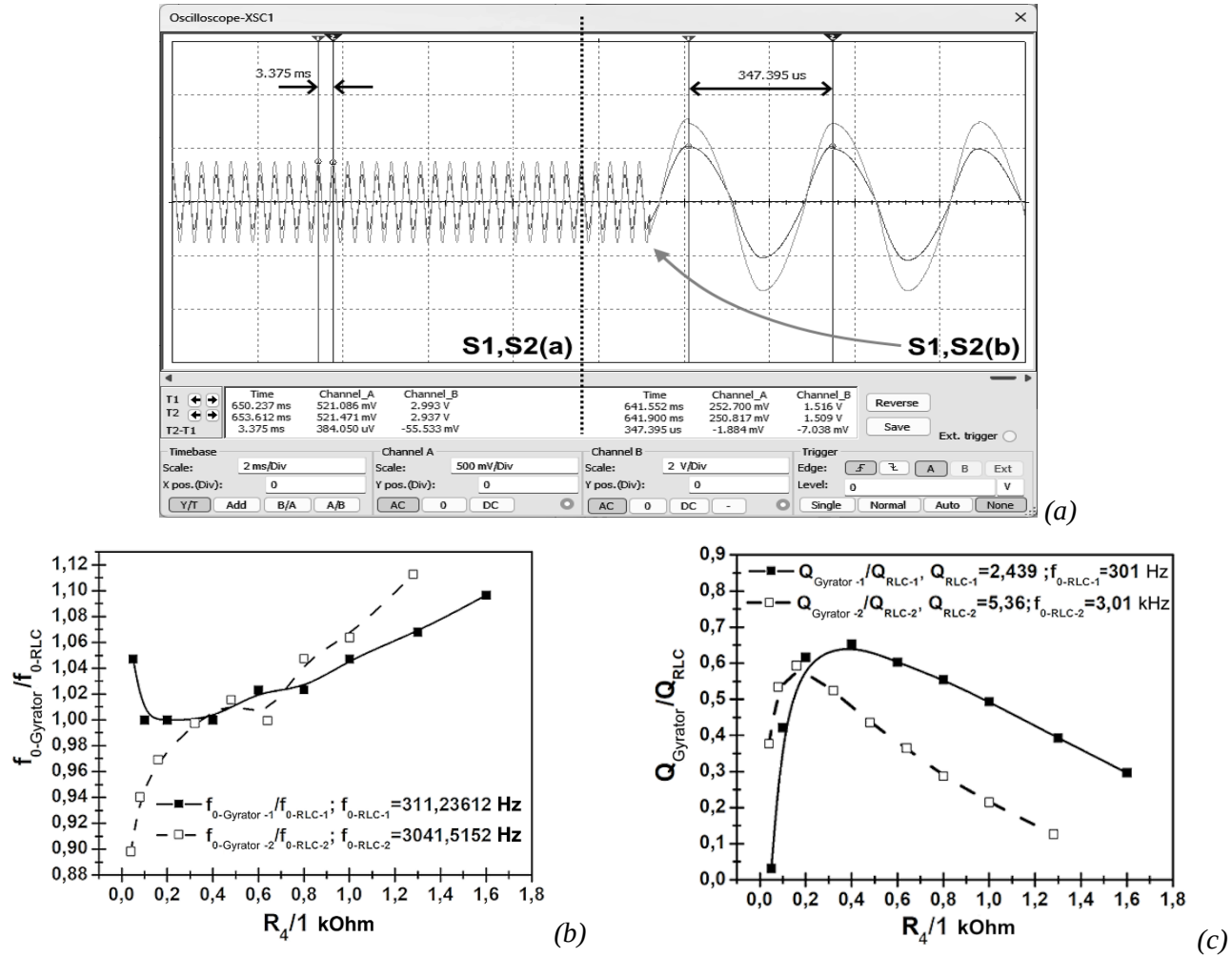

Fig. 2. Simulation results: (a) – oscillograms of signals from the generator in the mode "3 kHz (S1, S2(a))" and transition to the mode "300 Hz (S1, S2(b))"; (b) – change of a relative resonant frequency of the RLC-circuit with the gyrator $f_{(0\text{-Gyrator-1})}$ and $f_{(0\text{-Gyrator-2})}$ compared to the resonant frequency of the RLC-circuit with an inductor $f_{(0\text{-RLC-1})}$ and $f_{(0\text{-RLC-2})}$ depending on the resistance of the feedback resistor R4; (c) – dependences of the Q factor of the RLC-circuit with a gyrator ($Q_{(Gyrator\text{-}1)}$ and $Q_{(Gyrator\text{-}2)}$), normalized to the value of the Q factor of the RLC circuit with an inductor ($Q_{(RLC\text{-}1)}$ and $Q_{(RLC\text{-}2)}$), on the relative change in the resistance of resistor R4

The proposed harmonic oscillator circuit requires fewer identical tunable elements than a Wien bridge oscillator, but requires of improvement of the output amplitude stabilization circuit.

References

[1] Peltz G. LC-Oszillator für (fast) beliebige L/C-Verhaltnisse / Günter Peltz. // Funkschau. 1978. №18. – P. 898.

[2] I.I. Bekh. "Analog electronic devices". Textbook. Kyiv: Publishing Laboratory of the Radiophysics Faculty of the Taras Shevchenko National University of Kyiv, 2024, 258 p.

RADIOPHYSICAL LIMITATIONS OF CELLULAR RADIO COMMUNICATIONS GENERATIONS

Chernogor L.F.*, *, Shevelev M.B.*, Wang J.**, Zhdanko Ye.*, Zheng Yu.*****

**V.N. Karazin Kharkiv National University, Kharkiv, Ukraine, e-mail: leonid.f.chernogor@gmail.com*

*** School of Microelectronics, Tianjin University, Tianjin, China*

Qingdao Institute for Ocean Technology, Tianjin University, Qingdao, China

Shandong Engineering Technology Research Center of Ocean Information Awareness and Transmission, Qingdao, China.

**** College of Electronic Information, Qingdao University, Qingdao, China*

Today, one of the main tasks of radio physics is to master the terahertz range and predict the rates of further growth of the capabilities of wireless telecommunications networks. The purpose of the work is to develop simple mathematical models that predict the growth rate of the capabilities of cellular communication networks for the next 20–25 years. The work makes use of an analytical review of the research problems, system analysis, and mathematical modeling. The 8G generation has been proved to be the last in the evolution of wireless communications and to be developed in 2040–2045. For the THz range, the maximum value of the data transfer rate will be 300–1000 Tbit/s.

Introduction

The growth of the frequency capacity of the terahertz range, information content, the emergence of terahertz technologies, devices and systems inevitably leads to revolutionary changes in radioelectronic systems, in particular, in telecommunications systems. The development of telecommunications systems is one of the most defining milestones in the progress of civilization. First of all, this applies to cellular networks. This mode of communication has been rapidly developing and improving, starting from the late 1970s. Over the last 40–45 years, the data transmission rate has increased by a factor of tens of millions, and the duration of its transmission has decreased by approximately the same amount. The prediction of the rate of a further growth of the capabilities of wireless (cellular) telecommunications networks is urgently needed. The description of the capabilities of each generation of these systems is presented in a number of works, and the interdisciplinary nature of the problems in developing new wireless technologies is shown. Today, specialists have different views on the further evolution of cellular networks. Some believe that 6G will be the last generation. Others think that the development of wireless communications will proceed at an accelerated pace. Some consider the 7G and 8G generations as only some improvement of 6G. In this paper, the authors set out their own view on the problem of FG (Future Generation) of wireless communication networks.

The purpose of the work is to develop simple mathematical models that predict the growth rates of cellular network capabilities over the next 20–25 years.

Results

Model of Cellular Communication Evolution. The main parameter of any communication system is the data transfer rate (system bandwidth) C. Using known data, a scatter plot is constructed and a regression equation is found, as given by

$$\ln C = 0.3977t + 4.3609,\ R^2 = 0.9822,\ \sigma = 1.1090 \text{ bit/s}. \quad (1)$$

Here t is the time in years, counted from 1970; C is the data transfer rate, bit/s; R^2 is the reliability coefficient; σ is the root-mean-square deviation of the approximation. From (1) it follows that the e-folding increase time for C is $\tau_0 = 2.51$ yr. In 1970 $C_0 = 78$ bit/s, then $C(t) = C_0 e^{t/\tau}$, i.e. it is grows exponentially with time. In this case, $C(t)$ is a solution of the following differential equation

$$dC / dt = C / \tau, \qquad C(0) = C_0. \quad (2)$$

Accelerated and Decelerated Evolution Model. Some experts believe that the transition from 5G will occur at an accelerated pace, while others believe that it will occur at a slowed pace. This means that the characteristic scale

time τ in Equation (2) decreases or increases over time. The condition $\tau = \tau(t)$ yields the solution to Equation (2) of the form $C(t) = C_0 e^{J(t)}$, where $J(t) = \int_{t_1}^{t} dt / \tau(t)$. Here t_1 is the time from which the time scale τ starts to decrease or increase. In the first case, the model can describe evolution with explosive instability. The "explosion" should occur at the time $t_{exp} = t_1 + \tau_1$, τ_1 is the characteristic time of change of τ. For $t_1 = 2020$, $\tau_0 = 2.51$ yr and $\tau_1 = 20$ yr. That is, at the specified parameters, the "explosion" should occur in 2040. Of course, this will not happen. The accelerated evolution of cellular communication will certainly slow down due to a number of objective reasons. In the second case, two models are possible: instability (slower than exponential) or instability with saturation at $t \to \infty$. In this case, $C(\infty)$ does not exceed 1.87 Tbit/s. This corresponds to the 6G generation. The transition to 7G, 8G, and 9G is theoretically possible for τ_1, which is 20, 30, and 40 yr. In this case, $C(\infty)$ will be equal to 100, 5.41×10^3, and 29.1×10^4 Tbit/s, respectively. The characteristic features of the considered models are that the characteristic evolution time τ(t) itself changes with time. The reason for this is not reflected in the evolution models. The saturation effect also arises for scientific and technical reasons. Mathematically, they can be described by models in which the rate of change of the data transmission rate depends on this speed. At the same time, the slowdown in evolution is associated with a significant increase in the data transmission rate, which was imperceptible at rather small values of C. The model of such evolution has the form given by

$$dC / dt = C / \tau_0 - \alpha C^2, C(0) = C_0, \; C(t) = C_0 C_\Gamma \left((C_\Gamma - C_0) e^{-t/\tau_0} + C_0\right)^{-1}, C_\Gamma = (\alpha\tau_0)^{-1}, \quad (3)$$

where τ_0 is a constant, α is a dimensional coefficient characterizing the process of the inhibition of evolution. Relation (3) also describes the instability with saturation. As α decreases, the value of C_∞ increases. The real values of α for generations 6G, 7G and 8G can reach 0.4, 0.04, and 0.004 $(\text{Tbit yr})^{-1}$ s, respectively. If the saturation process is faster than in (3), the following model is proposed:

$$dC / dt = C / \tau_0 - \beta C^3, C(0) = C_0, \; C(t) = C_0 C_\Gamma \left((C_\Gamma^2 - C_0^2) e^{-2t/\tau_0} + C_0^2\right)^{-1/2}, C_\Gamma = (\beta\tau_0)^{-1/2}, \quad (4)$$

where τ_0 is a constant, β is the dimensional coefficient characterizing the process of the inhibition of evolution. A decrease in β is accompanied by a slowdown in the inhibition process and an increase in C_∞. Generations 6G, 7G, and 8G can appear, respectively, at β equal to 0.1, 10^{-3}, and 10^{-5} $\text{Tbit}^{-2} \cdot \text{yr}^{-1} \cdot \text{s}^2$.

Summary

Using averaged data on the parameters of wireless communication networks of generations 1G–5G and the promising generation 6G, regressions are obtained that describe the increase in speed and decrease in the duration of data transmission with time up to 2050. Equations are proposed that describe the evolution of the main parameters of wireless communications. It is shown that from 1979 to the present time, the increase in the speed of data transmission is described by an exponential instability equation. In this case, the main parameter of the communication system grows according to an exponential law with a characteristic time of 2.51 yr. Models of accelerated evolution of cellular communication of future generations are proposed. It is shown that accelerated evolution is theoretically possible until approximately 2033–2034, and in addition, it allows for the possibility of explosive instability.

More realistic are the proposed models of the slowed evolution of cellular communication, one of which describes the saturation effect caused by the exponential growth of the characteristic evolution time, and the other describes a significant slowdown in the growth of the data transmission rate.

Models of FG-evolution have been proposed that lead to the saturation effect caused by the slowdown in the growth rate of the data transmission rate due to the growth of this speed.

The role of fundamental, conditionally fundamental, and scientific and technical radiophysical limitations is analyzed. The 8G generation has been proved to be the last in the evolution of wireless communications and to be developed in 2040–2045. In this case, C_{max} will be found in the range from 300 to 1000 Tbit/s.

DISTURBANCES OF THE TOTAL ELECTRON CONTENT IN THE IONOSPHERIC RADIO PROPAGATION CHANNEL

Chernogor L.F.*, Mylovanov Yu.B.*, Shevelev M.B.*
** V.N. Karazin Kharkiv National University, Kharkiv, Ukraine, e-mail: leonid.f.chernogor@gmail.com*

The latitudinal variations in the total electron content as main parameter of radio propagation channel are analyzed during the extreme geospace storm of May 2024.

Introduction

The Global Navigation Satellite System (GNSS) is designed to effectively solve the problem of object positioning. Positioning accuracy significantly depends on the state of the atmospheric-magnetospheric radio propagation channel. Under quiet conditions, the point positioning errors can reach 0.1 m. Under disturbed conditions, this error increases by 1–2 orders of magnitude. Moreover, GNSS malfunctions can occur, lasting several hours or even longer. The most severe disturbances of natural radio propagation channels are caused by solar storms. During these disturbances, the total electron content (TEC) in the ionosphere changes by tens of TECU. Moreover, random TEC fluctuations increase several-fold, leading to an increase in the random component of the error Δr and even to GNSS malfunctions.

The purpose of this talk is to present the results of an analysis of latitudinal variations in TEC as main ionospheric radio propagation channel during the extreme geospace storm of May 10−11, 2024.

Methods

To study global TEC disturbances, 20 GNSS stations in the Western Hemisphere along the 68°W meridian and 21 stations in the Eastern Hemisphere along the 112°E meridian were selected. TEC was determined with an error of approximately 0.1 TECU. The largest TEC disturbances occurred on May 10 and 11, 2024. May 9, 2024, was selected as the reference day. Along with TEC variations, N_V, the variations in geographic latitude, φ, geographic longitude, λ, and local time, LT, were analyzed.

Results

An analysis of measurements at 41 stations revealed an exceptionally complex picture of TEC disturbances during the extreme geospace storm of May 2024. Positive ionospheric storms alternated with negative ones. The characteristic scale was 1-2 Mm.

Ionospheric storms at high, mid, and low latitudes differed both qualitatively and quantitatively. At high latitudes, the Prompt Penetrating Electric Field (PPEF) effects were pronounced. At low latitudes, the equatorial ionization anomaly (EIA) and plasma drift in the crossed electric **E** and magnetic **B** fields, as well as the rise of plasma bubbles, played a significant role.

An example of temporal variations in $N_V(t)$ in the extended EIA region is shown in Fig. 1. From Fig. 1, it is evident that on May 10, N_V values increased by 60−70 TECU compared to the TEC values on May 9, 2024. The variations in $N_V(t)$ were non-monotonic, and a positive ionospheric storm was evident.

$N_V(t)$ variations at practically the same longitude, but at a latitude of about 24°S, were completely different (Fig. 2). A negative ionospheric storm was present. The TEC decrease was 20–45 TECU. This also occurred in the EIA region, where under quiet conditions $N_V \approx$ 80−100 TECU.

An example of $N_V(t)$ variations practically near the same meridian, but at high northern latitudes is shown in Fig. 3, where a negative ionospheric storm with an N_V decrease of approximately 10–15 TECU occurs. The TEC values fluctuate strongly, with the fluctuation range attaining 20−30%. A negative ionospheric storm is recorded at the BAIE station in the mid-latitudes of the western hemisphere (Fig. 4). In this case, the TEC decrease reaches 9.5 TECU (a factor of 3). The TEC fluctuations on May 11, 2024, are highly non-stationary, when the TEC bursts exceed 7 TECU (a factor of 1.5) at night.

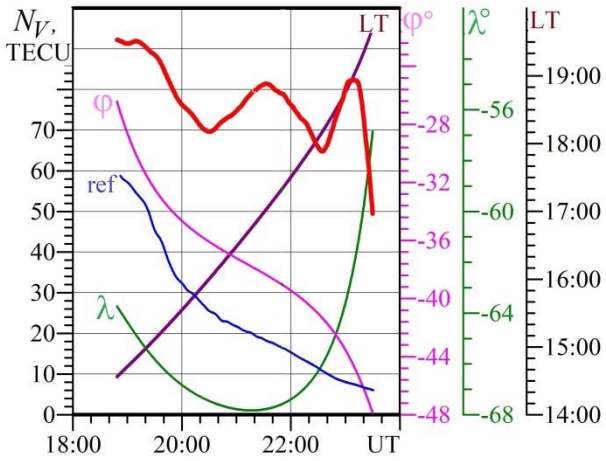

Fig. 1. UT dependence of TEC (thick curve) along the G19 satellite flyby relative to the ANTC station (37.15°S, 71.53°W), Antuco, Chile, May 10, 2024

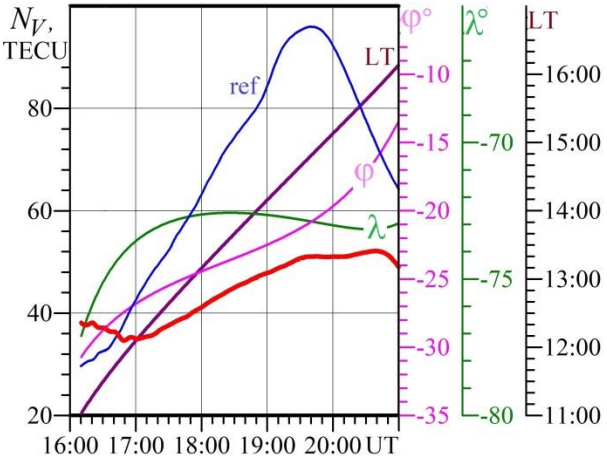

Fig. 2. Same as Fig. 1, for the G05 satellite flyby relative to the ANTF station (23.56°S, 70.42°W), Antofagasta, Chile

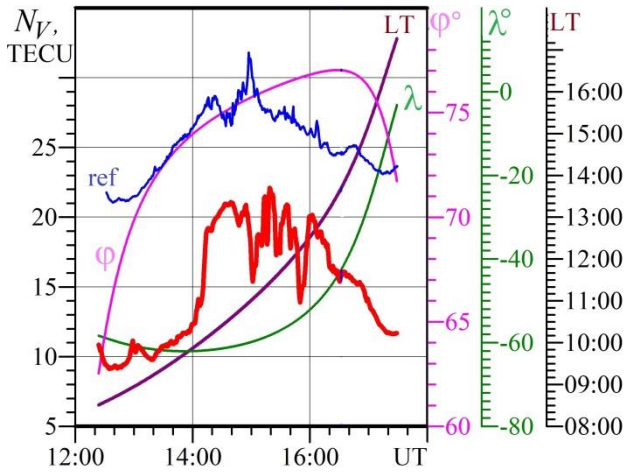

Fig. 3. Same as Fig. 1, for the flyby of satellite G02 relative to station THU2 (76.45°N , 68.83°W), Narssârssuk, Grønland

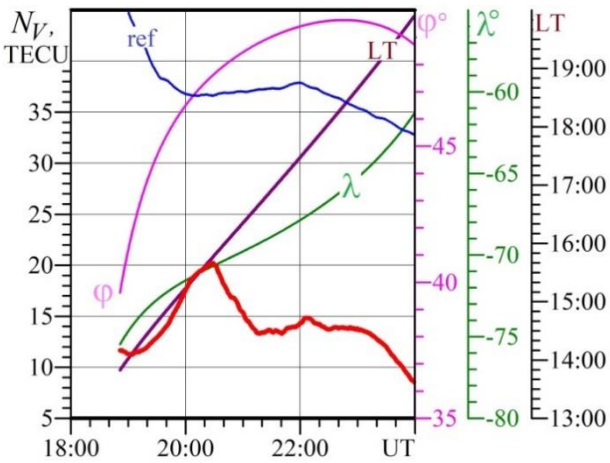

Fig. 4. Same as Fig. 1, for the G05 satellite flyby relative to the BAIE station (49°N, 68.83°W), Baie-Comeau, Canada

In the figures, φ and λ are the geographic coordinates of a measurement point, LT is local time, «ref» is the UT dependence of TEC on May 9, 2024.

Summary

1. An extreme geospace storm caused a very strong and complex ionospheric storm, with positive and negative ionospheric storms alternating in space and time.

2. During positive ionospheric storms, TEC values increased by 60–70 TECU (a factor of 7–8). During negative ionospheric storms, TEC values decreased by 20–50 TECU (a factor of 1.5–12).

3. Ionospheric storm manifestations significantly depend on geographic (magnetic) coordinates and time of day. This is explained by the prevalence of specific storm mechanisms in each specific region of the globe.

ACOUSTIC-GRAVITY WAVES FROM THE EXPLOSION OF A POWERFUL VOLCANO

Chernogor L.F.*, Liashchuk O.I., Rudycheva O.*, Shevelev M.B.*, Tilichenko N.M.***
** V.N. Karazin Kharkiv National University, Kharkiv, Ukraine, e-mail: leonid.f.chernogor@gmail.com*
*** Main center of special monitoring, Kosmichna str. 1, urban village Gorodok,*
Zhytomyr region, Ukraine, 12265, e-mail: alex_liashchuk@ukr.net

Using the Ukrainian network of infrasound stations, global disturbances in atmospheric pressure variations within the atmospheric acoustic propagation channel, caused by the eruption of a super volcano, were detected. The main parameters of the observed disturbances were evaluated.

Introduction

The eruption of the Tonga super volcano on January 15, 2022, triggered large-scale physical disturbances affecting nearly all geospheres from the lithosphere to the magnetosphere. According to studies [1–3], the explosion generated shock waves, Lamb waves, acoustic-gravity waves that circled the Earth multiple times. Infrasound signals were recorded at over 50 IMS stations. Observations [3, 4] showed that Lamb waves propagated at speeds of 308–320 m/s, while acoustic-gravity waves (AGWs) traveled at 240–270 m/s. Analysis [5, 6] revealed changes in atmospheric pressure, electron content, geomagnetic fields. This event provided a unique source of data for studying global disturbances. The purpose of the report is to determine the main parameters of acoustic-gravity waves generated by the explosion of the Tonga volcano.

Techniques and Equipments

Infrasound pressure fluctuations were registered by the acoustic stations GRDI and LUGA during two separate time intervals. Data processing utilized System Spectral Analysis (SSA), which includes Short-Time Fourier Transform (SFT), Adaptive Fourier Transform (AFT), and Wavelet Transform (WT), allowing for optimal resolution in both time and frequency domains.

Results and Discussion

SSA revealed clear wave packets and the dominant period ranges at the analyzed stations and intervals.

GRDI station. First interval (18:30 – 20:50 UT January 15, 2022): The recorded disturbance was characterized by velocities from 288 to 301 m/s, signal durations from 15 to 30 min and main periods from 200 to 400 s. Wavelet transform showed stable activity in this range. For the second interval (approximately 00:00 – 03:00 UT. January 16, 2022) the arrival velocities varied from 307 to 318 m/s, the durations of the pressure variation disturbances reached about 45 min, and the main periods were slightly longer - from 400 to 600 s.

LUGA station. For the first interval (approximately 18:00 – 22:00 UT January 15, 2022) of pressure variation data, we have a velocity range of 258 to 297 m/s, a duration of about from 1.5 to 2 h, and periods with maximum energy density of 300 to 600 s. The second interval (approximately 01:30 – 03:30 UT January 16, 2022) showed that velocities varied within the range of 289-303 m/s, durations from 20 to 40 min, and the range of periods of maximum spectral density was within the range of 600-800 s.

Conclusions

1. Atmospheric pressure disturbances, characteristic of global-scale AGWs propagation, were successfully detected and analyzed at the GRDI and LUGA stations.

2. The application of SSA allowed for the clear identification dominant spectral periods and intervals, which is crucial for distinguishing between various types of atmospheric wave sources and propagation mechanisms.

3. The results confirm the presence of strong wave energy in the AGW range (up to 800 s), indicating a powerful source generating global-scale atmospheric oscillations.

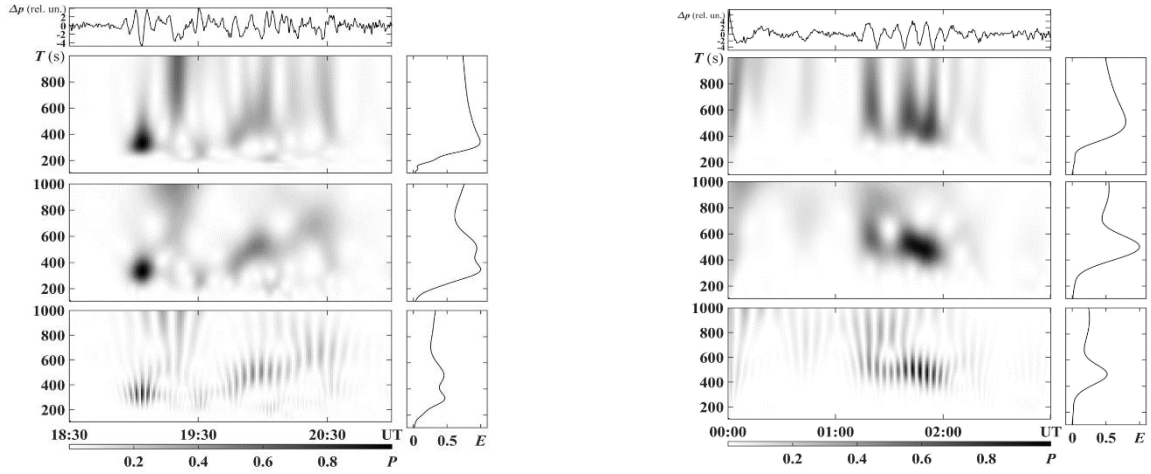

Fig. 1. Results of bandpass filtering and SSA of pressure fluctuations registered at station GRDI for the first (left) and second (right) intervals. Panels from top to bottom: waveform, SFT, AFT, and WT results. Energygrams are shown on the right of the spectral panels

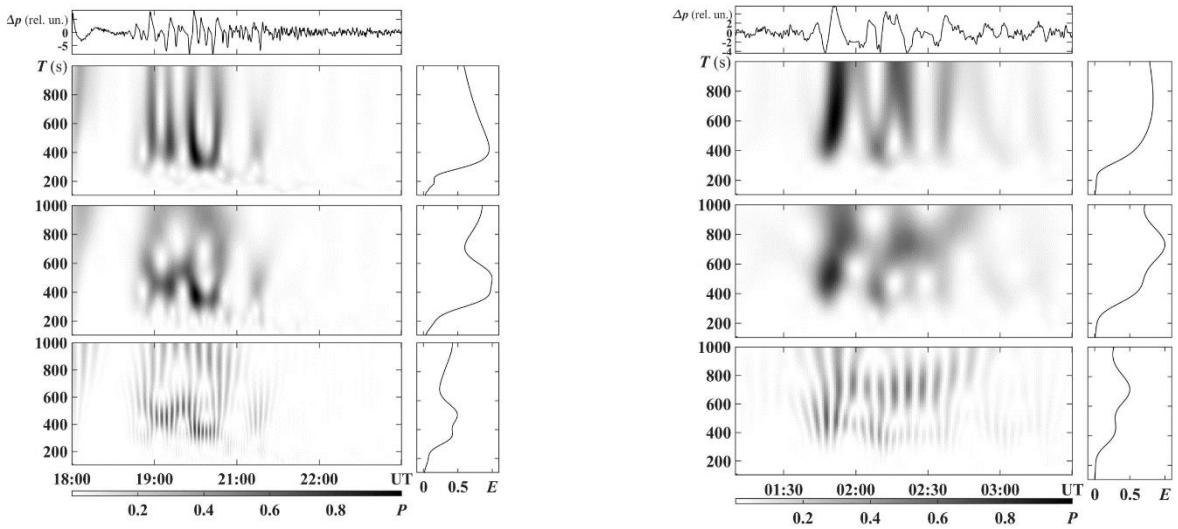

Fig. 2. The same as in Fig. 1, for the station LUGA

References

[1] L.F. Chernogor, "Physical effects from the powerful Tonga volcanic eruption of January 15, 2022, in the Earth–atmosphere–ionosphere–magnetosphere system," J. Atmos. Solar-Terr. Phys., vol. 253, id:106157, 2023.

[2] D.A. Yuen, M.A. Scruggs, F.J. Spera et al., "Under the surface: Pressure-induced planetary-scale waves, volcanic lightning, and gaseous clouds caused by the submarine eruption of Hunga Tonga-Hunga Ha'apai volcano provide an excellent research opportunity," Earthquake Research Advances, vol. 2, no. 3, id:100134, 2022.

[3] R.S. Matoza, D. Fee, J.D. Assink et al., "Atmospheric waves and global seismoacoustic observations of the January 2022 Hunga eruption," Tonga. Science, vol. 377, no. 6601, pp. 95—100, 2022.

[4] J. Vergoz, P. Hupe, C. Listowski et al. "IMS observations of infrasound and acoustic-gravity waves produced by the January 2022 volcanic eruption of Hunga, Tonga: A global analysis," Earth Planet. Sci. Lett., vol. 591, id:117639, 2022.

[5] C.J. Wright, Neil P. Hindley, M.J. Alexander, "Surface-to-space atmospheric waves from Hunga Tonga–Hunga Ha'apai eruption," Nature New Biol., vol. 609, pp. 741–746, 2022.

[6] P.A. Inchin, A. Bhatt, S.A. Cummer et al., "Multi-Layer evolution of acoustic-gravity waves and ionospheric disturbances over the United States after the 2022 Hunga Tonga volcano eruption," AGU. Adv. Earth and Space Sci., vol. 4, is. 6, id:e2023AV000870, 2023.

PROTOTYPE SOFTWARE SOLUTION FOR AUTOMATING QUALITATIVE AND QUANTITATIVE ANALYSIS OF THIN LAYER CHROMATOGRAPHY IMAGES

Kushnir O.A.*, Olszewski S.V.**

Taras Shevchenko National University of Kyiv, 64/13, Volodymyrska str., Kyiv 01601, Ukraine,
** e-mail: xelambert@knu.ua, ** e-mail: solaristics@gmail.com*

Research problem

To solve the problems of segmentation and classification of objects in two-dimensional images covering various areas of human activity (medicine, military affairs, energy, metalworking and mechanical engineering, etc.), the use of a number of machine learning methods was analyzed [1–6]. However, for the field of thin-layer chromatography (TLC) research, there are no studies in the literature on the use of these methods, in particular for the purpose of automating the stages of qualitative and quantitative analysis of TLC images. Currently, the specified analysis is performed by organoleptic control (visually) [7]. To improve the process of identifying optimal segmentation models for TLC tasks and further using the models to automate the work of scientists who are faced with the task of analyzing TLC images, it is necessary to solve the problem of creating an appropriate program solution.

Software solution

A prototype of a program in Python was developed to solve the above analysis automatization problem, and the program was tested on a set of different machine learning models and a set of TLC images. The software solution allows you to select a model to obtain analysis results, TLC images, obtain segmentation results for the selected models and images, determine the substance zone (namely: the lower and upper boundaries of the substance zone and the center of the substance object, the pixel coordinates of which are determined as the average value of both coordinates of all pixels of the substance; these data are displayed in a separate section of the program window in the form of lines and red dots), quantitative analysis of the analyte object by the area metric, qualitative analysis of the analyte object by the R_f (Retention factor) and hR_f metrics [8]:

$$R_f = \frac{z_x}{z_f - z_0}$$

, where z_x is the distance traveled by the zone, and $z_f - z_0$ is the distance from the start line to the solvent front;

$$hR_f = R_f \cdot 100$$

Also, the resulting segmented image is saved in a separate folder for further use of this file.

Thus, the current version of the developed utility allows automation of several stages of the routine work of an analytical chemist, namely: determination of the substance zone, quantitative analysis of the analyte by the area metric and qualitative analysis by the R_f and hR_f metrics (Fig. 1). This provides the opportunity to obtain objective results at the specified stages of TLC image analysis, the values of which are not influenced by the human factor; as well as the opportunity to obtain these results in less time (for example, when performing one image processing with this utility on a PC, the time to obtain results is typically less than 0.5 s; while when processing manually, the time required is in the range of 5–10 min). These facts indicate the possibility of using this utility to reduce the time for spectrometrists to perform routine work and obtain objective analysis results at the above-mentioned stages of TLC image analysis. It should be noted separately that the developed utility allows to study the features of the results of TLC image analysis using various segmentation models, in particular in cases of transfer learning of individual models.

Further prospects

Extending the software solution for TLC image analysis capabilities includes the expansion of the library of TLC image analysis models, the implementation of the functionality for analyzing a number of TLC images, the creation of a library of correspondences of the values of qualitative analysis metrics to certain substances, the implementation of the functionality for predicting the correspondence of a substance in an image analyzed by the utility to a certain substance from the library. The implementation of the above functionality will allow to automate even more stages of TLC image analysis, and therefore to further increase the objectivity and speed of this process.

The expansion of the model library with solutions that, according to objective indicators, best solve the problem of TLC image segmentation according to number of precision metrics, will allow, in particular, to increase the accuracy of the specified process.

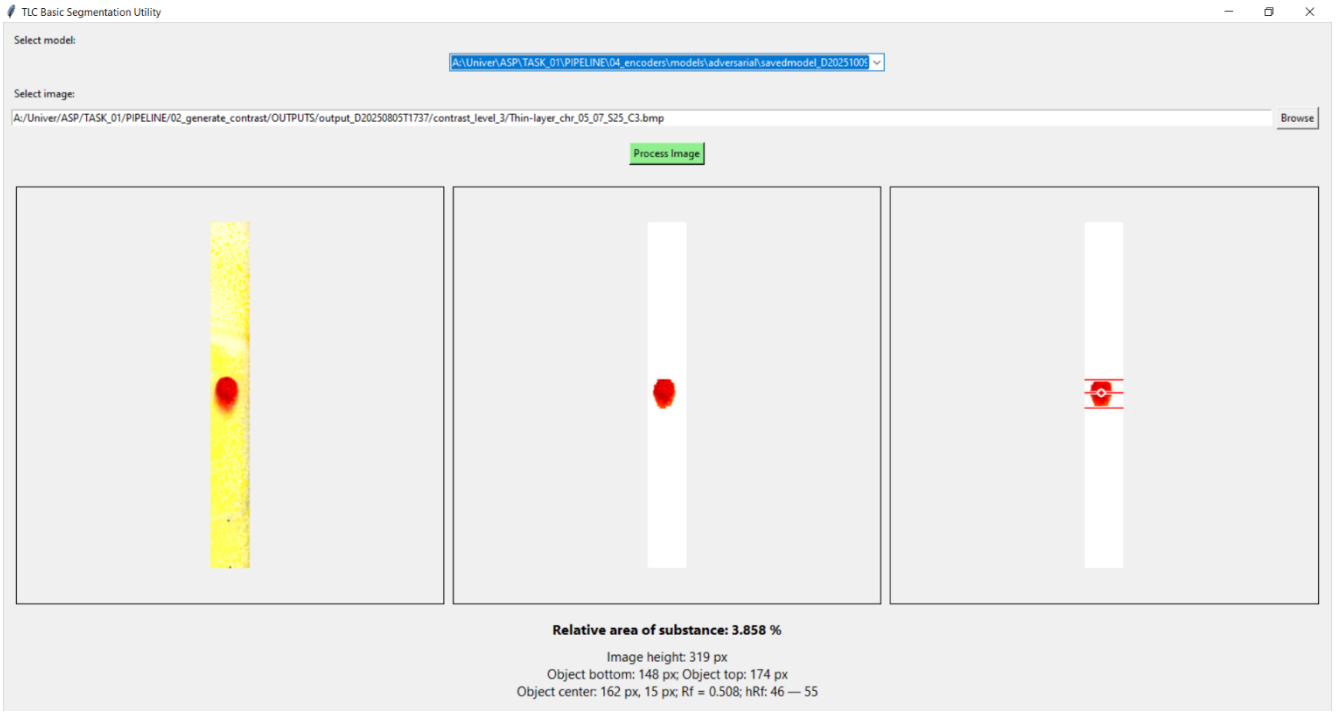

Fig. 1. – Program solution work demonstration

References

[1] Rahel Hamad. An Assessment of Artificial Neural Networks, Support Vector Machines and Decision Trees for Land Cover Classification Using Sentinel-2A Data. Applied Ecology and Environmental Sciences. Vol. 8, No. 6, 2020, pp 459-464, doi: 10.12691/aees-8-6-18

[2] M.P. Karthikeyan, R. Venkatesan. Interpolative Leishman-Stained transformation invariant deep pattern classification for white blood cells // Soft Computing. – 2020. – Vol. 24, №16. – P. 12215-12225, doi: 10.1007/s00500-019-04662-4

[3] Ronneberger, Olaf; Fischer, Philipp; Brox, Thomas. U-net: Convolutional networks for biomedical image segmentation. In: International Conference on Medical image computing and computer-assisted intervention. Cham: Springer international publishing, 2015. p. 234-241, 10.48550/arXiv.1505.04597

[4] K. -W. Huang et al. Nasopharyngeal carcinoma segmentation via HMRF-EM with maximum entropy // 2015 37th Annual International Conference of the IEEE Engineering in Medicine and Biology Society (EMBC). – 2015. – P. 2968-2972, doi: 10.1109/EMBC.2015.7319015

[5] Chen, Liang-Chieh, et al. Deeplab: Semantic image segmentation with deep convolutional nets, atrous convolution, and fully connected CRFs. IEEE transactions on pattern analysis and machine intelligence, 2017, 40.4: 834-848, doi: 10.48550/arXiv.1606.00915

[6] R. Castellanos, S. Mitra. Segmentation of Magnetic Resonance Images Using a Neuro-Fuzzy Algorithm // 13th IEEE Symposium on Computer-Based Medical Systems. CBMS 2000, Houston, TX, USA – 2000. – P. 207-212, doi: 10.1109/CBMS.2000.856901

[7] Meyers, C.L.F. (2000), Thin-Layer Chromatography. Current Protocols in Nucleic Acid Chemistry, 3: A.3D.1-A.3D.8, doi: 10.1002/0471142700.nca03ds03

[8] Hahn-Deinstrop E. Applied Thin-Layer Chromatography. — 2nd Ed. — Wiley, 2007. — ISBN 978-3-527-31553-6

AUTOMATED SYSTEM FOR RECEIVING METEOROLOGICAL DATA FROM NOAA WEATHER SATELLITES

H.O. Moskalenko*, I.O. Derkach* and V.A. Moiseienko**
**Taras Shevchenko National University of Kyiv, Kyiv 01033, Ukraine,*
e-mail: hermanmoskalenko@gmail.com, derkachivan2003@gmail.com
***Independent Research & Development Laboratory "200k Electronics", Kyiv, Ukraine,*
e-mail: vamrpd@gmail.com

In this work experimentally studied a prototype of an amateur automated system for receiving meteorological data from NOAA weather satellites.

In recent years, increasing attention has been devoted to the development of low-cost automatic ground stations for meteorological satellites using software-defined radio (SDR) technology. In this work, we implemented an autonomous system for receiving NOAA satellites in the VHF band at frequency 137 MHz based on an RTL-SDR receiver with the R820T2 tuner.

For stable reception of Automatic Picture Transmission (APT) signals, a quadrifilar helix (QFH) antenna was calculated, constructed, and optimized specifically for this frequency band. The antenna provides omnidirectional coverage with right-hand circular polarization, which significantly improves signal quality during low-elevation passes.

The reception chain was automated with SatDump software, performing demodulation, decoding, and image generation in real time. All decoded meteorological images were automatically stored in a dedicated directory and further published via Pigallery2 for remote monitoring. Initial experiments confirmed that the designed QFH antenna, in combination with SDR-based processing, ensures reliable reception of high-quality NOAA imagery, thereby demonstrating the effectiveness of such low-cost systems for continuous environmental observations.

Fig. 1a shows the appearance of the QFH antenna. This figure also shows an example of data received from low-orbit weather satellites, in particular, a cloud map over Kyiv (Fig. 1b) and a map of rain clouds with color markings for the probability of rain (Fig. 1c). Noise stripes are present in the images as a result of dense urban development around the receiving antenna.

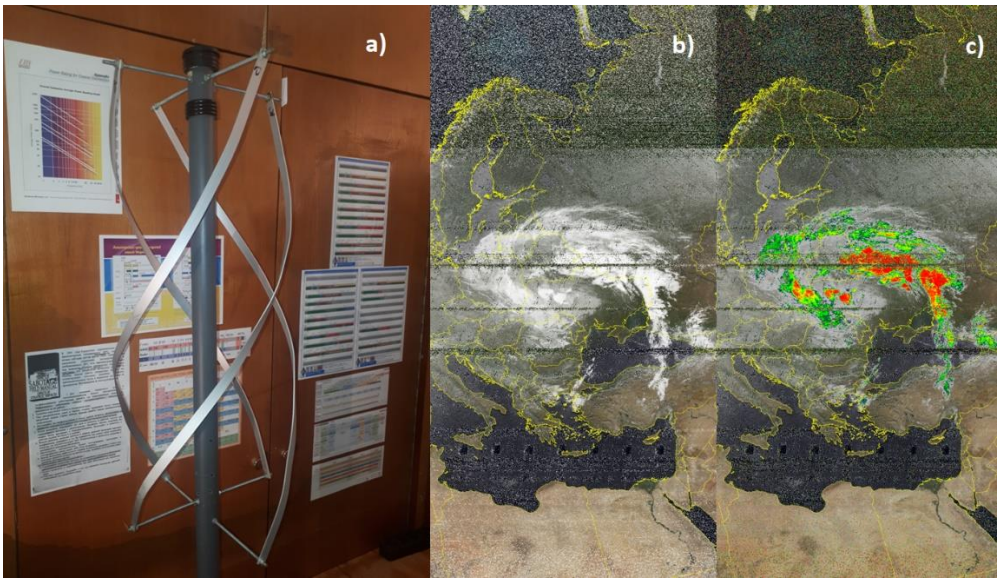

Fig. 1. The appearance of the QFH antenna

THE IMPACT OF SOLAR FLARES ON THE IONOSPHERIC RADIO CHANNEL PARAMETERS

L.F. Chernogor, R.M. Kovalov
Department of Space Radio Physics, V. N. Karazin Kharkiv National University, Kharkiv, 61022, Ukraine,
e-mail: Leonid.F.Chernogor@gmail.com, ruvym.kovalov@student.karazin.ua

The aim of this talk is to present a study of the ionospheric total electron content (TEC) response to the solar flares that occurred on May 8–14, 2024, using data from 12 GNSS stations. The global ionospheric response to the solar flares was quantitatively evaluated with high temporal resolution. Theoretical estimates showed that ultraviolet (UV) radiation accounts for about 80% of the impact, while X-ray radiation contributes about 10%, indicating the dominant role of the UV component in TEC disturbances. The results are consistent with theoretical models and demonstrate the efficiency of GNSS-based methods for analyzing photon-induced ionospheric perturbations. The obtained data are important for refining the mechanisms of solar activity influence on space weather conditions and for improving the operation of radio navigation, telecommunication, radar, and radio astronomical systems of both space- and ground-based types.

Introduction

The Earth's ionosphere is highly sensitive to electromagnetic radiation fluxes generated during solar storms (solar flares) [1, 2]. Under the influence of ultraviolet (UV) and X-ray radiation, the level of ionization in the middle and lower ionosphere increases, leading to short-term variations in the total electron content (TEC). Research on the TEC response to solar flares has been conducted for several decades. It has been established that while solar storms share certain general characteristics, each event also exhibits individual features. This highlights the importance of investigating the effects of new solar storms throughout all regions of the Earth's atmosphere. This is particularly relevant for extreme storms, such as the one that occurred in May 2024.

The aim of this work is to evaluate the variations in TEC in the ionosphere caused by solar flares on May 8–14, 2024, based on GNSS data, and to compare the results with theoretical calculations.

Data and Methods

To monitor TEC variations, dual-frequency GNSS measurements from 12 stations of the global International GNSS Service (IGS) network were used. Data were received from GPS satellites (G05, G06, G13, G14, G17, and G20) at stations located near the corresponding subsolar meridian for each flare. For the ten events on May 10–11, 2024, data from six stations located along 112° E longitude were used. For the events on May 14, 2024, data from six stations along 68° W longitude were analyzed. The analysis was performed with a temporal resolution of 1 minute, and the typical TEC measurement error did not exceed 0.1 TECU. X-ray fluxes in the ranges 0.05–0.4 nm and 0.1–0.8 nm were obtained from the XRS (X-Ray Sensor) instrument onboard the GOES-18 satellite, according to NOAA data (https://data.ngdc.noaa.gov/platforms/solar-space-observing-satellites/goes/goes18/). For the ultraviolet component, synthetic spectral fluxes from the FISM2 (Flare Irradiance Spectral Model) were used, available through the SDO/EVE mission archive (https://lasp.colorado.edu/eve/data_access/evewebdata/fism/flare_hr_data/). Between May 8 and 14, 2024, twelve powerful X-class solar flares were recorded on the Sun, accompanied by a sharp increase in X-ray and ultraviolet radiation. The strongest of them were X3.9 (May 10), X5.8 (May 11), and X8.7 (May 14). In the numerical evaluations, the dependence of X-ray flux density on wavelength was taken into account.

Results

Response to X-class flares. The most powerful flares on May 10 and 11 were more clearly detected in the eastern hemisphere. On May 10, 2024, the highest TEC values were observed at low-latitude stations, HKSL (22° N, 114° E), where, for different satellites, $N_{V0} \approx 92–110$ TECU, and XMIS (10° S, 114° E), where $N_{V0} \approx 75–113$ TECU. Such high TEC values can be explained by the influence of the equatorial ionization anomaly.

With increasing latitude, in both the northern and southern hemispheres, the TEC gradually decreases to approximately 39–45 TECU at 52° N and 46–52 TECU at 29° S.

On May 10, 2024, depending on latitude, the TEC enhancement ΔN_V ranged from 0.8 to 5.5 TECU, while the relative variation δN_V was approximately 1.2–4.9%. The largest effect was recorded at the XMIS station, where $\Delta N_V \approx 5.5$ TECU and $\delta N_V \approx 4.9\%$.

Similarly on May 10, 2024, on May 11 the TEC values decreased with increasing latitude. At the HKSL and XMIS stations, the TEC varied in the ranges 49–92 TECU and 55–65 TECU, respectively. At 52° N latitude, the TEC did not exceed 13–22 TECU, while at 29° S it ranged between 22–25 TECU. On May 11, 2024, depending on latitude, the TEC enhancement ΔN_V ranged from 1.1 to 19.9 TECU, while the relative variation δN_V was approximately 6.1–27.5%. The largest effect was recorded at the HKSL station, where $\Delta N_V \approx 19.9$ TECU and $\delta N_V \approx 27.5\%$.

The X8.7 flare that occurred on May 14, 2024, was clearly observed from the western hemisphere, and the TEC variations within 77–85 TECU and 85–94 TECU were observed at low-latitude stations BOGT (4.61° N, 74.08° W) and POVE (8.65° S, 63.90° W), respectively. With increasing latitude, the TEC values decreased: at the SCH2 station (54.65° N, 88.83° W) they were 30–32 TECU, while at the Antarctic station PALM (64.63° S, 64.05° W) they ranged between 14–20 TECU. Depending on latitude, the TEC enhancements ΔN_V reached 0.5–2.3 TECU, and the relative variations in δN_V were approximately 0.6–6.2%. The largest absolute effect was recorded at the RDSD station ($\Delta N_V \approx 2.3$ TECU, $\delta N_V \approx 3.5\%$), while the largest relative effect occurred at the PALM station ($\Delta N_V \approx 1.2$ TECU, $\delta N_V \approx 6.2\%$). During each flare, an increase in UV radiation intensity was recorded, ranging from 2.8% to 96%. The strongest UV enhancement occurred during the X8.7 flare, while the X5.8 and X3.9 flares were also accompanied by significant UV increases of 38% and 16%, respectively.

Summary

It has been confirmed that the magnitude of TEC enhancements strongly depends on the geographic coordinates of the observation station, the solar zenith angle (local time), and the intensity of the solar flare. The largest TEC increases (up to 3–20 TECU or 3–28%) occurred within the region of the equatorial ionization anomaly. In mid-latitudes, TEC disturbances usually did not exceed 1–3 TECU or 1–17%. The increase in TEC due to ionization of N_2 and O_2 molecules in the D-region of the ionosphere by hard X-rays was within 0.1–0.3 TECU. The TEC enhancements in the E-region, caused by the ionization of N_2 and O_2 molecules by soft X-rays, did not exceed 0.1–0.4 TECU. The contribution of UV-induced ionization in this region was minor (less than 0.1 TECU). A more significant effect was observed in the F_1-layer, where ionization of N_2 and O_2 molecules by ultraviolet radiation caused TEC disturbances of 2.8–13.2 TECU. Even larger enhancements (up to 30–60 TECU) could result from the ionization of atomic oxygen in the F_2-layer of the ionosphere. The estimates showed that the magnitude of TEC disturbances strongly depends on the spectral composition of solar radiation. The observational results and theoretical estimates show good overall agreement.

References

[1] L.F. Chernogor, “Physics of Geospace Storms (in Ukrainian),” Space Sci. & Technol., vol. 27, No. 1 (128), pp. 3–77, 2021. https://doi.org/10.15407/knit2021.01.003

[2] Y. Luo, L. Chernogor, K. Garmash, “The Geomagnetic Response to the X-class Solar Flares of September 2017,” Advances in Space Research, vol. 72, No. 11, pp. 4911–4922, Dec. 1, 2023. https://doi.org/10.1016/j.asr.2023.09.043

[3] L.F. Chernogor, “Energetics of Physical Processes Operated on May 8–12, 2024: From the Solar Storm to Lithospheric Disturbances,” Advances in Space Research, vol. 75, No. 6, pp. 4825–4849, Mar. 15, 2025. https://doi.org/10.1016/j.asr.2024.12.069

[4] L.F. Chernogor, “What are a Geospace Storm and a Pan-Planetary Storm?,” Advances in Space Research, vol. 76, No. 9, Nov. 1, 2025, pp. 5640–5657 2025. https://doi.org/10.1016/j.asr.2025.08.016

THE IMPACT OF POWERFUL ATMOSPHERIC VORTICES ON THE ATMOSPHERIC-IONOSPHERIC RADIO PROPAGATION CHANNEL

L.F. Chernogor*, Yiyang Luo*
*V.N. Karazin Kharkiv National University, 4 Svobody Sq., Kharkiv 61022, Ukraine,
Leonid.F.Chernogor@gmail.com; yiyangluo@163.com

This study investigates the disruptive effects of powerful atmospheric vortices on the atmospheric-ionospheric radio propagation channels, with particular focus on tropospheric ducting mechanisms that enable over-the-horizon (OTH) SHF/UHF/VHF radio location and communication. Through analytical modeling and numerical simulation, we demonstrate how vortex-induced disturbances degrade both surface-based waveguides and upper atmospheric propagation paths. Our results show that vortices systematically destroy the refractive structures essential for SHF/UHF/VHF ducting while simultaneously generating infrasound disturbances that propagate to ionospheric altitudes. These coupled effects produce significant impairments for critical systems including OTH radar, satellite communications, and navigation networks during severe weather events.

Introduction

The reliable operation of long-range radio communication, radar, and navigation systems is fundamentally dependent on the state of the atmospheric-ionospheric radio propagation channel. A primary mechanism for the OTH propagation of centimeter, decimeter and meter radio waves is waveguide trapping within surface-based and evaporation ducts in the troposphere [1]. These ducts form under specific inversion layers of temperature and humidity, creating a gradient of the modified refractive index that traps electromagnetic waves (EMWs) with wavelengths shorter than a critical value ($\lambda < \lambda_{cr} \approx 8.5\times10^{-4}\times h^{3/2}$), guiding them over hundreds of kilometers [1]. The critical wavelength λ_{cr} is a function of the duct height h, with typical values provided in Table 1.

Table 1: Critical Wavelength for the Surface-based Ducts in the Troposphere

Duct Height, h (m)	10	30	50	100	300	500	1000	3000
Critical Wavelength, λ_{cr} (m)	0.027	0.14	0.30	0.85	4.4	9.5	26.9	140

However, these radio propagation channel are highly vulnerable to powerful atmospheric vortices—intense meteorological systems characterized by pressure deficits of 1–10 kPa and wind speeds exceeding 100 m/s [2, 3]. These intense meteorological systems generate complex disturbances (multi-physical coupling) that propagate through the atmosphere, simultaneously disrupting tropospheric waveguides and coupling energy to the ionosphere. Vortex-induced disturbances disrupt tropospheric waveguides through violent mixing and pressure perturbations, while simultaneously coupling energy to the ionosphere via infrasound radiation (0.2–5 Hz) [4]. This vertical coupling mechanism demonstrates that mesoscale meteorological events can substantially degrade radio system performance through atmospheric interactions spanning from the planetary boundary layer to the ionospheric altitudes.

The purpose of this study is to systematically investigate the multi-physical impact and the mechanism of powerful atmospheric vortices on atmospheric-ionospheric radio propagation channels. A dissipative soliton-based vortex dynamics model is proposed to quantify the main parameters of hydrodynamic, electrical, and magnetic disturbances, along with noise infrasound radiation.

Physical Mechanisms and Disturbance Modeling

Atmospheric vortices disrupt radio propagation through three principal mechanisms operating across subsystems of the Earth-Atmosphere-Ionosphere-Magnetosphere (EAIM) system, including: (1) *Hydrodynamic mechanism.* Vortices destroy tropospheric ducting structures through turbulent mixing and pressure perturbations, with radial pressure gradients disrupting refractive index profiles essential for waveguide trapping [5]; (2) *Electrical mechanism.* Triboelectric charging generates intense electric fields (10^2-10^6 V/m) that produce lightning

discharges and broadband electromagnetic interference, which overwhelm receivers through noise floor elevation [6]; (3) *Infrasound wave mechanism.* Vortex-generated infrasound (0.2-5 Hz) propagates vertically to ionospheric altitudes, where energy deposition in the E and F regions generates traveling ionospheric disturbances (TIDs) [7]. Electron density fluctuations in the ionosphere cause phase and amplitude scintillations that degrade HF communications and Global Navigation Satellite Systems (GNSS) positioning across regional scales.

Discussion

The disturbances generated by powerful atmospheric vortices influence the atmospheric-ionospheric radio propagation channel and produce significant degradation in a lot of critical radio systems. For instance, OTH radar and communication links experience catastrophic path loss through destruction of tropospheric waveguide structures, with signal attenuation increasing during intense vortex passage. Satellite communication systems encounter significant performance degradation through ionospheric phase and amplitude scintillations, with fading depths and phase variations scaling with vortex intensity and proximity to the propagation path. GNSS exhibit particularly sensitive response to vortex-induced electron density flutuations, with positioning errors significant increasing by during EF4-EF5 (Enhanced Fujita Scale) events. The electron density perturbations associated with ionospheric disturbances introduce variable group delays and carrier phase advances that compromise both absolute and differential positioning accuracy. Radar systems operating within affected regions encounter beam distortion and elevated clutter levels through refractive index modifications in the lower atmosphere, while radio astronomical observations experience wavefront degradation through turbulent phase perturbations along the propagation path.

Conclusion

Powerful atmospheric vortices generate disturbances that significantly impair the atmospheric-ionospheric radio propagation channels. Our proposed dissipative soliton model effectively characterizes vortex dynamics and multi-physical coupling mechanisms, enabling predictive assessment of system degradation. Understanding these interactions supports the development of resilient communication architectures and adaptive operational protocols for maintaining performance during severe meteorological weather events. Future research should focus on advancing predictive modeling capabilities and developing adaptive system technologies that can dynamically respond to these challenging propagation conditions.

References

[1] M.P.M. Hall, *Effects of the Troposphere on Radio Communication*, New York, NY: Stevenage , 1989.

[2] A.B. Smith and R.W. Katz, "US billion-dollar weather and climate disasters: Data sources, trends, accuracy and biases," Nat. Hazards, vol. 67, pp. 387–410, 2013.

[3] A.M. Makarieva and V.G. Gorshkov, "Condensation-induced kinematics and dynamics of cyclones, hurricanes and tornadoes," Phys. Lett. A, vol. 373, pp. 4201–4205, 2009.

[4] L.F. Chernogor, "Tropical Cyclone or Typhoon as an Element of the Earth–Atmosphere–Ionosphere–Magnetosphere System: Theory, Simulations, and Observations," Remote Sensing, vol. 15, id:4919, 2023.

[5] L.F. Chernogor, "Electromagnetic Coupling of Geospheres: 1. Disturbances in the Lower Ionosphere," Kinematics and Physics of Celestial Bodies, vol. 41, pp. 1–13, 2025.

[6] L.F. Chernogor, "Electromagnetic Coupling of Geospheres: 2. Disturbances in the Magnetosphere," Kinematics and Physics of Celestial Bodies, vol. 41, pp. 43–60, 2025.

[7] L.F. Chernogor, *Physics and ecology of catastrophes: Monograph*, Kharkiv, Ukraine: V. N. Karazin Kharkiv National University Publ., 2012.

THE IMPACT OF GLOBAL SEISMIC ACTIVITY ON ATMOSPHERIC-IONOSPHERIC RADIO PROPAGATION CHANNELS

L.F. Chernogor*, Yiyang Luo*, I.G. Zakharov
**V.N. Karazin Kharkiv National University, 4 Svobody Sq., Kharkiv 61022, Ukraine,*
Leonid.F.Chernogor@gmail.com; yiyangluo@163.com; giz-zig@ukr.net

This study discusses the influence mechanism of powerful global seismic processes on atmospheric-ionospheric radio channel parameters. Through the comprehensive analysis of multiple independent geophysical data sets, the continuous planetary-scale coupling effect of global seismic activity (GSA) on the atmosphere, the ionosphere and even the magnetosphere is revealed. This coupling effect has an important impact on radio transmission channels that depend on these media properties. The research results show that local transient phenomena such as earthquakes must be reinterpreted as an integral part of a periodic continuous global process, and the disturbances generated by them can be detected in the quiet area of the earthquake thousands of kilometers away from the epicenter, although the magnitude has been attenuated.

Introduction

In accordance with the system paradigm of Chernogor, in the dynamic open nonlinear system Earth (inner core)-atmosphere-ionosphere-magnetosphere (EAIM) there are direct and reverse positive and negative connections between subsystems [1-3]. In particular, seismic processes in the tectonosphere and lithosphere can cause noticeable or significant disturbances in other subsystems above. There are a number of mechanisms of influence of seismic processes on these subsystems. These include the following: electrical, electromagnetic and a mechanism caused by the generation of acoustic-gravitational waves. It is important that a powerful seismic process can lead to disturbance of the key parameters of the atmosphere and the ionosphere, and therefore impair the parameters of atmospheric-ionospheric radio channels on a global scale [3].

Data Sources and Methodology

This research analyzes daily measurements from multiple geophysical fields, including: space weather parameters, solar activity index $F_{10.7}$ and geomagnetic activity index *Ap*; ionosphere data: from Pruhonis (50.0°N, 14.6°E) and Grinding Stone Mountain (42.6°N, 71. 5°W) critical frequency of the F2 layer (foF2) of the station; atmospheric pressure data: surface atmospheric pressure (*P*) of the meteorological station cooperating with the ionosphere observatory; lithosphere index: the daily global maximum Earthquake amplitude (M_{max}) as a GSA agent. The data comes from the following sources: space weather index of NOAA/SWPC (ftp://ftp.swpc.noaa.gov/pub/indices), ionosphere parameters of UMLCAR DIDBase and NASA CDDIS, Gismeteo's atmospheric pressure and USGS's seismic catalog. Ionospheric characterization employs Total Electron Content (TEC) data derived from GPS signal analysis. The utilization of slant TEC measurements enables global mapping with minimal interpolation requirements, including oceanic regions. Global Ionospheric Maps (GIM) from the CODE analysis center (http://www.aiub.unibe.ch/download/CODE/) provide 1-2 hour temporal resolution data. Analysis focuses on 40° N latitude at 5° longitudinal increments, selected to minimize space weather influences that dominate higher and tropical latitudes. Diurnal variations are removed through daily averaging, with TEC values expressed in TECU (1 TECU = 10^{16} electrons/m^2). The analysis adopts the superimposed era method and uses the non-parametric Friedman test [4] for statistical verification.

The TEC value used to calculate the local effect is calculated at the time of the main thrust at different times in the local time, which makes it possible to evaluate the seismic effects of the daytime (11 cases) and night (10) conditions of the ionosphere respectively; the result of an earthquake during the transition period is not considered. It is determined that the daily effect is similar to that shown in Figure 1a, but the amplitude is slightly smaller. In the evening, in addition to the main maximum value and the amplitude of about 8% two days before the earthquake, there is also a weak maximum value on the first day after the earthquake.

Epicentral TEC changes (Figure 1a) show that the main predecessor (about 6% amplitude) appears two days before the main shock ($p < 0.1$). Before and after this maximum value, the TEC value is still suppressed. The absence of aftershock peaks constitutes a key local-global response difference. Since the global impact permeates all locations, Figure 1a represents a comprehensive response of local and global. The isolated pure local component (Figure 1b) reveals the early onset and sudden termination after the main shock. Local analysis using the main impact timing can separate the day (11 events) and night (10 events) responses. The result of an earthquake during the transition period is not considered. It is determined that the daily effect is similar to that shown in Figure 1a, but the amplitude is slightly smaller. In the evening, in addition to the main maximum value and the amplitude of about 8% two days before the earthquake, there is also a weak maximum value on the first day after the earthquake. Figure 2 demonstrates close correspondence between ΔTEC maxima and seismicity distribution in both coordinate systems. The poleward ΔTEC increase and geomagnetic equatorial minimum suggest dependence on the vertical geomagnetic field component, though low equatorial TEC values may contribute to this pattern.

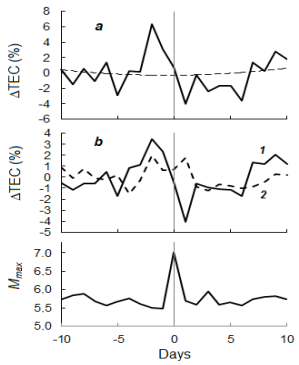

Fig. 1. Epicentral TEC variations: (a) observed response, (b) isolated local effect (curve 1) vs. global effect (curve 2).

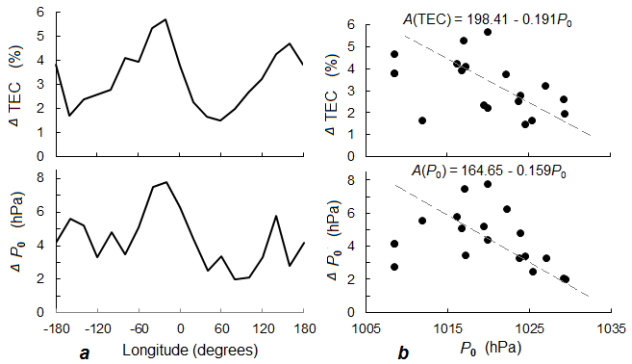

Fig. 2. The amplitude of the lithospheric effect in the atmosphere and the ionosphere: a) - longitude dependence; b) - dependence on surface atmospheric pressure.

Conclusion

This study confirms that there is a persistent and potentially continuous planetary-scale coupling between the lithosphere, the atmosphere, the ionosphere and the magnetosphere, which is partly regulated by spatial weather conditions. Therefore, the effects of local transient phenomena such as earthquakes must be reinterpreted as components of periodic continuous global processes. This global coupling is manifested as detectable disturbances in seismically quiet areas thousands of kilometers from the epicenter and worsens the stability of ionospheric-atmospheric radio channels.

References

[1] L.F. Chernogor, "The Earth – atmosphere – geospace system: main properties and processes," International Journal of Remote Sensing, vol. 32, no. 11, pp. 3199–3218, 2011. DOI: 10.1080/01431161.2010.541510.

[2] L.F. Chernogor, *Mechanisms of Geospheres Interaction: Monograph*. Kharkiv: V. N. Karazin Kharkiv National University, 2025.

[3] Y. Luo, L.F. Chernogor, K.P. Garmash, Q. Guo, and Y. Zheng, "Seismic–Ionospheric Effects: Results Of Inclined Radio Sounding Of The Ionosphere," Radiophysics and Radio Astronomy, vol. 25, no. 3, pp. 218–230, 2020.

[4] I.G. Zakharov and L.F. Chernogor, "Twenty-seven-day zonal wind fluctuations in the troposphere and lower stratosphere under the influence of solar activity," Kinematics and Physics of Celestial Bodies, vol. 41, no. 1, pp. 14–25, 2025. DOI: 10.3103/S0884591325010052.

POLARIMETRY: THEORY AND APPLICATIONS

ANALYSIS OF POLARIMETRIC DEFECTOSCOPY APPLICABILITY FOR SILICON MEDIA IN GENERAL-PURPOSE MICROPROCESSORS

Andrii Fesenko*, Sergey N. Savenkov**
Faculty of RadioPhysics, Electronics and Computer Systems, Taras Shevchenko National University of Kyiv, Kyiv 01601, Ukraine
** e-mail: fesenkoandrew@gmail.com, andriy.fesenko@knu.ua*
*** e-mail: sns@univ.kiev.ua*

Polarimetric methods of anisotropic media analysis have properties that make them attractive for the purposes of structural analysis and defectoscopy, specifically, remote and non-destructive nature of measurements.

Within this talk, an original research is discussed based on Stokes polarimetry, with the goal of initial applicability analysis of Stokes polarimetry for the purpose of non-destructive quality control of general-purpose microprocessors, with potential Jones/Mueller matrix methods applications for a more nuanced analysis. The research was conducted using a constructed Stokes polarimeter and obtained samples of Intel Xeon CPU dies, de-lidded for direct access to silicon chips, and the main methodology of the experimental research consisted of measuring the Stokes parameters of a coherent light source reflected off the surface of studied samples, with various forms of controlled defects introduced into the samples for comparison.

The results of the research were promising, where some of the specific introduced defects were clearly distinguishable based on changes in gathered polarimetric data compared to the data gathered from undamaged samples of silicon dies. The applicability of the used methodology was validated by testing it on multiple experimental samples, where the changes in anisotropic polarization properties were reproducible based on the nature of introduced controlled defects.

A method of quality control is planned to be proposed after further data analysis and generalization. Further refinement of the methodology and experimental setup will allow for quick and concise defectoscopy using relatively widely available equipment for industrial use.

INFLUENCE OF GEOMETRY AND FIELD ON THE REMANENT MAGNETIZATION AND ANISOTROPY OF MAGNETIC NANOPARTICLES IN BIPOLAR STRUCTURES

T.I. Biriukov, O.M. Ivanyuta
Faculty of Radiophysics, Electronics and Computer Systems,
Taras Shevchenko National University of Kyiv, Ukraine, Kyiv, Acad. Glushkova av., 4-g
e-mail: biriukov_t@knu.ua; oleksandr.ivanyuta@knu.ua

Modern additive technologies open new possibilities for creating functional polymer composites with magnetic properties [1]. The formation of an ordered magnetic structure during 3D printing remains a challenging task due to the lack of a clear transition boundary between opposite polarities in a conventional permanent magnetic field. To obtain a distinctly defined polarity, electromagnets must be used, as they can generate a controlled bipolar field that changes the direction of magnetic intensity according to a specific law [2].

Printing inside a solenoid, where a bipolar field $H(t)=H_0 \sin(\omega t)$ is formed, helps partially reduce the area of chaotic nanoparticle arrangement within the polymer matrix. As a result, the orientation of magnetic moments becomes more stable than in a monopolar field; however, the disordered zone still remains significantly larger than the width of a Bloch magnetic wall [3].

Physically, each domain in a ferromagnetic material consists of a large number of dipoles oriented in the same direction. When neighboring dipoles share the same orientation, a domain region with minimal internal energy is formed. If, due to local fluctuations, the directions of adjacent dipoles begin to deviate by a certain angle, a transition zone arises between the domains — the so-called Bloch wall, whose width is determined by the balance between exchange interaction energy A and anisotropy energy K [3,4]:

$$\delta = \pi\sqrt{\frac{A}{K}} \quad .$$

For iron nanoparticles in a polymer matrix, $\delta \approx 10^{-8}$ m, while the typical disordered region in an FDM-printed filament reaches $10^{-5} – 10^{-4}$ m.

Thus, the magnetic barrier between regions of opposite polarity exceeds the Bloch wall thickness by 3–5 orders of magnitude, i.e. $\Delta E_{bar} \approx 10^{3-5} E_{Bloch}$ [4].

To overcome this barrier, a magnetic impulse (spin) must perform work:

$$W = \mu_0 M_S H_c V \ ,$$

where M_S — is the saturation magnetization, H_c — the coercive force, and V — the volume of the switching region.

This energy condition limits the possibility of domain rearrangement in printed structures, explaining the absence of giant magnetoresistance in the obtained samples [5].

To achieve effects such as GMR (Giant MagnetoResistance), a difference in magnetization directions between neighboring layers or nanodomains with a controlled wall thickness is required — something currently unattainable in polymer systems.

Therefore, even when using the solenoid's bipolar field, where the alternating magnetic intensity H(t) reduces the randomness of nanoparticle orientation, the ordering remains partial, since magnetic interaction does not form

a rigid boundary between opposite dipole directions. Gradual temperature decrease during extrusion leads to the "freezing" of a partially ordered configuration without clear domain separation.

The remanent magnetization M_r in such samples increases by 1.5–2 times compared to non-oriented structures, confirming the effectiveness of external influence [6], although complete domain alignment does not occur.

The orientation parameter $S = \langle\frac{3\theta - 1}{2}\rangle$ remains below 0.5, corresponding to partial anisotropy. If $S \to 1$, the orientation would be fully aligned, but such a situation is currently unattainable in polymer composites due to viscosity limitations and weak interparticle coupling.

Thus, printing in a bipolar field significantly reduces randomness but does not overcome the energy barrier between oppositely magnetized regions.

This explains why the resulting structures do not exhibit the properties of active magnetic elements, such as those based on the giant magnetoresistance (GMR) effect, which requires controlled domain switching under an external field.

The obtained results demonstrate the fundamental difference between monopolar and bipolar magnetization. In the first case, a unidirectional dipole orientation is formed without polarity change, while in the second, dynamic particle reorientation allows the formation of a partially ordered domain structure — an intermediate state between a chaotic configuration and full domain separation. Further technological improvements are possible through filament size reduction, increased bipolar field intensity, and control of temperature gradients during polymer solidification.

References

[1] Shirakawa H., McDiarmid A., Heeger A. Twenty-five Years of Conducting Polymers // Chem. Commun. – 2003 – pp. 1–4.

[2] Wang Z. et al. Additive manufacturing of polymer-based magnetic composites: a review // Composites Part B: Engineering. – 2022 – Vol. 236 – 109805.

[3] Schwitalla J., Györffy B. L., Szunyogh L. Electronic theory of Bloch walls in ferromagnets // Physical Review B. – 2001 – Vol. 63 – 104423.

[4] García-Cervera C. J. Structure of the Bloch Wall in Multilayers // University of California, Santa Barbara, 2004.

[5] Baibich M. N., Broto J. M., Fert A. et al. Giant Magnetoresistance of (001)Fe/(001)Cr Magnetic Superlattices // Physical Review Letters. – 1988 – Vol. 61 – No. 21 – P. 2472–2475.

[6] Reduction Control of Fluid Structure Disorder Degree by Cryoelectronics Methods, Biriukov T., Ivanyuta O. / Proceedings of 20th International Scientists Conference on Applied Physics, Kyiv, 2024.

[7] Biriukov T., Ivanyuta O. Temperature-Dependent Molecular Docking and Structural Ordering in Cryoelectronic Polymer Systems. – 2024.

[8] Biriukov T., Ivanyuta O. Influence of Geometry and Field on the Remanent Magnetization and Anisotropy of Magnetic Nanoparticles. – 2025.

MATHEMATICAL PROBLEMS OF APPLIED PHYSICS

MULTI-FRACTAL ANALYSYS
USING THE WTMM AND THE MFDFA METHODS IN APPLIED PHYSICS

Leonid F. Chernogor*, Oleg V. Lazorenko, Andriy A. Onishchenko*****
** School of Radiophysics, Biomedical Electronics and Computer Systems,*
V.N. Karazin Kharkiv National University, Kharkiv 61022, Ukraine e-mail: Leonid. F. Chernogor@gmail.com
*** School of Physics, V.N. Karazin Kharkiv National University, Kharkiv 61022, Ukraine,*
e-mail: Oleg.V.Lazorenko@karazin.ua
**** Faculty of Automatics and Computerized Technologies, Kharkiv National University of Radioelectronics,*
Kharkiv 61166, Ukraine, e-mail: Andrey.Onishchenko@nure.ua

Basing on the mono-fractal analysis results obtained for the sunspot numbers time series, the effectiveness of the Hurst fractal dimension calculated with rescaled range method application was shown. A good example of the second order fractal existence in practice was considered.

Introduction

In this work, to describe the multi-fractal properties of a fractal process or signal, two multi-fractal analysis methods, namely, the Wavelet Transform Module Maxima (WTMM) method and the Multi-Fractal Detrended Fluctuation Analysis (MFDFA), are used (see, for example, [1]). To show the pecularities of the multi-fractal analysis used in such way for the applied physics, the sunspot numbers time series as a well-known fractal natural process was chosen.

Previous Studies of Multi-Fractal Properties of the Sunspot Numbers Time Series

The time series of sunspot numbers, called as the Wolf numbers too, characterizes solar activity and is associated with the counting of sunspots. The observations of this unique process have been conducted since 1610, although complete and reliable data have only been available since 1849 (see, for example, [2]). It is well known that it has a pronounced 11-year cycle, superimposed perhaps on another slower component with a period of about a hundred years (see, for example, [3]). However, this information was obtained in the "pre-fractal" era (before 1975). It is important to note, that first mono-fractal analysis of the time series of Wolf numbers was successfully carried out by B. Mandelbrot and J. Wallis in 1969 in the paper [4]. The short review and comparison of the following similar results can be found, for example, in the work [5]. But the time series of Wolf numbers was occurred to be not mono-fractal, but multi-fractal at all. In particular, this was successfully confirmed in the work [5] by the results of the mono-fractal analysis been performed with the rescaled-range analysis application. Since 2006, regular studies of the multi-fractal properties of the Wolf number series have been conducted. It has been found that the sinusoidal trend has a significant negative impact on the estimates obtained. After its removal, it turned out that the fractal dimension of the series as a whole is $D \approx 1.88 \pm 0.01$ [6]. And this value differs significantly from that given by mono-fractal analysis methods, where in bounds of the generalized Brownian motion model, the fractal dimension D of this process had been obtained in the range $D \approx 1.1-1.3$. The possible explanation for this is seems to be simple: it is necessary to compare either the results obtained without a trend or with a trend and don't mix them in any case. Moreover, in 2009, in the work [7], a different mechanism for removing the sinusoidal trend was proposed and used, and the value for the fractal dimension turned out to be different: $D \approx 1.26$, which is quite consistent with the results of the mono-fractal analysis. Let us add that one of the first attempts to study the multi-fractal properties of the sunspot number series was made in 2005 in the work [8]. The refinement of individual aspects of the multifractal properties of the sunspot number series continues to this day (see, for example, [9]).

Multi-Fractal Analysys of the Sunspot Numbers Time Series

For present analysis, the daily total sunspot numbers from 1/1/1818 till 31/07/2024 were chosen [10]. The most popular from all existing multi-fractal analysis methods are appeared to be the Wavelet Transform Module Maxima (WTMM) method and the Multi-Fractal Detrended Fluctuation Analysis (MFDFA). First of them is

suitable for investigations of multi-fractal properties of whole signal and second of them is convenient for estimations of multi-fractal characteristics in sliding window in time domain.

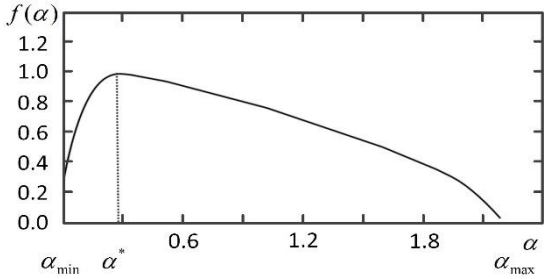

Fig. 1. The multi-fractal spectrum function $f(\alpha)$ of the whole Wolf time series.

In bounds of the WTMM method, it was found that the multi-fractal characteristics of the whole sunspot time series are following: $\alpha_{\min} = -0.02$, $\alpha_{\max} = 2.21$, $\Delta\alpha = \alpha_{\max} - \alpha_{\min} = 2.23$, $\alpha^* = 0.28$. The corresponding multi-fractal spectrum is shown at the fig. 1. A good agreement between the Hurst fractal dimension $D_H = 1.78$ [5] and the fractal dimension $D_\alpha = 2 - \alpha^* \approx 1.72$ is found. Moreover, it is suitable to suppose that both the properties mono-fractal and multi-fractal can be non-stationary in sense of their numerical characteristics should be been This was realized as with R/S method for the time-varying Hurst exponent $H(t)$, as with MFDFA for $\alpha_{\min}(t)$, $\alpha_{\max}(t)$, $\Delta\alpha(t)$ and $\alpha^*(t)$. All these time functions were smoothed with the window, which had the width been equal to 1/20 of all function length in time domain. There is a good agreement between time variations of $H(t)$ and $\alpha^*(t)$. All calculations were performed with the time domain window with width $T_w = 11$ years, which corresponds with well-known period existing in time-frequency structure of the sunspot number series. Using the continuous wavelet transform (see, for example, [11]), the existence of the tree-like structure confirms well the presents of fractal properties for the sunspot numbers series.

References

[1] O.V. Lazorenko, L.F. Chernogor, “Fractal radio physics. 2. Fractal and multifractal analyses of signals and processes” Radio Phys. Radio Astron., vol. 28, no. 1, pp. 5 – 70, 2023 (in Ukrainian).

[2] Yu.I. Vitinskii, “Solar activity forecasting”, NASA TTF-289 TT65-50115, 1965.

[3] M. Frame, A. Urry, *Fractal Worlds: Grown, Built, and Imagined, New Haven*. London: Yale University Press, 2016.

[4] B. Mandelbrot, J.R. Wallis, “Computer experiments with fractional Gaussian noises”, Water Resources Res., vol. 5. no. 1, pp. 228-241, 1969.

[5] L.F. Chernogor, O.V. Lazorenko, A.A. Onishchenko. “Mono-Fractal Analysis with the Hurst Dimension Usage in Applied Physics”, Proc. of the XX Int. Conf. “Electronics and Applied Physics”, Kyiv, Ukraine, pp. 48 – 49, 2024.

[6] M.S. Movahed, G.R. Jafari, F. Ghasemi, S. Rahvar, M.R.R. Tabar, “Multifractal detrended fluctuation analysis of sunspot time series”, Journal of Statistical Mechanics: Theory and Experiment, vol. 02, P02003–P02003, 2006.

[7] J. Hu, J. Gao, X. Wang, “Multifractal analysis of sunspot time series: the effects of the 11-year cycle and Fourier truncation”, Journal of Statistical Mechanics: Theory and Experiment, vol. 02, P02066, 2009.

[8] O.V. Lazorenko, S.V. Lazorenko, L.F. Chernogor, “Wavelet analysis in problrms of the geospace physics”, Kosmichna nauka i technologiya, vol. 11, no. 5/6, pp. 22 – 29, 2005 (in Russian).

[9] N. Wu, Q.-X. Li, P. Zou, “Multifractal properties of solar filaments and sunspots numbers”, New Astronomy, vol. 38, pp. 1–10, 2015.

[10] https://www.sidc.be/SILSO/datafiles.

[11] S. Mallat, *A Wavelet Tour of Signal Processing*, San Diego, CA: Academic Press, 1998.

USE OF COMPOSITIONS OF FUZZY RELATIONS AND TRANSITIVE CONCLUSIONS FOR THE ANALYSIS OF EXPERT EVALUATIONS OF INVESTMENT PROJECTS

D.T. Nidzelsky, M.V. Maksyuta, V.V. Obukhovsky
Faculty of Radiophysics, Electronics and Computer Systems, Taras Shevchenko National University of Kyiv, Kyiv, Glushkova Ave., 4g, e-mail: anonimnay005@gmail.com

A consistent methodology for analyzing expert evaluations of investment projects based on fuzzy set theory is presented. From the initial assessments (experts × factors × projects), the matrices "Expert × Factor" and "Factor × Project" are constructed. Then, compositions of fuzzy relations (max–min and max–product) are applied to obtain the "Expert × Project" matrix, as well as the "Factor × Factor" relation and its transitive closure. Comparing the max–min and max–product compositions makes it possible to assess the stability of the project ranking. The closure demonstrates the near-transitivity of the factor structure and forms stable clusters on α-sections, providing convenient criteria for selecting the most attractive project.

In this study, which continues the research initiated in [1], relations are constructed and their transitive closures are computed. To construct the "Expert × Factor" matrix, the average membership degrees across projects are calculated for each of the ten factors and five experts, followed by normalization across factors (to obtain a weight vector $w_e(x_k)$ on the interval [0, 1] with a unit sum):

$$\mu_e(x_k) = \frac{\mu_e^A(x_k) + \mu_e^B(x_k) + \mu_e^C(x_k)}{3},\ w_e(x_k) = \frac{\mu_e(x_k)}{\sum_{l=1}^{10}\mu_e(x_l)}.$$

When constructing the "Factor × Project" matrix, the average membership degrees across experts are computed for each (factor, project) pair and normalized across projects (a vector for each factor):

$$\nu_k(j) = \frac{1}{5}\sum_{e=1}^{5}\mu_e^j(x_k),\ \sigma_k(j) = \frac{\nu_k(j)}{\sum_{j=(A,B,C)}\nu_k(j)}.$$

The compositions are defined as follows (see [2]):

$$r_{ej}^{mm} = \max_{k=1,\ldots,10}\min\left[w_e(x_k), \sigma_k(j)\right],\ r_{ej}^{mp} = \max_{k=1,\ldots,10}\left[w_e(x_k)\cdot\sigma_k(j)\right].$$

These two types of composition yield different interpretations of the results, and the final project support value represents the average evaluation among experts:

$$\langle r_j \rangle = \frac{1}{5}\sum_{e=1}^{5} r_{ej}.$$

This approach provides both a "cautious" view (max–min, sensitive to individual assessments) and a "smooth" view (max–product, emphasizing overall consistency). Structural factor analysis is performed using the "Factor × Factor" matrix $\hat{R}$, where each element is the average of the minimum paired estimates (experts × projects):

$$R_{ij} = \frac{1}{15}\sum_{e=1}^{5}\sum_{P=(A,B,C)}\min\left[\mu_e^P(x_i), \mu_e^P(x_j)\right],\ i,j = 1,\ldots,10.$$

Next, the following transitive closures are iteratively calculated:

$$R^{(t+1)} = \max\left[R^{(t)}, R^{(t)} \circ R^{(t)} \right] \quad (\max - \text{prod}),$$

$$R^{(t+1)} = \max\left[R^{(t)}, R^{(t)} \circ R^{(t)} \right] \quad (\max - \min).$$

The closure adds indirect connections (through intermediate factors), making the relation compositionally stable and suitable for α-clustering. If necessary, a reflexive addition to the diagonal $r_{ii} = 1$ can be applied to interpret the relation as one of similarity.

In the experimental dataset, both compositions produce a consistent project ranking (the difference between max–min and max–product is small), which indicates the stability of the conclusions regarding the choice of priority. The matrix $\hat{R}$ has a "stepped" structure, reflecting an almost uniform order of factor importance; transitive closure modifies it only slightly – a sign of the near-transitivity of the basic relation. α-slices form a stable core of strong factors at high α levels and show a gradual inclusion of weaker factors as the threshold decreases. Factors with low joint activity remain peripheral and can be considered unique targets for focused improvement.

The proposed approach combines transparent aggregation of expert judgments, interpretable compositions of relations, and verification of logical consistency through closure. In practice, this provides two key advantages: a reasoned ranking of competing investment projects with an assessment of stability with respect to the choice of *t*-norm; and a structural map of factor influences with cluster identification and bottleneck detection, which directly suggests directions for management intervention.

In conclusion, we note that when using methods of fuzzy set theory, as demonstrated here with various fuzzy relations, it becomes possible to more predictably select investment projects based on more objective expert evaluations than those proposed in traditional approaches (see, for example, [3]).

References

[1] M.V. Maksyuta, D.T. Nidzelsky, V.V. Obukhovsky. Features of channtling positiveli charged particles along pyramidal directions in hexagonal crystals, Book of proceedings of the 20-th Int. Conf. on Electronics and applied physics, Taras Shevchenko National University of Kyiv, Faculty of RadioPhysics, October 20 – 25, 2024, Kyiv (Ukraine), pp. 56 – 57.

[2] A. Kaufmann, Introductson a la théorie des sous-enstmbles flous. – Paris – New York – Barcelone – Milan: "Masson", 1977.

[3] M.V. Dobryanska, Investment support for technological renewal of machine-building enterprises (dissertation for obtaining the scientific degree of Candidate of Economic Sciences). – Lviv: Lviv Polytechnic Publishing House, 2016. – 216 p.

CALCULATION OF INTERACTION POTENTIALS OF POSITIVELY CHARGED PARTICLES WITH THE MAIN AXES IN CRYSTALS WITH A FLUORITE STRUCTURE

M.V. Maksyuta, V.I. Vysotskii, D.M. Maksyuta, S.V. Efimenko, A.O. Stakhova
Faculty of Radiophysics, Electronics and Computer Systems, Taras Shevchenko National University of Kyiv, Kyiv, Glushkova Ave., 4g, E-mail: maksyuta.dima@outlook.com

In this work, the interaction potentials of positively charged particles with the main crystallographic axes [100], [110], and [111] in complex crystals with a fluorite structure (CaF_2, SrF_2 and BaF_2) were calculated using the Moliere, Firsov, and Barrett approximations at a temperature of T = 300°K. It is shown that the deepest potential wells are formed when positively charged particles are channeled along the [100] and [110] charged axes.

In [1], it was shown that for positively charged particles (positrons, protons) moving along charged axes in ionic crystals with the CsCl structure, potential wells with a depth of about 1 – 3 eV arise. In [2], it was demonstrated that for positively charged particles moving along the c-axes in many hexagonal crystals, potential wells with a depth of about 3 – 15 eV can occur, making it possible to realize effective channeling, for example, of positron beams with different Lorentz-factors and angular divergences to obtain intense spontaneous short-wavelength radiation. Continuing this research, in the present work we calculate the interaction potentials of positively charged particles with the main axes [100], [110], and [111] in complex ionic crystals with the fluorite structure CaF_2, SrF_2, and BaF_2.

We start from the single-particle potentials $\varphi_{\pm}(r) = e\left(Z_{\pm} \mp e^*_{\pm}\right)\chi\left(r/b_{\pm}\right)\Big/ r \pm e^*_{\pm} e/r$ for positively charged ions Ca^{2+}, Sr^{2+}, Ba^{2+}, and the negatively charged ion F^-. Here, $b_{\pm} \approx 0.885 a_0 Z_{\pm}^{-1/3}$ are the Thomas – Fermi screening radius, a_0 is the Bohr radius, and $\chi(x) = \sum_j \alpha_j \exp\left(-\beta_j x\right)$ (the parameters α_j and β_j for the approximations used can be found, for example, in [1, 2]); $Z_{\pm}$ and $e^*_{\pm}$ are the nuclear and effective charges of the corresponding ions in units of the elementary charge. The values $e^*_{\pm}$ for the Ca^{2+}, Sr^{2+}, Ba^{2+}, and F^- ions are equal to $e^*_+ = 2\alpha_{1,2,3}$, $e^*_- = -\alpha_{1,2,3}$, where $\alpha_1 \approx 0.86$, $\alpha_2 \approx 0.85$, $\alpha_3 \approx 0.87$ [3]. Averaging the first terms in the expressions $\varphi_{\pm}(r)$ both along the axes and over thermal vibrations yields

$$\left\langle \Phi_{0\pm}(\rho) \right\rangle_{u_{\pm}} = \frac{2e\left(Z_{\pm} \mp e^*_{\pm}\right)}{d_{\pm}} \exp\left(-\frac{\rho^2}{2u_{\pm}^2}\right) \sum_j \alpha_j \int_0^{\infty} K_0\left(\frac{\beta_j u_{\pm} s}{b_{\pm}}\right) I_0\left(\frac{s\rho}{u_{\pm}}\right) \exp\left(-\frac{s^2}{2}\right) s\,ds\,,$$

where $d_{\pm}$ are the distances between like-charged ions along the principal axes, $u_{\pm}$ are the amplitudes of thermal oscillations of these ions, $K_0(x)$, $I_0(x)$ are, respectively, the Macdonald function zero order and the modified Bessel function of zero order. Similar averaging is performed for the second (Coulomb) terms in the expressions $\varphi_{\pm}(r)$, with an additional summation over electrically neutral shells (see [1]). Figures 1a, b, c show 3D plots of the total interaction potentials of positively charged particles with the main axes in the CaF2 crystal. The contour plots below them present the potential level lines with a step of 0.25 eV.

Table 1 summarizes the depths of the potential wells for the main axes in CaF_2, SrF_2, and BaF_2 crystals, obtained using the three approximations.

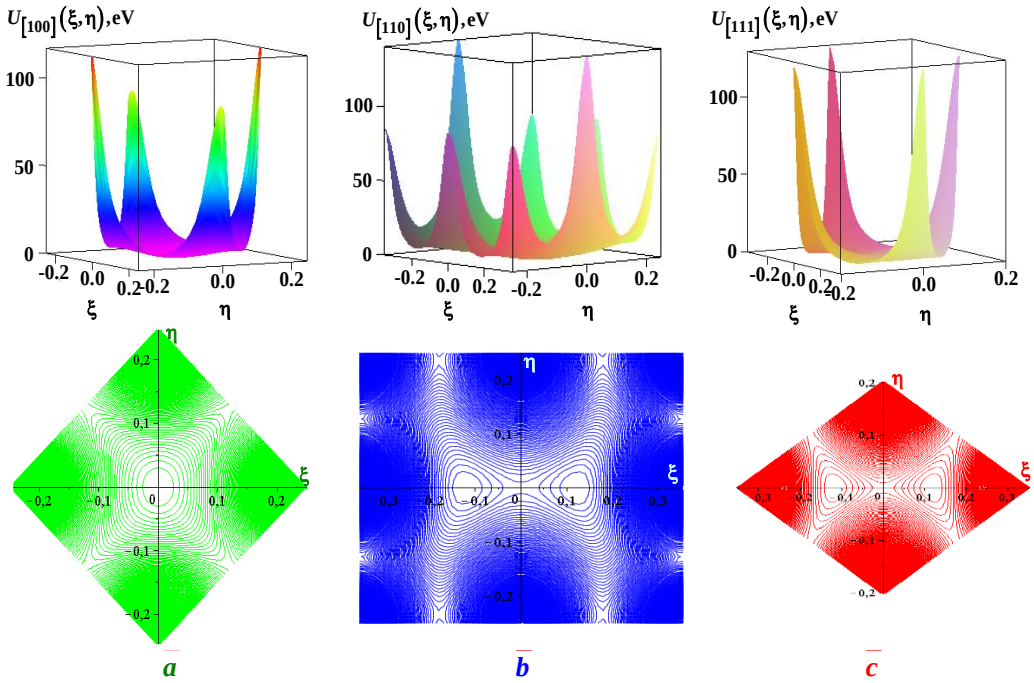

Fig. 1. 3D plots and contour lines of the interaction potential of positively charged particles with the crystallographic axes [100] – (a), [110] – (b), and [111] – (c) in the fluorite crystal CaF_2

Table 1: Depths of potential wells (in eV) calculated using the Molière, Firsov, and Barrett approximations for positively charged particles channeled along the main axes [100], [110], and [111] in CaF_2, SrF_2, and BaF_2 crystals at T = 300°K

Approximation	Moliere			Firsov			Barrett		
Crystal \ Axis	[100]	[110]	[111]	[100]	[110]	[111]	[100]	[110]	[111]
CaF_2	3.75	6.25	1.00	2.50	4.00	0.75	4.50	7.25	1.25
SrF_2	5.00	7.25	1.50	2.50	3.50	1.00	3.00	6.75	0.75
BaF_2	4.25	6.75	1.25	2.25	3.25	0.75	2.25	6.25	0.50

From Table 1 it follows that, for crystals with a fluorite structure, sufficiently deep potential wells are formed along the [100] and [110] charged main axes.

References

[1] N.V. Maksyuta, V.I. Vysotskii, S.V. Efimenko, *Channeling and quasi-characteristic radiation of charged particles in charged axes of CsCl-type ionic crystals*, *Nuclear Instruments and Methods*, B, 355 (2015) 90 – 93.

[2] N.V. Maksyuta, V.I. Vysotskii, D.N. Maksyuta, S.V. Efimenko, *Study of spontaneous radiation during axial channeling of relativistic positrons in hexagonal crystals*, *Nuclear Instruments and Methods*, A, 1058 (2024) 168891.

[3] S.S. Batsanov. Structural chemistry (facts and dependences), Dialogue – MGU, Moscow, 2000.

CONTENTS OF THE CONFERENCE